AGN ACCRETION DISK MEGAMASERS

Dominic Walter Pesce
Westhampton, New York

B.A. Astrophysics & Physics, Harvard College, 2012

M.S. Astronomy, University of Virginia, 2014

A Dissertation Presented to the Graduate
Faculty of the University of Virginia
in Candidacy for the Degree of
Doctor of Philosophy

Department of Astronomy

University of Virginia

May 2018

Committee Members:

James A. Braatz
Shane W. Davis
Aaron S. Evans
D. Mark Whittle
Diana Vaman

© Copyright by

Dominic Walter Pesce

All rights reserved

May 31, 2018

Abstract

Water vapor masers emitting at a frequency of 22 GHz are often associated with active galactic nuclei (AGN), where they are called "megamasers" because of their large luminosities. Very long baseline interferometric (VLBI) observations of these megamasers reveal that they reside in a thin, edge-on accretion disk orbiting the supermassive black hole (SMBH) at sub-parsec radii. The research presented in this thesis has leveraged the unique geometry and simple dynamics of disk megamaser systems to provide powerful astrophysical tools for studying AGN, SMBHs, and cosmology. Using the large dataset of GBT megamaser spectra collected by the Megamaser Cosmology Project (MCP) we have investigated a mechanism for maser excitation, explored the prospects of disk reverberation, discovered an instance of interstellar scintillation, and placed limits on the presence of disk magnetization. We have presented 321 GHz ALMA observations of several AGNs, detecting for the first time H_2O megamaser emission at this frequency towards NGC 4945. We have also introduced the idea of using H_2O accretion disk megamasers as dynamical tracers for measuring SMBH peculiar motion, and we have measured the galaxy recession velocities for a sample of 10 maser disk systems using a combination of spatially resolved neutral hydrogen (HI) disk modeling, spatially integrated HI profile fitting, and optical spectral line and continuum fitting. Our technique achieves a typical precision of $\lesssim$10 km s^{-1} in the SMBH peculiar velocity measurement. As part of the MCP, we have conducted spectral monitoring and VLBI mapping observations of the megamaser disk galaxy CGCG 074-064 to measure its distance. In our preliminary fitting of a three-dimensional warped-disk model to the data, we measure a SMBH mass of $2.28^{+0.20}_{-0.18} \times 10^7$ M$_\odot$ and a geometric distance to the system of $82.98^{+7.33}_{-6.48}$ Mpc. From the results of the disk modeling, we constrain the Hubble constant to be $H_0 = 83.91^{+7.83}_{-7.45}$ km s^{-1} Mpc^{-1}.

"The road to wisdom? Well, it's plain
and simple to express:
err, and err, and err again,
but less, and less, and less."

Acknowledgments

Back in January of 2012, while I was attending a AAS meeting and fretting over my remaining grad school application deadlines, an NRAO astronomer by the name of Jim Braatz stopped by my poster and engaged me in conversation about my research. He then invited me over to his own poster, where I was first exposed to the world of megamasers and captivated by the scientific promise they held. I am happy to say that this interest has proven to be anything but momentary, and it is my great pleasure to thank Jim for taking me on as his student for these past six years. Between imparting his radio astronomy wisdom, laying down the laws of good scientific writing, and putting up with my endless stream of impromptu questions (do you have a few minutes?), Jim has consistently demonstrated a pragmatism and stamina that I can only strive to emulate. I feel fortunate to have had such an exemplary mentor guide me through my graduate career, and I look forward to continuing our collaboration into the future.

I would be remiss not to mention some of my other collaborators, many of whom are also members of the MCP. I have Cheng-Yu Kuo and Feng Gao to thank for numerous conversations about the intricacies of VLBI data reduction. Jim Condon and the late Fred Lo were always happy to provide insight into the various fundamentals of cosmology and radio astronomy, and they demonstrated patience even when my questions were undoubtedly rudimentary. Mark Reid has been an invaluable resource in my quest to learn more about numerical techniques, model fitting, and statistical analyses.

I'd like to thank many of my professors here at UVa, and especially those on my thesis committee, for cultivating a thoroughly welcoming environment that I feel I was able to thrive in. Zhi-Yun Li deserves special mention for letting me regularly crash his bi-weekly group meetings, even though I've still never done any work on star and/or planet formation (maybe one day!). I wish to extend a particularly heartfelt thank-you to Mark Whittle for all of the wonderful conversations about cosmology, pedagogy, and astronomy in general, and for his unwavering support through the full duration of my time here (extra credit goes to Mary, Matthew, and Lizzy for that last bit).

I have benefited from the companionship of many of my fellow graduate students. The Downstairs Office™ wouldn't have been complete without the folks occupying it, that dream team consisting of Chenliang, Haifeng, Nick, Oza, Scott, and Sun Meng. We had the office on lock for three full years, and I couldn't have picked a better bunch to spend it with. Scott and Haifeng deserve a shout-out for sticking with it through a fourth year, and Oza for being the social glue that got it all started (and also for the desk I inherited). I'd like to acknowledge a more sincere debt of gratitude that I owe to Scott, primarily for holding the unenviable position of being the person who has had to deal with the largest volume of my nonsense over the past four years.

Rewinding a bit, I must acknowledge some of those who had a hand in setting me on this path in the first place. Mr. Bob Mirro – sole proprietor of email address thephysicsteacher@gmail.com – taught me my very first physics course (may the net force be with you!), and I continue to look forward to chatting with him every time I visit Long Island. I'd also like to thank Bob Kirshner – the second Bob I've been able to call a mentor – for introducing me to research and for encouraging (and abetting) my often unorthodox problem-solving mindset.

A quick thank-you also goes to my friends from back home, primarily Andy, Casey, and Paul. As some of my last remaining ties to the real world, I believe it's fair to say that I owe a large chunk of my sanity to these kids. Paul especially – partially by virtue of living nearby, but more importantly by virtue of caring so much – has been a much-needed anchor during some pretty stormy days.

And of course, I must thank my family for the role they have played in shaping my life. My parents in particular, despite choosing such practical fields to spend their own lives working in, have never once questioned the wisdom of their wayward son in pursuing what might reasonably be viewed as the height of frivolity. Their support from literal Day 1 has been one of my life's great constants, and the highest praise I could ever hope to receive would be that this work lives up to my mother's standard of rigor and my father's standard of integrity.

Table of contents

List of figures

List of tables

Chapter 1

Introduction

1.1 Masers

It has been recognized since Einstein's seminal work (Einstein 1916, Einstein 1917) that electromagnetic fields can cause quantum mechanical systems to transition between energy states in three distinct ways. For a two-state system with energy levels E_1 and E_2 separated by $E_2 - E_1 = h\nu_0$ and having statistical weights g_1 and g_2, these are:

1. Spontaneous emission of a photon, causing the system to transition from E_2 to E_1. This process is characterized by a coefficient A_{21} that gives the probability per unit time (units of s^{-1}) for the transition to occur.

2. Absorption of a photon, causing the system to transition from E_1 to E_2. This process is characterized by a coefficient B_{12} (units of $\mathrm{erg}^{-1}\ \mathrm{cm}^2\ \mathrm{sr}$) that, when multiplied by the line-averaged mean intensity J (for a normalized line profile ϕ_ν, the line-averaged mean intensity is defined to be $J \equiv \int_0^\infty J_\nu \phi_\nu d\nu$), yields the probability per unit time for a photon with energy $h\nu$ to be absorbed from the ambient radiation field with mean intensity J_ν.

3. Stimulated emission of a photon, causing the system to transition from E_2 to E_1. This process is analogous to reverse absorption, and it is characterized by a coefficient B_{21} that (when multiplied by J) gives the probability per unit time for a photon with energy $h\nu$ to be emitted.

These three coefficients satisfy the Einstein relations,

$$A_{21} = \frac{2h\nu_0^3}{c^2} B_{21}, \tag{1.1a}$$

$$g_1 B_{12} = g_2 B_{21}, \tag{1.1b}$$

such that knowledge of a single coefficient is sufficient to determine the remaining two. Einstein found that a stimulated emission process must exist for the thermal equilibrium radiation field to obey Planck's law.

The radiative transfer equation can be written in terms of the Einstein coefficients as (Rybicki & Lightman 1986)

$$\frac{dI_\nu}{ds} = -\frac{h\nu}{4\pi}\left(n_1 B_{12} - n_2 B_{21}\right)\phi_\nu I_\nu + \frac{h\nu}{4\pi} n_2 A_{21}\phi_\nu, \tag{1.2}$$

where n_1 and n_2 are the number densities of systems in states E_1 and E_2, respectively, and s is the distance along the radiation propagation direction. Equation 1.2 can be written in the standard form $\frac{dI_\nu}{ds} = -\alpha_\nu I_\nu + j_\nu$ by defining the absorption coefficient α_ν and emission coefficient j_ν as

$$\alpha_\nu \equiv \frac{h\nu}{4\pi}\left(n_1 B_{12} - n_2 B_{21}\right)\phi_\nu = \frac{h\nu}{4\pi} n_1 B_{12}\left(1 - \frac{n_2 g_1}{n_1 g_2}\right)\phi_\nu \tag{1.3}$$

and

$$j_\nu \equiv \frac{h\nu}{4\pi} n_2 A_{21}\phi_\nu, \tag{1.4}$$

respectively. If α_ν and j_ν are constant in s, then Equation 1.2 has the solution

$$I_\nu(s) = I_\nu(0)e^{-\alpha_\nu s} + \frac{j_\nu}{\alpha_\nu}\left(1 - e^{-\alpha_\nu s}\right), \tag{1.5}$$

where $I_\nu(0)$ is the incident radiation intensity.

For systems in thermal equilibrium, the level populations n_1 and n_2 obey the Maxwell-Boltzmann distribution

$$\frac{n_2 g_1}{n_1 g_2} = \exp\left(-\frac{h\nu_0}{kT}\right) < 1, \tag{1.6}$$

meaning that $\frac{n_1}{g_1} > \frac{n_2}{g_2}$ for all T. However, it is possible to have nonequilibrium systems satisfying $\frac{n_1}{g_1} < \frac{n_2}{g_2}$, in which case we say that the population is inverted. We can see from Equation 1.3 that an inverted population will have a negative absorption coefficient, causing the radiation intensity to increase exponentially with s. Such a system is called a maser – which is an acronym that stands for microwave amplification by stimulated emission of radiation – and it is the radio-frequency equivalent of a laser.

Though it requires rather sophisticated equipment to produce a maser or laser here on Earth, where thermal equilibrium is the norm, it turns out that there are astrophysical environments in which a population inversion can be sustained across a region large enough to amplify the maser emission to a level that can be seen across cosmic distances. Reviews on the status of astrophysical maser research have been written roughly once a decade since their initial discovery in 1965 (Gundermann 1965, Weaver et al. 1965), and can be found in Litvak (1974), Reid & Moran (1981), Elitzur (1992), and Lo (2005). This thesis is primarily concerned with extragalactic H_2O masers, dubbed "megamasers" because of their large luminosities compared to interstellar Galactic masers.

1.1.1 The water molecule

In molecular spectroscopy, the H_2O molecule is described as an asymmetric top with rotational energy levels typically labeled using the notation J_{K_a,K_c}, with J being the rotational angular momentum quantum number. The labels K_a and K_c arise from solving the Schrödinger equation in a symmetric top basis, and they describe the projection of the angular momentum onto the molecular symmetry axis in the limit that the molecule is deformed into a prolate and oblate top, respectively (Bernath 2005). For a given value of J, there are $2J + 1$ energy levels having energies that increase with K_a and decrease with K_c.[1] The nuclear spins of the hydrogen atoms' protons can be aligned (for a total nuclear spin of $I = 1$) or anti-aligned ($I = 0$), giving rise to two spin isomers of water molecules that are called ortho-water and para-water, respectively, and which share no dipole-allowed transitions between them. Figure 1.1 shows the H_2O rotational energy levels for different values of J, K_a, and K_c.

The primary transition of interest for this thesis is the $6_{1,6}$–$5_{2,3}$ rotational transition in the ground vibrational state of ortho-H_2O (see the left panel of Figure 1.1), which is typically referred to as "the 22 GHz transition" or even just "the water

[1]For this reason the energy levels are sometimes labeled as J_τ, with $\tau = K_a - K_c$ running from $-J$ to $+J$ in order of increasing energy. This labeling scheme is in some sense more physically meaningful, as neither K_a nor K_c is a good quantum number except in the limiting case of a symmetric top.

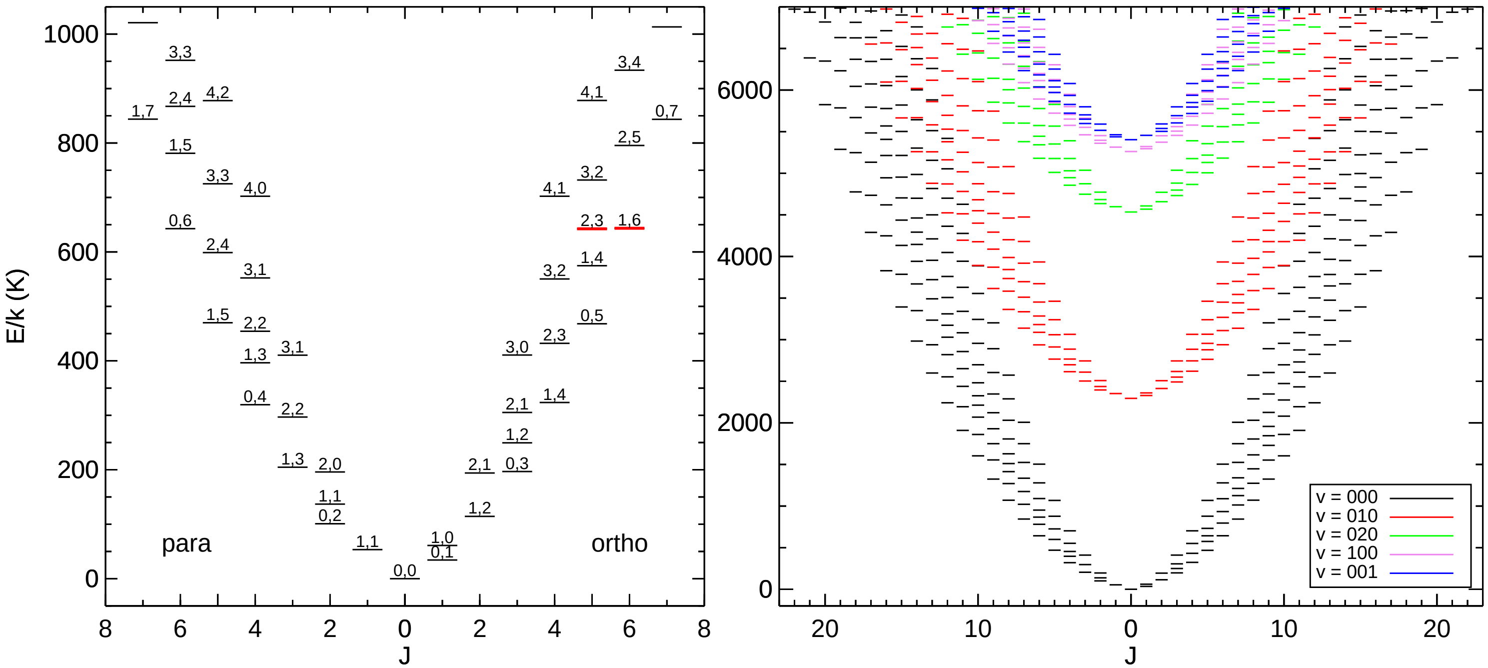

Fig. 1.1.— Rotational energy level diagrams for the H_2O molecule, with the horizontal axes showing angular momentum quantum number J and the vertical axes giving the energy in temperature units. All energy and quantum number information used in these plots has been taken from the HITRAN2012 molecular spectroscopic database (Rothman et al. 2013). *Left*: rotational energy levels up to 1000 K in the ground vibrational state. Each energy level is labeled with its corresponding (K_a, K_c) pair, and the para and ortho transitions are plotted separately on the left and right sides of the plot, respectively. The two energy levels ($6_{1,6}$ and $5_{2,3}$) corresponding to the 22 GHz maser transition are highlighted in red. *Right*: rotational energy levels up to 7000 K in the first few vibrational states. The vibrational states are labeled as $v = v_1 v_2 v_3$, with v_1 corresponding to the symmetric stretch mode, v_2 to the bending mode, and v_3 to the asymmetric stretch mode. Para and ortho transitions are again plotted separately on the left and right sides of the plot, respectively.

maser line." The water maser line is actually a blend of six hyperfine components (a splitting caused by the interaction between the nuclear spins of the hydrogren atoms with the molecular rotational angular momentum) having an intensity-weighted mean frequency (in local thermodynamic equilibrium) of 22.23507985 GHz (Kukolich 1969).

1.1.2 Saturation and beaming

Maser radiative transfer is complicated by the physical process known as saturation. If the stimulated emission rate exceeds the rate at which level populations can be replenished by collisional or radiative processes, then the level populations themselves will be strongly affected by the masing and the maser is said to be saturated. In a saturated maser, I_ν no longer grows exponentially with s.

Ignoring statistical weights (i.e., setting $g_1 = g_2 = 1$), we can write the rate equations for the upper and lower levels of the maser transition as (Goldreich & Keeley 1972)

$$\frac{dn_1}{dt} = R_1 (n - n_1 - n_2) + (n_2 - n_1) B_{21} J + n_2 A_{21} - \Gamma n_1, \tag{1.7a}$$

$$\frac{dn_2}{dt} = R_2 (n - n_1 - n_2) - (n_2 - n_1) B_{21} J - n_2 A_{21} - \Gamma n_2, \tag{1.7b}$$

where n is the total number density of the masing species, Γ is the maser decay rate (assumed to be the same for both states), and R_1 and R_2 are the pump rates per molecule into the lower and upper states, respectively. At the number densities typical of H_2O masers, the maser decay rate will be dominated by collisions and an order-of-magnitude value can be approximated as

$$\Gamma \approx n\sigma v \approx \left(10^9 \text{ cm}^{-3}\right) \left(\pi (1 \text{ Å})^2\right) (2 \text{ km/s}) \approx 0.1 \text{ s}^{-1}. \tag{1.8}$$

Compared to the spontaneous emission rate of $A_{21} = 2 \times 10^{-9}$ s^{-1} (Sullivan 1973), we see that $\Gamma \gg A_{21}$ and so we can safely ignore the spontaneous emission term.

For a steady-state system ($\frac{dn_1}{dt} = \frac{dn_2}{dt} = 0$), we can manipulate Equations 1.7a and 1.7b to write the population inversion

$$\Delta n \equiv n_2 - n_1 = (n_1 + n_2)\frac{\Delta R}{R}\frac{\Gamma}{\Gamma + 2B_{21}J}, \tag{1.9}$$

where $R \equiv R_1 + R_2$ and $\Delta R \equiv R_2 - R_1$ are the sum and difference of the pump rates into the two levels, respectively. From Equation 1.9 we can see that Δn will start to be strongly affected by stimulated emission (the condition for saturation) once $2B_{21}J$ becomes comparable to Γ, yielding a natural expression for the saturated mean intensity,

$$J = \frac{\Gamma}{2B_{21}}. \tag{1.10}$$

Because of the initially exponential nature of maser amplification, the specific intensity seen from a masing cloud of gas will be a very strong function of the line-of-sight path length through the cloud over which this amplification occurs (see, e.g., Lang & Bender 1973, Litvak 1973). This amplification region is known as the "gain path." The maser intensity will be strongest where the gain path is longest, and it will drop dramatically away from the region of highest gain. This highly directional emission behavior is referred to as maser beaming, and it will cause the apparent size of the maser cloud to be strongly influenced by the cloud geometry. The observed location and extent of the maser emission will be dictated by wherever the line-of-sight gain path is longest rather than by the overall distribution of masing material.

For maser emission beamed into a solid angle Ω, the mean intensity J_ν is related to the specific intensity I_ν by $J_\nu = \frac{\Omega}{4\pi} I_\nu$ (Goldreich & Kwan 1974), allowing us to rewrite Equation 1.10 in terms of the saturated specific intensity as

$$I_\nu = \frac{2\pi\Gamma}{B_{21}\Omega}. \tag{1.11}$$

In the saturated regime, we thus have that $\alpha_\nu \propto \Omega^{-1} I_\nu^{-1}$, so that $\frac{dI_\nu}{ds} \propto \Omega^{-1}$ and the maser no longer experiences exponential amplification. Instead, the intensity growth depends on $\Omega(s)$, which for typical geometries (e.g., spherical or cylindrical) scales as $\Omega \propto s^{-2}$ (e.g., Elitzur et al. 1991). In such cases, the intensity in the saturated region will grow as $I_\nu \propto s^3$ and the flux ($F_\nu \propto I_\nu \Omega \propto s$) grows linearly. The exact solution to the radiative transfer equation for a maser with arbitrary geometry has been derived by Elitzur (1990).

1.2 The first disk megamaser

The H_2O maser system in the galaxy NGC 4258 (also known as M106) was discovered by Claussen et al. (1984) while performing a 22 GHz survey of galactic nuclei using the 40-meter telescope of the Owens Valley Radio Observatory (OVRO). Only the systemic features were initially seen, as the $\sim$1300 km s^{-1} bandwidth of the spectrometer precluded the immediate detection of any high-velocity maser features. The authors therefore ascribed the maser activity to star formation originating from a nuclear starburst. However, previous detections of exceptionally luminous H_2O masers towards the nuclei of NGC 4945 (Dos Santos & Lepine 1979) and the Circinus galaxy (Gardner & Whiteoak 1982), along with the concurrent detection of the maser system in NGC 1068 by Claussen et al. (1984) themselves, hinted at the possibility – which the authors allowed for – that an active galactic nucleus (AGN) might have something to do with this new class of bright extragalactic masers.[2]

Followup observations with the VLA (Claussen & Lo 1986)[3] constrained the spatial extent of the systemic maser emission in NGC 4258 to a region no larger than $\sim$1.3 pc in size and centered on the galactic nucleus, thereby eliminating the possibility of a starburst origin. The authors also presented monitoring observations that showed large variability (factor of $\sim$5 over a few months) in individual maser features, which one would not expect if they arose from a superposition of the emission from many star-forming regions. Instead, they proposed that the masers originated from the circumnuclear environment, either in a disk (which had recently been inferred to exist in NGC 1068 by Antonucci & Miller 1985) or in an associated outflow (similar to

[2]Though NGC 4258 had not yet been confirmed to host an AGN, Heckman (1980) had classified its optical spectrum as being intermediate between Seyfert and LINER, and the "anomalous spiral arms" traced by Hα emission (Courtes & Cruvellier 1961) and radio continuum emission (van der Kruit et al. 1972) were thought to indicate past nuclear activity.

[3]The Claussen & Lo (1986) paper appears to be the first instance of the term "megamaser" being used to describe an extragalactic H_2O maser system, though it had previously been applied to the OH masers in IC 4553 (see Baan & Haschick 1984; Norris 1984).

the picture proposed by Elmegreen & Morris 1979 for protostars). The circumnuclear association was solidified with very long baseline interferometric (VLBI) observations of the megamaser system in NGC 4258, which were first made by Claussen et al. (1988) using a transcontinental array consisting of the OVRO 40-meter, the phased VLA, the 43-meter dish at Green Bank, and the Effelsberg 100-meter. The authors detected the strongest maser features in their narrow (instantaneous bandwidth of 2 MHz) spectral window, which showed that the individual masers were separated by roughly $\sim$0.1 mas and that the total extent of the systemic features covered $\sim$1 mas.

A major breakthrough in our understanding of the NGC 4258 maser system was prompted by the detection of high-velocity (offset by $\sim$1000 km s^{-1} to either side of the recession velocity) maser features by Nakai et al. (1993), who used a new spectrometer (bandwidth of 285 MHz) on the Nobeyama 45-meter telescope. Incorporating the Kashima 34-meter telescope to create a two-element interferometer, they also showed that the redshifted high-velocity features were located within 50 mas of the systemic features (the blueshifted features were too faint to detect with these observations). The authors considered three different models that might explain the observed spectral structure: (1) a rotating molecular structure orbiting a massive central object, (2) a bipolar outflow from the nuclear region, or (3) stimulated Raman scattering that produces an up- and down-shifted (by a value equal to the plasma frequency) version of the systemic maser features at lower amplitude. Sensitive VLBI observations would be the most straightforward way of distinguishing between these possibilities, as the high-velocity features should reside within a disk for case (1), fall above and/or below the disk for case (2), and be spatially coincident with the systemic features for case (3).

Though the first VLBI maps were not long in coming, there was such a flurry of activity following the Nakai et al. (1993) results that quite a bit of important work got done prior to the publication of any VLBI observations. Makishima et al. (1994) observed NGC 4258 in X-rays using the Advanced Satellite for Cosmology and Astrophysics (ASCA). After correcting for the heavy absorption (amounting to a hydrogen absorbing column of $N_H = 1.5 \times 10^{23}$ cm^{-2}), the total observed luminosity in the 2-10 keV band (4×10^{40} erg s^{-1}) confirmed that the galaxy hosts a low-luminosity

AGN. Haschick et al. (1994) presented 7 years of single-dish (Haystack 36.6-meter) monitoring data on the systemic features in NGC 4258, demonstrating that these features display large ($\sim$10 km s^{-1} yr^{-1}) line-of-sight accelerations.[4] These acceleration measurements were corroborated by Greenhill et al. (1995a), who conducted a separate series of monitoring observations (using the Effelsberg 100-meter telescope) that also included the high-velocity features (which were found to have a line-of-sight acceleration consistent with zero). Watson & Wallin (1994) were the first to fit many of these pieces together into something resembling what is now considered to be the canonical picture for disk maser geometry (see § 1.3). Their model contains only a single ring of masing gas, but it reproduces many of the salient observed properties including the line-of-sight accelerations of the systemic maser features, the lack of a similar acceleration in the high-velocity features, and the overall "triple-peaked" spectral profile (see, e.g., Figure 1.3).[5]

Then came the first of the VLBI maps. Greenhill et al. (1995b)[6] made a map of the systemic features, showing that they form a linear pattern on the sky with a constant line-of-sight velocity gradient. Miyoshi et al. (1995) presented the first complete map containing both the systemic and high-velocity features (see Figure 1.2). The high-velocity features are spatially offset to either side of the systemic features in what appears to be a warped edge-on disk structure, and they trace out a Keplerian ($v \propto r^{-1/2}$) rotation curve when plotted in position-velocity space. The authors also demonstrated the ability to use these high-velocity features to precisely measure the interior mass density, providing the strongest and most direct evidence to date that supermassive black holes (SMBHs) were indeed the "massive dark objects" known to be situated in galactic nuclei (see, e.g., Kormendy & Richstone 1995, Maoz 1995). In a companion paper, Moran et al. (1995) expand on the discussion from Miyoshi et al.

[4] Haschick et al. (1994) actually did one better than just measuring the accelerations of systemic features – they also measured a *gradient* in the accelerations with velocity, increasing from $\sim$6 km s^{-1} yr^{-1} at a velocity of $\sim$430 km s^{-1} up to $\sim$10 km s^{-1} yr^{-1} at a velocity of $\sim$540 km s^{-1}. This acceleration gradient was later confirmed by Humphreys et al. (2008), and might be explained by the presence of spiral structure in the disk.

[5] In the acknowledgments section of their paper, Watson & Wallin (1994) write: "It is a pleasure to acknowledge that this investigation arose as a result of discussions with K.-Y. Lo."

[6] First presented in Greenhill et al. (1994).

(1995) and describe how striking the discovery of near-perfect Keplerian rotation of the high-velocity features was. The authors point out the "puzzling realization" that while the systemic masers seem to be confined to a narrow annulus, the high-velocity features show a large spread in orbital radius. They also provide a discussion of the (unresolved) disk scale height, on which they place an upper limit of 0.01 mas (corresponding to ∼76 AU). The implied aspect ratio of $H/R \approx 2.5 \times 10^{-3}$ can be converted into a limit on the gas temperature for a disk in hydrostatic equilibrium ($T \lesssim 1000$ K), or into a limit on the toroidal magnetic field strength ($B \lesssim 0.25$ G) if the disk is magnetically supported.

Herrnstein et al. (1996b) were the first to develop a "global disk-fitting model" for the maser disk in NGC 4258, using VLBI position and velocity data for every maser spot. The details of the model and fitting procedure are outlined in Herrnstein's PhD thesis (Herrnstein 1997). While the original analyses detailed in Miyoshi et al. (1995) and Moran et al. (1995) had an elegant simplicity that captured the orderly structure of the maser disk (i.e., that of a nearly flat, nearly edge-on disk), the data showed clear evidence for unmodeled structure at a level significant enough to warrant further attention. The algorithm presented in Herrnstein (1997) represented a marked increase in sophistication over the previous analyses, and incorporated disk warping in both position angle and inclination (parameterized as polynomials), generalized maser locations within the disk (i.e., no longer restricting the high-velocity features to the midline and the systemic features to a single orbital radius), and relativistic effects (both special and general). Herrnstein used this disk model to obtain two independent geometric distance estimates to NGC 4258, one based on systemic feature accelerations (see also § 1.3.1) and the other based on their proper motions. These two distance measurements show remarkable agreement, as detailed in Herrnstein et al. (1999), and together yielded a value of 7.2 ± 0.5 Mpc (a ∼7% uncertainty) for the distance to the galaxy. This value represented the most precise absolute extragalactic distance measurement obtained to date.

The next step forward in maser disk modeling came from an observing campaign based out of the Harvard-Smithsonian Center for Astrophysics (CfA) with the goal of decreasing the uncertainty in the distance measurement to NGC 4258 (Humphreys

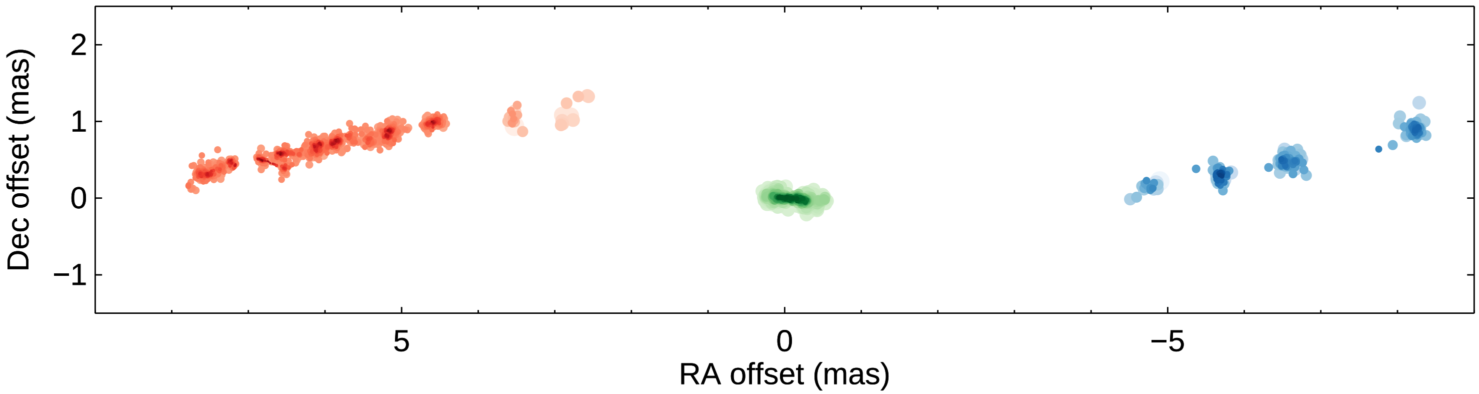

Fig. 1.2.— VLBI map of the maser system in NGC 4258. The data points are colored by velocity group, with the red points corresponding to redshifted features, the blue points to blueshifted features, and the green points to systemic features. The colors are darker for stronger maser spots, and the symbol sizes are proportional to the inverse square root of the maser amplitude (so that data points with larger positional uncertainties appear larger). The data used to generate this map have been taken from Argon et al. (2007).

et al. 2005a). The motivation behind this campaign was to use NGC 4258 as an anchor in the cosmic distance ladder, capable of providing a zeropoint for Cepheid variable luminosity calibration and thereby serving as a crucial stepping stone for standard candle measurements of H_0. Argon et al. (2007) detail the map of the maser system made from 18 dedicated VLBI tracks, and Humphreys et al. (2008) describe the acceleration measurements made from combining spectral monitoring observations spanning over a decade (from 1994 April to 2004 May). These two classes of observations were synthesized in Humphreys et al. (2013), who performed a global disk fit to the data using an improved version of the technique pioneered by Herrnstein et al. (1996b).[7] The authors simultaneously fit the position, velocity, and acceleration measurements for every maser spot in the context of a 3D warped thin disk system, allowing for the possibility of non-circular orbital motion. Their updated distance measurement of 7.60 ± 0.23 Mpc (a $\sim$3% uncertainty[8]) remains the most precise absolute distance to any extragalactic system.

The galaxy NGC 4258 showcases the remarkably broad utility of AGN accretion disk megamaser systems as astrophysical tools. They uniquely probe the accretion disk on sub-parsec scales and yield access to measurements of the molecular gas distribution, magnetic field strengths, SMBH masses, and geometric distances.

1.2.1 Alternative theories

The edge-on disk picture does an excellent job of explaining the observed properties of the NGC 4258 maser system, and it defines the modern consensus. But what seems evident in hindsight wasn't always necessarily so clear, and various alternative theories have been put forward at one point or another to explain different aspects of the maser emission seen towards NGC 4258. In this section we briefly discuss a number of these other theories, along with the observations that could test (or already have tested) them.

[7]This new disk-fitting algorithm actually saw its debut in the Megamaser Cosmology Project measurement of the maser system in the galaxy UGC 3789 (Reid et al. 2013).

[8]The systematic uncertainty component was later reduced even further by Riess et al. (2016), who used the same technique as Humphreys et al. (2013) but performed substantially longer (by a factor of 100) MCMC runs. The authors obtained a distance of 7.54 ± 0.20 Mpc (a $\sim$2.7% uncertainty).

Crusius & Schlickeiser (1988b) proposed that the emission seen from NGC 4258 was mostly synchrotron maser emission, with an interstellar water maser having a luminosity typical of Galactic masers ($\sim$0.1 $L_\odot$) providing the seed photons. Relativistic electrons near an AGN can develop a sharply-peaked energy distribution because the acceleration timescale (from Fermi acceleration across shocks) is much shorter than the timescale for escaping from the acceleration region (see Schlickeiser 1984). The resulting electron distribution is nearly monoenergetic, with the peak energy corresponding to the value where the energy gain by shock wave acceleration is balanced by the energy losses from radiation. Crusius & Schlickeiser (1988a) showed that such an electron energy distribution can lead to a negative synchrotron absorption coefficient, which will then permit strong maser emission if the medium is optically thick enough. In the proposed model for NGC 4258, an interstellar water maser source lies along the line of sight *behind* the acceleration region for the electrons. The negative absorption coefficient in the foreground acceleration region boosts the background maser emission (and the surrounding continuum) to the observed levels. However, this synchrotron maser picture also predicts a broad (several GHz) amplified continuum bump in the vicinity of the maser features, which is not seen in observations. Additionally, an interstellar maser is incapable of accounting for the large central mass implied by the high-velocity feature rotation curve. The synchrotron maser explanation is thus effectively ruled out.

Haschick & Baan (1991) presented monitoring observations of the systemic features in NGC 4258, observed at a $\sim$monthly cadence between 1986 July and 1990 June using the 36.6-meter Haystack dish. The strongest maser feature appeared to show periodic flaring behavior with a period of $\sim$85 days, which the authors interpreted as caused by a variable pumping rate from a Mira-type star. The linewidth of the flaring feature was correlated with its intensity roughly as $\Delta\nu \propto I^{-0.5}$, which is the expected relation for unsaturated masers. In this model, a foreground variable star is providing a variable pump rate for inverting the H_2O in its immediate environment, which in turn is amplifying the background continuum from the AGN. The (negative) optical depth for the (unsaturated) foreground medium need only be on the order of $\sim$6 to give rise to the observed maser intensity; the authors note that such a system would likely not be visible if it weren't for the background continuum.

Deguchi (1994) proposed that the high-velocity features in NGC 4258 are caused by stimulated Raman scattering, whereby the masers reside behind region of dense ionized gas (e.g., a compact HII region). In this picture, a systemic maser photon interacts with longitudinal plasma waves in the ionized gas, stimulating the creation of two daughter photons having frequencies up-shifted and down-shifted from the original systemic frequency by an amount equal to the plasma frequency $\nu_p = \sqrt{n_e e^2/(\pi m_e)}$. To attain a plasma frequency that can account for the $\sim$1000 km s^{-1} offsets of the high-velocity features from the systemic features, the electron density must be $n_e \approx 6.8 \times 10^7$ cm^{-3}. If Raman scattering produces the high-velocity maser features, then they should coincide spatially with the systemic features when observed with VLBI. As many observations have shown the separations between high-velocity and systemic masers to be much larger than the intrinsic sizes of the masers (see, e.g., Miyoshi et al. 1995; Argon et al. 2007), we discard the Raman scattering hypothesis.

Moran (1997) discusses the possibility that the high-velocity maser features in NGC 4258 arise from either infall or outflow, rather than Keplerian rotation.[9] For freely (i.e., ballistic) infalling material that started from rest at infinity, the velocity at a distance r from the central mass can be obtained from energy conservation,

$$v_{\rm in}(r) = \sqrt{\frac{2GM}{r}}. \tag{1.12}$$

In this picture, the redshifted high-velocity features lie in front of the disk midplane and are falling radially towards the central mass, while the blueshifted high-velocity features are doing the same thing but approaching from behind the midplane. A ballistic outflow (launched at the escape velocity) would follow the same velocity law, with the only difference being a sign change in the direction of motion for both sets of high-velocity features. Within the context of this model, the upper limits on line-of-sight accelerations and proper motions for the high velocity features correspond to a

[9]In fairness to Jim Moran, no real effort was made on his part to advocate this alternative model. As he explains in a charming disclaimer from the conclusion of the paper: "Since the Keplerian disk model fits the data so beautifully, I hesitated to bring up alternate possibilities. However, it is interesting to note that the infall/outflow model can be ruled out on plausibilitiy arguments, but not, strictly speaking, on the basis of the available measurements."

constraint on the angle ϕ between the line of sight and the direction of infall/outflow. Because Equation 1.12 scales with r in the same way that a Keplerian orbit does (see Equation 1.13), this model is in principle consistent with the data. However, the level of coincidence required to account for the observed geometry seems implausible; the high-velocity features would need to be infalling/outflowing in a direction that is almost perfectly aligned with both the line of sight and the plane of the disk as defined by the systemic features.

1.3 Disk megamasers in general

The discovery of the first extragalactic H_2O maser was made by Churchwell et al. (1977) towards M33, and the system showed every sign of being a typical Galactic-style maser associated with star forming regions. Other nearby galaxies have also been observed to host star formation masers (e.g., Lepine & Marques Dos Santos 1977, Huchtmeier et al. 1978, Henkel et al. 1986, Ho et al. 1987), but the first galaxy containing a H_2O maser of a seemingly fundamentally different variety was NGC 4945 (Dos Santos & Lepine 1979). The maser emission seen towards NGC 4945 had an isotropic luminosity that was an order of magnitude larger than the strongest known Galactic masers and several orders stronger than typical Galactic masers. Over the next few years, similarly overluminous "megamaser" emission was seen towards the Circinus galaxy (Gardner & Whiteoak 1982), NGC 1068 and NGC 4258 (Claussen et al. 1984), and NGC 3079 (independently discovered by Henkel et al. 1984 and Haschick & Baan 1985). Each of these galaxies harbors an AGN, and the maser emission in all five cases originates from the galactic nucleus.

Claussen & Lo (1986) were the first to suggest that at least some of these megamasers (specifically in NGC 4258 and NGC 1068) were associated with the circumnuclear disk, which is capable of providing the long gain paths necessary for sufficient amplification. The specific "triple-peaked" spectral structure characteristic of a masing annulus within an edge-on rotating disk was first described by Ponomarev et al. (1994) in the context of the hydrogen maser system seen towards MWC 349. Watson & Wallin (1994) adapted this idea to explain the megamaser system in NGC 4258, though their model again restricted the maser emission to a single thin annulus. It wasn't until Miyoshi et al. (1995) published the full VLBI map of the masers in NGC 4258 that the geometry of the system was well-understood (see also § 1.2), marking it as the first confirmed disk megamaser.

Since NGC 4258, many other megamaser systems have been found to originate from or be associated with AGN accretion disks. After a lull lasting roughly a decade during which no new megamasers were detected, Braatz et al. (1994) presented initial results from a distance-limited survey of active galaxies to search for megamasers. The authors presented five new detections (which at the time constituted a doubling in the number of known megamasers), including the most distant source to date in the galaxy Mrk 1. The completed survey of 354 active galaxies was presented in Braatz (1996) (published in Braatz et al. 1996), out of which 10 were detected as megamasers (including the five galaxies from the initial results paper). This survey showed that megamasers were detected only in Seyfert 2 and LINER galaxies, and never in Seyfert 1 or starburst galaxies. A followup paper (Braatz et al. 1997) subjected the sample to a battery of statistical tests that robustly confirmed this finding, which when interpreted in light of the unified model of AGN (Antonucci 1993) and an understanding of maser beaming lent strong statistical support to a connection between megamasers and AGN accretion disks.

With some understanding of the host galaxy demographics, megamaser discovery rates began to pick up around the late 1990's. At the same time, VLBI observations were confirming that while many of the earliest-detected (i.e. strongest, most nearby) megamaser systems were associated with AGN accretion disks, they often lacked the orderly dynamics of the NGC 4258 system. Greenhill et al. (1996) presented a VLBI map of the masers in NGC 1068, which show a sub-Keplerian rotational signature consistent with an origin on the surface of a thick, massive torus or flared disk structure. Greenhill et al. (1997b) used the southernmost three stations of the VLBA to create a VLBI map of the maser system in NGC 4945. The map suffers from poor sensitivity and *uv*-plane coverage, but the masers appear to trace a linear structure on the sky consistent with them being situated in an edge-on disk. Trotter et al.

(1998) made the first VLBI map of the maser system in NGC 3079[10], showing that the masers trace an extended structure that the authors claim could be an edge-on disk. However, there is a second population of masers spatially offset from the putative disk component (perhaps tracing an outflow), and followup VLBI observations (Sawada-Satoh et al. 2000, Yamauchi et al. 2005) have challenged the original disk picture. The disk interpretation was ultimately upheld by Kondratko et al. (2005), who performed sensitive VLBI observations covering the full velocity extent of the maser emission and showed that the masers displayed a sub-Keplerian rotation curve consistent with residing in a massive disk. A VLBI map of the megamaser system in Circinus, made by Greenhill et al. (2003b), showed that the masers trace both a warped accretion disk and a molecular outflow.

Prior to the start of science operations at the Green Bank Telescope (GBT), roughly 1000 galaxies had been surveyed for H_2O megamaser emission (e.g., Hagiwara et al. 2002, Hagiwara et al. 2003, Greenhill et al. 2003a, Kondratko et al. 2003), with only 22 detections in total (Braatz 2002). Of these, only three[11] showed the triple-peaked spectral signature of a "clean" (i.e., orderly velocity structure that is uncontaminated by non-disk components) Keplerian disk system: NGC 4258, IC 2560 (Ishihara et al. 2001), and Mrk 1419 (Henkel et al. 2002). With the improved sensitivity and larger bandwidths afforded by the new GBT K-band spectrometer, Braatz et al. (2004) re-observed 145 previously surveyed galaxies and discovered 11 new megamasers, including four systems showing disk-like spectra (in the galaxies NGC 591, NGC 4388, Mrk 78, and NGC 6323).

As of the writing of this thesis there are nearly 200 known H_2O megamaser sources, the majority of which have been discovered using the GBT.[12] At least 32 systems show spectral structure indicative of an accretion disk origin (Pesce et al. 2015), and half of these were discovered as part of the survey component of the Megamaser Cosmology

[10]The maser system in NGC 3079 was previously observed with VLBI by Haschick et al. (1990), but the four-element interferometer had poor *uv*-plane coverage and the authors did not attempt to synthesize an image.

[11]The galaxy NGC 2639 shows evidence for accelerating systemic features (Wilson et al. 1995, Braatz et al. 2003), but no high-velocity features have ever been observed for this system.

[12]A list of all known H_2O megamaser sources is maintained on the Megamaser Cosmology Project website: `https://safe.nrao.edu/wiki/bin/view/Main/PublicWaterMaserList`.

Project (MCP; see also § 1.4).

1.3.1 The "megamaser technique"

When observing disk maser systems with VLBI and spectral monitoring, we have direct access to three dynamical quantities for each maser "spot": its plane-of-sky angular position (x, y), its line-of-sight velocity v, and its line-of-sight acceleration a. Each of these quantities is a projected version of its true three-dimensional value, and to convert back to 3D requires that we make some assumptions. The standard and most well-motivated assumption is that the masers reside within a thin, nearly edge-on Keplerian disk, though in principle any model having globally ordered motion could be applied. With such a model in hand, it becomes possible to deproject the dynamical quantities and obtain access to global properties of the system.

Let's consider the simplest case of a flat, perfectly edge-on and circularly rotating disk system sitting in a point-mass potential. It's possible to account for disk inclination, warping, eccentric orbits, and alternative potentials by using additional model parameters, but the increased model complexity comes at the cost of decreased transparency regarding how different observational quantities pin down the underlying physical parameters. For gas in circular Keplerian motion about the central SMBH, the orbital velocity as a function of radius is given by

$$v_\phi = \sqrt{\frac{GM}{r}} = \sqrt{\frac{GM}{\theta_r D}}, \tag{1.13}$$

where M is the mass of the SMBH and we have related the physical orbital radius r to an angular equivalent θ_r by incorporating the distance D to the system. The direction of v will always be azimuthal for circular orbits. Similarly, the acceleration as a function of radius will be

$$a_r = \frac{v^2}{r} = \frac{GM}{r^2} = \frac{GM}{\theta_r^2 D^2}, \tag{1.14}$$

and it will always be pointed radially inwards.

Each maser spot in the disk has an associated orbital radius $r = \theta_r D$ and azimuthal position ϕ, as illustrated in Figure 1.3. For a SMBH located at a position (x_0, y_0) and having a line-of-sight velocity v_0, the observed (projected) quantities are related to their true values by

$$\sqrt{(x - x_0)^2 + (y - y_0)^2} = \theta_r \sin(\phi), \tag{1.15a}$$

$$v - v_0 = v_\phi \sin(\phi), \tag{1.15b}$$

$$a = a_r \cos(\phi). \tag{1.15c}$$

The high-velocity features are located near $\phi \approx \pm 90°$, meaning that the line-of-sight velocities are a good approximation for the true orbital velocities v_ϕ and the measured (angular) separations $\theta \equiv \sqrt{(x - x_0)^2 + (y - y_0)^2}$ are a good approximation for the true (angular) orbital radii θ_r. We thus have (from Equation 1.13)

$$\frac{v^2 \theta}{G} \approx \frac{M}{D}, \tag{1.16}$$

such that the high-velocity position and velocity measurements (i.e., the measured rotation curve) constrain the ratio of the SMBH mass to its distance.

Similarly, the systemic features are located near $\phi \approx 0$, meaning that the line-of-sight accelerations are a good approximation for the true accelerations a_r. If we assume that the systemic features occupy similar orbital radii to the high-velocity features, then we have (from Equation 1.14)

$$\frac{a \theta^2}{G} \approx \frac{M}{D^2}, \tag{1.17}$$

such that the systemic feature accelerations constrain the ratio of the SMBH mass to the square of its distance. Taken together, Equations 1.16 and 1.17 enable us to estimate both M and D from observable quantities.

The simple picture outlined above gives an illustration of how the data constrain the desired measurements, but in practice we can eliminate many of the required assumptions. Performing a simple accounting, for a single maser spot there are four measured quantities (x, y, v, a) and eight quantities that need to be fit as part of the

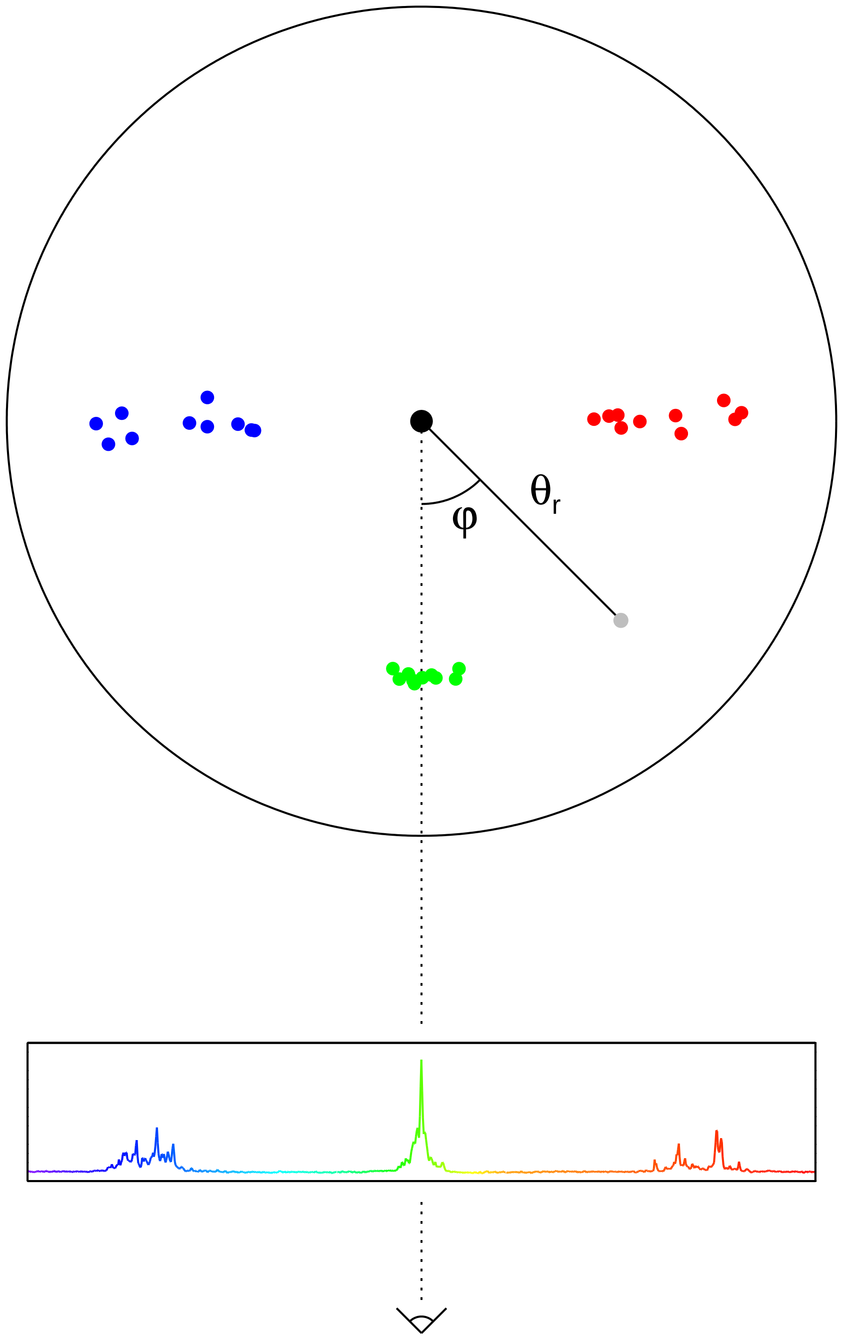

Fig. 1.3.— A cartoon illustrating the typical layout of masers in an edge-on AGN accretion disk system, with the observer situated at the bottom of the page. The maser spots are colored by velocity group, with the red points corresponding to redshifted features, the blue points to blueshifted features, and the green points to systemic features. A gray spot is included to diagram the coordinate system used in § 1.3.1. The inset plot shows a sketch of the characteristic “triple-peaked” spectrum observed from such a maser system; the three sets of maser lines in the spectrum correspond to the three groups of masers in the disk.

basic model (M, D, x_0, y_0, v_0, r, ϕ). If we have two maser spots then there will be eight measured quantities, but only an additional two fitted quantities (the extra r and ϕ for the new maser spot), for a total of 10 model parameters. Adding one more maser spot brings the total number of measured quantities and model parameters to 12 each, making the problem well-posed in the sense that there are in principle enough constraints from the data to fit the degrees of freedom in the model. Fortunately, typical disk maser systems have $\gtrsim$100 maser spots and thus provide many more constraints than free parameters. This additional freedom allows us to add more global parameters to the model, enabling fits of disk warping in both position angle and inclination, as well as higher-order effects such as eccentric orbits, massive disks, or thick disks (see, e.g., Humphreys et al. 2013, Kuo et al. 2017a).

1.3.2 Dynamics-limited gain paths

The characteristic "triple-peaked" spectrum seen in single-dish observations of disk maser systems (e.g., Figure 1.3) is understood to arise from the dynamics of the masing gas. My goal with this section is to provide a transparent and quantitative derivation of the expected gain path lengths through an edge-on accretion disk exhibiting Keplerian rotation, thereby motivating the form of the gain path as a function of line-of-sight velocity that produces the observed spectral structure.

To get significant maser amplification, the emitting material along the gain path must have a total line-of-sight velocity difference roughly less than or equal to the line width of $\Delta v \approx 2$ km s^{-1}. If this condition is not met – either because the photons are Doppler shifted by the Keplerian motion of the gas or gravitationally redshifted by climbing out of the SMBH potential – then the incoming photons will be too far out of resonance to stimulate further emission. We say that a gain path whose length is limited by the line-of-sight velocity coherence within a globally ordered flow (as opposed to, e.g., by the continued availability of an inverted population of water molecules, or by small-scale turbulence) is "dynamics-limited." The spatial distribution of masers in disk systems is thought to be dictated by such dynamics-limited gain paths.

For the rotation curve given by Equation 1.13, the redshift z_D imparted by the Doppler effect will be (Rybicki & Lightman 1986)

$$1 + z_D = \gamma \left(1 - \frac{v}{c} \cos(\theta) \right) , \tag{1.18}$$

where $\gamma = \left(1 - \frac{v^2}{c^2} \right)^{-1/2}$ is the Lorentz factor and θ is the angle between the velocity vector and the line of sight. For a photon originating from a location (r, ϕ) in the disk (with $\phi = 0$ corresponding to the line pointing from the SMBH to the observer), Equation 1.18 becomes

$$1 + z_D = \gamma \left(1 + \frac{v}{c} \sin(\phi) \right) . \tag{1.19}$$

In a Schwarzschild spacetime, the gravitational redshift z_g of a photon emitted at radius r and received at infinity is given by (Schutz 2009)

$$1 + z_g = \left(1 - \frac{R_s}{r} \right)^{-1/2} , \tag{1.20}$$

where $R_s = 2GM_{\mathrm{BH}}/c^2$ is the Schwarzschild radius for the SMBH. Combining the gravitational and Doppler shifts (and ignoring cosmological motion) then yields the total redshift of the photon,

$$1 + z = (1 + z_D)(1 + z_g) . \tag{1.21}$$

Equation 1.21 gives the redshift of the photon as it would be observed infinitely far away from the disk, but what we'd really like to know is the relative velocity shift along the line of sight between two points (r_1, ϕ_1) and (r_2, ϕ_2) in the disk. For small velocity shifts $\Delta v \ll c$, we can write

$$\Delta v = c(z_2 - z_1), \tag{1.22}$$

where z_1 and z_2 are the redshifts (as seen from infinity) of photons that are emitted from (r_1, ϕ_1) and (r_2, ϕ_2), respectively. Ultimately, we will impose the condition that Δv be smaller than the maser line width to determine the length of the maximum gain path along the line of sight for a photon leaving from (r_1, ϕ_1).

Plugging in for z_1 and z_2 in Equation 1.22 and consolidating terms a bit yields

$$\frac{\Delta v}{c} = \frac{1 + r_1 \sin(\phi_1)\sqrt{\frac{R_s}{2r_2^3}}}{\sqrt{\left(1 - \frac{R_s}{2r_2}\right)\left(1 - \frac{R_s}{r_2}\right)}} - \frac{1 + \sin(\phi_1)\sqrt{\frac{R_s}{2r_1}}}{\sqrt{\left(1 - \frac{R_s}{2r_1}\right)\left(1 - \frac{R_s}{r_1}\right)}}, \tag{1.23}$$

where we've used the condition that both points lie along the line of sight to impose the equality $r_1 \sin(\phi_1) = r_2 \sin(\phi_2)$ and eliminate ϕ_2 from the expression. We can determine the gain path ℓ geometrically in terms of r_1, r_2, and ϕ_1,

$$\ell = \sqrt{r_2^2 - r_1^2 \sin^2(\phi_1)} - r_1 \cos(\phi_1), \tag{1.24}$$

where we've assumed that $r_2 > r_1$ (i.e., the photon is moving outwards) so that ℓ is always positive. Using Equation 1.24 to replace r_2 in Equation 1.23, and recasting (r_1, ϕ_1) as (r, ϕ), we obtain the unwieldy but analytic expression

$$\frac{\Delta v}{c} = \frac{1 + r\sin(\phi)\sqrt{\frac{R_s}{2(\ell^2+2\ell r\cos(\phi)+r^2)^{3/2}}}}{\sqrt{\left(1 - \frac{R_s}{2\sqrt{\ell^2+2\ell r\cos(\phi)+r^2}}\right)\left(1 - \frac{R_s}{\sqrt{\ell^2+2\ell r\cos(\phi)+r^2}}\right)}} - \frac{1 + \sin(\phi)\sqrt{\frac{R_s}{2r}}}{\sqrt{\left(1 - \frac{R_s}{2r}\right)\left(1 - \frac{R_s}{r}\right)}}. \tag{1.25}$$

After specifying values for Δv and M_{BH}, Equation 1.25 can be solved numerically for the gain path ℓ as a function of location (r, ϕ) within the disk. In practice, it is only the absolute value of Equation 1.25 that matters, because the line profile is assumed to be symmetric in v. Figure 1.4 illustrates how ℓ varies throughout the disk.

To better understand the different contributions to Equation 1.25, we can use the fact that $r \gg R_s$ for the maser disk systems to Taylor expand the expression:

$$\frac{\Delta v}{c} = \frac{\sin(\phi)}{\sqrt{2}}\left(\frac{R_s}{r}\right)^{1/2}\left(\frac{1}{\left(\frac{\ell^2}{r^2} + \frac{2\ell}{r}\cos(\phi) + 1\right)^{3/4}} - 1\right) + \frac{3}{4}\left(\frac{R_s}{r}\right)\left(\frac{1}{\left(\frac{\ell^2}{r^2} + \frac{2\ell}{r}\cos(\phi) + 1\right)^{1/2}} - 1\right) + \ldots. \tag{1.26}$$

The dominant term corresponds to the contribution from nonrelativistic Doppler

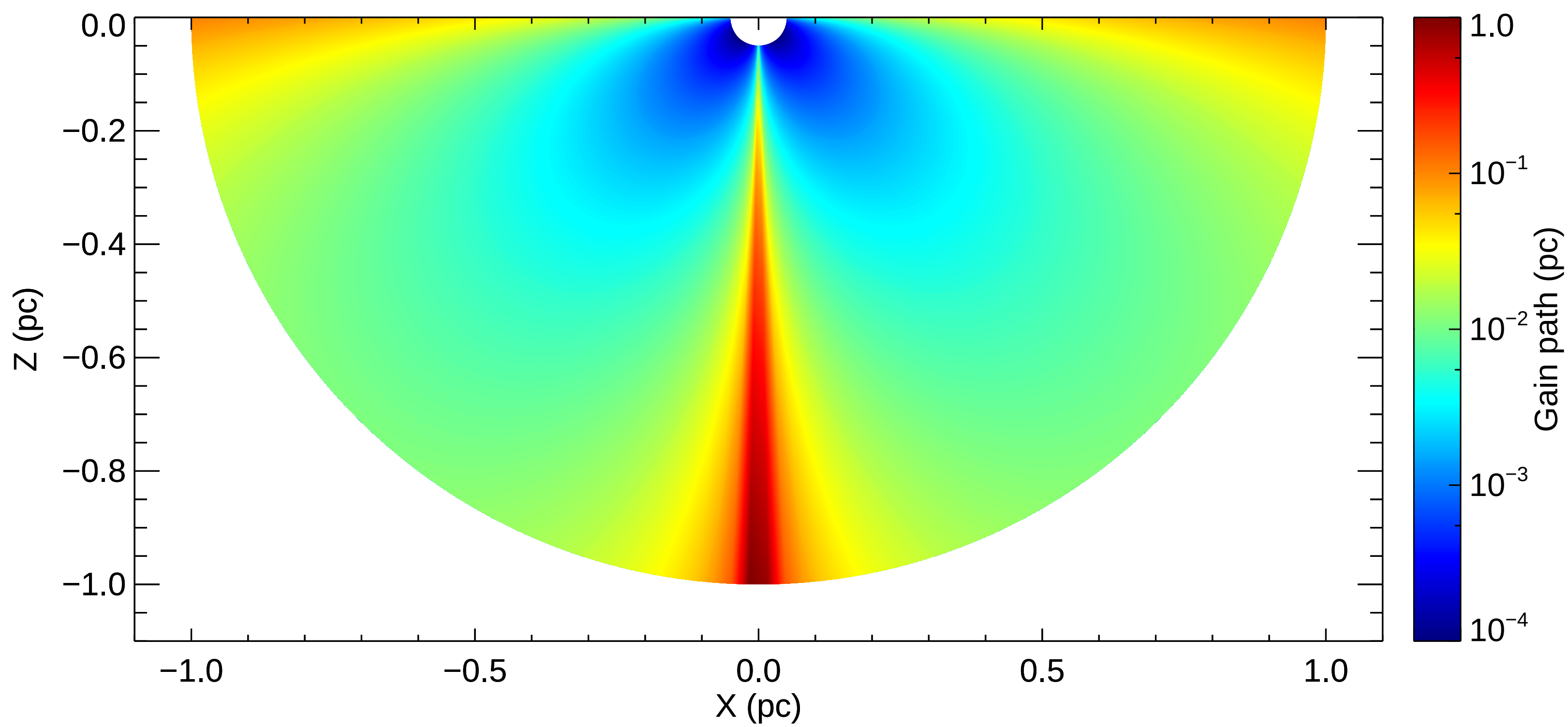

Fig. 1.4.— A plot of the dynamics-limited gain path ℓ as a function of location within the disk, computed using Equation 1.25; the observer sits at $X = Y = 0$, $Z = -\infty$, and the SMBH sits at the origin. We have used $M_{\rm BH} = 10^7$ $\mathrm{M}_\odot$ and $\Delta v = 2$ km s^{-1}. The regions of the disk that we observe to support maser activity correspond to those with the longest gain paths.

motion, and it is responsible for the characteristic "triple-peaked" structure of disk maser spectra (see Figure 1.5).[13] The next term contains the lowest-order relativistic corrections, with both special and general relativity contributing comparably (one-third special, two-thirds general). Throughout most of the disk the second term is $\lesssim$1% the magnitude of the first, but very close to $\phi = 0$ (i.e., near the systemic features) it becomes the dominant term. Because this term is symmetric in ϕ while the Doppler term (before taking an absolute value) is asymmetric, the sum of these two terms results in an increase in gain path lengths on the blueward (approaching) side of the disk and a decrease in those on the redward (receding) side[14]. All remaining higher-order terms are smaller by at least another factor of $(R_s/r)^{1/2} \lesssim 0.01$ and are therefore unimportant at current instrument sensitivity levels.

1.4 The Megamaser Cosmology Project

Possibly the first proposed use of H_2O masers as extragalactic distance-measuring tools came from Kardashev (1986), who suggested leveraging the motion of the solar system with respect to the cosmic microwave background (CMB) as a baseline for VLBI trigonometric parallax measurements. Reid et al. (1988) put forward a similar idea for using the large-scale velocity fields from, e.g., rotating galaxies to convert proper motion measurements of H_2O masers within those galaxies to distance measurements. Both of these works considered only typical Galactic-style masers, as disk megamaser systems had yet to be identified. The notion of using masers to measure extragalactic distances gained substantial popularity after the megamaser technique (see § 1.3.1) was recognized as a viable means of determining the distance to NGC 4258. Though the distance to NGC 4258 was measured using two separate techniques – one using proper motions and the other using accelerations (see § 1.2) – the mag-

[13] A calculation similar to that performed in this section was presented by Kartje et al. (1999), who considered the special case of high-velocity masers residing on the midline of the disk. The authors accounted only for nonrelativistic Doppler motion and took the limit where $\ell \ll r$, and their result matches the first term in Equation 1.26 when the same limit is applied. I thank Moshe Elitzur for drawing my attention to the original version of this calculation.

[14] This asymmetry seems to have been first recognized by Spaans (2005) in the context of NGC 4258, though that work remains unpublished.

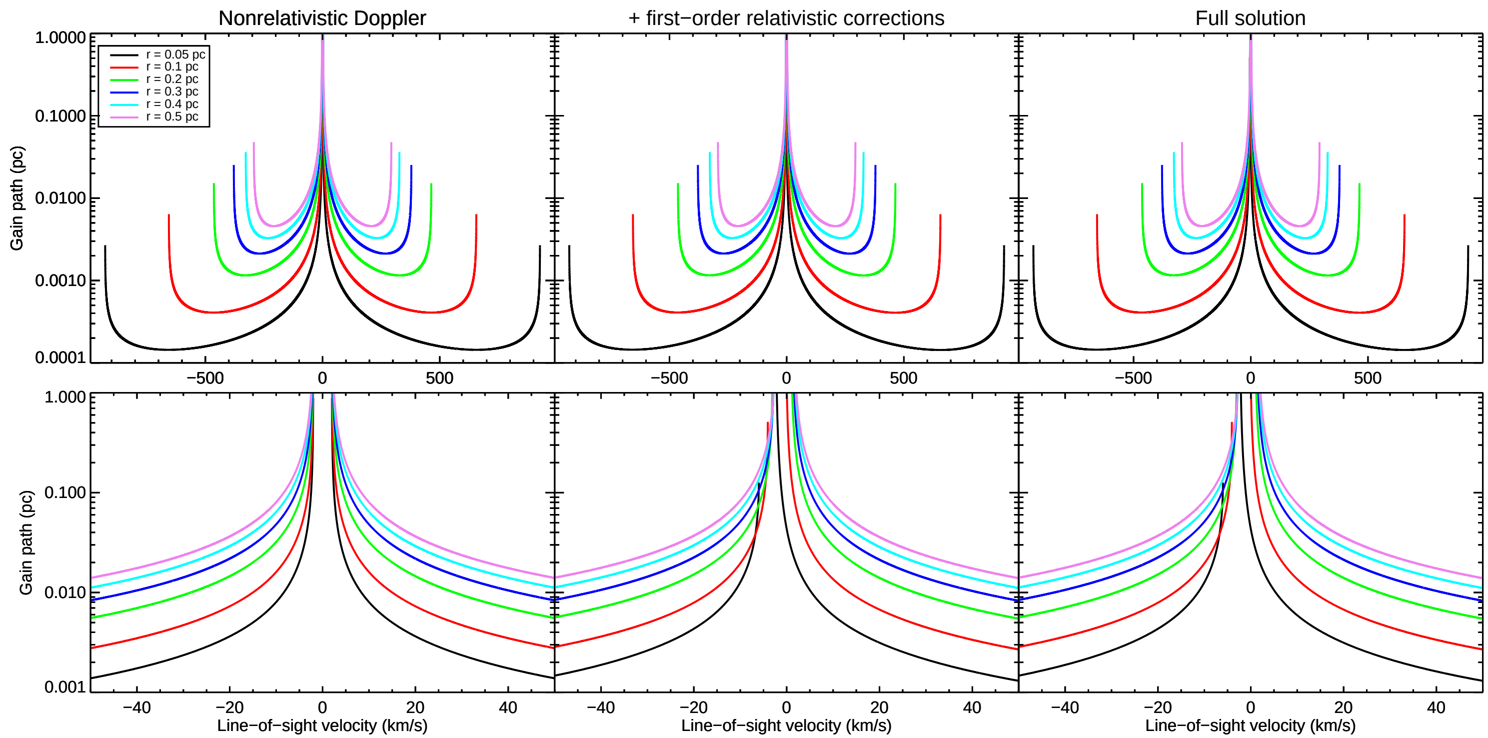

Fig. 1.5.— The dynamics-limited gain path ℓ as a function of observed (line-of-sight) velocity for different choices of orbital radius (plotted as different colored lines), again using $M_{\rm BH} = 10^7$ $\rm M_{\odot}$ and $\Delta v = 2$ km s^{-1}. *Left*: the gain path calculation considering only the nonrelativistic Doppler motion (absolute value of the first term in Equation 1.26). The top panel shows the full velocity extent of the gas, and we can see that the gain path as a function of velocity for any single radius peaks in three separate locations symmetrically arranged about the systemic velocity (which falls at zero in these plots). These three peaks in gain path give rise to three corresponding peaks in the intensity of observed emission, yielding a "triple-peaked" spectral profile. The bottom panel shows a zoom-in on the centermost 100 km s^{-1}. *Center*: the gain path calculation including the leading-order relativistic effects (absolute value of the first two terms in Equation 1.26). Though the gain path at high velocities is basically unchanged from the nonrelativistic Doppler case, near the systemic velocity we now see a pronounced asymmetry. This asymmetry is especially apparent at small orbital radii, where the relativistic effects are strongest. *Right*: the gain path calculation including all terms (absolute value of Equation 1.25). The higher-order terms are sufficiently small for there to be no discernable difference between these plots and those containing only the first-order relativistic corrections.

nitude of the proper motions ($\sim$30 μas yr^{-1} in NGC 4258) would be too small to measure well in more distant galaxies. Line-of-sight accelerations, however, can be measured even for maser features in distant galaxies.

Kennicutt et al. (1995) seem to have been the first to specifically propose extending this idea to measurements of the Hubble constant, H_0. The value of the Hubble constant sets the current-day expansion rate of the Universe, and it relates recession velocities of low-redshift galaxies to their distances via

$$H_0 = \frac{v}{D}. \tag{1.27}$$

Here, D is the distance to a galaxy and v is its cosmological recession velocity (i.e., not including any peculiar motion). Equation 1.27 is often called the Hubble Law, or Hubble's Law, as the observed linear relationship between velocity and distance was first published in Hubble (1929). NGC 4258 itself cannot accurately constrain H_0 because although its distance is measured precisely, its recession velocity of $\sim$450 km s^{-1} is comparable in magnitude to its expected peculiar velocity and the two cannot be accurately disentangled. However, for galaxies well into the Hubble flow (i.e., at distances $\gtrsim$50 Mpc) the peculiar velocity drops to $\lesssim$10% of the recession velocity and precise measurements of H_0 become feasible.

A dedicated project to measure H_0 using megamaser galaxies was introduced by Braatz et al. (2007). The goal of the Megamaser Cosmology Project (MCP) is to constrain H_0 to a precision of $\sim$3% by using the megamaser technique to measure one-step geometric distances to galaxies in the Hubble flow. The experimental design of the MCP contains three primary observational components:

1. A survey component to discover new megamaser disk systems that exhibit Keplerian rotation. Over the course of a decade the MCP has used the GBT to survey more than 3000 nearby ($z \lesssim 0.05$) AGN at an unprecedented level of sensitivity (Braatz et al. 2015), obtaining a median 1σ noise level of $\sim$2 mJy per 1 km s^{-1} of bandwidth. The overall detection rate is $\sim$3% for all H_2O megamasers and $\sim$1% for "clean" disk systems potentially conducive to distance measurements (Kuo et al. 2017b).

2. A spectral monitoring component to measure the accelerations of maser features in the discovered disk systems. Each disk system has been monitored with the GBT at a ~monthly cadence for ~2 years, which is the time baseline required for accurate acceleration measurements.

3. A sensitive VLBI imaging component to map the geometry of the maser disk systems. Each disk selected for a distance measurement has been targeted using the High Sensitivity Array (HSA), composed of the VLBA and the GBT, with the phased VLA and the 100-meter Effelsberg telescope also incorporated on a case-by-case basis.

There is also a fourth post-observation component to the project, that of combining the heterogeneous datasets and modeling the maser disk to make a distance measurement.

As of the writing of this thesis, the MCP has published distance and H_0 measurements for four megamaser galaxies: UGC 3789 (Braatz et al. 2010, Reid et al. 2013), NGC 6264 (Kuo 2011, Kuo et al. 2013), NGC 6323 (Kuo et al. 2015), and NGC 5765b (Gao et al. 2016). A fifth galaxy, CGCG 074-064, has been measured as part of this thesis (see Chapter 5). Observations have been completed and analysis is underway for an additional four galaxies.

1.4.1 Current status of H_0 measurements

Observational cosmology was famously described by Sandage (1970) as "a search for two numbers" – namely the Hubble constant H_0 and the deceleration parameter q_0 – that together would determine the nature, history, and fate of the Universe. Though the discovery of dark energy (Riess et al. 1998) has thrown something of a wrench into this original concept, H_0 remains a fundamental parameter of all cosmological models.

Historically, H_0 has proven to be a difficult quantity to pin down. Starting in the 1920's with Hubble's original value near ~500 km s^{-1} Mpc^{-1} (Hubble 1929), measured values of of H_0 have famously been "shrinking" over time as systematic uncertainties are identified and addressed (Trimble 1996; see also Figure 1.6). The modern value of $\sim$70 km s^{-1} Mpc^{-1} was solidified by the Hubble Space Telescope (HST) Key Project, reported in Freedman et al. (2001), and at the time the reported uncertainty was 11%. The HST Key Project combined distance measurements made using a variety of standard candles (Cepheid variable stars, Type Ia supernovae, Type II supernovae), surface brightness fluctuations, the Tully-Fisher relation, and the fundamental plane of galaxies to arrive at their final H_0 value of 72 ± 8 km s^{-1} Mpc^{-1}. Since then, the measurement uncertainty has dropped considerably while the value has remained essentially unchanged. Current local Universe measurements of H_0 made using distance ladder methods are 74.3 ± 2.8 km s^{-1} Mpc^{-1} (Freedman et al. 2012; a 3.8% measurement made using infrared observations of Cepheid variables with the Spitzer Space Telescope to refine the calibration of the HST Key Project sample) and 73.24 ± 1.74 km s^{-1} Mpc^{-1} (Riess et al. 2016; a 2.4% measurement made by refining the Type Ia supernova calibration with near-infrared measurements of Cepheid variable stars in supernova-hosting galaxies).

Though local Universe measurements of H_0 have a long (and checkered) history spanning nearly a century, it is only in the past $\sim$15 years that CMB measurements have played a comparable role. In a standard six-parameter ΛCDM cosmological model, measurements of the angular power spectrum of the CMB radiation precisely constrain the angular size θ_* of the sound horizon at the surface of last scattering (see, e.g., Planck Collaboration et al. 2014b). This angular size is set by a combination of the physical size r_s of the sound horizon, which depends sensitively on the matter density parameters Ω_m and Ω_b, and the angular diameter distance $D_{\rm A}$ to the CMB surface, which depends on the geometry and late-time evolution of the Universe (and is thus sensitive to the value of H_0). Within the CMB model parameter space, the two-dimensional subspace $\Omega_m H_0^3 =$ constant coincides approximately with a surface of constant θ_*, and this combination of parameters is thus also precisely constrained by the spacing of acoustic peaks in the angular power spectrum. The amplitudes of the acoustic peaks provide similar constraints on the parameter combination $\Omega_m H_0^2$, enabling the degeneracy between Ω_m and H_0 to be modestly broken and measurements (albeit heavily model-dependent ones) of the individual quantities to be made. The

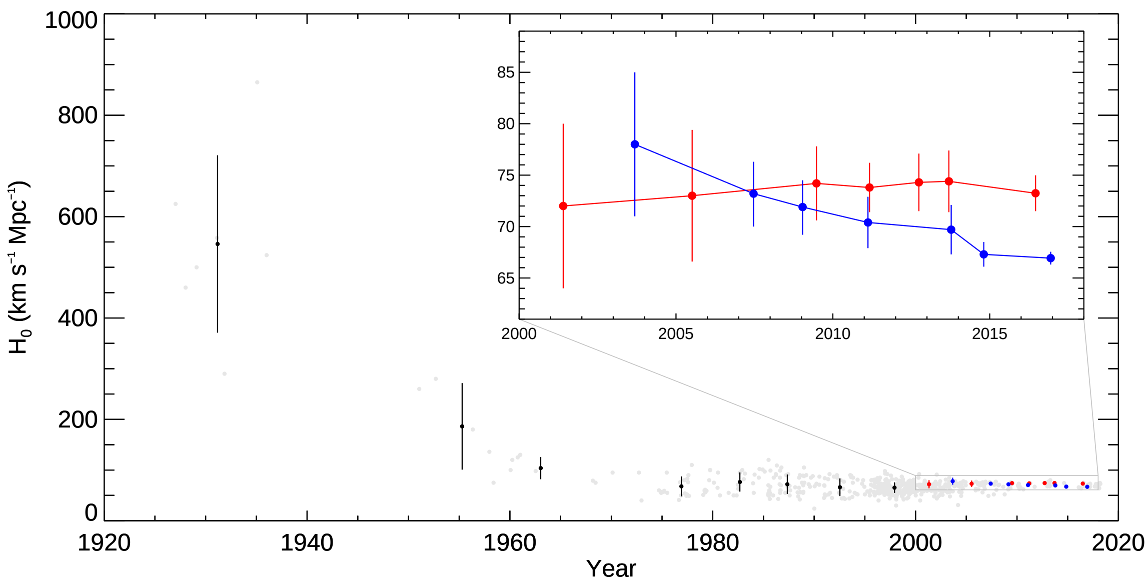

Fig. 1.6.— Measurements of H_0 versus publication date. The gray points mark individual measurements, and the black points show running averages with error bars indicating the RMS scatter of all measurements contained in the average. Starting with the 2001 HST Key Project results (Freedman et al. 2001), HST standard candle measurements of H_0 are plotted as red points with error bars corresponding to published uncertainties. Similarly, CMB measurements are shown in blue starting with the first-year WMAP results (Peiris et al. 2003). The inset plot zooms in on the CMB and standard candle measurements, showing the progression leading up to the current "tension" (see § 1.4.1). Pre-2010 published H_0 values have been compiled by John Huchra as part of the NASA/HST Key Project on the Extragalactic Distance Scale, and can be found at `https://www.cfa.harvard.edu/~dfabricant/huchra/hubble/`.

nine-year Wilkinson Microwave Anisotropy Probe (WMAP) dataset measures $H_0 = 69.7 \pm 2.4$ km s^{-1} Mpc^{-1} (Hinshaw et al. 2013), while measurements made using the Planck satellite find $H_0 = 66.93 \pm 0.62$ km s^{-1} Mpc^{-1} (Planck Collaboration et al. 2016c).

Viewed in one light, the ~8% agreement between H_0 measurements made at opposite ends of the Universe represents an extraordinary success story for modern cosmology. However, the quoted uncertainties in both sets of measurements are sufficiently small that the difference amounts to a 3.4σ "tension" between the local and high-z values (see Figure 1.6).[15] It is currently unknown whether this tension is caused by unrecognized systematics in the CMB data (e.g., Spergel et al. 2015), local measurements (e.g., Efstathiou 2014), or both, or whether it is a hint that new physics might be at play beyond what is currently incorporated in the standard cosmological model (e.g., Planck Collaboration et al. 2016b).

Exciting though the possibility of new physics may be, it seems prudent to first ensure that the seemingly inconsistent values of H_0 cannot otherwise be reconciled by identification (followed hopefully by correction) of unaccounted-for systematic uncertainties in one or another of the measurements. A number of projects are currently underway to provide independent measurements of H_0 having sufficient precision to "take a side" amid the mounting tension. The most promising of these projects span a healthy variety of measurement techniques, including measurements of the infrared Tully-Fisher relation and large-scale velocity flows from the Cosmicflows project (Sorce et al. 2012, Tully et al. 2016), time delays between background images in strong gravitational lens systems from the H0LiCOW project (Suyu et al. 2013, Suyu et al. 2017), and of course megamaser distances from the MCP itself.

[15] Somewhat amusingly, this is not the first time the astronomical community has been divided between two values of the Hubble constant. For several decades there were two camps, one championed by Allan Sandage and advocating a Hubble constant of ~50 km s^{-1} Mpc^{-1} (e.g., Sandage & Tammann 1976) and the other led by Gérard de Vaucouleurs, who preferred a value of ~100 km s^{-1} Mpc^{-1} (e.g., de Vaucouleurs & Bollinger 1979). The reported uncertainties from both sides mutually excluded the other option, and of course at the end of it all the true value of H_0 seems to fall very nearly at the mean of these two extremes.

Chapter 2

Investigating disk physics using spectral monitoring observations

Note: the material presented in this chapter has been published in Pesce et al. (2015).

2.1 Introduction

The Megamaser Cosmology Project (MCP) aims to determine the value of H_0 by measuring angular-diameter distances to galaxies in the Hubble flow. Using the megamaser technique pioneered on the galaxy NGC 4258 (see Herrnstein et al. (1999)), the MCP has published distances to the galaxies UGC 3789 (Reid et al. 2013), NGC 6264 (Kuo et al. 2013), and NGC 6323 (Kuo et al. 2015), and additional galaxies are currently being measured. The ongoing project is a multi-year effort of surveying, monitoring, and mapping maser disks using the Robert C. Byrd Green Bank Telescope (GBT), the Karl G. Jansky Very Large Array (VLA), and the Very Long Baseline Array (VLBA) plus the 100-meter Effelsberg telescope.

The MCP's monitoring campaign uses the GBT of the National Radio Astronomy Observatory (NRAO) to take regular ($\sim$monthly) spectra of megamaser sources targeted for distance measurements. These spectra are used to measure the accelerations of maser features as part of the determination of H_0. Here we take advantage of this rich dataset to probe the innermost parsec ($\sim$0.1-0.5 pc) of the AGN. These size scales are roughly an order of magnitude smaller than the dust structures that have been resolved by optical/infrared interferometric studies of the torus region in nearby AGN (see, e.g., Jaffe et al. 2004).

The structure of this chapter is as follows. The observations and data reduction procedures are described in § 2.2. We present the data in § 2.3 and § 2.5.1, in the form of time-averaged and dynamic spectra, respectively. In § 2.4 we examine a theory of disk maser excitation proposed by Maoz & McKee (1998) (hereafter MM98), in § 2.5.2 we present evidence for the presence of interstellar scintillation in ESO 558-G009, in § 2.6 we check the maser disks for signs of propagating disturbances, and in § 2.7 we use the spectra to place limits on the magnetic field strengths in the maser disks.

2.2 Observations and data reduction

The analyses presented in this chapter are based on 22 GHz water maser spectra, almost all of which were taken using the GBT over the period March 2003 – April 2015.

The majority of these spectra were obtained as part of the survey and monitoring components of the MCP; see Reid et al. (2009) and Braatz et al. (2010) for details. We include several non-MCP spectra from the NRAO data archive, most notably for the galaxies NGC 4258 and NGC 3393.

For each MCP spectrum the GBT spectrometer was configured with two 200 MHz spectral windows, one of which was centered on the recession velocity of the galaxy while the other was offset redward by 180 MHz. Each window had 8192 channels spaced at 24 kHz channel width, which at 22 GHz corresponds to approximately 0.33 km s^{-1}. Both left circular polarization (LCP) and right circular polarization (RCP) were observed simultaneously in each of the two beams of the K-band receiver, and the telescope was nodded on a 2.5-minute cycle to alternate which beam was pointed at the target. Observations after May 2011 used two of the seven beams of the K-band Focal Plane Array (KFPA) in the same nodding scheme. Integration times for the monitored sources were typically between 1 and 3 hours during a single observing session.

We reduced GBT data using the same methods outlined in previous MCP papers (see, e.g., Braatz et al. 2010). Our measurements of Zeeman splitting (§ 2.7.2) use spectra at their native resolution, prior to Hanning smoothing.

Integrated line fluxes in some of our spectra are affected by a broad ($\sim$1500 km s^{-1}) sinusoidal baseline ripple. The baseline ripples are generally comparable in amplitude to the RMS channel noise, but their contributions to the flux measurements can be the dominant source of uncertainty for our best-sampled sources. To characterize the flux uncertainty from the baseline ripple, we averaged the frequency-offset spectral windows from each observation. These spectra are free of maser emission, were taken concurrently with the science spectra using the same instrument configuration on the GBT, and have all undergone the same data reduction procedure. We measured the RMS of the integrated flux inside a boxcar window placed randomly inside the averaged spectrum, as a function of the spectral width of that window. The line flux uncertainty behaves approximately quadratically as a function of window width, reaching a maximum of $\sim$0.1 Jy km s^{-1} for a window width of $\sim$750 km s^{-1}. We thus assign a baseline ripple uncertainty to each line flux measurement that follows the empirical relation given by

$$\sigma_{\mathrm{S},0.1} = -\left(\Delta v\right)_{750}^{2} + 2\left(\Delta v\right)_{750} \tag{2.1}$$

Here, $\sigma_{\mathrm{S},0.1}$ is the baseline ripple's contribution to the line flux uncertainty (in units of 0.1 Jy km s^{-1}) and $(\Delta v)_{750}$ is the spectral window width (in units of 750 km s^{-1}).

2.3 Identifying Keplerian disk megamasers

Our aim is to examine the spectral characteristics of maser emission from accretion disks, including flux ratios, secular velocity drifts, and variability. We thus seek to identify maser systems with spectra dominated by emission from edge-on, Keplerian disks.

To date, 16 megamaser disk systems have published VLBI maps. Eight of these were mapped by the MCP (NGC 1194, NGC 2273, Mrk 1419, NGC 4388, NGC 6323 in Kuo et al. 2011; UGC 3789 in Reid et al. 2009; NGC 6264 in Kuo et al. 2013; and NGC 5765b in Gao et al. 2016), and eight were mapped by other groups (NGC 1068 in Greenhill & Gwinn 1997; NGC 4945 in Greenhill et al. 1997b; NGC 5793 in Hagiwara et al. 2001; Circinus in Greenhill et al. 2003b; NGC 3079 in Kondratko et al. 2005; NGC 4258 in Miyoshi et al. 1995; NGC 3393 in Kondratko et al. 2008; and IC 1481 in Mamyoda et al. 2009). Of these 16 mapped disks, nine have "clean" Keplerian rotation curves, and all nine share a distinctive single-dish spectral profile. To maximize the uniformity and size of the sample for the analysis in this chapter, we therefore selected sources based on the appearance of their single-dish (usually GBT) spectra.

A "clean" disk megamaser is an edge-on maser in Keplerian rotation around the central SMBH, in which the disk maser emission dominates over any jet or outflow maser components. These systems have characteristic spectra that are marked by three sets of maser components. The "systemic" set of features coincides roughly with the recession velocity of the galaxy, and the masing arises along a line of sight through the disk to the central AGN. The two "high-velocity" sets of features (the "redshifted features" and "blueshifted features") are spectrally offset to either side of the galaxy's recession velocity. These features arise from the midline of the accretion disk, along lines of sight that are tangent to the orbital motion (which ensures velocity coherence throughout the column of gas). For an edge-on disk, the midline is the diameter through the disk that falls perpendicular to the line of sight.

To select clean disk megamasers, we use the following criteria. The spectra must show at least two of the three expected distinct sets of maser features (in maser disks with only two sets of features, the third set is presumably present but below the detection threshold). Furthermore, at least one of the sets of features should have components that are offset from the recession velocity by at least 300 km s^{-1} (an empirically-determined high galactic rotation cutoff; see Cresci et al. 2009), to avoid contaminating the sample with interstellar masers (from, e.g., a strong starburst) and sub-Keplerian rotators. For a spectrum with only two sets of maser features, we require either that one of these feature sets be coincident with the recession velocity of the galaxy or that both feature sets be offset from the recession velocity by at least 300 km s^{-1}.

Though we have attempted to be comprehensive in our selection of sources, there are several known disk (or disk-like) H_2O megamasers that do not make it into our sample because the disk emission is contaminated by non-disk components. Circinus (Gardner & Whiteoak 1982) contains a masing accretion disk, but it also has maser emission associated with an outflow (Greenhill et al. 2003b). Similarly, NGC 1068 (Claussen et al. 1984) has maser emission arising from both a disk and a radio jet encountering a dense molecular cloud (Gallimore et al. 1996). Complexities like these confuse the maser spectrum and make it difficult to associate individual spectral features with either the disk or outflow/jet components without a VLBI map. For this reason, none of these sources passes our selection criteria.

The final list of 32 clean megamaser disk systems used in our study is given in Table 2.1. Figure 2.1 shows the weighted average spectra of these sources, where the weighting $\tau/T_{\rm sys}^2$ was chosen to minimize the RMS noise of each spectrum (τ is the exposure time and $T_{\rm sys}$ is the system temperature). The emission from the remaining $\sim$130 known water megamaser galaxies may arise from nuclear sources other than the accretion disk (e.g., molecular gas in an outflow) or from extranuclear sources elsewhere within these galaxies (e.g., star-forming regions).

For completeness, we reproduce the spectrum of ESO 269-G012 in Figure 2.1 from Greenhill et al. (2003a); see that paper for details about the observations and data reduction.

2.3.1 Observed properties of disk megamasers

Table 2.1 also lists several observational properties of each galaxy. We obtained the recession velocities from the NASA/IPAC Extragalactic Database (NED), favoring velocities measured from neutral hydrogen (HI) over those made from optical lines. HI measurements have the advantage that they average over all internal motions of a galaxy, while optical lines are preferentially emitted from regions with a sufficiently energetic radiation field to excite the transitions. In the case of active galaxies, like those present in our sample, the optical emission could very well be dominated by gas that is kinematically driven by the nuclear activity (e.g., outflows). This could result in a systematic offset between the recession velocity of the galaxy and the velocity measured using optical lines (e.g., Comerford et al. 2013). We do see such offsets in several of the spectra shown in Figure 2.1.

We measured line fluxes separately for each set of features: blueshifted, systemic, and redshifted. To maximize the signal-to-noise for those spectra with weak features, we integrated only over spectral windows that contained clear signal. In some cases this meant integrating over several distinct, narrow windows to obtain the total line flux for a particular set of features. For several spectra, the systemic set of features is absent; in these cases we list an upper limit on the line flux for the systemic features obtained by integrating over the spectral region located between the high-velocity features (i.e., the region redward of the blueshifted features and blueward of the redshifted features).

To obtain the total isotropic luminosities listed in Table 2.1, we integrated each spectrum across the full span of maser emission. For a measured line flux S, the isotropic luminosity is given by

Table 2.1. Observational properties for the disk maser sample

Target	R.A. (J2000)	Dec. (J2000)	$V_{\rm rec}$ (km s^{-1})	Velocity type	τ (hours)	RMS (mJy)	$L_{\rm iso}$ ($L_\odot h_{70}^{-2}$)	Blue (Jy km s^{-1})	Sys (Jy km s^{-1})	Red (Jy km s^{-1})	log(R)	Ref.
J0109-0332	01:09:45.1	$-$03:32:33	16369 $\pm$ 30	O	1.7	3.08	2086 $\pm$ 180	0.37	0.48	0.86	0.37 $\pm$ 0.10	(a)
J0126-0417	01:26:01.7	$-$04:17:56	5639 $\pm$ 33	O	3.2	1.40	105 $\pm$ 18	0.11	$<$ 0.08	0.48	0.64 $\pm$ 0.16	(a)
NGC 591	01:33:31.2	+35:40:06	4549 $\pm$ 5	H	6.6	0.69	38 $\pm$ 10	0.20	0.01	0.16	$-$0.10 $\pm$ 0.41	(b)
NGC 1194	03:03:49.1	$-$01:06:13	4076 $\pm$ 5	H	100.8	0.24	131 $\pm$ 7	0.51	0.38	0.79	0.19 $\pm$ 0.12	(a)
J0437+2456	04:37:03.7	+24:56:07	4835 $\pm$ 40	O	119.2	0.25	155 $\pm$ 11	0.70	0.53	0.16	$-$0.64 $\pm$ 0.16	(a)
NGC 2273	06:50:08.7	+60:50:45	1840 $\pm$ 4	H	99.5	0.27	37 $\pm$ 1	0.25	0.73	1.33	0.73 $\pm$ 0.20	(e)
ESO 558-G009	07:04:21.0	$-$21:35:19	7674 $\pm$ 27	O	114.0	0.29	709 $\pm$ 14	0.96	0.98	0.63	$-$0.18 $\pm$ 0.06	(a)
UGC 3789	07:19:31.6	+59:21:21	3325 $\pm$ 24	H	187.8	0.16	357 $\pm$ 2	3.17	1.73	2.00	$-$0.20 $\pm$ 0.02	(f)
Mrk 78	07:42:41.7	+65:10:37	11194 $\pm$ 29	O	4.3	0.87	104 $\pm$ 60	0.05	0.04	0.14	0.45 $\pm$ 1.25	(b)
IC 485	08:00:19.8	+26:42:05	8338 $\pm$ 10	H	8.0	0.74	1061 $\pm$ 26	0.03	3.06	0.29	0.99 $\pm$ 0.18	(a)
J0836+3327	08:36:22.8	+33:27:39	14810 $\pm$ 120	O	2.4	1.16	937 $\pm$ 67	0.24	0.55	0.17	$-$0.15 $\pm$ 0.21	(g)
J0847-0022	08:47:47.7	$-$00:22:51	15275 $\pm$ 32	O	1.4	2.37	2945 $\pm$ 129	0.83	0.62	1.29	0.19 $\pm$ 0.06	(a)
Mrk 1419	09:40:36.4	+03:34:37	4947 $\pm$ 7	H	151.4	0.20	565 $\pm$ 5	2.42	1.07	1.39	$-$0.24 $\pm$ 0.03	(h)
IC 2560	10:16:18.7	$-$33:33:50	2925 $\pm$ 2	H	27.4	0.79	210 $\pm$ 4	0.71	3.55	1.07	0.18 $\pm$ 0.05	(d)
Mrk 34	10:34:08.6	+60:01:52	15292 $\pm$ 12	O	3.8	0.41	814 $\pm$ 64	0.52	$<$ 0.11	0.37	$-$0.15 $\pm$ 0.14	(i)
NGC 3393	10:48:23.4	$-$25:09:43	3750 $\pm$ 5	H	5.0	0.66	259 $\pm$ 3	1.39	0.74	1.91	0.14 $\pm$ 0.03	(g)
UGC 6093	11:00:48.0	+10:43:41	10805 $\pm$ 10	H	40.5	0.33	1048 $\pm$ 24	0.43	0.87	0.63	0.17 $\pm$ 0.07	(a)
NGC 4258	12:18:57.5	+47:18:14	448 $\pm$ 3	H	21.6	0.66	89.7 $\pm$ 0.2†	0.36	57.0	9.45	1.42 $\pm$ 0.09	(j)
NGC 4388	12:25:46.7	+12:39:44	2517 $\pm$ 4	H	13.4	0.63	13 $\pm$ 3	0.15	$<$ 0.05	0.30	0.30 $\pm$ 0.41	(b)
ESO 269-G012	12:56:40.5	$-$46:55:34	5014 $\pm$ 13	H	1.4	10.2	496 $\pm$ 53	2.68	0.10	1.90	$-$0.15 $\pm$ 0.04	(k)
NGC 4968	13:07:06.0	$-$23:40:37	2988 $\pm$ 15	O	3.8	2.92	54 $\pm$ 5	0.08	0.53	0.62	0.89 $\pm$ 0.21	(a)
J1346+5228	13:46:40.8	+52:28:37	8737 $\pm$ 12	O	10.6	0.68	380 $\pm$ 29	0.18	0.84	0.16	$-$0.05 $\pm$ 0.35	(a)
CGCG 074-064	14:03:04.5	+08:56:51	6886 $\pm$ 29	O	5.3	1.62	852 $\pm$ 21	0.44	2.78	0.56	0.49 $\pm$ 0.06	(a)
NGC 5495	14:12:23.3	$-$27:06:29	6737 $\pm$ 9	H	6.7	0.85	625 $\pm$ 18	0.47	1.93	0.53	$-$0.05 $\pm$ 0.10	(g)
NGC 5765b	14:50:51.5	+05:06:52	8333 $\pm$ 19	O	62.2	0.37	2553 $\pm$ 17	1.10	5.56	1.11	0.00 $\pm$ 0.05	(a)
UGC 9618b	14:57:00.7	+24:37:03	10094 $\pm$ 5	O	3.5	0.97	794 $\pm$ 54	0.19	0.54	0.90	0.68 $\pm$ 0.39	(g)
UGC 9639	14:58:36.0	+44:53:01	10886 $\pm$ 17	O	8.3	0.88	264 $\pm$ 62	0.16	0.10	0.23	0.16 $\pm$ 0.29	(a)
CGCG 165-035	15:14:39.8	+26:35:39	9622 $\pm$ 2	H	0.85	1.68	1447 $\pm$ 22	1.71	0.75	0.88	$-$0.29 $\pm$ 0.05	(a)
NGC 6264	16:57:16.1	+27:50:59	10177 $\pm$ 28	O	103.5	0.23	1634 $\pm$ 11	1.07	0.81	1.48	0.14 $\pm$ 0.05	(g)
J1658+3923	16:58:15.5	+39:23:29	10292 $\pm$ 11	O	3.2	1.41	427 $\pm$ 44	0.41	$<$ 0.12	0.65	0.20 $\pm$ 0.10	(a)
NGC 6323	17:13:18.0	+43:46:56	7772 $\pm$ 35	O	134.1	0.19	839 $\pm$ 21	0.85	0.45	1.65	0.29 $\pm$ 0.03	(b)
CGCG 498-038	23:55:44.2	+30:12:44	9240 $\pm$ 27	O	2.5	1.40	280 $\pm$ 32	0.25	0.19	0.23	$-$0.04 $\pm$ 0.42	(a)

Note. — Observational properties of the 32 disk megamasers. The recession velocities ($V_{\rm rec}$) use the optical convention in the barycentric reference frame (velocities and errors were taken from NED and references therein). In the "velocity type" column, H indicates that the recession velocity was measured using HI 21-cm data, O means that it was measured using optical/IR lines. The total integration time (τ) and final RMS are listed for the averaged spectra (see Figure 2.1). The isotropic luminosities ($L_{\rm iso}$) have been calculated assuming a Hubble constant of 70 km s^{-1} Mpc^{-1}; the associated uncertainties are statistical and do not account for any systematic flux calibration offsets (which may be as large as $\sim$20%) or peculiar velocities (which may be important for nearby galaxies). Columns labeled "Blue," "Sys," and "Red" list the integrated line fluxes for the blueshifted, systemic, and redshifted feature sets, respectively; when measured line fluxes are smaller than the uncertainty, 1σ upper limits are listed instead. The logarithms of the red-to-blue flux ratios are given in the column labeled log(R). The reference ("Ref.") column lists a citation for the discovery paper for each source, specified below. A comprehensive list of extragalactic H_2O masers is maintained on the MCP website (`https://safe.nrao.edu/wiki/bin/view/Main/PublicWaterMaserList`). References: (a) MCP survey; (b) Braatz et al. (2004); (c) Greenhill et al. (2009); (d) Braatz et al. (1996); (e) Zhang et al. (2006); (f) Braatz & Gugliucci (2008); (g) Kondratko et al. (2003); (h) Henkel et al. (2002); (i) Henkel et al. (2005); (j) Claussen et al. (1984); (k) Greenhill et al. (2003a).

†For NGC 4258, the distance measurement from Humphreys et al. (2013) of 7.6 Mpc was used instead of the Hubble law value.

Fig. 2.1.— Spectra for disk megamasers used in our analysis of the MM98 model. Each spectrum is a weighted average (see § 2.3) taken over all epochs; the date of the first epoch is located at the top right. Galaxy recession velocities and associated 1σ errors (see Table 2.1) are overplotted in red.

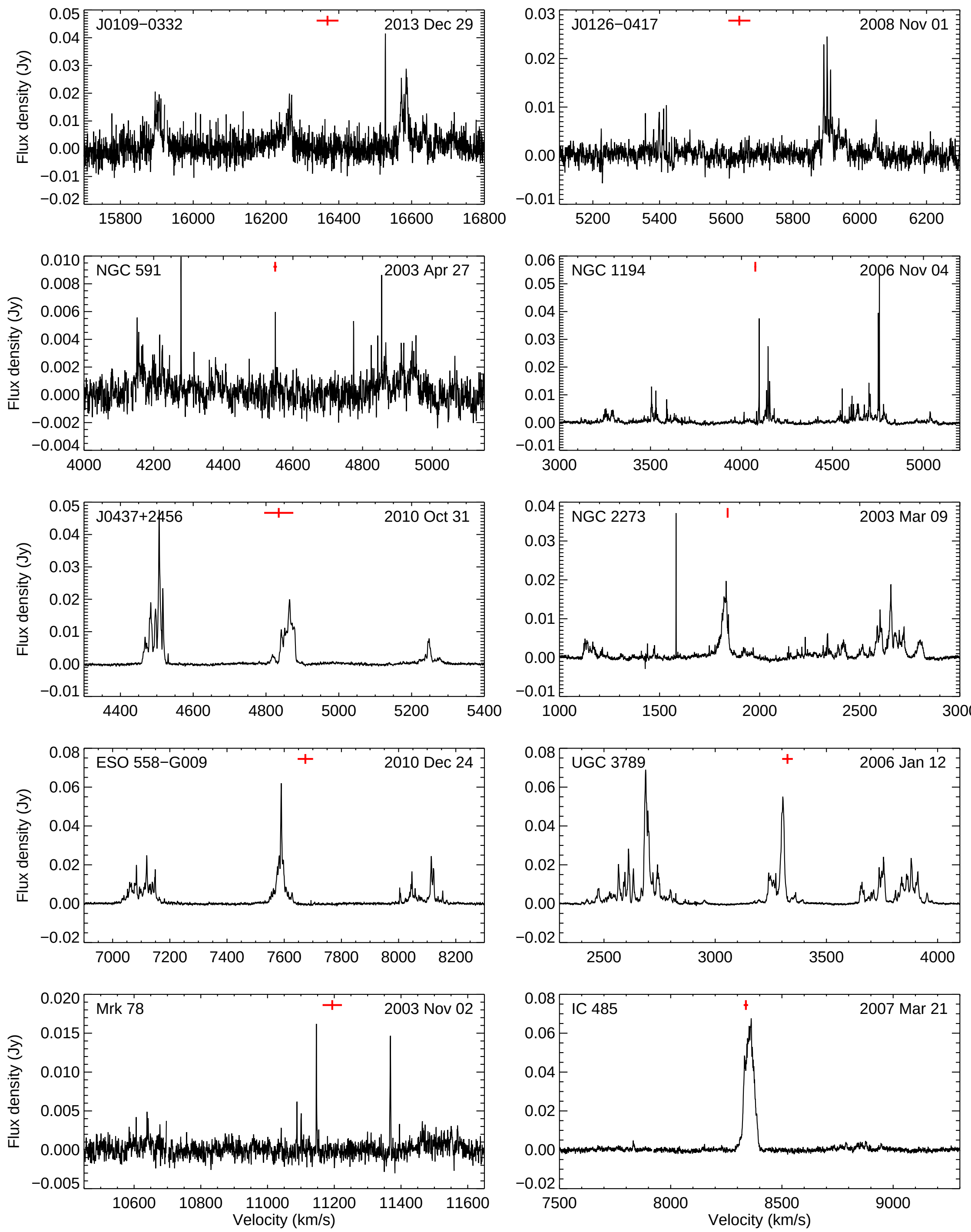

Fig. 2.1.— (continued)

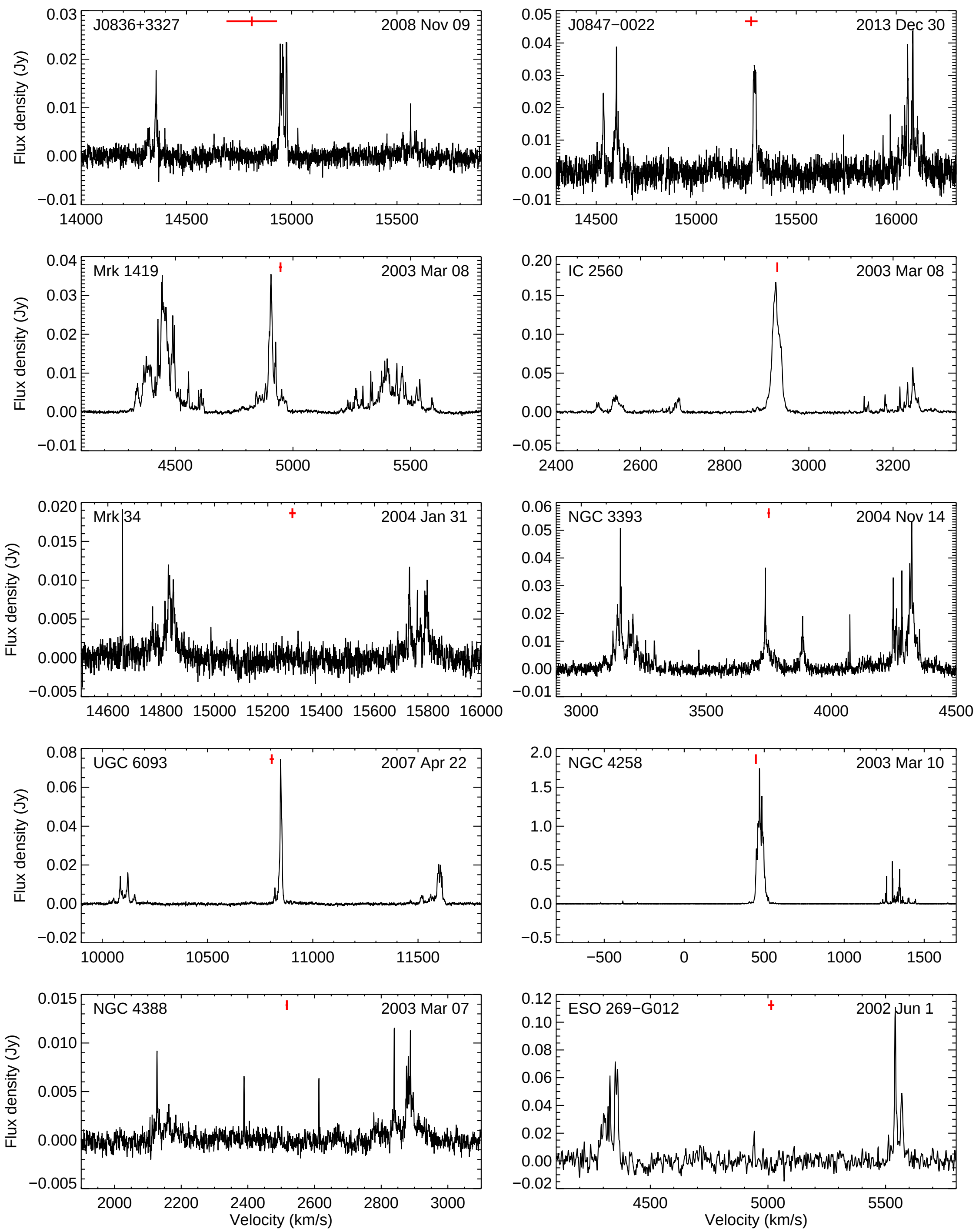

Fig. 2.1.— (continued)

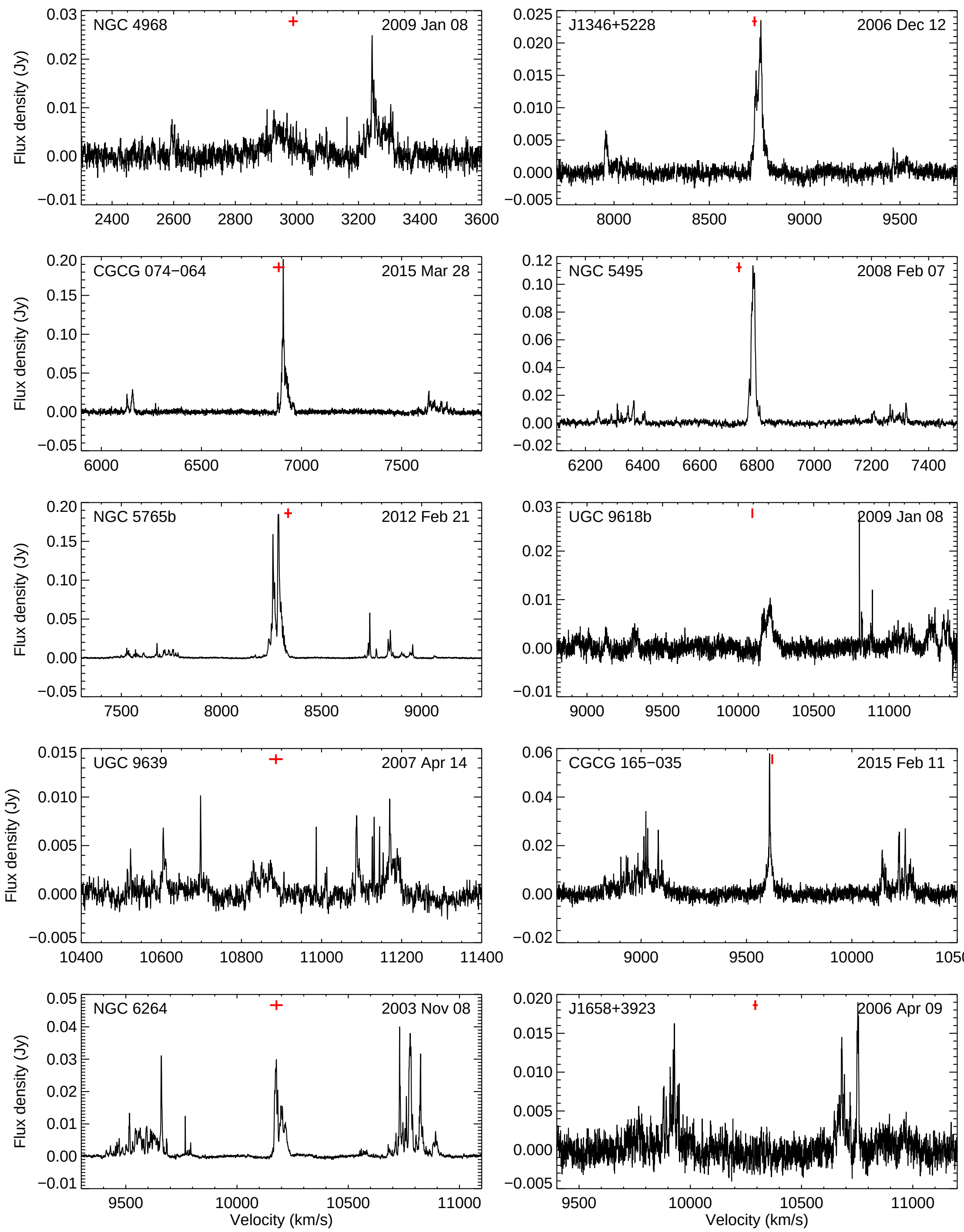

Fig. 2.1.— (continued)

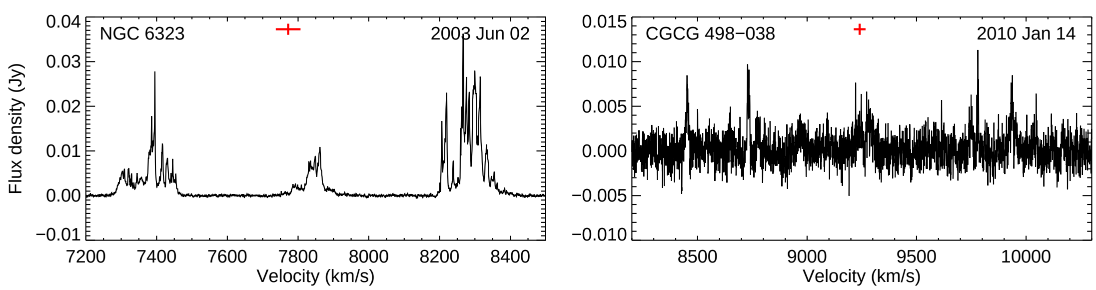

$$L_{\rm iso} = \frac{4\pi v^2 S}{H_0^2}. \tag{2.2}$$

Here, v is the recession velocity of the galaxy. This expression is accurate for low-redshift ($z \lesssim 0.1$) sources, and all of our galaxies fall into this category so we use it throughout. In our calculations, we assume a Hubble constant of $H_0 = 70$ km s^{-1} Mpc^{-1}. Figure 2.2 shows a histogram of the isotropic luminosities. To alleviate the somewhat arbitrary nature of histogram bin sizes and endpoints, we have overplotted a kernel density estimate using a Gaussian kernel. The area of each kernel is equal to that of a histogram bin with a bin size determined using Silverman's rule; see Appendix A for details.

The measured isotropic luminosities span over two orders of magnitude, and the observed distribution (see Figure 2.2) appears to be consistent with a sensitivity-limited sample (i.e, the highest luminosity masers tend to be found at large distances, and vice versa). While some of this spread is undoubtedly caused by intrinsic power differences among the many systems, most of it is likely the result of viewing angles. Though the exact angular dependence of the maser emission is a strong function of the source geometry and saturation, it always drops off exponentially from the beam center, which falls along the path of maximum gain (Elitzur 1992). Thus, even a slight ($\lesssim 5°$) inclination of the maser beam from the line of sight could cause the observed intensity to drop by an order of magnitude or more. This is especially true if the masers are unsaturated. The unknown contribution from maser beaming precludes us from correcting the Malmquist bias and turning Figure 2.2 into a true luminosity function.

2.4 Testing a model of disk maser excitation

In their 1998 paper, Maoz & McKee (MM98) sought to explain the observation in NGC 4258 that the line flux of the redshifted features is much higher than the line flux of the blueshifted features. In their model, population inversion (and thus masing) only occurs in post-shock gas on the trailing edge of a spiral shock in the accretion

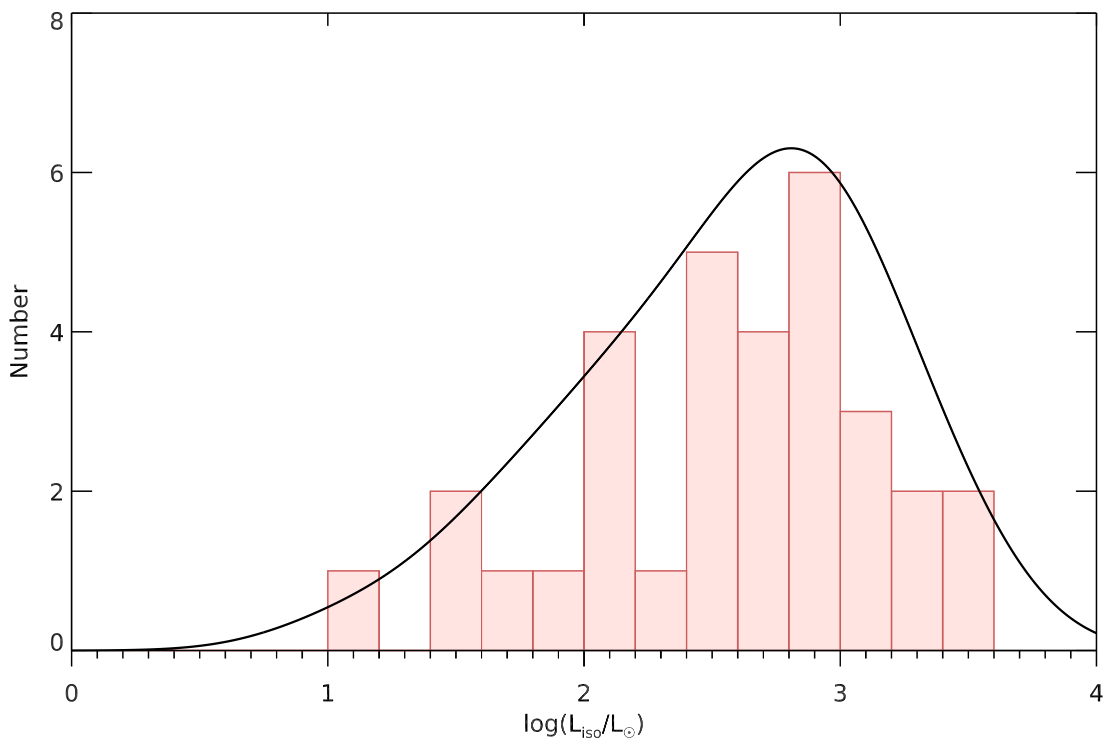

Fig. 2.2.— Histogram showing the distribution of isotropic luminosities for our sample of disk megamasers. The solid black line shows the kernel density estimation obtained using a normal kernel, with Silverman's rule applied for the kernel Gaussian width (see Appendix A).

disk. Observed high-velocity maser features then occur wherever the line of sight falls tangent to a shock front, for an edge-on disk system.

The geometry of the trailing spiral shocks causes redshifted maser emission to preferentially originate from the region of the disk that lies in front of the midline, while blueshifted maser emission arises from behind the midline. The blueshifted photons would thus pass through a sightline of velocity-coherent (but noninverted) gas, leading to absorption that is not present for the redshifted photons. The model thereby predicts that the redshifted high-velocity features observed for disk maser systems should be systematically stronger than the blueshifted high-velocity features. See Fig. 1 in MM98 for an illustration of this geometry.

Owing to their offsets from the midline, the MM98 model predicts nonzero line-of-sight "accelerations" for the high-velocity features; specifically, the blueshifted features should show a mean positive acceleration while the redshifted features show a negative one. These arise because as the trailing spiral shock passes through the disk, the inversion region (and thus the segment of spiral structure that is tangent to the line of sight) moves radially outwards with time. The line-of-sight component of the velocity decreases in magnitude with increasing radius, so the result is an observed velocity drift in the high-velocity maser lines. Though such behavior mimics an acceleration, it is actually tracing the rotating spiral structure rather than the Keplerian motion of the gas in the disk, and we therefore refer to the phenomenon as a "velocity drift" rather than as an acceleration (see § 2.4.2 for details). This prediction runs counter to that of the "standard" model, which has a uniformly masing disk with high-velocity features falling close to the midline. The standard model predicts that the high-velocity features should have nearly zero line-of-sight accelerations on average.

The model proposed by MM98 was inspired by the red-blue flux asymmetry in NGC 4258, which we note from Table 2.1 has a uniquely high value of $\log(R) = +1.42$ not seen in any other maser disk. It is an open question whether such an excitation mechanism applies to maser disks in general; indeed, it is an open question whether this mechanism even holds for NGC 4258 (see, e.g., Bragg et al. 2000). We checked this model by measuring the flux asymmetry and velocity drifts of high-velocity features in our Keplerian disk sample.

2.4.1 Statistical analysis

For each disk maser in our sample we made a weighted average spectrum from all epochs of observation (see Figure 2.1 and § 2.3). The averaging reduces the noise and mitigates the effects of variability. We then identified the regions of each spectrum corresponding to the redshifted and blueshifted high-velocity features. By integrating over these spectral segments, we obtained the redshifted and blueshifted fluxes. The ratio, R, of the redshifted to the blueshifted flux should be greater than 1 for the MM98 model. The values of $\log(R)$ for our sample are listed in Table 2.1 and their histogram is plotted in Figure 2.3.

The null hypothesis is that the redshifted and blueshifted fluxes are on average equal; that is, the logarithm of the ratio of the redshifted to the blueshifted flux should be a distribution centered on zero. We use the logarithm of the flux ratios (rather than the ratios themselves) to avoid the skewing of the distribution that arises from a direct ratio.

To test whether our results are consistent with the null hypothesis, we employ a likelihood analysis to determine whether the sample we observe has been drawn from a parent population with an intrinsic flux ratio distribution centered on zero. The data point corresponding to NGC 4258 is not included in this analysis, as it was used to generate the original hypothesis. Here we utilize a technique analogous to that presented in Richards et al. (2011).

To simplify notation, we define $X \equiv \log(R)$, where $R = \rho/\beta$ is the ratio of the redshifted flux (denoted ρ) to the blueshifted flux (denoted β). We assume that the parent distribution of X is a Gaussian centered on X_0, with a standard deviation of σ_0. We also assume that the observational uncertainties associated with each measurement are normally distributed about the intrinsic value for that measurement.

For a single observation of a source with intrinsic redshifted flux of ρ_t, the probability to observe the value ρ_i with uncertainty $\sigma_{r,i}$ is given by

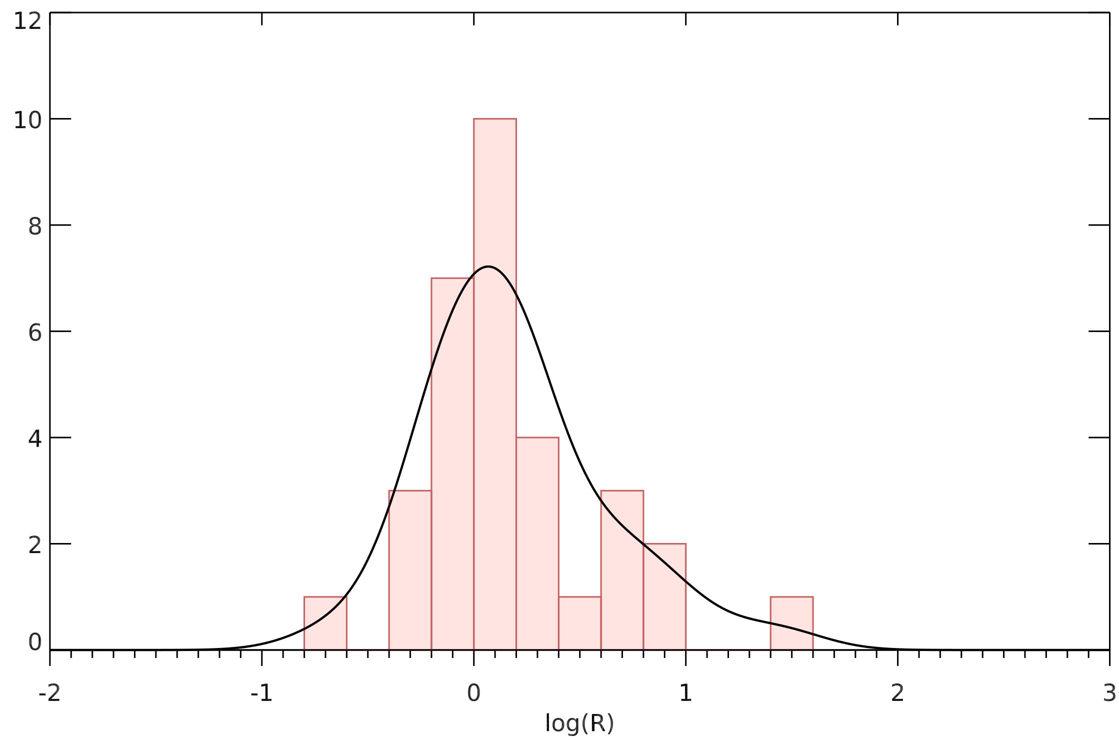

Fig. 2.3.— Histogram showing the distribution of the logarithm of the red/blue flux ratios for our sample of disk megamasers. The solid black line again shows the kernel density estimation, obtained using the same normalization as in Figure 2.2. NGC 4258 occupies the rightmost histogram bin, causing the red tail of the distribution to be noticeably longer and heavier than the blue tail. Though we include it in this plot, NGC 4258 was not included in the statistical analysis performed in § 2.4.1 to avoid biasing the results (i.e., since the proposed hypothesis was based on observations of NGC 4258, its observed properties necessarily agree with the hypothesis).

$$P_r = \frac{1}{\sigma_{r,i}\sqrt{2\pi}} \exp\left[-\frac{(\rho_t - \rho_i)^2}{2\sigma_{r,i}^2}\right]. \tag{2.3}$$

Similarly for an observation of a source with intrinsic blueshifted flux of β_t, the probability to observe the value β_i with uncertainty $\sigma_{b,i}$ will be

$$P_b = \frac{1}{\sigma_{b,i}\sqrt{2\pi}} \exp\left[-\frac{(\beta_t - \beta_i)^2}{2\sigma_{b,i}^2}\right]. \tag{2.4}$$

We also have the probability for the source to have an intrinsic flux ratio of $X_t = \log(\rho_t/\beta_t)$, given the parent distribution

$$P_t = \frac{1}{\sigma_0\sqrt{2\pi}} \exp\left[-\frac{(X_t - X_0)^2}{2\sigma_0^2}\right]. \tag{2.5}$$

The resulting likelihood of the observation is then given by an integral over the product of these probability density functions,

$$\ell_i = \int_0^\infty \int_0^\infty P_r P_b P_t d\rho_t d\beta_t. \tag{2.6}$$

For N observations, the joint likelihood will then be the product of the individual measurement likelihoods:

$$\mathcal{L}(X_0, \sigma_0) = \prod_{i=1}^{N} \ell_i. \tag{2.7}$$

Once the joint likelihood function is known, we can marginalize over the parameter σ_0. The marginalized likelihood, $\mathcal{L}(X_0)$ (shown in Figure 2.4), can then be integrated to determine the fraction of the likelihood that falls below $X_0 = 0$:

$$p = \left(\int_{-\infty}^{0} \mathcal{L}(X_0) dX_0\right) \left(\int_{-\infty}^{\infty} \mathcal{L}(X_0) dX_0\right)^{-1}. \tag{2.8}$$

Evaluating p for the flux values listed in Table 2.1 yields $p = 0.020$. The likelihood analysis therefore rejects the null hypothesis at the 2σ level.

NGC 4258 stands out as an 18σ outlier, which most likely indicates that this Gaussian model is not a good description of the parent population. Nevertheless, it is sufficient to show that the null hypothesis is at least moderately discrepant with the data and that NGC 4258 is substantially removed from the bulk of the observed distribution.

2.4.2 Velocity drifts of high-velocity features

The MM98 model also predicts that the high-velocity maser features will be systematically offset from the midline of the disk, and that they should thus exhibit nonzero line-of-sight velocity drifts as the spiral structure rotates. For spiral shocks having a pitch angle of θ_p (the pitch angle is the opening angle of the spiral, defined at any point to be the complement of the angle between the tangent to the spiral and the outward radial direction from the black hole), we can calculate a characteristic value for the velocity drifts expected for the high-velocity features. For a logarithmic spiral, the MM98 model predicts a velocity drift of

$$|\dot{v}| = 0.05 \left(\frac{\theta_p}{2.5^\circ} \right) \text{km s}^{-1} \text{ yr}^{-1}. \tag{2.9}$$

This drift is towards smaller rotation velocities, and it is shared by all high-velocity masers. The observed velocity drift, in this model, is caused by the passage of the trailing spiral structure through the gas disk; it is *not* a centripetal acceleration from the Keplerian rotation of the gas. As the spiral shock moves through the disk, the portion tangent to the line of sight intercepts gas farther out in radius, which has a lower rotational velocity. Thus we would expect to observe a negative line-of-sight velocity drift for the redshifted features and a positive drift for the blueshifted features.

Bragg et al. (2000) measured velocity drifts in NGC 4258, and showed that the values were inconsistent with the predictions of the MM98 model. They established that no choice of pitch angle can reproduce their data, as statistically significant measurements of both negative and positive velocity drifts were made for both sets of features. These results were corroborated by Humphreys et al. (2008), who used an increased number of epochs to further refine the measurements. Table 2.2 lists published measurements of high-velocity drifts for several other megamaser disks, plus

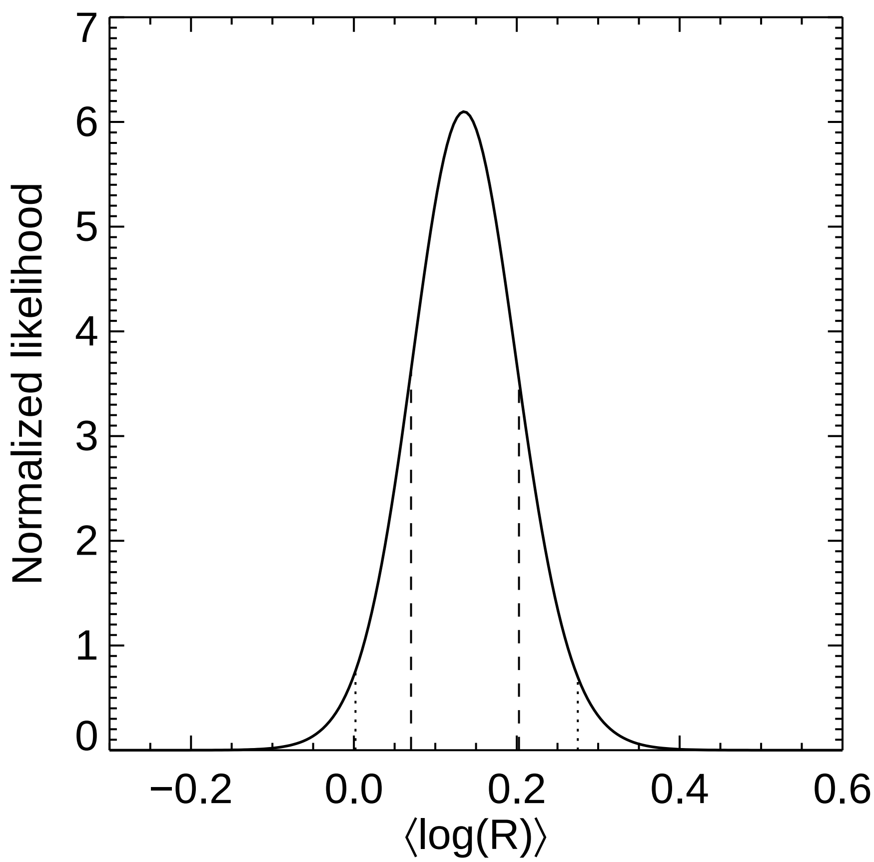

Fig. 2.4.— The normalized likelihood for the model presented in § 2.4.1 as a function of the average flux ratio $X_0 = \langle \log(R) \rangle$, marginalized over σ_0. Ranges corresponding to 1σ and 2σ are shown as dashed and dotted vertical lines, respectively.

our new measurements, where we have estimated velocity drifts for several additional galaxies using the eye-tracking method described in Kuo et al. (2013). To account for systematic uncertainties, we also adopt the error floor of 0.3 km s^{-1} yr^{-1} from Kuo et al. (2013) for all new acceleration measurements.

Nine of the 22 velocity drift measurements (counting redshifted and blueshifted separately) presented in Table 2.2 are incompatible with the MM98 model (i.e., negative blueshifted velocity drifts or positive redshifted velocity drifts). For those values that are compatible, we used Equation 2.9 to assign a maximum pitch angle to any spiral structure that is consistent with the measured drifts. As a comparison, the minimum pitch angle in NGC 4258 (obtained by assuming that the spatial grouping of the blueshifted features arise from consecutive windings of a single logarithmic spiral) is about $\theta_p \gtrsim 1.7^\circ$ (Humphreys et al. 2013).

2.4.3 Discussion

Our analysis of the flux ratio data indicate a small deviation from the null hypothesis, in favor of the MM98 model, though the magnitude of this deviation fails to meet the nominal 3σ threshold. However, the measured velocity drifts of high-velocity features do not match the MM98 predictions (Table 2.2). The maser features are equally likely to have a positive drift as a negative one, regardless of whether they're blueshifted or redshifted (6 of 11 targets display negative velocity drifts for both sets of features). Furthermore, though we have reported only the averaged values for the redshifted and blueshifted velocity drifts for each target, several of these targets have statistically significant measurements of both negative and positive drifts within the same set of features. On the whole, the high-velocity drifts are consistent with masing gas that is near the midline of the disk (i.e., any observed velocity drifts can be explained as centripetal accelerations caused by small offsets on both sides of the midline).

We note that the MM98 model is based on the characteristics of NGC 4258, which has an atypically large flux ratio between the redshifted and blueshifted high-velocity features. This apparent anomaly could be the result of a selection bias. If NGC 4258 were located at a distance of ~ 100 Mpc, which is more typical of our sample, it would

Table 2.2. High-velocity feature accelerations

Target	Blue drifts (km s^{-1} yr^{-1})	Red drifts (km s^{-1} yr^{-1})	θ_p (degrees)	Reference
NGC 4258	-0.140 ± 0.03	0.001 ± 0.004	...	Humphreys et al. (2008)
UGC 3789	-0.046 ± 0.04	0.125 ± 0.06	...	Reid et al. (2013)
NGC 6264	0.010 ± 0.02	-0.130 ± 0.01	< 0.50 (b)	Kuo et al. (2013)
NGC 6323	0.030 ± 0.15	-0.067 ± 0.09	< 1.50 (b)	Kuo et al. (2015)
Mrk 1419	0.007 ± 0.14	0.052 ± 0.14	< 0.35 (b)	...
NGC 1194	0.031 ± 0.13	0.039 ± 0.14	< 1.55 (b)	Litzinger et al. (*in prep.*)
NGC 2273	0.074 ± 0.23	-0.011 ± 0.18	< 0.55 (r)	...
J0437+2456	0.036 ± 0.14	-0.011 ± 0.48	< 0.55 (r)	...
ESO 558-G009	-0.157 ± 0.23	-0.047 ± 0.22	< 6.25 (r)	...
IC 2560	0.011 ± 0.15	-0.063 ± 0.13	< 0.55 (b)	...
NGC 5765b	-0.049 ± 0.04	0.008 ± 0.008	...	Gao et al. (2016)
All	-0.036 ± 0.014	-0.012 ± 0.003	< 0.60 (b)	

Note. — This table lists the mean velocity drifts of high-velocity maser features in the best-sampled targets, along with their 1σ statistical errors. Values taken from the literature are accompanied by the appropriate citations; all other values are new measurements (see § 2.4.2). Pitch angles are listed as upper limits, and they are calculated from the velocity drifts of either the redshifted (r) or blueshifted (b) features depending on which gives a tighter constraint. Values incompatible with the MM98 model have no associated pitch angle.

likely not have been identified as a disk maser. The systemic features would peak at about 25 mJy, and the strongest high-velocity features would only be about 3 mJy (i.e., marginally detectable in a single-epoch GBT spectrum). However, it is also true that our selection criteria (see § 2.3) allowed for the presence of highly asymmetric flux ratios in the sample (e.g., an NGC 4258 analogue at a distance of 50 Mpc), yet we found none other than NGC 4258 itself. We thus retain the assertion that NGC 4258 is truly anomalous in having such a large flux ratio.

2.5 Variability

There are several classes of variability present in the megamaser spectra, with different timescales and presumed underlying physical causes. We qualitatively outline these classes in this section.

Long-term ($\sim$hundreds of days) "bulk variability" in the line flux of maser feature sets is seen in all sufficiently monitored galaxies. The dynamical timescale for a $\sim$1 pc accretion disk around a $\sim 10^7$ $M_\odot$ black hole is $\sim 10^4$ years, so if this bulk variability has a dynamical origin, then it likely originates from activity much closer to the central AGN than any observed masers. Gallimore et al. (2001) argue that the megamasers in NGC 1068 respond to changes in the central power source, via a reverberation mechanism. We investigate this possibility for several other galaxies in § 2.6.

Many maser galaxies also display short-term ($\sim$monthly) flaring variability, where a single maser line increases enormously in amplitude, often by several orders of magnitude over the course of only $\sim$a week and lasting for several weeks. This flaring may be caused by the chance alignments of individual masing gas clumps in the disk (see, e.g., Kartje et al. 1999). In this picture, masing occurs in localized clouds which are orbiting ballistically in the accretion disk. When one cloud passes in front of another while maintaining velocity coherence (as might happen, e.g., for two high-velocity clouds on either side of the disk midline), the foreground cloud further amplifies the emission from the background cloud, resulting in a rapid increase in line luminosity. This provides another potential mechanism for the bulk variability, as it could be the combined flares of many weak, blended maser lines.

Extremely short-term (intra-day) variability that is also uncorrelated among different spectral features has been observed in two megamaser galaxies: Circinus (McCallum et al. 2005) and NGC 3079 (Vlemmings et al. 2007). This variability has been attributed to interstellar scintillation, and in § 2.5.2 we present evidence for such scintillation in a third megamaser galaxy, ESO 558-G009.

We note that our observations are only sensitive to variability on timescales between 5 minutes $\lesssim t \lesssim 4$ hours and 1 month $\lesssim t \lesssim 10$ years.

2.5.1 Dynamic spectra

One way to effectively visualize both the bulk variability and the flaring variability is through dynamic spectra. In Figure 2.5 we present dynamic spectra for 9 of our best-sampled sources. To create the dynamic spectra, we linearly interpolated the flux densities between consecutive GBT spectra, which were taken at a roughly monthly cadence. For the MCP's monitoring campaign, targets were not observed during the North American summer because atmospheric conditions in Green Bank make K-band observations inefficient during this season. Summer periods with no data are blanked.

Kinematic differences between the systemic and high-velocity features, corresponding to differences in line-of-sight accelerations, are immediately apparent in the dynamic spectra. Figures 2.5(a) and 2.5(h) match well with Fig. 2 from Braatz et al. (2010) and Fig. 1 from Kuo et al. (2013), respectively. Further, we note that the systemic feature located initially at $\sim$3380 km s^{-1} in UGC 3789, which was not used for the distance determination by Reid et al. (2013) in their acceleration analysis for signal-to-noise reasons, shows a clear acceleration in the dynamic spectrum. This feature is offset by about 15 km s^{-1} from the nearest systemic features for which an acceleration was measured, so including it would expand the velocity span of the systemic feature set by $\sim$12% and potentially improve the disk model and associated distance measurement.

Along with the kinematic information, the dynamic spectra also illustrate how the flux densities and overall spectral shape change with time. If we follow, for instance, the systemic features at $\sim$3270 km s^{-1} in UGC 3789, we can see that they vary in amplitude by more than an order of magnitude during the $\sim$6-year span of these observations. We can also see features near this velocity appearing and disappearing with time. Several of the blueshifted features bracketing 2600 km s^{-1}, on the other hand, remain quite stable in both amplitude and structure during the same time range. There are also marked differences in feature stability among different galaxies; NGC 5765b, for instance, has a very consistent spectrum compared to the others. As a result of this spectral stability, NGC 5765b has the most precisely-measured distance of any MCP galaxy to date (Gao et al. 2016). NGC 1194, on the other hand, is observed to be extremely variable; this variability has made measurements of this galaxy challenging (Litzinger et al. *in prep*).

Additionally, we can compare the lifetimes of different flaring features in the spectra. The 3270 km s^{-1} systemic feature in UGC 3789 flared at around day 1700, and it lasted roughly 200 days. This duration is considerably longer than that of the 3810 km s^{-1} redshifted feature, which flared around day 1500 but only lasted $\sim$50 days. Compare this to the 1580 km s^{-1} feature in NGC 2273, which lasted for at least 400 days, and the 8005 km s^{-1} feature in ESO 558-G009, which had a duration of $\sim$100 days.

2.5.2 Scintillation

Interstellar scintillation (ISS) in the Galactic ionized ISM is considered to be the primary mechanism causing the rapid intraday variability observed in pulsars and many extragalactic radio sources (predominantly quasars; see, e.g., Bignall et al. 2004). For a distant source whose emission is undergoing scattering in the turbulent ISM of our Galaxy, it is simplest to treat the sum contribution from the line-of-sight electron column as originating from a single thin "scattering screen" located a distance D from the Earth. In this picture, turbulence is generated on timescales that are much longer than the time it takes a phase-coherent region of the scattering medium (dubbed a "scintle") to cross the source. That is, the phase variations introduced by

(a) UGC 3789

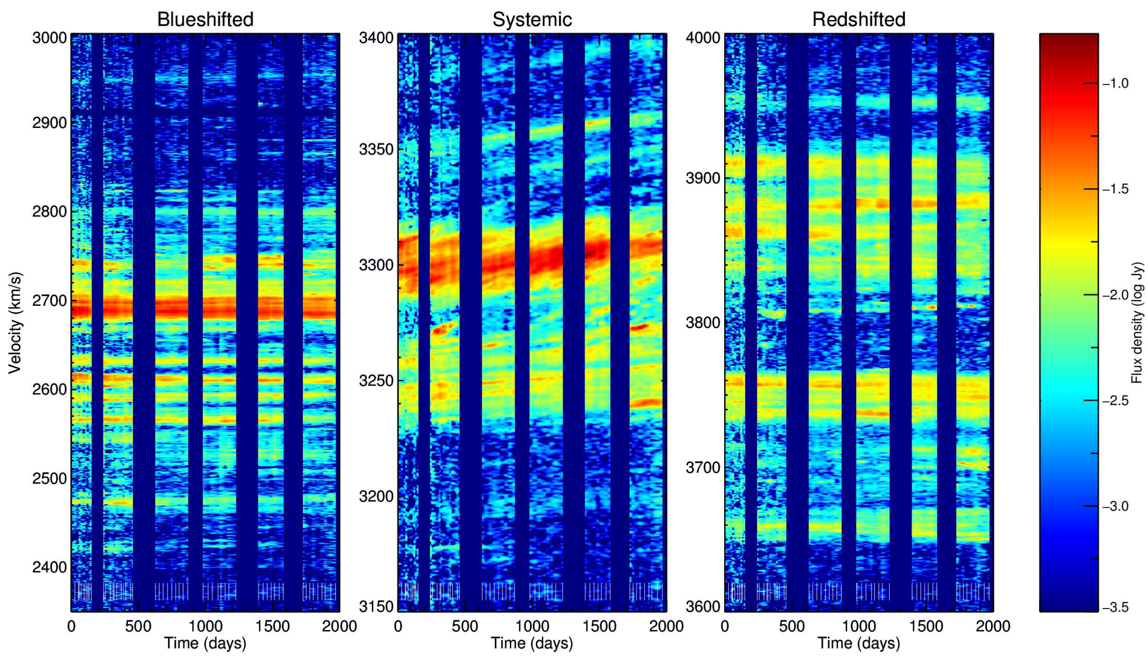

Fig. 2.5.— Dynamic spectra for our best-sampled disk megamasers. For ease of viewing, the three sets of features have been split up and the spectral regions in between (which are devoid of maser features) are not shown. The color scale maps to the logarithm of the flux density, as shown in the colorbar on the right. Individual observation dates are indicated by white tick marks near the bottom of each plot, and day zero is set as the date of the first observation (see Figure 2.1). Velocities are measured in the barycentric frame, using the optical velocity convention.

Fig. 2.5.— (continued)

(b) ESO 558-G009

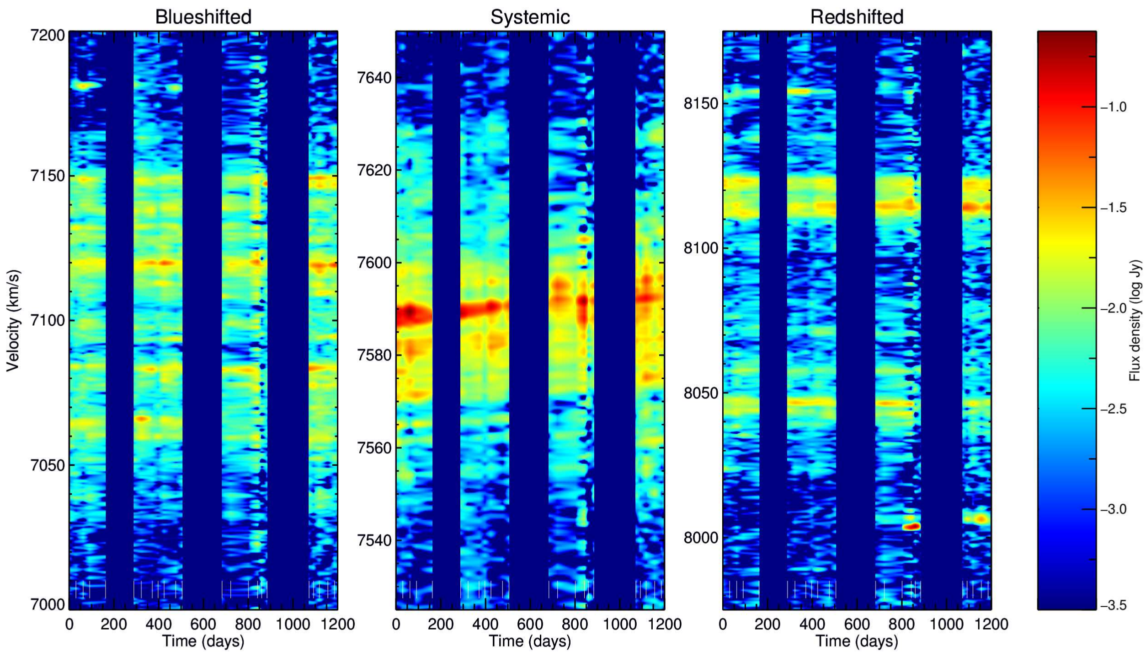

(c) J0437+2456

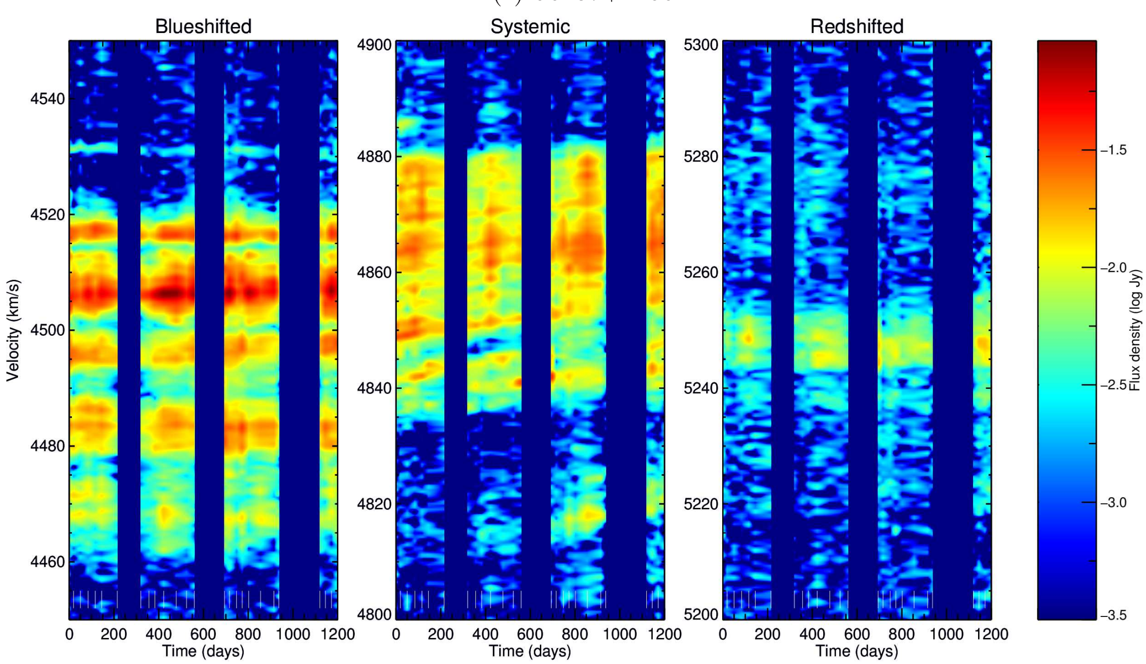

Fig. 2.5.— (continued)

(d) Mrk 1419

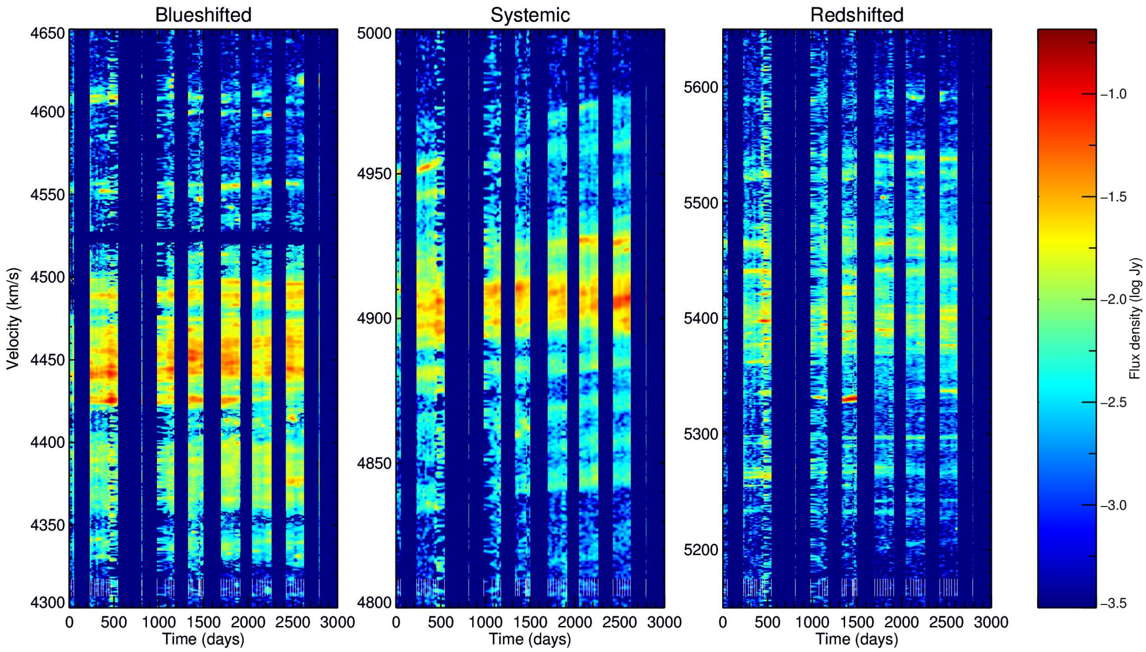

(e) NGC 1194

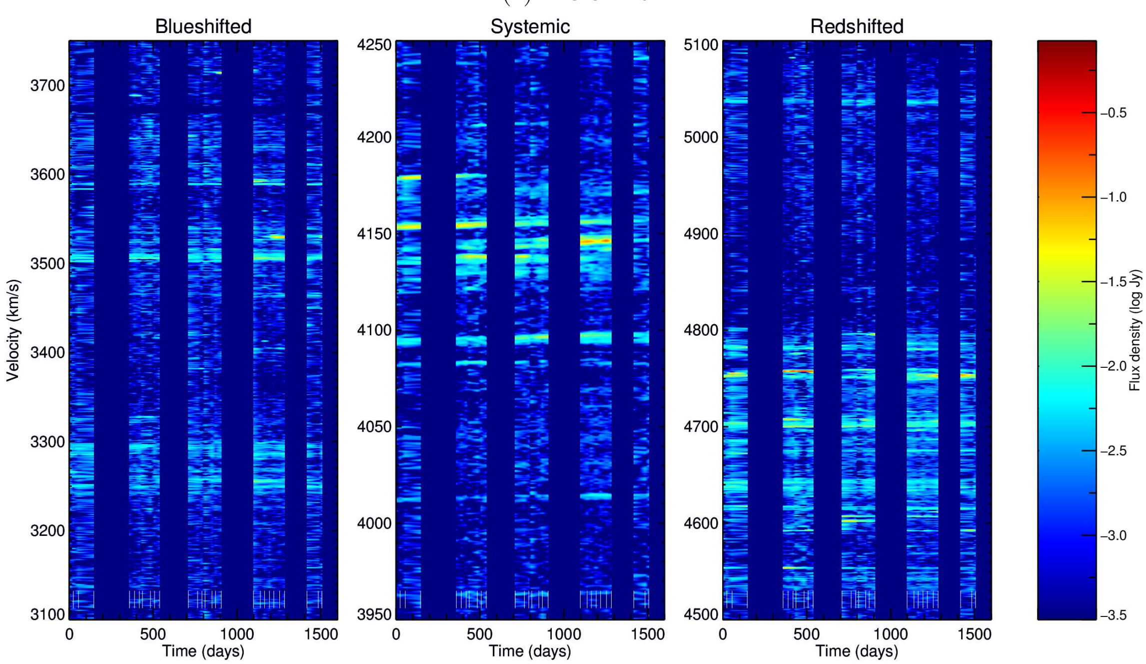

Fig. 2.5.— (continued)

(f) NGC 2273

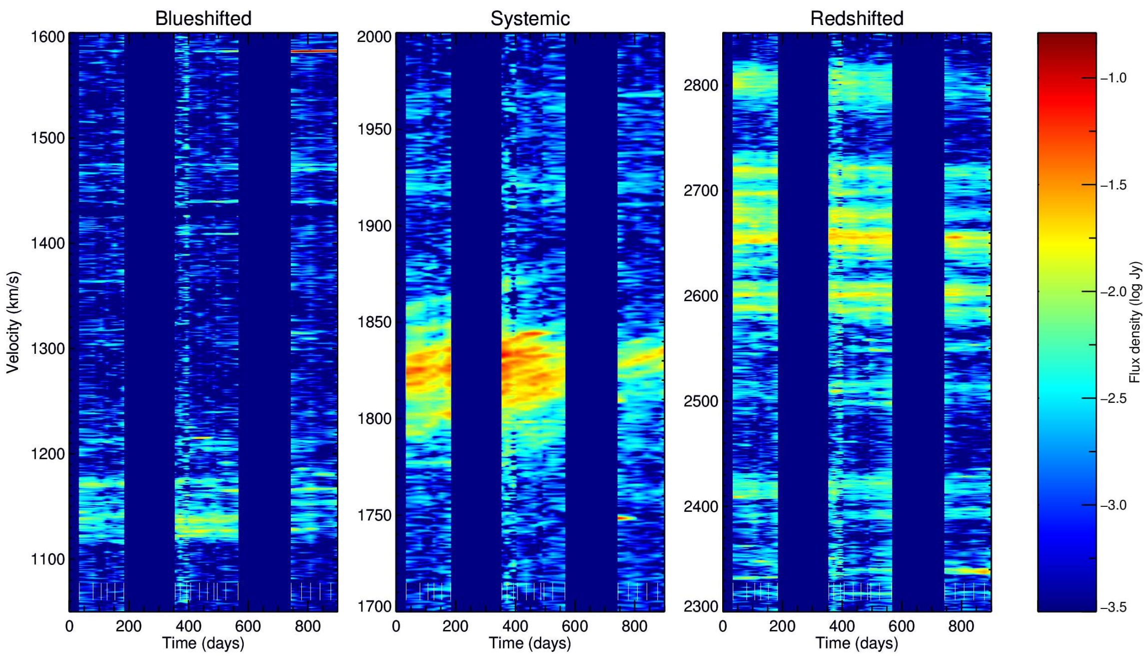

(g) NGC 5765b

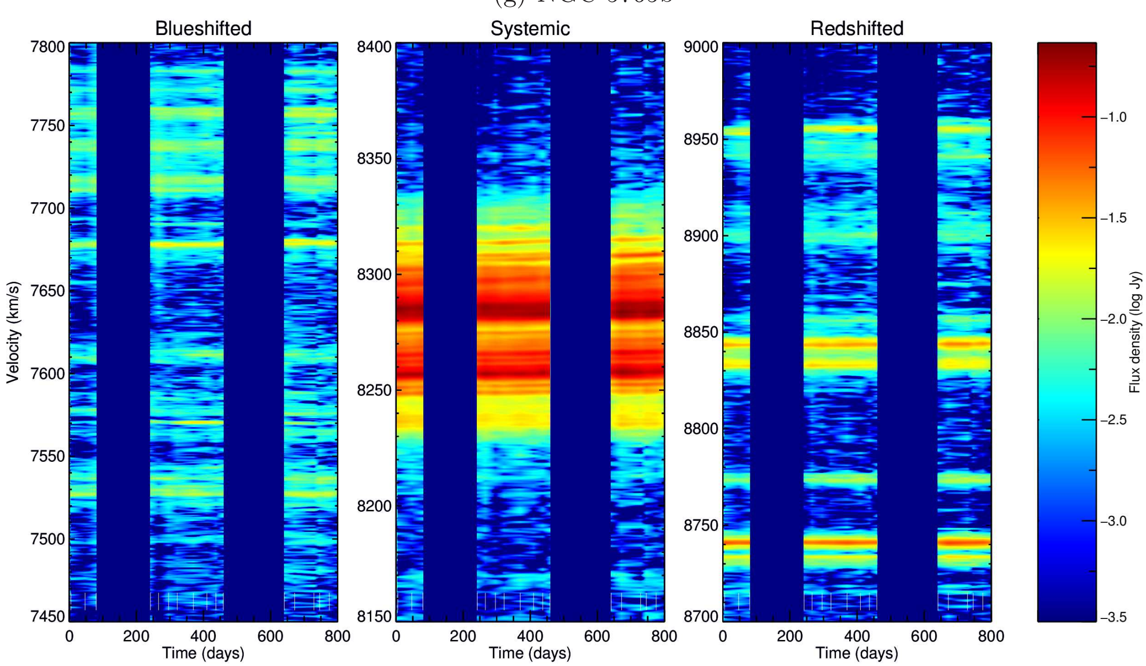

Fig. 2.5.— (continued)

(h) NGC 6264

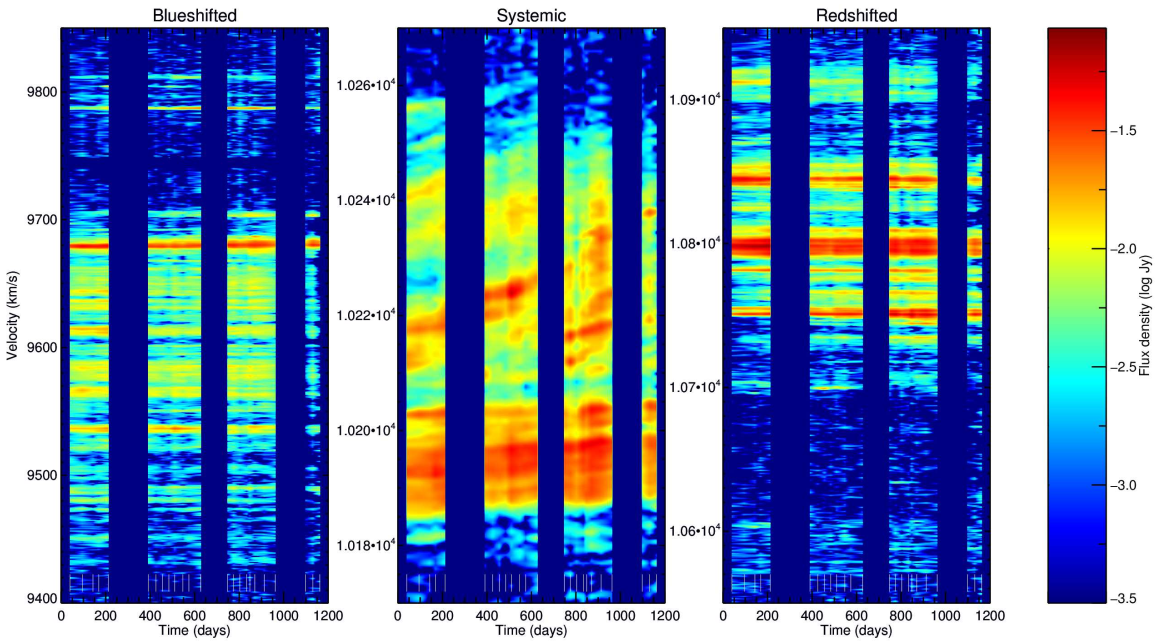

(i) NGC 6323

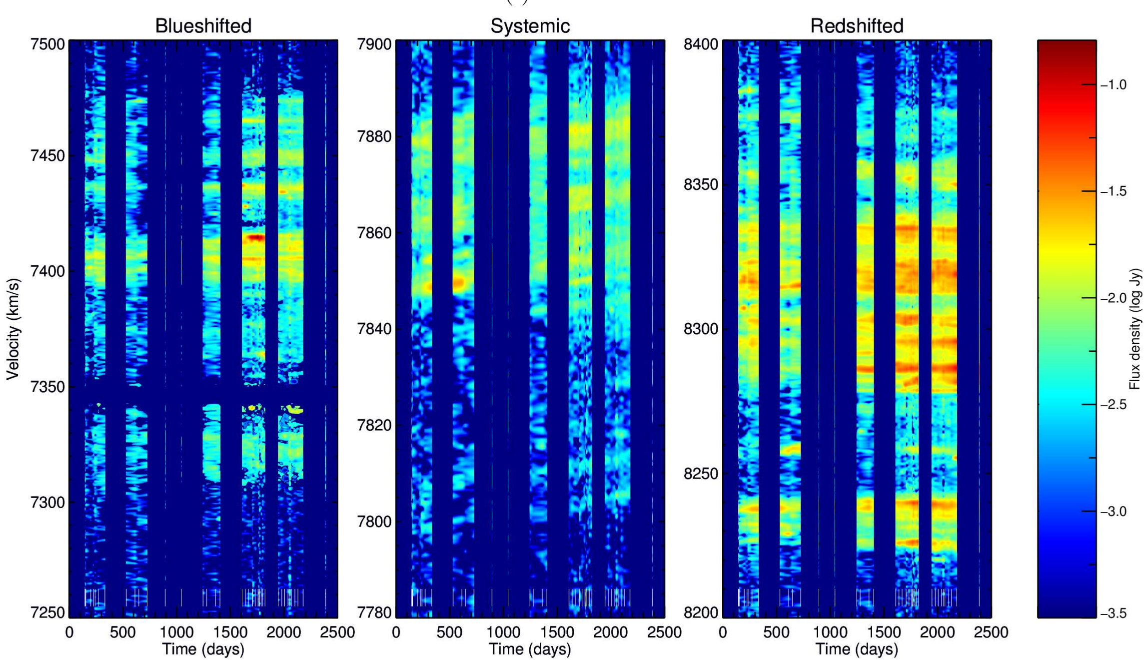

the screen are essentially "frozen" as the screen passes across the line of sight. Thus, the scintillation timescale is set by the size and transverse velocity of the scattering scintle.

There are two important ISS regimes separated by a "transition frequency" ν_t: the weak ($\nu > \nu_t$) and strong ($\nu < \nu_t$) scattering limits. We give a brief overview of some relevant properties of these limits here; for a thorough review of this topic, see Narayan (1992) and references therein.

In the weak scattering limit, the size of the scintle is of order the Fresnel scale, defined to be the transverse distance from the line of sight to a point through which the increase in path length from the source to observer (compared to the direct, line-of-sight path) results in a phase change of 1 radian. For a source at infinity and an observing wavelength $\lambda \ll D$, the Fresnel scale is given by $r_{\mathrm{F}} = \sqrt{\lambda D/2\pi}$. If the scattering screen has transverse velocity (relative to the Earth) of v, the variability timescale will be $\tau \approx r_{\mathrm{F}}/v$.

In the strong scattering limit, the scintle has a characteristic size called the diffractive scale, r_{diff}. This length scale functions equivalently to the Fresnel scale in weak scintillation (i.e., the RMS phase difference between two points on the screen separated by a distance r_{diff} is approximately 1 radian), but the physical origin of the size scale is different. In the strong scattering regime, the value of r_{diff} is determined by the turbulent properties of the ISM plasma rather than by the geometry of the observer-screen-source setup. We thus have $r_{\mathrm{diff}} \ll r_{\mathrm{F}}$ for strong scattering, while $r_{\mathrm{F}} \ll r_{\mathrm{diff}}$ for weak scattering. The scintillation timescale will then be $\tau \approx r_{\mathrm{diff}}/v$. The strong scattering regime can be further subdivided into two different types of strong scattering, diffractive and refractive. Refractive scintillation occurs on much longer timescales ($\sim$days) than diffractive scintillation, so it is not relevant for this study.

A standard measure of variability strength is the modulation index, $\mu = \sigma/\langle S\rangle$, where σ is the standard deviation of the observed amplitude and $\langle S\rangle$ is its average value. The modulation index for a point source undergoing weak scattering is roughly the ratio of the Fresnel to the diffractive scale, $\mu \approx (r_{\mathrm{F}}/r_{\mathrm{diff}})^{5/6}$ (Narayan 1992). For diffractive scintillation, the modulation index should be unity. In the case of an extended source (i.e., a source with an angular size larger than the diffractive scale), the diffractive scintillation is said to be "quenched," since the resolved source is effectively diluting the variability amplitude by averaging the phase fluctuations over several adjacent scintles. An extended source of angular size θ will have a modulation index given by $\theta_{\rm diff}/\theta$.

ISS has been proposed as an explanation for the extremely rapid (intra-hour) variability observed in the 22 GHz maser spectra from the Circinus galaxy and NGC 3079. Vlemmings et al. (2007) use the high Galactic latitude of NGC 3079 ($b = +48.36°$) to justify their assumption of weak scintillation. From a measured characteristic timescale of $\tau \approx 1000$ s, corresponding to the crossing time for the Fresnel scale, they calculate a distance to the scattering screen of $D \approx 25$ pc.

McCallum et al. (2005) measured the timescale in Circinus to be $\tau \approx 700$ s, but were unable to say definitively whether the variability was caused by weak scintillation in a nearby screen ($D \approx 20$ pc) or quenched diffractive scintillation in a more distant screen ($D \approx$ 230-1000 pc). Followup observations from McCallum et al. (2007) showed spectral variations that lent strong support to the diffractive scintillation interpretation, and they further uncovered longer-timescale ($\sim$1 day) variations consistent with refractive scintillation.

Scintillation in ESO 558-G009

We present here observations of the third megamaser galaxy observed to show signs of ISS. Figure 2.6 shows light curves for two epochs of the galaxy ESO 558-G009 on which we've applied our scintillation analysis. These epochs were chosen because of their long observation durations ($\gtrsim$ 3 hours each) and because they both contained the same strong systemic maser feature ($\gtrsim$ 0.15 Jy), which was detectable in a single 5-minute scan. We examined the spectra for all the other megamasers that met these same criteria (long-duration observation and strong maser feature), but only ESO 558-G009 showed significant variability. Figure 2.6 also shows the discrete autocorrelation functions (DACFs) for both of the light curves, calculated using the technique outlined by Edelson & Krolik (1988). The dates of the observations are listed in Table 2.3.

The light curves show variability timescales on the order of $\sim$2100 s, during which the peak flux can vary by a factor of $\sim$3; this is comparable to the amplitude modulations observed in the quasar J1819+3845, the extragalactic source exhibiting the strongest ISS-induced continuum variability (Dennett-Thorpe & de Bruyn 2002). Though it's possible for pointing errors or a changing atmospheric opacity to cause the amplitudes of spectral features to vary with time, we don't expect these effects to exceed $\sim$20%. Further, if such factors were the cause of the observed amplitude changes then we would expect to see them across spectra of all galaxies, which is not the case. As a final check, we measured the total flux of the systemic and high-velocity features (outside of the targeted line) over time during the observations, and we found that it is constant to within $\sim$15% throughout a single observing session.

If the variability were intrinsic to the maser, then such large amplitude changes must result from increases in the maser gain path that are of order the gain length, ℓ, which for an unsaturated maser is the path length corresponding to an e-fold increase in amplification (i.e., it is the length over which the optical depth τ changes by $\sim$1). For conditions typical of those found in megamaser disks, $\ell \gg 1$ AU (Greenhill et al. 1997a). Given the light-travel distance of $\sim$4 AU derived from the characteristic timescale, the observed variability would require changes in the gain path to propagate at approximately the speed of light. Barring radiative pumping (which is not expected to be important in these systems; see, e.g., Lo 2005), we do not know of any mechanism capable of driving such rapid changes. This leaves foreground scintillation as the best available explanation for the variability.

Following Rickett et al. (2002), we define the characteristic observed scintillation timescale, τ, to be the half-width at half-maximum (HWHM) of the autocorrelation function. If the masers behave as a point source (i.e., if their angular size is smaller than the angular size of the scattering screen, $\theta < \theta_s$), then a measurement of τ allows us to establish a characteristic size, r_s, for the scattering screen (i.e., the size of a scintle) of

$$r_s = v_s \tau. \tag{2.10}$$

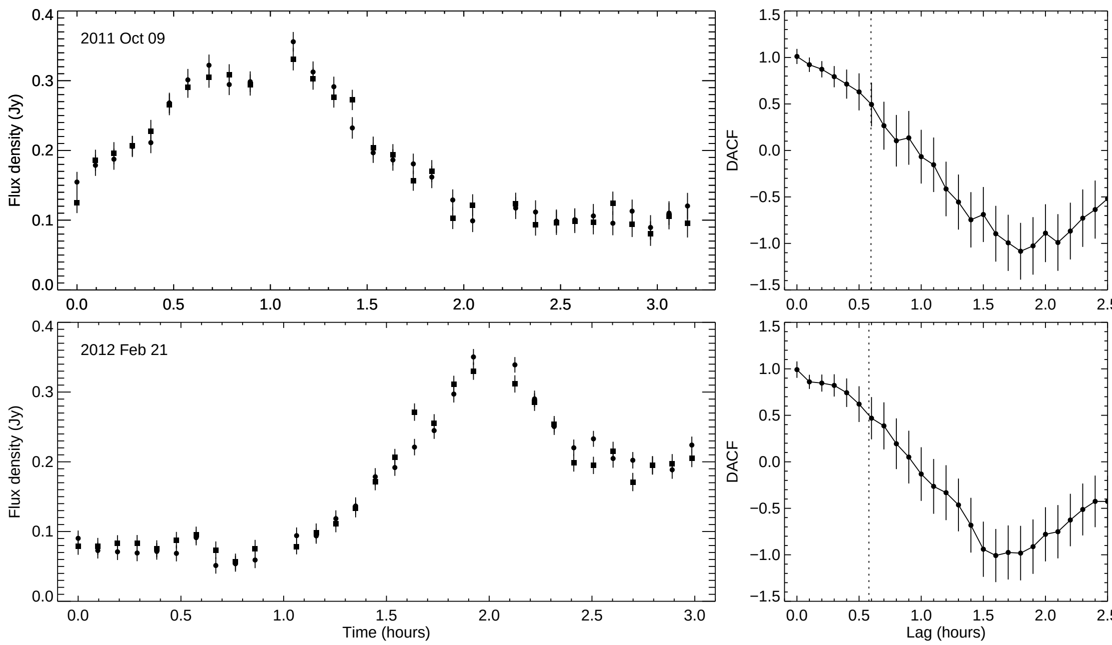

Fig. 2.6.— Light curves (left) and discrete autocorrelation functions (DACF, right) for two observations of ESO 558-G009. In the light curves, the LCP and RCP peak flux densities of the 7590 km s^{-1} maser line are plotted (with circles and squares, respectively) at the $\sim$ 5-minute cadence corresponding to individual nod scan pairs. The dotted vertical line in the DACF marks the location of τ (i.e., where the DACF drops to a value of 0.5).

Here, v_s is the transverse velocity of the screen relative to Earth. In Appendix B we have outlined how this transverse velocity is obtained for an individual observation, using a model that combines the Earth's orbital motion and the Sun's peculiar and orbital motion. Table 2.3 lists v_s for each observation, assuming a nearby ($D \lesssim 100$ pc) screen; the measured values for τ are also listed.

Our model assumes that the scattering screen itself has no peculiar motion. From time-delay measurements of the intra-day variability in the quasar J1819+3845, Dennett-Thorpe & de Bruyn (2002) found that the scattering screen (for that target) must have a transverse peculiar velocity of about 25 km s^{-1}. McCallum et al. (2009) used the same technique to place a lower limit of 22 km s^{-1} on the transverse velocity of the ISM along the line of sight to Circinus. We have no reason to expect that the scattering screen towards ESO 558-G009 should behave any differently. However, with two free parameters already in the model (D and r_s) and only two measurements, we have no room to add the two additional parameters that would be necessary to properly account for peculiar motion. We are thus only able to place relatively crude constraints on the model parameters. Figure 2.7 shows these constraints, with the more relevant $\theta_s = r_s/D$ plotted in place of r_s. We can see that our measurements, which have a formal "best fit" at about $D \approx 70$ pc and $\theta_s \approx 5$ μas, are compatible with a wide range of parameters. A scintle angular size of 5 μas corresponds to a lower limit on the maser brightness temperature of $\sim 3 \times 10^{13}$ K.

If we assume that the scintillation occurs in the weak scattering regime, then we have $r_s \approx r_{\mathrm{F}}$, and we can use the Fresnel scale to determine D. Doing so yields a distance to the scattering screen between 40 and 50 pc. From Walker (1998), we can use the modulation index to determine the transition frequency. Between the two observations, $\mu \approx 0.5$, so we obtain $\nu_t \approx 13.6$ GHz.

Like Circinus, ESO 558-G009 is located near the plane of the Galaxy ($b = -6.96°$), so we would expect to see greater-than-average scattering along this line of sight. From the NE2001 model for the electron density along different lines of sight in the Milky Way (Cordes & Lazio 2002), the transition frequency between weak and strong scintillation towards ESO 558-G009 should actually be about 30 GHz; since this is higher than the observing frequency of 22 GHz, it would put us in the strong limit. We note that the Cordes & Lazio (2002) model attempts to map the Galactic electron density in a primarily spatially smooth manner, while the true distribution is known to have mesoscale and microscale structure. We thus expect significant model uncertainties along any specific line of sight.

In the strong scintillation regime the measured timescale maps to the angular size of the source rather than to that of a scintle. The modulation index should be equal to the ratio $\theta_{\rm diff}/\theta_{\rm s}$, so a modulation index of $\mu \approx 0.5$ (see Table 2.3) indicates that the angular size of the maser must be a factor of $\sim$2 larger than that of the scintle. For a screen distance of 70 pc we have $\theta_{\rm s} \approx 5$ μas. For the ESO 558-G009 distance of 110 Mpc, we thus obtain an approximate physical size of the masing region of $\sim$1100 AU. This is comparable to the 0.001–0.006 pc clump sizes estimated by Kondratko et al. (2005) for the disk of NGC 3079.

2.6 Testing for disk reverberation

Claussen & Lo (1986) noted that the apparent systematic flux variations in the nuclear masers in NGC 1068 suggested that the masers share a common pumping source. If all masers in a given galaxy are powered by a common source, presumably at the nucleus, then we would expect variability in the power source to propagate to the maser system. This variation would reverberate through the masing disk at some propagation velocity which, if it is on the order of the speed of light, would be fast enough to pass through the entire masing portion of the disk on timescales of a year or two. Gallimore et al. (2001) measured a correlation between the variability of redshifted and blueshifted maser features in NGC 1068, which they used to argue that the masers respond to variability in the central engine.

Since the fiducial picture of circumnuclear megamaser disk geometry (for a Keplerian rotation curve) allows us to uniquely associate any high-velocity maser feature with a radial location within the accretion disk, we attempt here to detect the propagation of some signal through the masing disks of our best-sampled targets. A measurement of disk reverberation would not only lend support to the idea of a common pumping source, but it could also potentially enable an independent means of

Table 2.3. Scintillation parameters for ESO 558-G009

Date	v (km s^{-1})	v_s (km s^{-1})	$\langle S\rangle$ (Jy)	σ (Jy)	μ	τ (hours)
2011 Oct 09	7589.8	24.4	0.186	0.082	0.44	0.60 ± 0.07
2012 Feb 21	7590.3	27.4	0.166	0.088	0.53	0.58 ± 0.08

Note. — Scintillation parameters for ESO 558-G009. The column titled v lists the Doppler velocity for the targeted line, v_s is the modeled transverse velocity at the observation date (see Appendix B for details), $\langle S\rangle$ is the mean flux density for the line during the observation, σ is its standard deviation, μ is the modulation index, and τ is the measured characteristic variability time.

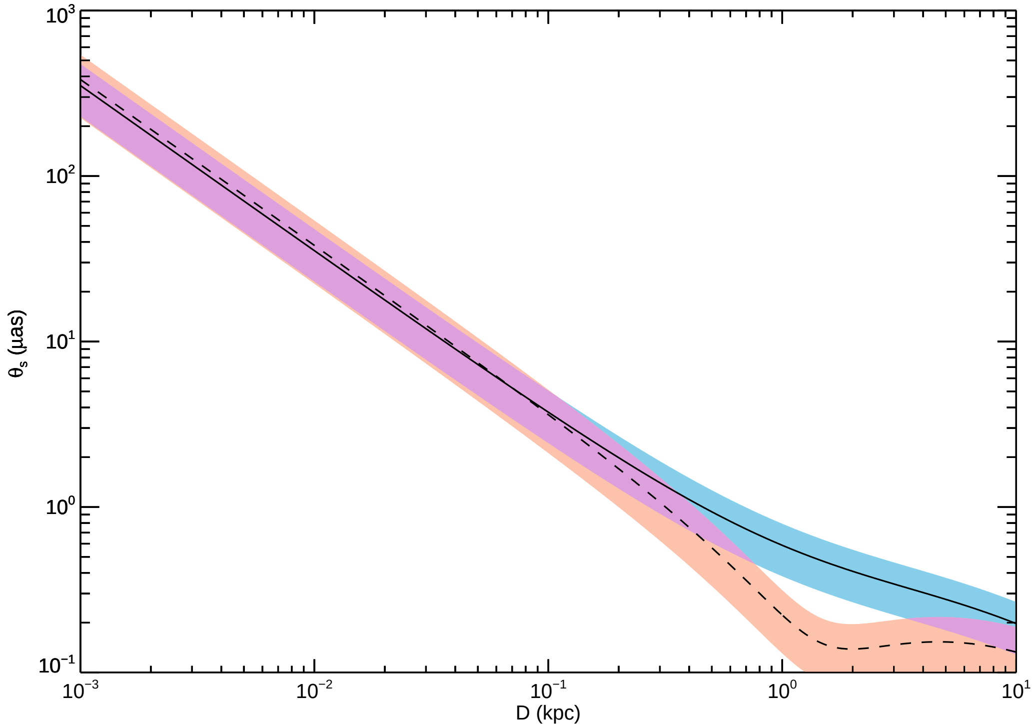

Fig. 2.7.— Constraints on the angular size of the scintles and the distance to the scattering screen along the line of sight to ESO 558-G009. The solid line (with 3σ error in blue) shows the constraint from the 2011 October 9 observation, and the dashed line (with 3σ error in red) shows the constraint from the 2012 February 21 observation. The plotted errors account only for the statistical errors arising from the measurement of τ; no systematic errors from the velocity modeling are included.

measuring the mass of the central SMBH and the distance to the host galaxy (provided the propagation velocity of the reverberation signal is known). If we denote the outward propagation speed as v_s, then a reverberation signal passing through the spectrum at a rate $\dot{v}$ corresponds to a black hole mass of

$$M_{\mathrm{BH}} = -\frac{v_s(v - v_0)^3}{2G\dot{v}}. \tag{2.11}$$

Here, v is the observed velocity (i.e., as seen in the spectrum) and v_0 is the velocity of the dynamic center (i.e., the motion of the black hole itself, which is presumably almost identical to the recession velocity of the galaxy). We note that $\dot{v}$ will in general be a function of v; that is, for a constant value of v_s the rate at which the reverberation signal passes through the spectrum depends on where in the spectrum it is located. Once the black hole mass is known, the distance to the galaxy can be determined by comparing the angular orbital radii of the maser spots (measured using VLBI) to the orbital radii calculated using the single-dish spectra (from $r = GM_{\mathrm{BH}}/v^2$).

2.6.1 Extracting a reverberation signal

Here we outline the procedure used to check for the spectral signature of radially-propagating excitation in a time series of GBT disk maser spectra. The relevant parameters are the mass of the central black hole, M_{BH}, the recession velocity of the dynamic center, v_0, and the propagation speed of the signal, v_s. The observed response of a high-velocity maser offset by a distance D (see bottom panel in Figure 2.8) is delayed by D/v_s relative to the response of all systemic masers.

We subtract a weighted average spectrum (see § 2.3) of the target from each epoch to remove stable (i.e., non-propagating) high-velocity features from each spectrum. We then map each velocity channel, v_i, to a radial position, r_i, within the maser disk. The mapping assumes that the high-velocity maser spots are all located on the midline of the disk, and that they are all on circular Keplerian orbits:

$$r_i = \frac{GM_{\mathrm{BH}}}{(v_i - v_0)^2}. \tag{2.12}$$

We refer to the original GBT spectra as the "velocity spectra" and the new, radially-mapped spectra as the "radial spectra." An example of these two for the source UGC 3789 is shown in Figure 2.8.

To account for the time delay between the detection of a propagating signal in consecutive epochs, each radial spectrum is temporally shifted according to the signal propagation speed and that spectrum's date of observation, relative to some reference epoch. For simplicity, we have defined the temporal zeropoint to be the date of the first observation, given in Figure 2.1. This process is illustrated in Figure 2.9.

After shifting, the radial spectra are then averaged over all epochs. If a target has been observed for N epochs, each of which has an associated radial spectrum $S_n(r, t_n)$, then this procedure can be written as

$$S(r) = \frac{1}{N} \sum_{n=1}^{N} S_n(r - v_s t_n, t_n). \tag{2.13}$$

Here, $S(r)$ is the final combined radial spectrum. The radial zeropoint is defined to be the center of the disk (i.e., the location of the SMBH) at the date of the first observation.

The purpose of this procedure is to stack spectra in such a way that a radially-propagating signal will add coherently across all epochs.

2.6.2 Sensitivity

The sensitivity of our method depends on several factors, including the number of epochs and overall time baseline of observation, as well as the intrinsic variability of the target. We restrict our analysis to well-sampled (i.e., $\gtrsim$20 epochs of observation) galaxies that have reliably measured black hole masses (see Kuo et al. 2011).

Some of these targets are more variable than others. In general, the more flaring a source displays, the less sensitive this measurement will be. Flaring events are not removed well when subtracting an epoch-averaged spectrum, and so sufficiently strong flares can appear as false positives in the final radial spectrum.

Although we've chosen to test only those sources for which $M_{\rm BH}$ is known to

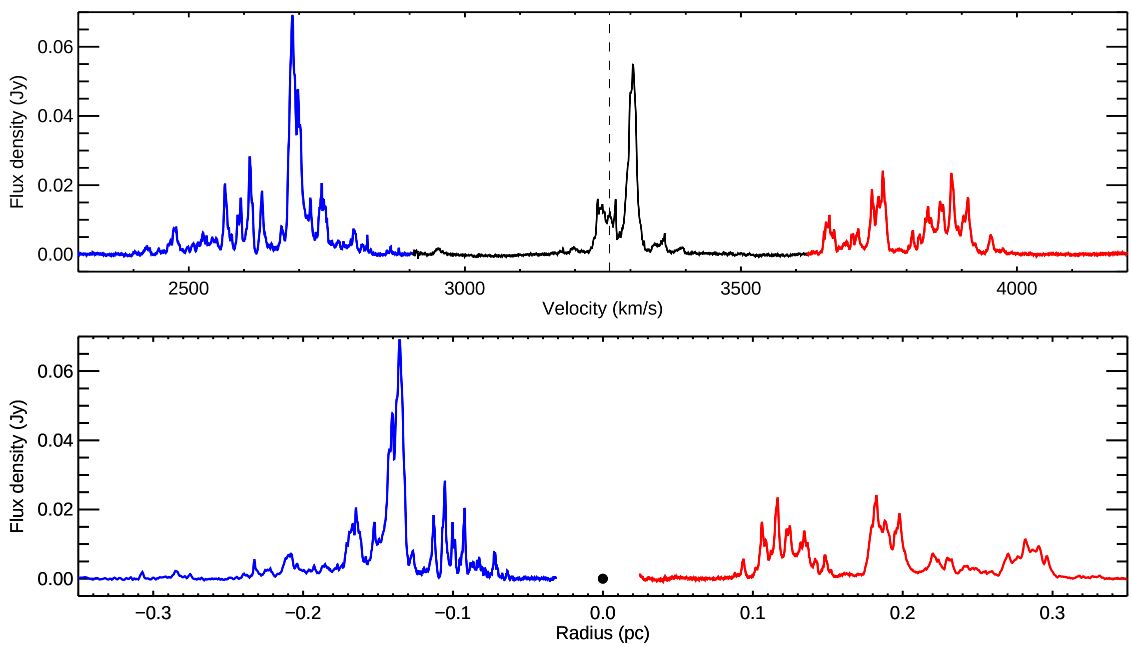

Fig. 2.8.— Illustration of the conversion between a velocity spectrum (top) and a radial spectrum (bottom), using Equation 2.12. The dashed line in the upper spectrum shows the recession velocity of the system, and the black point in the lower spectrum shows the location of the SMBH. The blueshifted portion of each spectrum is plotted in blue, while the redshifted portion is plotted in red. The source chosen for this example is the galaxy UGC 3789.

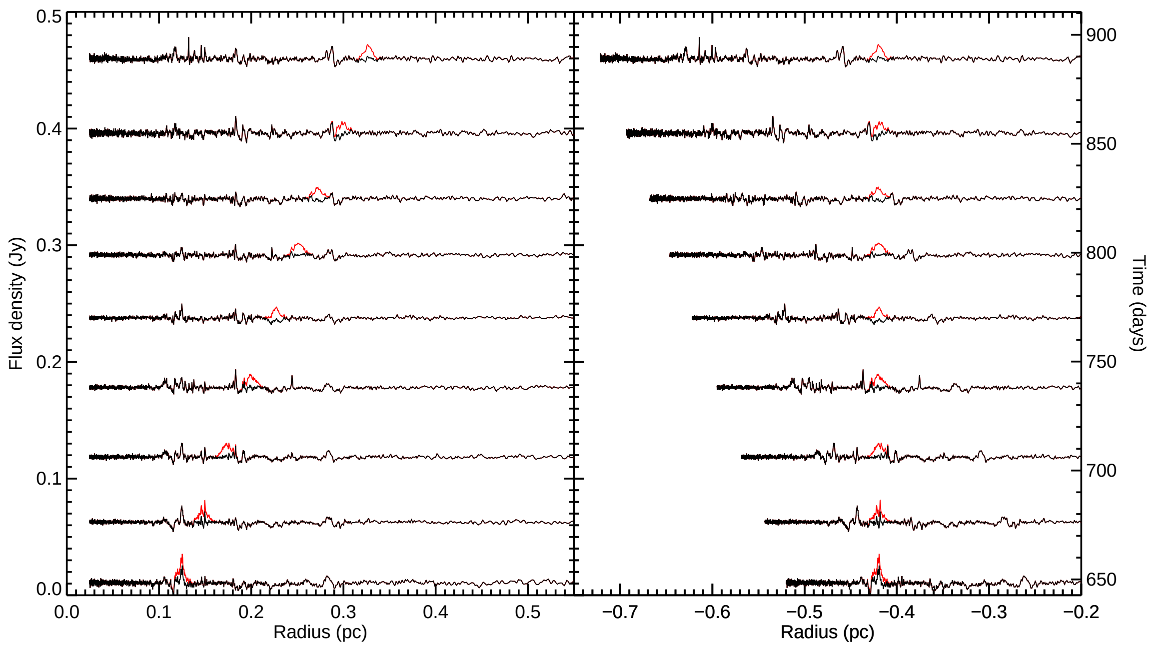

Fig. 2.9.— These plots show the radial spectra before (left) and after (right) accounting for the time delay caused by the propagation of the signal. The black spectra are real spectra of UGC 3789, and the red line includes the artificially injected 10 mJy signal. In the panel on the left, we can see that the artificial signal is propagating outwards with time. In the panel on the right, the spectra have been temporally shifted using $v_s = c$; as a result, when stacking these spectra the signal will add coherently. In both panels, the spectra have been vertically offset by an amount proportional to the time between observations; the time since the first observation is shown on the right axis. The radial zeropoint corresponds to the position of the SMBH at the time of the first observation. Only the redshifted high-velocity features are shown in these plots.

$\sim$10% or better, it's possible that our method requires the value to be even more precisely known to ensure recovery of a propagating signal. To test the sensitivity of our method on the input values of v_s and $M_{\rm BH}$, we injected an artificial propagating signal into a series of spectra. The signal was a Gaussian pulse of fixed width and amplitude, propagating with a fixed velocity from a black hole of known mass. We found that the tolerance threshold for both v_s and $M_{\rm BH}$ was approximately 5%; if either of these inputs is off from the true value by more than this amount, the signal is not recovered or is severely degraded.

2.6.3 Discussion

We tested for reverberation in the six maser galaxies listed in Table 2.4. For each galaxy, we checked for signals propagating at velocity increments of $0.01c$, with minimum and maximum propagation velocities of $0.8c$ and $1.2c$, respectively[1]. We also adjusted the black hole masses within a range $\pm$20% of the measured value, in increments of 1%. No reverberation signals were detected in any of the galaxies, with limiting flux densities listed in Table 2.4. Given that the spectra for these galaxies typically vary at the $\sim$tens of mJy level (see § 2.5), we can see that any contribution from a propagating signal must constitute only a small ($\lesssim$10%) fraction of the total variability.

The detection thresholds listed in Table 2.4 are simply the 3σ noise levels in the final combined spectra. We emphasize that this threshold gives only a limiting value for a signal that is perpetually coherent (i.e., always maintains its profile shape and moves at constant velocity) and that is present in all available spectra (i.e., it does not fade in and out as it propagates). This procedure is less sensitive to a more complex signal.

[1] We actually investigated propagation speeds down to $0.0c$, but the sensitivity of the method starts to drop considerably below a certain speed. This is because the individual maser features – which in general aren't perfectly matched to the average spectrum, so they don't subtract out well – begin to add semi-coherently, rather than averaging out like noise. To give an example, the 3σ threshold for UGC 3789, which is about 0.8 mJy for propagation speeds between $0.8c$ and $1.2c$, increases to $\sim$5 mJy for a propagation speed of $0.5c$. This also makes it more difficult to differentiate between a propagating signal and a coherently-added maser feature, so we only quote sensitivities between $0.8c$ and $1.2c$ in Table 2.4.

Furthermore, we note that the timescale for variability of the pumping source influences our measurements. If the source doesn't vary much over the ∼few-year timescales probed by these data, then the signal won't be radially localized and our technique will not help to detect it.

2.7 Magnetic field strengths from Zeeman splitting

Magnetic fields in AGN accretion disks are thought to drive several important physical processes. The magnetorotational instability (MRI), first described in a general astrophysical context by Balbus & Hawley (1991), is likely the primary means by which angular momentum is transported in accretion disks. Magnetic fields are also necessary for launching outflows, from the classic MHD disk wind (Blandford & Payne 1982) to more modern incarnations that also incorporate radiation pressure (e.g., Keating et al. 2012). In this section, we use measurements of the Zeeman effect to place limits on the magnetic field strength in several megamaser disks.

The maser emission that we observe at 22 GHz arises from one or more of the six hyperfine transitions of the 6_{16}-5_{23} rotational transition of the water molecule (see Fiebig & Güsten 1989). Since this molecule is non-paramagnetic, Zeeman splitting of these hyperfine energy levels arises from the coupling between the nuclear magnetic moments and an external magnetic field. This causes the effect to be much weaker (by a factor of $\sim 10^3$) in water than in molecules such as OH, where the unpaired electron's spin couples with the magnetic field. The drastic difference in magnitude arises because the Bohr magneton and the nuclear magneton differ by the ratio of the electron to the nucleon mass, $m_e/m_p \approx 1/1836$.

An external magnetic field causes each hyperfine level to split into three groups of lines: the π components and the $\sigma^{\pm}$ components, corresponding to magnetic quantum number changes of $\Delta M_F = 0$ and $\Delta M_F = \pm 1$, respectively (Modjaz et al. 2005). The $\sigma^{\pm}$ components are circularly polarized about the magnetic field direction, and they are symmetrically offset from the parent frequency. For weak magnetic fields (i.e.,

Table 2.4. Disk reverberation sample

Target	v_0 (km s^{-1})	$M_{\rm BH}$ (10^7 M$_\odot$)	Epochs	Threshold (mJy)
UGC 3789	3262	1.04	58	0.8
Mrk 1419	4954	1.16	55	1.4
NGC 6323	7829	0.94	44	1.2
NGC 1194	4063	6.5	43	4.1
NGC 2273	1832	0.75	38	1.8
NGC 6264	10194	2.91	28	0.8

Note. — Galaxies tested for a reverberation signal. The threshold column lists the 3σ detection cutoffs; a signal stronger than this value would be classified as a detection. Note that the velocity of the dynamic center (v_0) need not be the same as the recession velocity of the galaxy listed in Table 2.1, as the v_0 values were obtained by fitting Keplerian rotation curves to position-velocity data (Kuo et al. 2011).

$B \lesssim 1$ Gauss), this frequency offset is small compared to the line width; typically $(\Delta v_z/\Delta v_L) \sim 10^{-3}$–$10^{-4}$.

2.7.1 Method

In principle, the measured frequency difference between the left and right circular polarizations (corresponding to σ^+ and σ^-, respectively) allows us to determine the line-of-sight component of the magnetic field at the location of the maser spot. Since the offset is small compared to the width of the line profile, the Stokes V profile (given by $V = [\mathrm{LCP} - \mathrm{RCP}]/2$) is proportional to the derivative of the Stokes I profile (given by $I = [\mathrm{LCP} + \mathrm{RCP}]/2$). This leads to a characteristic S-shape of the Stokes V profile (see, e.g., Vlemmings et al. 2001, Fig. 2).

Modjaz et al. (2005) conducted a series of Monte Carlo simulations which established that the RMS sensitivity to the line-of-sight component of the magnetic field from a single maser line is consistent with what one would expect from a statistical treatment (see, e.g., Lenz & Ayres 1992), namely:

$$\sigma_B = \frac{\Delta v_L}{2A} \left[\frac{S}{N} \right]^{-1} . \tag{2.14}$$

Here, Δv_L is the FWHM line width, S/N is the Stokes I signal-to-noise ratio, and A is the Zeeman splitting coefficient (which is different for each hyperfine transition). After numerically solving the radiative transfer and rate equations for magnetized water masers, Nedoluha & Watson (1992) found that a value for A of 0.020 km s^{-1} G^{-1} was most appropriate for the merging of the three dominant hyperfine components. This value assumes that the three strongest hyperfine lines all contribute to a given observed maser line, and deviations from this value never exceeded a factor of $\sim$2 across the range of parameter space investigated in Nedoluha & Watson (1992). We thus adopt $A = 0.02$ km s^{-1} G^{-1} for our calculations, which in general follow the same procedure outlined in Modjaz et al. (2005).

For extragalactic sources, only three efforts to measure magnetic field strengths using the Zeeman effect in H_2O megamasers have been published. Modjaz et al. (2005) placed a 1σ upper limit of 30 mG on the radial component of the magnetic field in NGC 4258, using a cross-correlation method to handle the heavy blending of the spectral features. Vlemmings et al. (2007) used the same technique on NGC 3079, obtaining an upper limit of 11 mG for the blueshifted features. Both studies also measured limits for strong, isolated maser components, and combined these results with those from the cross-correlation method. Additionally, McCallum et al. (2007) measured isolated lines to place a 1σ upper limit of 50 mG on the toroidal component of the magnetic field in the Circinus galaxy.

2.7.2 Measurements

The most sensitive test for Zeeman splitting using individual (i.e., non-blended) maser lines occurs on lines that are both strong (large signal-to-noise) and narrow (small Δv_L). We therefore focused our test on strong ($S/N > 50$) flaring events.

For each selected maser flare, we separately reduced the LCP and RCP spectra without applying Hanning smoothing; this process retains the full spectral resolution. To compensate for errors in flux scale calibration, the peak value of the RCP spectrum was scaled to the value of the LCP spectrum prior to computing either the Stokes I or Stokes V spectra. Typical scaling offsets were of order 10%. We note that the absolute intensity scale is unimportant for these measurements.

We did not detect Zeeman splitting in any of the maser lines, so our results here yield only upper limits on the magnetic field strengths. These results are summarized in Table 2.5, and an example measurement (from NGC 1194) is shown in Figure 2.10.

2.7.3 Discussion

Since the Zeeman measurements are only sensitive to the line-of-sight magnetic field, $B_{\|}$, the high-velocity and systemic lines measure different equatorial components of this field. The high-velocity features measure the toroidal component of the field, $B_{\rm tor}$, while the systemic features measure the radial component, $B_{\rm r}$. None of the features directly measure the poloidal component of the magnetic field, but an appropriate model (see, e.g., Hawley et al. 1996) can estimate its magnitude using the values of the toroidal and radial components.

Even without knowledge of the poloidal component, we can still use the derived upper limits to constrain the support mechanism for the accretion disks. This is because only the components of the field that thread through the disk (i.e., only the radial and toroidal components) can provide vertical pressure support. For typical maser conditions of $n \approx 10^9$ cm^{-3} and $T \approx 1000$ K, the gas pressure amounts to roughly 10^{-4} erg cm^{-3}. The equivalent support from magnetic pressure would require a $\sim$50 mG magnetic field, which is comparable to (though still slightly below) our most stringent limits. It is worth noting that these numbers are also comparable to the $\sim$100 mG upper limit imposed by hydrostatic equilibrium for the disk thickness measured by Argon et al. (2007) in NGC 4258.

Table 2.5. Zeeman sample

Target	Date	$M_{\rm BH}$ (10^7 M$_\odot$)	v (km s^{-1})	$V_{\rm rot}$ (km s^{-1})	Peak (mJy)	S/N	Δv_L (km s^{-1})	$B_\parallel$ (mG)	Radius (pc)
NGC 1194	2007 Dec 26	6.5[a]	4757.6	694.6	340	141	0.58	<100 (t)	0.58
NGC 1194	2010 Apr 10	6.5	4146.4	83.4	210	97	0.87	<220 (r)	-
NGC 1194	2011 Dec 30	6.5	4097.2	34.2	1020	330	0.96	<73 (r)	-
NGC 1194	2011 Dec 30	6.5	4751.7	688.7	800	259	0.95	<91 (t)	0.59
NGC 2273	2009 Dec 12	0.75[a]	1582.5	−249.5	240	115	0.72	<160 (t)	0.52
NGC 3393	2006 Apr 28	3.1[b]	4050.9	300.9	230	95	0.84	<220 (t)	1.48
NGC 3393	2006 Dec 6	3.1	4260.8	510.8	350	94	1.1	<300 (t)	0.51
UGC 3789	2010 Dec 20	1.04[a]	3273.0	11.0	190	75	0.74	<250 (r)	-
NGC 6323	2008 Mar 25	0.94[a]	7395.2	−433.8	180	86	1.0	<300 (t)	0.21
ESO 558-G009	2013 Apr 22	1.8[c]	8003.7	329.7	490	81	0.99	<310 (t)	0.71
Mrk 1419	2007 Apr 14	1.16[a]	5330.8	376.8	220	56	1.6	<720 (t)	0.35

Note. — Maser lines tested for Zeeman splitting. For flaring lines appearing in more than one epoch, the listed observation date is that which yields the best upper limit on the line-of-sight component of the magnetic field. In addition to the Doppler velocity (v), we list the rotation velocity ($V_{\rm rot} = v - v_0$; blueshifted lines are negative, v_0 is the velocity of the dynamic center) and the measured line width (Δv_L) for each line. For all lines, $B_\parallel$ is quoted as a 1σ upper limit, and the letters in parentheses indicate whether the measurement is sensitive to the toroidal (t) component or the radial (r) component. For limits on toroidal magnetic field components, the radius column gives the corresponding radial location in the disk at which the limit holds.

[a] Kuo et al. (2011)

[b] Kondratko et al. (2008)

[c] Gao et al. (2016)

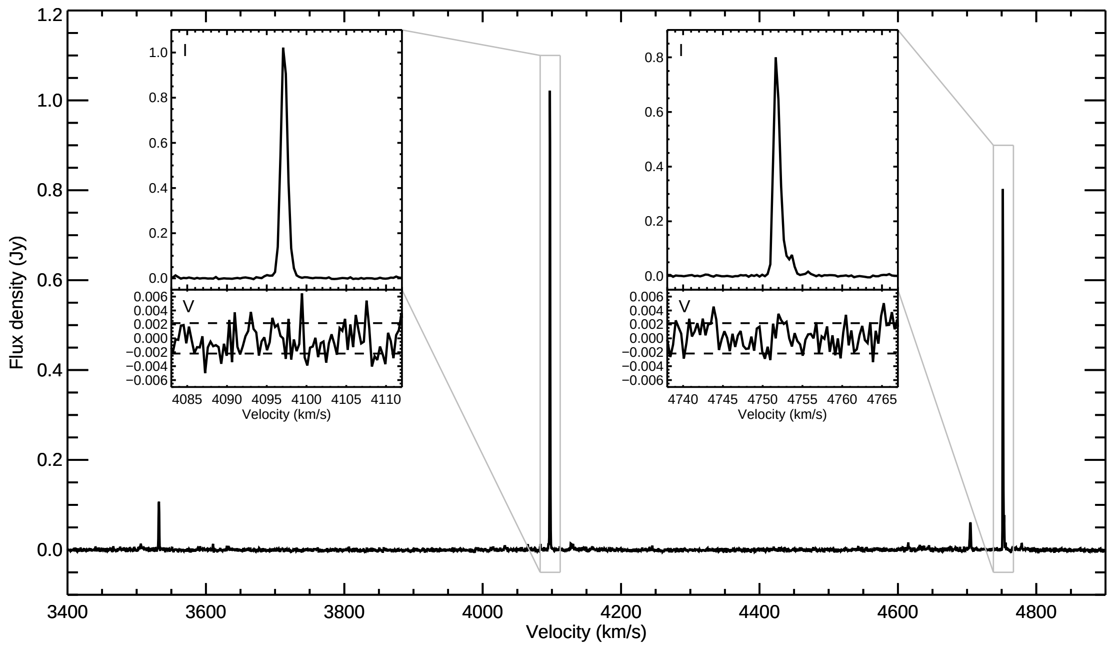

Fig. 2.10.— GBT spectrum of NGC 1194, taken on 2011 December 30. Inset are the Stokes I and V profiles for the 4097.2 km s^{-1} feature (left) and the 4751.7 km s^{-1} feature (right). The black dashed lines in the Stokes V plots show the 1σ RMS level for this spectrum. No Zeeman profile is evident for either of these lines; limits are given in Table 2.5.

Chapter 3

Submillimeter H_2O megamasers in NGC 4945 and the Circinus galaxy

Note: the material presented in this chapter has been published in Pesce et al. (2016).

3.1 Introduction

Nuclear water vapor megamasers currently provide the only direct means to map gas in active galactic nuclei (AGN) on size scales of ∼0.1–1 pc. Nearly all of the observational work on H_2O megamasers to date has focused on the $6_{16} - 5_{23}$ rotational transition at 22.235 GHz from the ortho-H_2O molecule (Lo 2005). More than 160 galaxies have been detected in this line so far, the result of some ∼4000 galaxies surveyed (e.g., Braatz et al. 2015). About 130 of the detections are associated with AGN, where they are called megamasers because of their large apparent luminosities. The physical conditions that give rise to maser activity at 22 GHz are also compatible with masing in other transitions of the H_2O molecule, many of which fall in the submillimeter wavelength band (Neufeld & Melnick 1991; Gray et al. 2016).

Humphreys et al. (2005b) presented the first observations of H_2O megamaser emission in a transition other than the 22 GHz, detecting maser emission at 183 GHz and (tentatively) at 439 GHz towards the galaxy NGC 3079. This galaxy had previously been known to host strong 22 GHz masers (Henkel et al. 1984), with VLBI observations confirming that the 22 GHz emission originates from the galactic nucleus (Trotter et al. 1998, Kondratko et al. 2005). Though the signal-to-noise of the (sub)millimeter detections (∼7σ for the 183 GHz transition) was too low to permit detailed study, the maser emission appears to arise from several narrow (spectrally unresolved) features spanning a velocity range comparable to that of the 22 GHz emission.

The 183 GHz transition was also detected towards Arp 220 by Cernicharo et al. (2006), where it displays a broad (∼350 km s^{-1}) and almost featureless spectral line structure. Interestingly, this galaxy has not been detected in 22 GHz emission (e.g., Henkel et al. 1986), suggesting that the masing gas has a low density ($n_{\mathrm{H}_2} \lesssim 10^6$ cm^{-3}) and temperature ($T \lesssim 100$ K). From consideration of these physical conditions and the observed line width, Cernicharo et al. (2006) interpret the 183 GHz masers in this galaxy as likely originating from a large number (∼10^6) of dense molecular cores rather than being associated with the galactic nuclei.

More recently, Hagiwara et al. (2013) used ALMA to detect 321 GHz H_2O megamaser emission towards the Circinus galaxy, another strong 22 GHz nuclear megamaser host (e.g., Greenhill et al. 2003b). The sensitivity of the Circinus observation was sufficient to showcase the richness of the high-frequency maser spectrum, opening up for the first time the possibility of using submillimeter masers in ways that had heretofore been restricted to the 22 GHz transition.

In this chapter we report the first detection of submillimeter maser emission from NGC 4945, and we present a new calibration of the maser spectrum for the Circinus galaxy. We note that Hagiwara et al. (2016) offer a parallel analysis of the NGC 4945 data presented here. The observations and data reduction procedures are described in § 3.2, and in § 3.3 we discuss the submillimeter emission and compare the 321 GHz masers to those at 22 GHz. Throughout this chapter we quote velocities using the optical definition in the heliocentric reference frame.

3.2 Observations and data reduction

We have analyzed archival Cycle 0 ALMA observations of five galaxies that are known to have strong (peak $S_\nu \gtrsim 200$ mJy) 22 GHz water maser emission associated with a central AGN: NGC 1068 (Claussen et al. 1984), NGC 1386 (Braatz et al. 1996), NGC 4945 (Dos Santos & Lepine 1979), Circinus (Gardner & Whiteoak 1982), and NGC 5793 (Hagiwara et al. 1997). All targets were observed at a rest-frame frequency of 321.226 GHz (ALMA Band 7), which corresponds to the $10_{2,9} - 9_{3,6}$ rotational transition of ortho-H_2O at an energy of $E_u/k \approx 1846$ K above ground[1]. NGC 5793 was further observed at a rest-frame frequency of 325.153 GHz, corresponding to the $5_{1,5} - 4_{2,2}$ rotational transition of para-H_2O at an energy of $E_u/k \approx 470$ K above ground. The total bandwidth for each dual-polarization observation was 1.875 GHz, which was split into 3840 channels spaced contiguously every 0.488 MHz (corresponding to a velocity resolution of $\sim$0.5 km s^{-1}). The longest baselines for these observations were $\sim$360 meters (corresponding to a typical resolution of $\sim 0.5''$), and there were between 18 and 25 antennas present (see Table 3.1).

[1]Frequencies, quantum numbers, and energy levels have been taken from Splatalogue: `http://www.cv.nrao.edu/php/splat/`.

We obtained datasets and initial calibration scripts from the ALMA archive; all post-processing reduction, imaging, and spectral analysis was done using the Common Astronomy Software Applications package (CASA)[2]. Table 3.1 lists the observing parameters for each galaxy.

We detected and imaged continuum emission for all five sources (shown in Figure 3.1), and in NGC 4945 the continuum was strong enough for self-calibration. Two of the galaxies – Circinus and NGC 4945 – also host 321 GHz maser emission; we self-calibrated the Circinus data using the line emission.

3.2.1 Circinus

Initial imaging was performed using CASA task `clean` with natural UV weighting; after using `uvcontsub` (specifying line-free channels) to remove the continuum contribution, we separately imaged the line and continuum emission. We then performed several iterations of phase-only self-calibration, using the $\sim$400 spectral channels with the strongest emission ($\gtrsim$ 100 mJy, corresponding to the velocity range $\sim$500–700 km s^{-1}) to determine the phase solutions. We found that a solution interval of 1 minute (averaging both polarizations) was optimal, yielding sufficiently continuous solutions (i.e., consecutive phase solution jumps of $\lesssim 30°$) to confidently interpolate the phases. The calibration solutions were then applied to both the line and continuum data using `applycal`, and we stopped iterating self-calibration once there was no noticeable increase in signal-to-noise ratio (SNR). We found that additional amplitude self-calibration did not improve the SNR, so we have retained the phase-only calibrations for analysis. The resulting continuum image is shown in Figure 3.1, and the spectrum extracted from the (spatially unresolved) line-only data cube is shown in Figure 3.2.

3.2.2 NGC 4945

The maser emission in NGC 4945 is not sufficiently strong for self-calibration, so we used the continuum emission instead. Because the continuum emission in NGC 4945

[2] `http://casa.nrao.edu/`

Table 3.1. ALMA Band 7 observational information

	NGC 5793		Circinus	NGC 4945	NGC 1068	NGC 1386
R.A. (J2000)	14:59:24.807		14:13:09.906	13:05:27.279	02:42:40.770	03:36:46.237
Dec. (J2000)	−16:41:36.55		−65:20:20.468	−49:28:04.44	−00:00:47.84	−35:59:57.39
$v_{\rm rec}$ (km s^{-1})	3491		434	563	1137	868
Observing date (UTC)	2012 Jun 01	2012 Jun 03	2012 Jun 03	2012 Jun 03	2012 Jun 06	2012 Aug 24
ν_0 (GHz)	321.226	325.153	321.226	321.226	321.226	321.226
$t_{\rm int}$ (min.)	6.3	21.0	19.1	15.3	15.8	11.6
PWV (mm)	1.35	0.40	0.55	0.60	0.54	0.64
Antennas (number)	21	20	18	18	20	25
Flux calibrator	Titan	Titan	Titan	Titan	Uranus	Uranus
Bandpass calibrator	3C 279	3C 279	3C 279	3C 279	3C 454.3	3C 454.3
Phase reference	J1517–243	J1517–243	J1329–5608	J1325–430	J0339–017	J0403–36
Beam size ($''$)	0.55 × 0.47	0.66 × 0.46	0.66 × 0.50	0.56 × 0.52	0.66 × 0.45	0.96 × 0.53
Beam PA (°)	48	−89	−18	24	32	82
RMS$_{\rm s}$ (mJy)	9.8	7.2	12.6[a]	9.9	7.4	9.2
RMS$_{\rm c}$ (mJy beam^{-1})	0.39	0.29	0.48	3.0	0.42	0.36
$R_{\rm ap}$ ($''$)	2.5	2.5	2.0	5.0	1.5	1.0
S_ν (mJy)	10.8	18.8	90.8	733	47.1	4.3
σ_{S_ν} (mJy)	2.1	2.4	5.6	26.7	4.5	0.36[b]
$M_{\rm ISM}$ (M$_\odot$)	4.0×10^8	6.6×10^8	...	1.5×10^8	...	...

Note. — Information about the observations. Listed coordinates (rows "R.A." and "Dec." for right ascension and declination, respectively) correspond to the tracking center entered for the observations, which might not precisely match the location of the target (we note in particular that the tracking center for NGC 4945 is displaced by approximately 2.5 arcseconds from the position listed in NED). The "$v_{\rm rec}$" row lists the galaxy recession velocity in km s^{-1} (taken from NED), "ν_0" gives the rest-frame observing frequency, "$t_{\rm int}$" denotes the on-source integration time in minutes, and "PWV" is the average level of precipitable water vapor during the observation. Half-power beam widths ("beam size" row) for the imaged data are given in arcseconds, and the beam position angles ("beam PA" row) are measured in degrees east of north. The "RMS$_s$" row lists the typical spectral sensitivity reached per 2 km s^{-1} vector-averaged channel, and the "RMS$_c$" row gives the brightness sensitivity of the continuum image. In general, the gradient in atmospheric opacity across a single spectrum causes the RMS$_s$ to increase by ∼30% from one end of the bandpass to the other, so that the quoted value is an average. The bottom section of the table lists the gas masses calculated from continuum observations. $R_{\rm ap}$ gives the radius of the aperture used to measure the continuum flux density (centered on the peak of the continuum emission), S_ν is the flux density measured inside of that aperture, σ_{S_ν} is the uncertainty in flux density, and $M_{\rm ISM}$ is the ISM gas mass calculated using the method outlined in § 3.3.1.

[a] The RMS$_s$ value for Circinus is given per 0.5 km s^{-1} channel.

[b] Since the continuum emission in NGC 1386 is unresolved, we measure the peak flux density instead of the integrated, and we use the RMS of the continuum image as the uncertainty in this value.

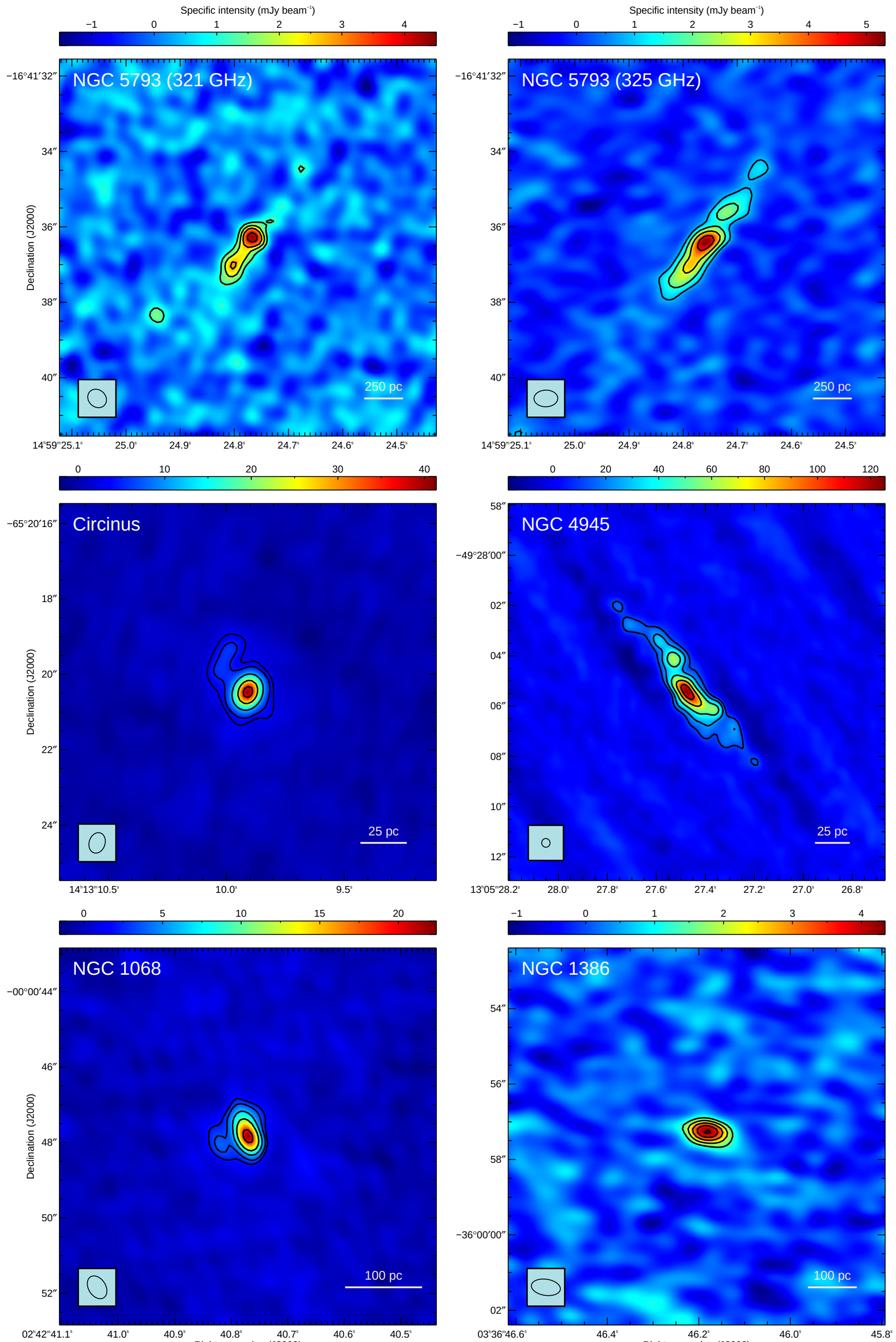

Fig. 3.1.— Continuum images. *Top left*: 321 GHz image of NGC 5793, with 3σ, 5σ, 7σ, and 10σ contours in black ($1\sigma = 0.39$ mJy beam^{-1}). *Top right*: 325 GHz image of NGC 5793, with 3σ, 6σ, 10σ, 15σ, and 20σ contours in black ($1\sigma = 0.29$ mJy beam^{-1}). *Center left*: 321 GHz image of Circinus, with 5σ, 10σ, 25σ, 50σ, and 75σ contours in black ($1\sigma = 0.48$ mJy beam^{-1}). *Center right*: 321 GHz image of NGC 4945, with 4σ, 8σ, 15σ, 25σ, and 35σ contours in black ($1\sigma = 3.0$ mJy beam^{-1}). *Bottom left*: 321 GHz image of NGC 1068, with 5σ, 8σ, 15σ, 25σ, and 45σ contours in black ($1\sigma = 0.42$ mJy beam^{-1}). *Bottom right*: 321 GHz image of NGC 1386, with 4σ, 6σ, 8σ, 10σ, and 12σ contours in black ($1\sigma = 0.36$ mJy beam^{-1}). Half-power restoring beam shapes are shown at the bottom left of each image, and scale bars are shown at the bottom right. For NGC 5793, we adopt a Hubble law distance of 50 Mpc, using $H_0 = 70$ km s^{-1} Mpc^{-1}. We use distances of 10.1 Mpc for NGC 1068 and 15.9 Mpc for NGC 1386; these were measured by Nasonova et al. (2011) and Tully et al. (2013), respectively, using the Tully-Fisher relation.

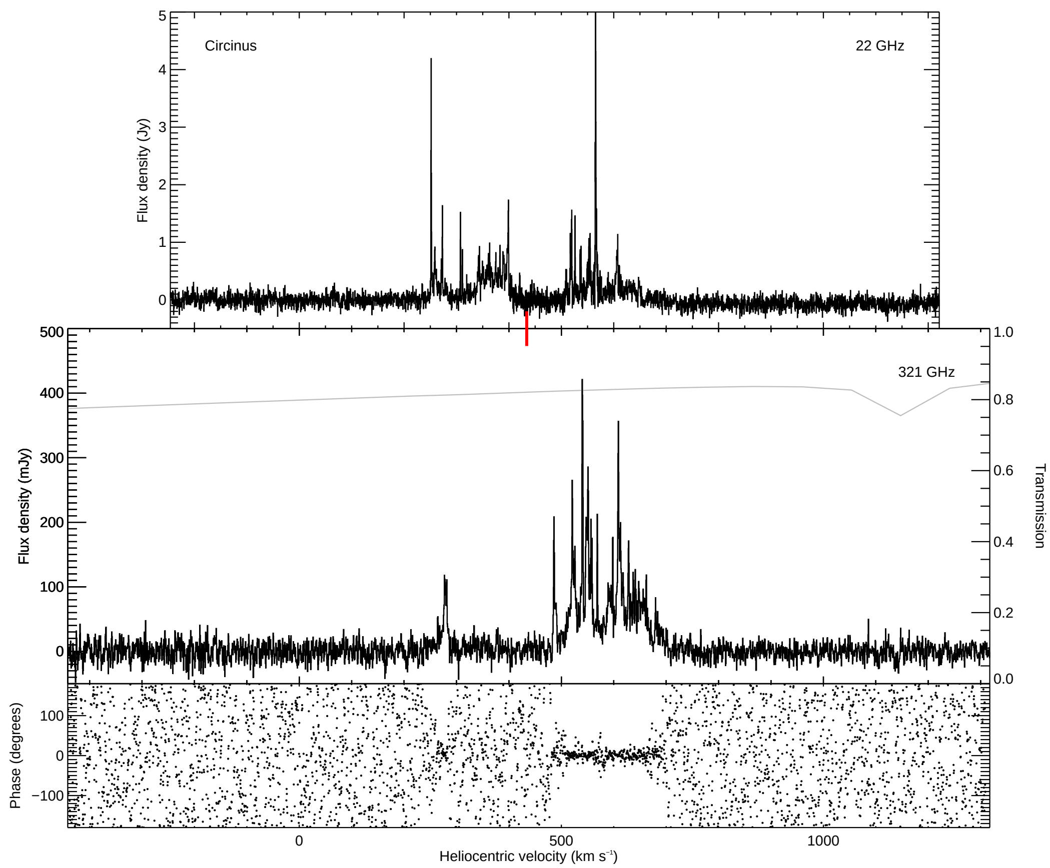

Fig. 3.2.— H_2O megamaser spectra of Circinus. *Top*: A reproduction of the 22 GHz spectrum taken with the 64 m Parkes telescope in 1998 August from Braatz et al. (2003). We have restricted the vertical axis range to more easily see the weaker features, resulting in the strongest feature (peaking at $\sim$18 Jy) getting cut off. *Middle*: 321 GHz spectrum extracted from the continuum-subtracted data cube. The channel width is 0.5 km s^{-1}. The atmospheric transmission curve, corresponding to a precipitable water vapor level matching that present during the observation, is overplotted in light gray. Atmospheric transmission curves have been taken from the Atacama Pathfinder Experiment (APEX) transmission calculator (`http://www.apex-telescope.org/sites/chajnantor/atmosphere/`). The recession velocity of the galaxy is marked by a vertical red line. *Bottom*: Phase plot for the calibrated 321 GHz spectrum.

is spatially resolved, we only used the longest baselines (> 150 m, corresponding to the unresolved, point-like nuclear component of the emission) to determine the phase solutions that were then applied to the spectral line data; no such baseline restrictions were imposed when self-calibrating the continuum image itself. We used a solution interval of 30 seconds, averaging both polarizations. Despite repeated iterations of self-calibration, the sensitivity of the continuum image from this "snapshot" observation remains dynamic-range limited (see Vila Vilaro et al. 2011). The resulting noise level of 3.0 mJy beam^{-1} is thus larger than what one would nominally expect from a sensitivity calculation.

The rest of the reduction procedure matches what was done for Circinus (see § 3.2.1). To account for the sizable ($\sim 2.5''$) offset of the emission center from the phase center, we used `impbcor` to apply a primary beam correction prior to extracting a spectrum from the data cube. The continuum image and spectrum for NGC 4945 are shown in Figures 3.1 and 3.3, respectively.

3.3 Discussion

3.3.1 Continuum emission

The continuum structures for NGC 5793 and NGC 4945 are both elongated in one direction (spanning $\sim 4'' \approx 1000$ pc in NGC 5793, and $\sim 9'' \approx 160$ pc in NGC 4945), and both appear to have substantial substructure. Both of these galaxies are edge-on spirals, and the elongation axes of the submillimeter continua are aligned with the large-scale optical major axes (Gardner et al. 1992; Elmouttie et al. 1997). The continuum in NGC 4945 is also resolved along the minor axis, spanning $\sim 1.5'' \approx 30$ pc. All of this indicates that the continuum emission in these galaxies traces the galactic disks, rather than originating from, e.g., a molecular torus region around the central AGN (though there may be a contribution to the emission in the centermost regions from such material).

At these wavelengths ($\lambda \approx 940$ μm), the continuum in NGC 5793 and NGC 4945 is likely dominated by optically thin thermal (i.e. blackbody) emission from large

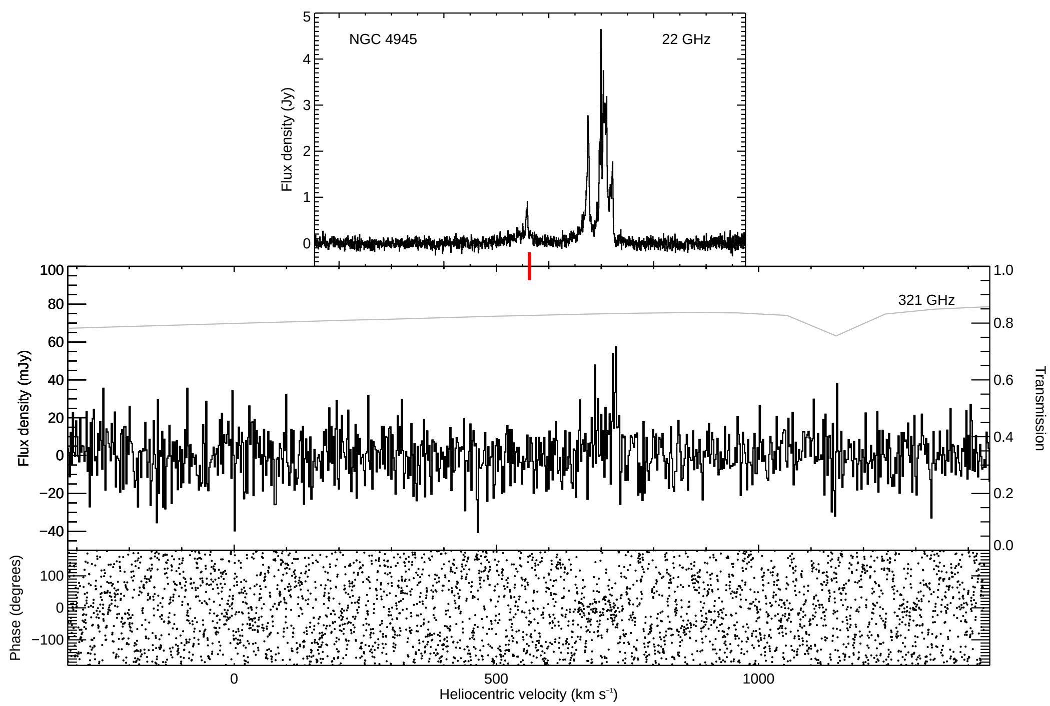

Fig. 3.3.— Same as Figure 3.2, but for NGC 4945. The channel size for the 321 GHz spectrum has been averaged to 2.0 km s^{-1}.

dust grains (see, e.g., Draine 2003; Compiègne et al. 2011). The spectral energy distribution (SED) of such emission is typically modeled as a modified blackbody function (e.g., Planck Collaboration et al. 2014a), with the free parameters being the optical depth τ, the dust temperature T_d, and the power-law index of the dust opacity β. With only a single SED point per galaxy, we must assume fiducial values for two of these parameters (e.g., β and T_d) to allow for a measurement of the third (e.g., τ). Further assumptions are then necessary to convert the optical depth to, e.g., a total interstellar medium (ISM) gas mass, M_{ISM}.

Fortunately, Scoville et al. (2014) have developed an empirical calibration of the relationship between dust emission and ISM gas mass. As long as the emission is measured in the Rayleigh-Jeans tail, the authors found that the calibration is relatively insensitive to whether the ISM is dominated by atomic or molecular gas, if the galaxy is normal or undergoing a starburst, or whether the dust lies in the inner or outer regions of the galaxy. Rewritten in a suitable form, the conversion is given by

$$M_{\mathrm{ISM}} = \frac{D^2 \lambda^2 S_\nu}{2k\kappa_{\mathrm{ISM}} T_d}. \tag{3.1}$$

Here, D is the luminosity distance to the galaxy, λ is the observing wavelength, S_ν is the observed flux density, k is the Boltzmann constant, κ_{ISM} is the dust opacity per unit mass of ISM, and T_d is the dust temperature. Most of the underlying physics here is contained in κ_{ISM}, which the authors calibrated using *Planck* data to be

$$\left(\frac{\kappa_{\mathrm{ISM}}}{4.84 \times 10^{-3}\ \mathrm{cm}^2\ \mathrm{g}^{-1}}\right) = \left(\frac{\lambda}{850\ \mu\mathrm{m}}\right)^{-\beta}. \tag{3.2}$$

When calculating gas masses, we use the results from Planck Collaboration et al. (2011) to fix $\beta = 1.8$, and we adopt a dust temperature of $T_d = 25$ K (following Scoville et al. 2014). We measure the total continuum flux density for each galaxy using a circular aperture centered on the continuum peak, and we estimate the uncertainty using the dispersion of integrated flux densities measured in 15 non-overlapping, identical apertures that are offset from the continuum emission in the same image. The results from these measurements are presented in the bottom portion of Table 3.1. The gas masses estimated from the 321 GHz and 325 GHz observations of NGC 5793 are broadly consistent, while the estimate for NGC 4945 is somewhat lower.

NGC 1068, NGC 1386, and Circinus all show continuum emission considerably more centrally-concentrated than in NGC 5793 and NGC 4945, so it is likely that AGN contributions to the continua for these galaxies are not negligible. Disentangling the thermal (i.e., blackbody) and nonthermal (e.g., electron-scattered synchrotron, free-free) components of the emission is nontrivial, and requires multi-frequency observations (see, e.g., Krips et al. 2011).

For NGC 1068, we can compare our observations to those of García-Burillo et al. (2014), who used ALMA to map the continuum at 349 GHz down to a 1σ level of 0.14 mJy beam^{-1}. Despite the factor of $\sim$3 higher sensitivity than the map presented in this chapter, we see consistent continuum structure and amplitude in the circumnuclear region (i.e., the region containing emission stronger than our sensitivity threshold) between the two observations.

3.3.2 321 GHz H_2O masers in NGC 4945

The 321 GHz maser detection in NGC 4945 – which represents the first time such emission has been seen in this galaxy – is considerably fainter than in Circinus (Figure 3.3). Individual maser features are detected at the $\sim$4–5σ level, though the entire complex between 650 km s^{-1} and 750 km s^{-1} is detected at $\sim 9\sigma$ in integrated intensity. We have calculated an isotropic luminosity using

$$L_{\text{iso}} = \frac{4\pi D^2 \nu_0}{c} \int S_v dv. \tag{3.3}$$

Here, D is the distance to the galaxy, ν_0 is the line rest frequency, and S_v is the flux density as a function of velocity v. Scaled to convenient units, this equation becomes

$$\left(\frac{L_{\text{iso}}}{L_\odot}\right) = 0.335 \left(\frac{D}{\text{Mpc}}\right)^2 \left(\frac{\int S_v dv}{\text{Jy km s}^{-1}}\right). \tag{3.4}$$

Adopting a distance to NGC 4945 of 3.7 Mpc (Tully et al. 2013), the observed flux of 0.88 Jy km s^{-1} corresponds to an isotropic luminosity of $L_{\text{iso}} = 4$ L$_\odot$. Though the flux density of individual features is down by a factor of $\sim$100 from what is observed at 22 GHz (e.g., Braatz et al. 1996), the isotropic luminosity is only lower by a factor of $\sim$10.

Insofar as we are able to discern spectral structure, we see that it appears to match reasonably well with previous observations of NGC 4945 at 22 GHz (top panel of Figure 3.3 has been reproduced from Braatz et al. 2003). The increasing feature strength with increasing velocity and the overall appearance of 2–3 dominant features are both reminiscent of the 22 GHz spectra. However, the 321 GHz features at $\sim$687 km s^{-1} and $\sim$726 km s^{-1} (with possibly a third at $\sim$660 km s^{-1}) don't map one-to-one with regions of 22 GHz emission. Rather, and quite intriguingly, the 321 GHz peaks fall precisely where the 22 GHz emission drops off.

Unlike with Circinus, the origin of the 22 GHz emission from NGC 4945 is not yet well understood. Greenhill et al. (1997b) made a VLBI map of NGC 4945 at 22 GHz using the southernmost antennas of the VLBA, and they found the spatial distribution of the masers to be approximately linear and distributed across $\sim$50 mas ($\sim$0.9 pc) from one end to the other. This – in particular the roughly symmetric location of redshifted and blueshifted emission to either side of the systemic velocity – is suggestive of masers situated in an accretion disk. The limited antennas available for mapping such a low declination source ($-49°$) resulted in the map being rather incomplete (i.e., there were several systemic and blueshifted features that were too faint to map), but it is the best available for this source. When measuring the positions of the 321 GHz maser spots, we found them to be spatially coincident (within the measurement uncertainties). If the intrinsic distribution of the 321 GHz masers matches that of the 22 GHz masers, this is consistent with what we would expect for the $\sim$0.5$''$ beam and low signal-to-noise of the observations.

Working under the assumption that the 321 GHz emission traces material with the same kinematics as the 22 GHz, the observed 321 GHz features correspond only to the redshifted gas in the accretion disk. If the 321 GHz spectral structure follows that of the 22 GHz emission, then the undetected blue and systemic features would be slightly below our detection threshold. The low signal-to-noise in the current observations precludes any detailed characterization of this system, which must await higher sensitivity, better angular resolution observations than those presented here.

3.3.3 321 GHz H_2O masers in Circinus

Hagiwara et al. (2013) discovered the 321 GHz maser in Circinus. Here we re-examine the data, using strong maser lines to apply phase self-calibration (see § 3.2.1). The new calibration improves the SNR by a factor of $\sim$2 compared to the initial analysis.

Published 22 GHz spectra of Circinus (e.g., top panel of Figure 3.2, reproduced from Braatz et al. 2003) show that the bulk of the maser emission occupies velocities between $\sim$250–650 km s^{-1} more or less contiguously, though often with a notable paucity of features near the systemic velocity. Greenhill et al. (2003b) (hereafter G03) observed Circinus between 1997 and 1998 using the Australia Telescope Long Baseline Array. They detected two populations of masers, one arising from a warped accretion disk and the other associated with a wide-angle, bipolar outflow.

The 321 GHz masers are weaker in flux density by a factor of $\sim$30–100 compared to their 22 GHz counterparts. Although the maser flux at 22 GHz is subject to interstellar scintillation (Greenhill et al. 1997a), this effect should be almost completely absent at 321 GHz (at such a high frequency, the diffractive scale of the turbulence will be much larger than the Fresnel scale; see Narayan 1992). At a distance to the galaxy of 4.2 Mpc (measured by Karachentsev et al. 2013 using the Tully-Fisher relation), the observed flux of 17.5 Jy km s^{-1} corresponds to an isotropic luminosity (via Equation 3.4) of $\sim$104 $L_\odot$; this is roughly a factor of four larger than the isotropic luminosity of the 22 GHz masers (e.g., Braatz et al. 1996).

The 321 GHz and 22 GHz spectra share broad structural similarities. Both have maser emission spanning comparable total velocity ranges and consolidated primarily into two groups located on either side of the systemic velocity, and in both cases the blueshifted group of features is weaker and sparser than the redshifted group. We can also see that the region around the systemic velocity in the 321 GHz spectrum is devoid of obvious features – either because no maser features exist at these velocities, or because they are below our detection threshold – which is reminiscent of the same segment of the 22 GHz spectrum.

The VLBI maps from G03 show that the extent of the 22 GHz maser emission in Circinus is roughly 50 $\times$ 80 mas ($\sim$1.0 $\times$ 1.6 pc), but as with NGC 4945 the

321 GHz maser spots are spatially co-located within our measurement uncertainties. Though the absolute astrometric precision for ALMA observations is typically limited to ~0.05 arcseconds without taking special calibration steps (Remijan et al. 2015; Reid & Honma 2014), the relative uncertainty in point-source position within the same primary beam (as a fraction of the half-power beam width) is inversely proportional to the SNR (see, e.g., Condon 1997). Future high-resolution ALMA observations should thus have little difficulty mapping the 321 GHz masers in Circinus.

In lieu of a high angular resolution map, we can use the information contained in the spectrum to glean some understanding of the spatial distribution of the masers. By applying a threshold proximity of 1 mas between any individual maser spot and the disk midline, G03 assigned a rough classification to each maser as originating from either the disk or the outflow. In doing so, they found that the outflow masers dominated the emission between ~300–600 km s^{-1}, and that disk maser emission dominated blueward of ~300 km s^{-1} and redward of ~600 km s^{-1} (see Figure 6 in their paper). With this picture from G03 as a guideline, we can compare the spectral distribution of the 22 GHz masers to that of the 321 GHz masers.

Their similar overall spectral structure suggests that the 321 GHz and 22 GHz masers are tracing roughly the same material. This is to be expected from consideration of the physical conditions required for strong maser activity in these transitions. Gray et al. (2016) have performed a thorough exploration of the relevant parameter space (i.e., gas density, kinetic temperature, and dust temperature) and found that the 321 GHz transition shares an optimal gas density ($n_{\mathrm{H}_2} \approx 10^9$ cm^{-3}) and collisional pumping scheme (i.e., low dust temperature) with the 22 GHz transition, though it prefers a somewhat larger kinetic temperature of $T_K \approx 1500$ K (compared to $T_K \approx 1000$ K for the 22 GHz transition)[3]. This could explain the apparent excess of 321 GHz maser emission between ~650–750 km s^{-1}, which is not typically seen in 22 GHz spectra (though we note that 22 GHz emission has been seen out to velocities

[3]We note that Gray et al. (2016) modeled water maser emission in the context of evolved stars, and their models do not necessarily probe all of the conditions present in AGN central engines. However, the calculations were performed assuming a minimally specific global geometry and dynamics (i.e., a plane-parallel medium with turbulence and a velocity gradient), and the explored region of parameter space covers the masing transitions relevant for this work (i.e., the 321 GHz and 325 GHz transitions). We thus believe it to be suitable for the present level of analysis.

as large as $\sim$900 km s^{-1}, albeit with a much lower flux density than the bulk of the emission; see Greenhill et al. 2003a). Under this interpretation, the 321 GHz emission redward of 650 km s^{-1} originates in the accretion disk at radii interior to where 22 GHz emission is found.

We see no features in the 321 GHz spectrum between $\sim$300–500 km s^{-1}, which is a spectral range dominated by outflow emission at 22 GHz. Either the 321 GHz emission does not trace the outflow at all or the 321 GHz outflow masers in this velocity range are much fainter than their 22 GHz counterparts (i.e., down by a larger factor from the higher-velocity emission to either side). If the 321 GHz masers in fact only trace the disk emission, then the features detected between $\sim$500–600 km s^{-1} indicate that some of these masers must originate farther out in the disk than the 22 GHz masers. Higher angular resolution observations will be able to discern whether any of the 321 GHz maser originate in the outflow or if they are all associated with the disk.

We note that the putative high-velocity maser features – seen at $\sim$1070 km s^{-1} and $\sim$1130 km s^{-1} in the 321 GHz spectrum and reported by Hagiwara et al. (2013) – coincide with an atmospheric line (see Figure 3.2) and almost certainly represent elevated noise rather than real maser emission.

Chapter 4

Measuring SMBH peculiar motion using H_2O megamasers

Note: the material presented in this chapter has been submitted to ApJ, and the work was done in collaboration with Jim Braatz, Jim Condon, and Jenny Greene.

4.1 Introduction

A supermassive black hole (SMBH) in kinetic equilibrium with its surrounding stellar environment will be nearly motionless ($v \ll 1$ km s^{-1}; Merritt et al. 2007) with respect to the system barycenter. Any larger relative motions can result from several mechanisms:

1. SMBH binary orbital motion: Even a relatively low-mass ($\sim 10^7$ M$_\odot$), wide-separation (hundreds of parsecs) SMBH binary can exhibit orbital motions exceeding 10 km s^{-1}. By the time dynamical friction has ceased being efficient and the binary has possibly stalled at the "final parsec" (Begelman et al. 1980; Milosavljević & Merritt 2003), the orbital velocities will be well in excess of 100 km s^{-1}.

2. Gravitational wave recoil: The merging of two SMBHs results in the anisotropic radiation (in the form of gravitational waves) of not only mass and angular momentum from the system, but also linear momentum (Bekenstein 1973). Depending on various details of the precursor systems (e.g., spin configuration and mass ratio), the resulting recoil of the remnant SMBH can easily be several hundred km s^{-1}, and in some cases might even reach thousands of km s^{-1} (Favata et al. 2004; Campanelli et al. 2007). The largest of these kicks would eject the SMBH from most stellar systems, but SMBHs with kicks not exceeding the escape velocity will experience orbital decay from dynamical friction with the surrounding stars, gas, and dark matter, causing them to undergo a damped oscillation about the center of the galaxy (Merritt et al. 2004).

3. Ongoing galaxy merger: As two galaxies merge, the SMBH from one galaxy will not initially be in equilibrium with the stellar system from the other galaxy (e.g., Comerford & Greene 2014). In this case, we might observe relative motion between the two resulting from our inability to observationally disentangle the velocity contributions from the two dynamically distinct stellar systems.

4. Massive perturbers: The presence of massive objects (e.g., star clusters, molecular clouds, etc.) in the SMBH's environment will cause the equilibrium velocity

dispersion ("gravitational Brownian motion") to increase over that expected from just the stellar population alone (Merritt et al. 2007). However, unless the massive objects constitute a non-negligible fraction of the environment by mass, the increase in SMBH velocity dispersion (which scales approximately as the square root of the characteristic perturber mass) will be unnoticeable. A more pronounced perturbation might occur when a massive perturber (e.g., molecular cloud) passes very close to the SMBH, an interaction which simulations have tentatively shown may result in large kicks (e.g., Gabor & Bournaud 2013).

5. Jet-powered rocket: If an AGN's jets are intrinsically asymmetric, the resulting net acceleration can propel the SMBH to observable displacements and velocities (Shklovsky 1982). This mechanism, if prevalent, could be weakened by "flip-flop" instabilities that cause the more strongly emitting jet component to repeatedly alternate sides (Rudnick & Edgar 1984). However, we note that the appearance of one-sided jets can often be explained by relativistic beaming without the need for any intrinsic asymmetry (e.g., Eichler & Smith 1983).

6. Three-body scattering: If a galaxy merger occurs where one of the galaxies contains a binary SMBH system, the SMBH from the other galaxy can experience strong three-body scattering off of the binary (Hoffman & Loeb 2006). Such a scenario potentially explains the "naked" quasar HE 0450-2958 (Magain et al. 2005), which is observed to be displaced by $\sim$7 kpc from a galaxy that appears to have undergone a recent merger (though other scenarios are possible; see, e.g., Kim et al. 2007).

For the majority of SMBH systems, we consider only the first three of these mechanisms to be likely causes of sizable (i.e., several km s^{-1} or larger) "peculiar velocities": i.e., motion of the SMBH relative to the stellar system that significantly exceeds what would be expected in equilibrium. Observational efforts to identify SMBH peculiar motion primarily attempt to detect one of three predicted signatures: (1) velocity offsets between the SMBH and the galactic barycenter (e.g., Comerford et al. 2009, Wang et al. 2009, Kim et al. 2016), (2) positional offsets between the

SMBH and the galactic barycenter (e.g., Komossa et al. 2003, Liu et al. 2013, Barrows et al. 2016), or (3) gravitational wave emission (e.g., Arzoumanian et al. 2014, Zhu et al. 2014, Babak et al. 2016). In this chapter we focus on the first of these signatures.

To spectroscopically identify SMBH peculiar motion, one can either compare the velocities of the SMBH and surrounding system at a single epoch or monitor the SMBH velocity over time. Both methods require some observational measure of the SMBH velocity, and the first method also requires an observational measure of the galactic velocity. A spectroscopic measurement of the SMBH velocity can only be made if the black hole has some emitting material that shares its motion (e.g., a gravitationally bound accretion disk), effectively limiting such measurements to active galactic nuclei (AGN).

Past efforts to make velocity measurements of SMBHs have typically used optical spectra, either decomposing the emission lines into broad and narrow components (e.g., Kim et al. 2016) or looking for shifts in the broad line centroids with time (e.g., Ju et al. 2013). The idea here is that the broad line region (BLR) traces gas in the immediate vicinity of the SMBH while the narrow line region (NLR) is thought to share the host galaxy's recession velocity. Any discrepancy between the BLR and NLR central velocities at the same epoch, or any change in the BLR velocity with time, could then be an indication of SMBH peculiar motion. There are many examples in the literature of this class of search (e.g., Bonning et al. 2007, Boroson & Lauer 2009, Eracleous et al. 2012, Wang et al. 2017).

Attempts to measure SMBH peculiar motions using optical spectra suffer from several difficulties. Single-epoch measurements of SMBH peculiar motion using optical lines are hindered by the broad and blended nature of the emission lines. The statistical uncertainty in any relative velocity measurement will be an increasing function of the widths of the lines used, thereby limiting the precision of such measurements. Differential reddening and flux asymmetries also heavily impact the accuracy of any velocity reconstruction made using broad lines (e.g., Richards et al. 2002). Systematic velocity offsets between the BLR and NLR (as traced using, e.g., [OIII]) are observed to be fairly common (e.g., Boroson 2005, Mullaney et al. 2009, Ludwig et al. 2012), and are likely produced by NLR dynamics (e.g., AGN-driven outflows) rather than by SMBH peculiar motion. Boroson 2005 in particular claims that the [O II] λ3727, [N II] λ6548, λ6584, and [S II] λ6716, λ6731 lines likely trace the systemic velocity of the galaxy, while the [O III] λ4959, λ5007 lines are often ($\sim$50% of the time) systematically blueshifted by tens to hundreds of km s^{-1} with respect to lower-ionization lines. Multiple-epoch measurements are further plagued by emission lines that depend sensitively on the spatial scales probed by the spectrum (see, e.g., Rice et al. 2006), and which can vary across epochs either intrinsically (e.g., Runnoe et al. 2017) or when different facilities or fiber/slit placements are used.

In this chapter we present a technique for measuring SMBH peculiar motions with unprecedented precision. H_2O megamasers residing in the accretion disks of AGN provide an excellent means of diagnosing the kinematic status of a SMBH. By tracing the Keplerian rotation curves of megamaser disks only tenths of a parsec from the nucleus, and well within the SMBH "sphere of influence," one can measure not only the mass of the SMBH but also the absolute on-sky position and line-of-sight velocity of the dynamic center (e.g., Kuo et al. 2011, Gao et al. 2017). Such measurements require a very long baseline interferometric (VLBI) map to spatially resolve the maser system. Coupling high-sensitivity VLBI maps with multi-year spectral monitoring further enables "full disk" modeling, yielding measurements of the 3-dimensional disk geometry, black hole mass, and distance to the system. The megamaser technique results in very precise measurements of several relevant quantities, with uncertainties generally $\lesssim$1 mas in the SMBH absolute position and $\lesssim$2 km s^{-1} in its velocity (e.g., Reid et al. 2013, Kuo et al. 2013, Humphreys et al. 2013, Kuo et al. 2015, Gao et al. 2016).

In principle, any method that uses orbital analysis to determine the mass of a SMBH (e.g., CO gas disks with ALMA; Barth et al. 2016) will also necessarily constrain its velocity. However, in extragalactic environments AGN disk masers are currently the only tools available that directly probe the SMBH gravitational sphere of influence without needing to account for various contaminating effects such as foreground reddening/absorption or the need to model the stellar distribution or gas turbulence profile. That is, *AGN disk masers exhibiting Keplerian rotation about the central SMBH currently provide the only direct and unambiguous measure of its* *velocity*, independent of the surrounding material.

This chapter is organized as follows. In § 4.2 we present both new and archival neutral hydrogen (HI) observations from the Karl G. Jansky Very Large Array (VLA), and we describe the data reduction and imaging procedures. In § 4.3 we outline the analyses performed on the HI data to extract galaxy recession velocity measurements, and in § 4.4 we describe the analyses for measuring the SMBH velocities using maser data. § 4.5 gives a detailed discussion of the results for each galaxy in our sample. Unless otherwise specified, all velocities referenced in this work use the optical definition in the barycentric reference frame.

4.2 Observations and data reduction

The galaxies analyzed in this chapter were selected because they have published VLBI observations of H_2O megamaser emission in Keplerian rotation around the SMBH. We present new VLA HI observations of 7 of these galaxies (from NRAO project 16A-238), out of which we detected 4. We have also retrieved VLA HI observations of NGC 1194, UGC 3789, Mrk 1419, and NGC 4258 from the NRAO archives; we note that the archival observations of NGC 1194, UGC 3789, and Mrk 1419 have been previously published in Sun et al. (2013). We do not present any new VLBI observations in this chapter, but we have re-analyzed the VLBI data from Kuo et al. (2011) to fit rotation curves to the maser disks in NGC 2273 and NGC 1194 (see § 4.4.1); see that paper for details on the data reduction. For the H_2O maser system in NGC 4258, we use the fitting results from Humphreys et al. (2013). Ultimately, only the HI observations of NGC 2273, NGC 1194, and NGC 4258 proved conducive to the tilted-ring model we sought to apply for measuring galaxy recession velocities (see § 4.3).

Information about the VLA observations is listed in Table 4.1. Nearly all observations were taken with the VLA in C configuration, with the one exception being the archival D configuration observations of NGC 4258. For observations from project 16A-238, the correlator was configured with a single 16 MHz spectral window centered on the HI 21 cm spin-flip transition (L-band). We observed in dual circular polarization using 4096 channels across the bandwidth, corresponding to a channel size of $\sim$3.91 kHz ($\sim$0.85 km s^{-1}). For the observations of NGC 4258, two 3 MHz spectral windows covered the HI line, with 0.68 MHz of overlap at the center. The observations were carried out in dual polarization, using 31 contiguous 97.7 kHz spectral channels ($\sim$20 km s^{-1}) across the bandwidth. Details on the observational setup for NGC 1194, UGC 3789, and Mrk 1419 are reported in Sun et al. (2013).

We reduced all VLA data using standard procedures with the Common Astronomy Software Applications (CASA) package[1]. After correcting for antenna positions and atmospheric opacity, we solved for delay and phase solutions on the flux calibrator (which also doubled as our bandpass calibrator). With these solutions applied to the flux calibrator we then used it to obtain the bandpass shape, applied the bandpass correction to all calibrators, and solved for the gains and fluxes. All solutions were applied to the target, after which we typically performed a round of flagging and iterated on the calibration once more before ultimately splitting out the calibrated science target. Radio frequency interference (RFI) was the most common reason for flagged data; we sliced the observations across time, frequency, polarization, and baseline to isolate and excise RFI. Prior to imaging, we performed continuum subtraction on the UV data. We used natural UV weighting when imaging the data cubes with CLEAN, and we subsequently corrected for primary beam attenuation before performing any of the visualization described in the next section.

4.2.1 Data visualization and masking

Rather than displaying the resulting image cubes using moment maps, which tend to be dominated by noise features in low signal-to-noise data, we opted for a parametric fitting approach similar to that employed by Sun et al. (2013). For every spatial pixel in each image cube, we used a Markov Chain Monte Carlo (MCMC) code to fit a Gaussian line profile to the spectrum extracted at that location. The resulting posterior distribution allows us to associate a best-fit line amplitude, velocity centroid, and velocity dispersion with every spatial pixel in the image cube, along with the

[1] https://casa.nrao.edu/

Table 4.1. VLA observations of maser disk galaxies

Galaxy	R.A. (J2000)	Decl. (J2000)	Date(s)	Gain calibrator	Flux calibrator	$t_{\rm tot}$ (min.)	Synthesized beam ($'' \times ''$, deg.)	Channel size (kHz)	Noise (mJy beam^{-1})	Peak intensity (mJy beam^{-1})
NGC 1194	03:03:49.1	−01:06:13	2010 Oct 08	J0323+0534	3C 48	212	22.2 × 16.8, −0.67	15.625	2.1	4.2
J0437+2456	04:37:03.7	+24:56:07	2016 Mar 17, Mar 20, Mar 24	J0431+2037	3C 138	276	18.0 × 16.9, −34.1	3.906	2.7	...
NGC 2273	06:50:08.6	+60:50:45	2016 Feb 28, Mar 13	J0614+6046	3C 147	297	27.1 × 17.4, −81.8	3.906	2.4	9.7
ESO 558-G009	07:04:21.0	−21:35:19	2016 Apr 24	J0706−2311	3C 147	92	35.8 × 15.4, −24.7	3.906	4.5	2.3
UGC 3789	07:19:30.9	+59:21:18	2010 Oct 07	J0614+6046	3C 147	198	23.6 × 16.9, 77.9	15.625	1.6	2.6
Mrk 1419	09:40:36.4	+03:34:37	2010 Nov 19	J0943+0819	3C 286	210	19.4 × 16.3, −30.1	15.625	0.96	1.0
NGC 4258	12:18:57.5	+47:18:14	1994 Jan 02, Jan 03	J1150+497	3C 48	37	74.5 × 54.3, −88.2	97.656	0.80	198
CGCG 074-064	14:03:04.4	+08:56:51	2016 Mar 29, Apr 08, Apr 09	J1347+1217	3C 286	280	23.7 × 17.7, 44.2	3.906	2.1	...
NGC 5765b	14:50:51.5	+05:06:52	2016 Mar 07, Mar 08	J1445+0958	3C 286	297	20.6 × 17.3, 10.4	3.906	2.1	1.4
NGC 6264	16:57:16.1	+27:50:59	2016 Mar 15, Mar 17	J1613+3412	3C 295	264	22.3 × 17.4, −67.7	3.906	2.7	...
NGC 6323	17:13:18.1	+43:46:57	2016 Mar 11, Mar 13	J1635+3808	3C 295	278	19.2 × 17.6, 82.0	3.906	2.2	0.73

Note. — Information about the VLA observations. The listed coordinates give the phase center supplied to the correlator. The total on-source observing time is denoted $t_{\rm tot}$), and the beam position angle is given in degrees east of north. The rms noise level achieved is quoted per spectral channel. For sources where HI was detected, the peak HI line intensity (as determined by the Gaussian fitting procedure described in § **4.2.1**) is given in the last column.

corresponding uncertainty (determined by the width of the marginalized posterior) in each parameter. These parameter values then enable us to construct the equivalent of moment maps using the fitted Gaussian profiles rather than the (noisy) data, resulting in considerable aesthetic improvement. More practically, this parametric fitting technique is also more sensitive to low-amplitude line emission than the "by-eye" detection methods that moment maps are often used for. Our image cubes for ESO 558-G009 and NGC 6323, for instance, do not show any obvious line emission in moment maps created using CASA, but the Gaussian fits are able to extract the extant signal without spectral or spatial averaging.

The parametric fitting technique also provides a natural way to mask the data when creating different moment maps (and equivalents). Rather than using a signal-to-noise cut, which for interferometric data inevitably results in either a "splotchy" image or (if a high enough signal-to-noise cut is used) ends up masking out some of the real signal, we instead used the uncertainties in the fitted line profiles to determine which pixels are trustworthy. For each image cube we performed a 4×4-pixel spatial smoothing of each fitted parameter, and we retained only those spatial pixels for which all smoothed parameter values exceeded 3 times the corresponding 1σ uncertainty. These masks were then applied to the original (unsmoothed) image maps.

Figures 4.1, 4.2, 4.3, 4.4, and 4.5 show the masked HI data for NGC 2273, ESO 558-G009, NGC 4258, NGC 5765b, and NGC 6323, respectively. The "moment 0" maps show the integral over velocity of the fitted Gaussian function at every spatial pixel, the "spectral line peak amplitude" maps show the best-fit Gaussian amplitude for the fitted function at every spatial pixel, and the "spectral line central velocity" maps show the best-fit velocity centroid for the fitted Gaussian function at every spatial pixel. We did not detect line emission from J0437+2456, CGCG 074-064, or NGC 6264. The HI maps for NGC 1194, UGC 3789, and Mrk 1419 have been previously published in Sun et al. (2013), and so we do not reproduce the images here.

Though in principle the line profile along any particular line of sight might not be well-fit by a Gaussian, this technique works well for visualization. Our primary quantity of interest is the line-of-sight velocity at every spatial pixel, and in this regard the parametric fitting technique performs at least as well as a moment map approach (and often much better). Furthermore, any deviation of the spectrum from a Gaussian shape will manifest as inflated uncertainties in the derived parameters, thereby increasing the likelihood of that pixel getting masked out.

Because of the clear systematic uncertainties present in assuming some parametric form for the line shape along any given line of sight, we note that the inputs to the tilted-ring fit described in § 4.3.2 did not undergo any CLEANing or parametric fitting. The analyses were instead performed directly on the "dirty" data cubes.

4.3 Measuring galaxy recession velocities using HI

Our goal is to measure the recession velocities of galaxies in a manner that is both independent of the SMBH velocity and which ideally can achieve an accuracy and precision comparable to the several km s^{-1} level of the maser measurements. Neutral hydrogen seen in emission is an appealing candidate for a tracer that can fulfill these conditions, as it is almost always optically thin (thus tracing the full volume of the galaxy) and it doesn't suffer from reddening or extinction. HI is also frequently present out to large (∼tens of kpc) galactic radii, which for quiescent systems will allow it to trace the global dynamics of the galaxy well outside of the SMBH sphere of influence. An accurate model of the global HI dynamics in a galaxy will necessarily incorporate its recession velocity, and so the construction of such a model allows us to make a precise measurement of that velocity.

To this end, we have analyzed spatially resolved HI observations for a number of galaxies (see Table 4.1). For several of these systems, the emission is either too weak (ESO 558-G009, Mrk 1419, NGC 6323) or too disordered (UGC 3789, NGC 5765b) to model it. Instead, for those we have made nominal recession velocity measurements using a technique often applied to single-dish HI observations. However, for three galaxies – NGC 2273, NGC 4258, and NGC 1194 – we have sufficiently high signal-to-noise data and the global HI dynamics are sufficiently orderly for a tilted-ring model to reasonably apply. In this section, we describe the modeling and fitting techniques used to extract the galaxy recession velocities from the HI data.

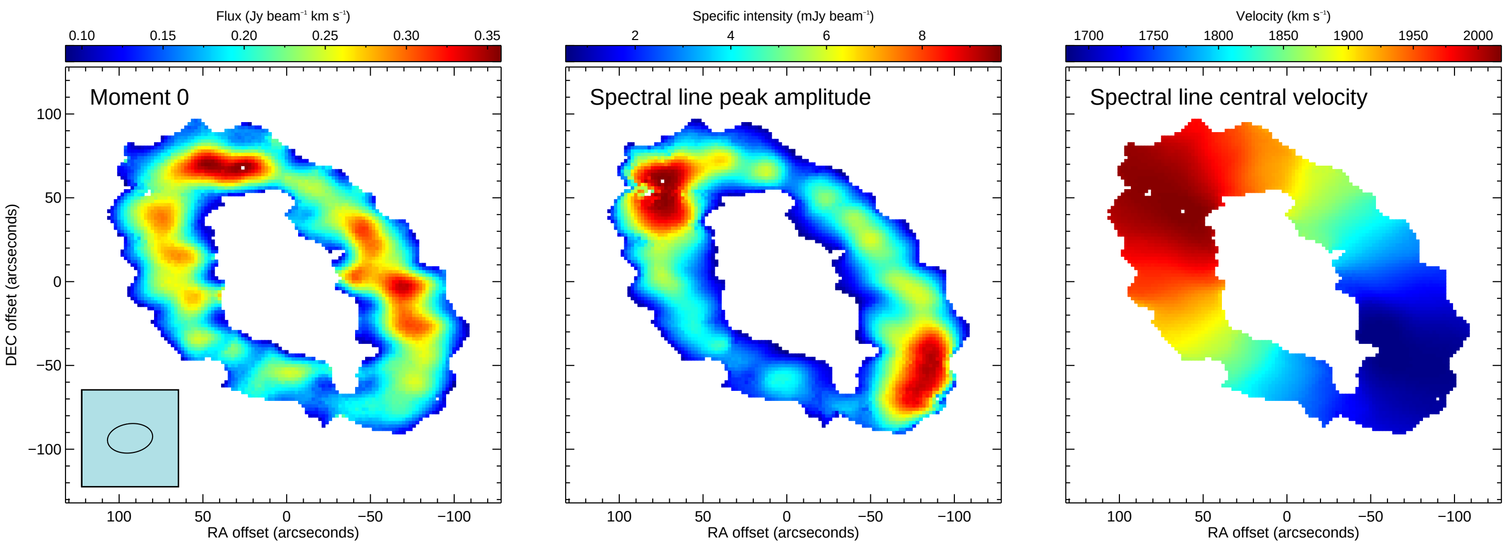

Fig. 4.1.— Moment 0 map (left), spectral line peak amplitude map (center), and velocity map (right) of the HI in NGC 2273, created and masked using the procedure described in § 4.2.1. The coordinate axes mark the offset in right ascension and declination from the phase center of the observations (see Table 4.1), and the half-power beam shape is shown in the bottom left-hand corner of the leftmost plot.

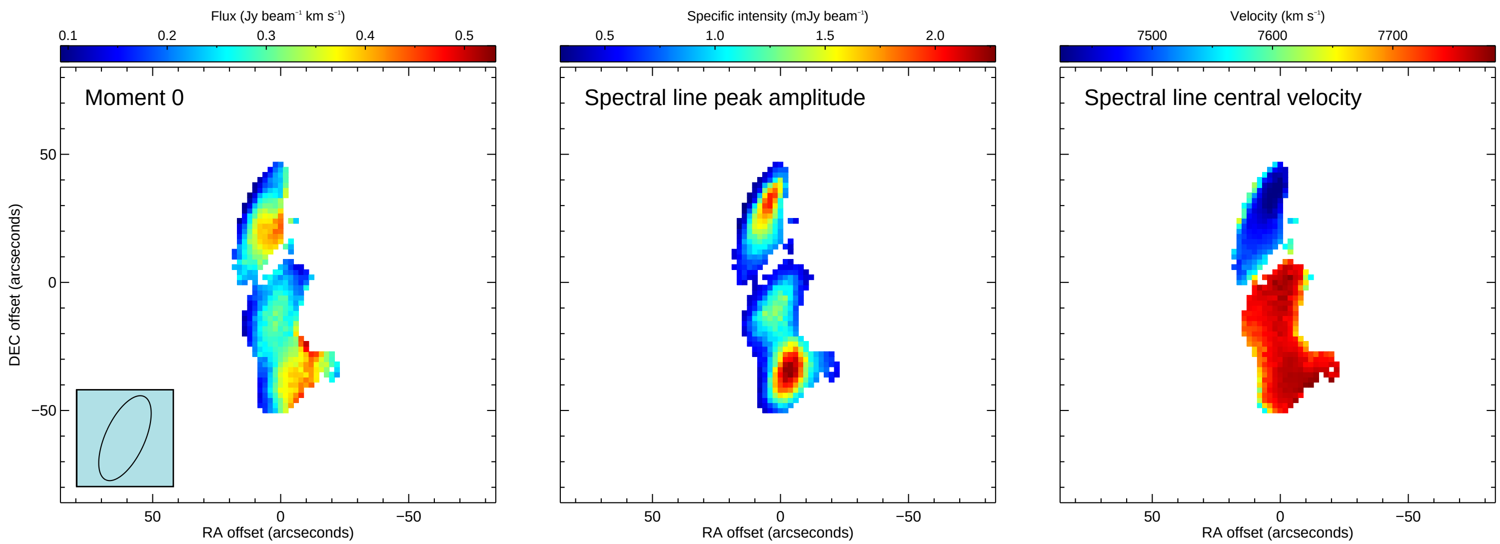

Fig. 4.2.— Same as Figure 4.1, but for ESO 558-G009.

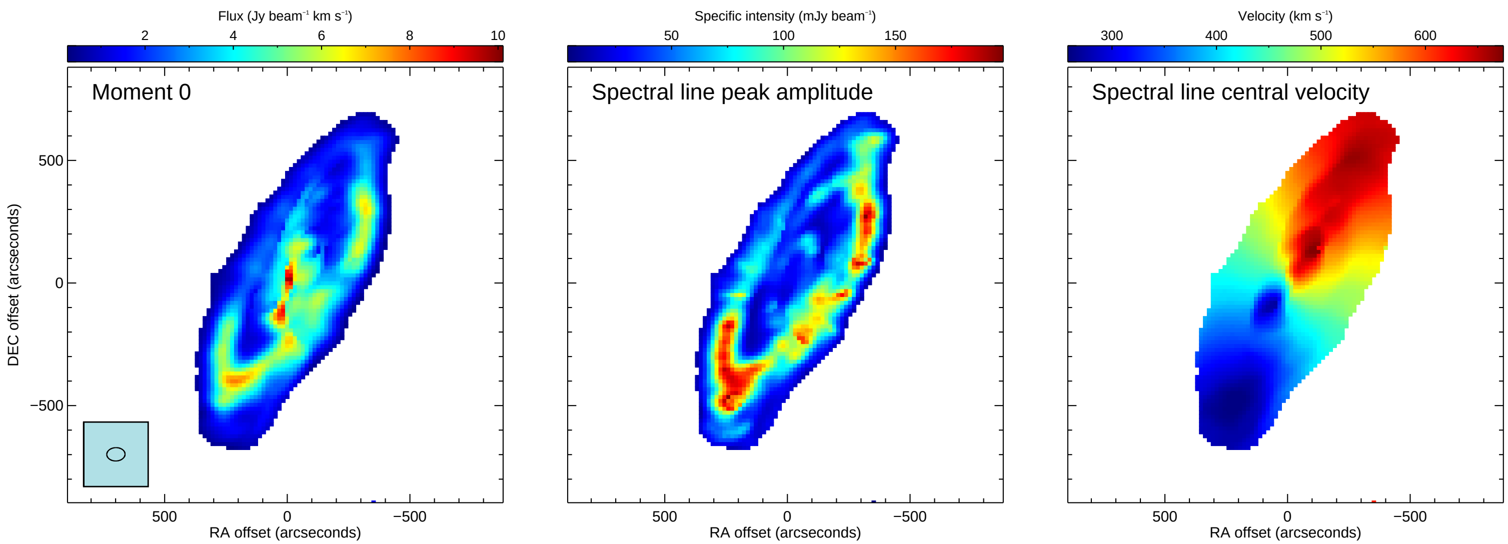

Fig. 4.3.— Same as Figure 4.1, but for NGC 4258.

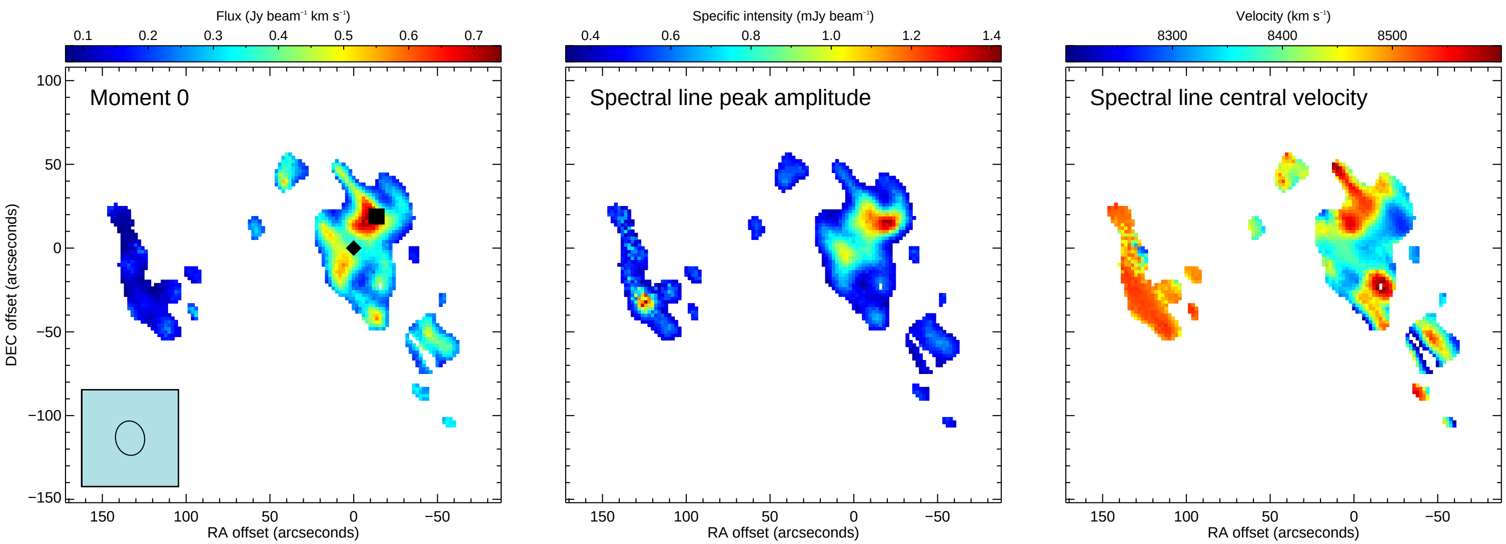

Fig. 4.4.— Same as Figure 4.1, but for NGC 5765b. The optical center of NGC 5765b is marked in the leftmost panel with a black diamond, while the optical center of NGC 5765a is marked with a black square. The positions of both galaxies have been taken from NED.

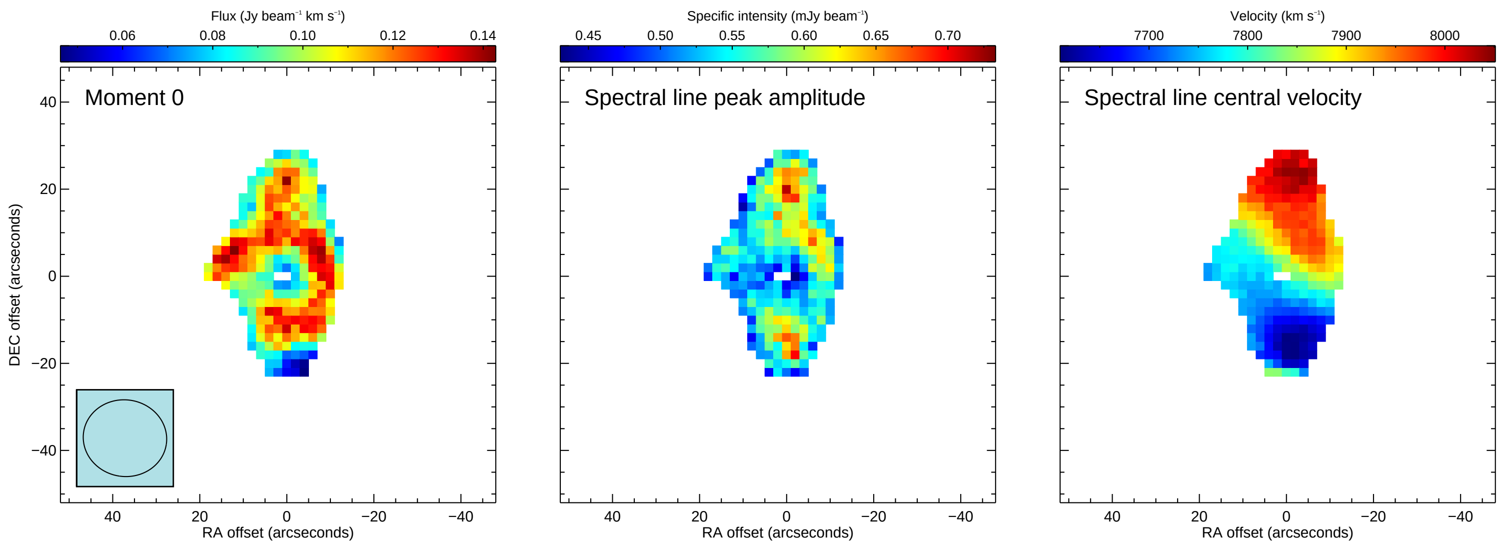

Fig. 4.5.— Same as Figure 4.1, but for NGC 6323.

4.3.1 Generating the HI model

We fit the HI rotation curves using a tilted-ring model (e.g., Begeman 1989, Józsa et al. 2007). In this scheme, the gas in the galaxy is modeled as a series of concentric circular annuli, with each annulus ("ring") having an associated circular velocity and fixed HI surface density. Since we do not view the rings perfectly face-on (i.e., they are "tilted"), they appear as elliptical annuli on the sky. The free parameters are the center position (x_0, y_0), the systemic velocity V_0, the circular velocity $V_c(r)$ and gas surface density $\Sigma(r)$ at the orbital radius of the ring, and two angular parameters (i, ϕ) describing the inclination angle (defined to be the angle between the normal to the ring and the line of sight; takes on values between 0° and 90°) and position angle (defined to be the angle measured counterclockwise from due north to the receding half of the major axis; takes on values between 0° and 360°) respectively. We allow V_c, Σ, i, and ϕ to vary between different rings, but x_0, y_0, and V_0 are global variables (i.e., they take on the same value for all rings).

For a galaxy disk divided into a discrete number N of rings, we use the subscript $n \in \{1, \ldots, N\}$ to denote the parameters for a single ring (e.g., a ring at mean orbital radius r_n would have associated inclination angle i_n and position angle ϕ_n). Each ring is uniformly populated with a large number ($\sim 10^5$) of point particles that carry non-gravitating HI mass (or equivalently HI flux); the actual number of particles scales with the ring's area so that the final model remains homoscedastic. All particle masses are the same within a single ring, and the mass of each individual particle is set so that the total mass in the annulus m_n is equal to the product of its area and surface density (i.e., $m_n = A_n \Sigma_n = \pi \left(r_n^2 - r_{n-1}^2 \right) \Sigma_n$, with $r_0 \equiv 0$). We note that modeling the HI distribution in this way assumes either that the gas is optically thin, or that it resides in many small (but individually optically thick) clouds.

In the frame of the galaxy we denote the location of a particle within a ring using polar coordinates (r, θ), where θ is measured counterclockwise from the receding half of the major axis. We relate the disk position (r, θ) to an on-sky location (x, y)

through

$$
\begin{aligned}
x &= x_0 - r\cos(\theta)\sin(\phi_n) - r\sin(\theta)\cos(\phi_n)\cos(i_n), && \text{(4.1a)}\\
y &= y_0 + r\cos(\theta)\cos(\phi_n) - r\sin(\theta)\sin(\phi_n)\cos(i_n). && \text{(4.1b)}
\end{aligned}
$$

Every particle within a single ring is treated as having the same circular velocity $V_c(r_n)$, so that the observed (i.e., on-sky) velocity $V(r,\theta)$ can be expressed as

$$V(r,\theta) = V_0 + V_c(r_n)\sin(i_n)\cos(\theta). \tag{4.2}$$

Within a single ring, each particle (r,θ) thus maps uniquely to a point (x,y,V) in the data cube phase space. Constructing a model cube from this cloud of particles is then simply a matter of binning them into 3D (x,y,V) voxels, with bin boundaries set to match those of the observed cube.

4.3.2 HI model fitting and parameter space exploration

The input we used for the fitting procedure described in this section was a "dirty" cube; that is, the UV data were transformed to the image plane, but no CLEANing was performed prior to performing the model fit. Instead, the model cube produced at each MCMC iteration was convolved with the "dirty beam" before being compared to the data cube. The goal is to alleviate systematic uncertainties that might be introduced into the data cube during the somewhat subjective CLEANing process.

If we denote the value associated with each observed (x,y,V) voxel in the data cube as z_i (with associated uncertainty σ_i) and the corresponding modeled voxel values as ζ_i, we can express the likelihood function as

$$\ln(\mathcal{L}) = -\frac{1}{2}\sum_i \left[\frac{(z_i-\zeta_i)^2}{\sigma_i^2} + \ln\left(\sigma_i^2\right)\right]. \tag{4.3}$$

Equation 4.3 assumes that each data point z_i deviates from the "true" value ζ_i by only a Gaussian-distributed noise factor with variance σ_i^2. For our purposes we assume that σ_i is the same for all data points (so that we can denote it as σ), and we have estimated the value of σ by computing the RMS in line-free channels of the data cube. Because the correlated noise present in interferometric images can result in systematically underestimated uncertainties, we introduce a new fitted parameter α that scales σ in the likelihood function,

$$\ln(\mathcal{L}) = -\frac{1}{2}\sum_i \left[\frac{(z_i - \zeta_i)^2}{\alpha^2\sigma^2} + \ln\left(\alpha^2\sigma^2\right)\right]. \tag{4.4}$$

We then treat α as a nuisance parameter in the final fit.

Our final model has two fixed parameters: the number of rings N and the outermost radius r_{max}. The value of r_{max} is chosen to lie near the outer edge of the visually obvious emission in the data cube, and N is then set to be roughly equal to the number of resolution elements that fit within a radius r_{max}. The model also has $4 + 4N$ adjustable parameters: the global parameters V_0, x_0, y_0, and α, and the ring-specific parameters V_c, Σ, i, and ϕ (for each of the N rings). We use a flat (i.e., uniform) prior distribution for all modeled parameters, with ranges given in Table 4.2. The posterior probability density is then computed as the product of the likelihood function and the prior distribution.

We performed a MCMC search of the parameter space, using the affine-invariant sampler `emcee` (Foreman-Mackey et al. 2013) to draw sample vectors from the posterior distribution. This sampler employs a large number (we use $\sim 10^3$ for our searches) of "walkers" that simultaneously explore the parameter space, with each walker's knowledge of the whereabouts of the other walkers allowing it to efficiently navigate even heavily degenerate spaces. For a detailed description of the algorithm, see Goodman & Weare (2010). We initialize each walker with parameter values that are randomly selected from the prior distributions.

4.3.3 HI integrated intensity profiles

For all of the galaxies in which we have detected HI, even those for which a full tilted-ring model is not appropriate (either because of low signal-to-noise or complicated

Table 4.2. Tilted-ring model parameter initializations

Parameter	Prior range (NGC 2273)	Prior range (NGC 4258)	Prior range (NGC 1194)
V_0	1700 – 2000 km s^{-1}	400 – 500 km s^{-1}	3950 – 4250 km s^{-1}
x_0	−30 – 30 arcsec	−240 – 240 arcsec	−30 – 30 arcsec
y_0	−30 – 30 arcsec	−240 – 240 arcsec	−30 – 30 arcsec
α	0 – 10	0 – 10	0 – 10
$V_{c,n}$	0 – 500 km s^{-1}	0 – 500 km s^{-1}	0 – 500 km s^{-1}
Σ_n	0 – 0.1 Jy arcsec^{-2}	0 – 0.1 Jy arcsec^{-2}	0 – 0.01 Jy arcsec^{-2}
i_n	$0 - \frac{\pi}{2}$	$0 - \frac{\pi}{2}$	$0 - \frac{\pi}{2}$
ϕ_n	$0 - \frac{\pi}{2}$	$\frac{3\pi}{2} - 2\pi$	$\frac{3\pi}{2} - 2\pi$
N	10	20	6
$r_{\rm max}$	160 arcsec	800 arcsec	140 arcsec

Note. — *Top*: Fitted parameters used in the tilted-ring model described in § 4.3.1. V_0 is the systemic velocity of the galaxy, x_0 and y_0 are the coordinates of the center (relative to the phase center of the observations; see Table 4.1), α is an uncertainty-scaling parameter, $V_{c,n}$ is the circular velocity of the nth ring, Σ_n is the surface brightness of the nth ring, i_n is the inclination angle of the nth ring, and ϕ_n is the position angle of the nth ring. All prior probabilities are uniform within the specified range and zero outside of it. *Bottom*: Fixed parameters for the tilted-ring model. N is the number of rings and $r_{\rm max}$ is the maximum radius used in the fit.

dynamics), we can still use the spatially integrated line emission to make a measurement of the recession velocity. Such velocity measurements using HI profiles are routinely made with single-dish radio telescopes, which typically don't have sufficient angular resolution for spatially resolved HI spectroscopy on most galaxies.

Figure 4.6 shows the integrated HI profiles for all detected galaxies in this work, generated using the masked parametric fitting results (see § 4.2.1). These HI profiles are much cleaner than any that could actually be obtained from real single-dish observations. The profiles are generated from summing many Gaussian fits to the data, which don't have noise. We only considered emission within the masked region and are thus able to, e.g., isolate the emission of UGC 3789 from that of UGC 3797 (separated by ∼4.3 arcminutes). We note that even with our VLA observations, the emission from NGC 5765b remains entangled with the emission from NGC 5765a (see Figure 4.4), so our integrated intensity profile actually contains contributions from both galaxies and therefore is not expected to provide a trustworthy recession velocity.

We use the method described in Fouque et al. (1990) to assign a recession velocity and uncertainty to each HI profile. The recession velocity, denoted V_{20}, is defined to be to the midpoint between the two points on the profile that rise to 20% of the peak amplitude. The authors explored a variety of different line profile shapes, and they settled on a generic form for the uncertainty associated with the velocity as given by

$$\sigma_V = \frac{4}{S}\sqrt{\frac{1}{2}R\,(W_{20} - W_{50})}, \tag{4.5}$$

where S is the signal-to-noise ratio (defined to be the peak amplitude divided by the RMS), R is the spectral channel spacing (in km s^{-1}), and W_{20} and W_{50} are the widths of the profile at 20% and 50% of the peak intensity, respectively. We note that this expression only accounts for the statistical uncertainty in the measurement of the velocity centroid. Systematic deviations between the integrated profile's centroid and the true recession velocity of the galaxy, especially for asymmetric profiles, remain a possibility.

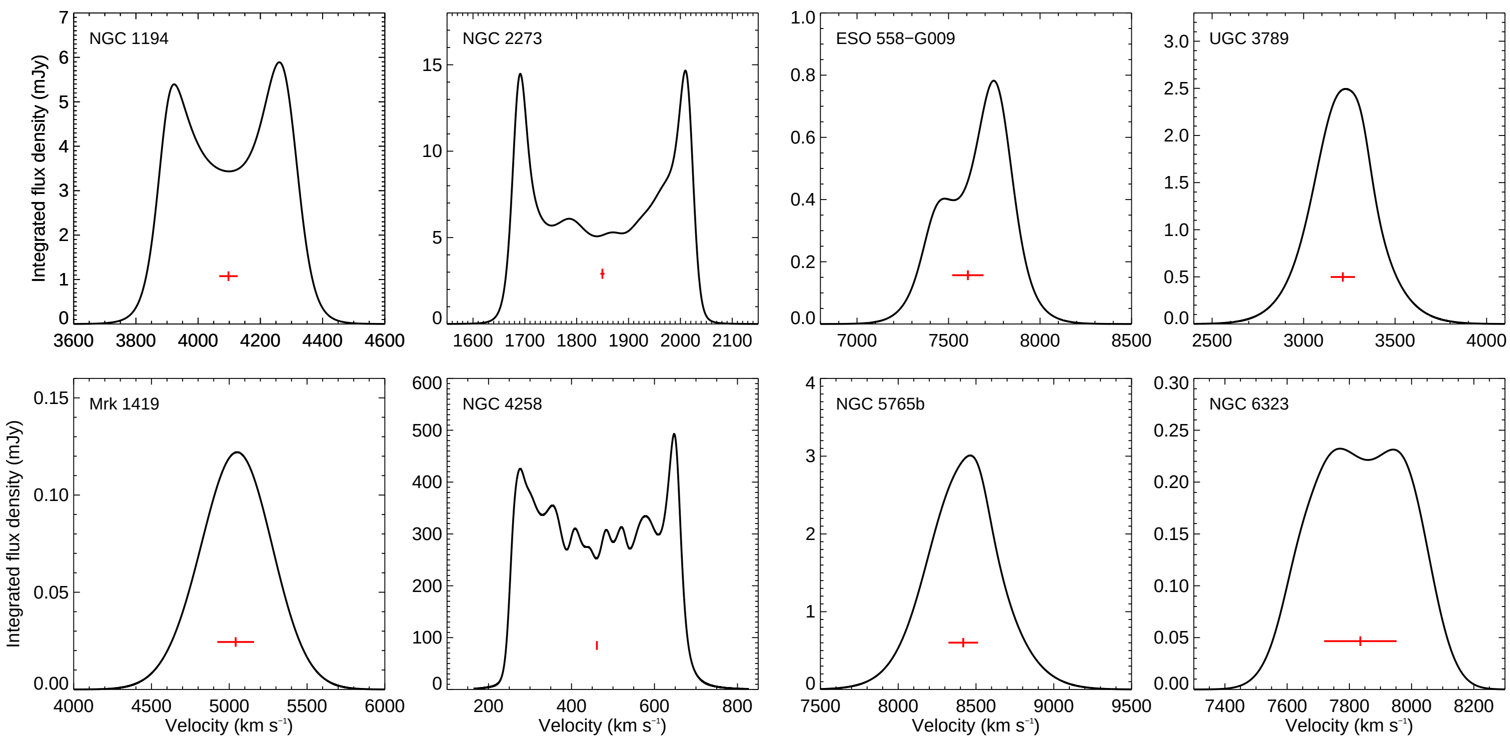

Fig. 4.6.— Spatially integrated HI profiles for all galaxies detected in HI, generated from the parameterized fits as described in § 4.3.3. Note: these plots are noiseless because they represent fits to the data rather than the data themselves. Measured V_{20} velocities are marked as vertical red lines, and the associated uncertainties are shown as the horizontal red lines. We note that the plot for NGC 5765b actually contains contributions to the HI profile from both NGC 5765b and its interacting companion, NGC 5765a, which is spatially blended with it in our VLA map.

4.4 Measuring SMBH velocites

All of the galaxies presented in this chapter have previously published maser rotation curves, and several of them also have associated full disk models. For the most part we simply quote these prior results, but for NGC 1194 and NGC 2273 we have elected to fit our own rotation curves to the VLBI data from Kuo et al. (2011). We do so because the uncertainties on the rotation curve-derived velocities given by Kuo et al. (2011) contain a systematic component that accounts for possible deviations of the SMBH location from some coordinate origin. However, such a deviation can actually be incorporated directly into the model, thereby potentially decreasing the uncertainty on the measured velocity. In this section we describe the maser disk model that we have used to measure the SMBH velocities in NGC 1194 and NGC 2273, using the VLBI data from Kuo et al. (2011).

4.4.1 Method for fitting maser rotation curves

Our model assumes that the maser spots reside in a flat (i.e., unwarped), edge-on accretion disk that feels only the point-source gravitational potential from the central SMBH. Each maser spot has a measured position (x_i, y_i) and velocity v_i.

The uncertainties in the position measurements are associated with the VLBI beam used to make the maser map, resulting in correlated uncertainties between the desired coordinates of right ascension and declination. For VLBI observations, we can describe the synthesized beam as having dimensions of $b \times a$ (Gaussian standard deviation, in mas $\times$ mas) oriented at a position angle of θ (in degrees east of north). Because this beam is Gaussian, we can construct a covariance matrix $\mathbf{S}$ for the uncertainties in the position of a point source using the method described in Appendix C.

Doing so yields expressions for the (co)variances in terms of the beam parameters

$$\sigma_x^2 = a^2\cos^2(\theta) + b^2\sin^2(\theta), \tag{4.6a}$$

$$\sigma_{xy} = a^2\sin(\theta)\cos(\theta) - b^2\sin(\theta)\cos(\theta), \tag{4.6b}$$

$$\sigma_y^2 = a^2\sin^2(\theta) + b^2\cos^2(\theta). \tag{4.6c}$$

In practice, the uncertainty in the position of any particular maser spot is only proportional to the beam shape (see, e.g., Condon 1997), with the constant of proportionality γ_i being inversely related to the signal-to-noise ratio R_i as

$$\gamma_i = \frac{1}{2R_i}. \tag{4.7}$$

Equation 4.7 is only approximately true for low signal-to-noise observations, but we have determined empirically that it holds well for $R_i \gtrsim 7$. Our expression for the covariance matrix $\mathbf{S}_i$ for a single maser spot can then be written as

$$\mathbf{S}_i = \gamma_i^2 \begin{pmatrix} \sigma_x^2 & \sigma_{xy} \\ \sigma_{xy} & \sigma_y^2 \end{pmatrix}. \tag{4.8}$$

The uncertainties in velocity measurements v_i are assumed to be negligible.

We parameterize the maser disk's on-sky appearance as being a line with position angle ϕ and perpendicular distance from the origin $b_\perp \equiv b\cos(\phi)$, with thickness determined by a Gaussian variance h^2 in the direction perpendicular from the line. This thickness parameter accounts for both any intrinsic scale height the masers in the disk might have, as well as real vertical scatter caused by unmodeled warping or inclination of the disk plane. In addition to the orientation and thickness of the masing disk, the model also fits for the SMBH location x_0, velocity v_0, and Keplerian constant $k \equiv GM$ (which effectively gives the mass of the black hole, assuming the distance to the galaxy is known). The value of y_0 (i.e., the SMBH location in the y-direction) is uniquely determined from ϕ, $b_\perp$, and x_0,

$$y_0 = x_0 \tan(\phi) + \frac{b_\perp}{\cos(\phi)}, \tag{4.9}$$

so it does not enter in as an additional free parameter.

Following Hogg et al. (2010), the log likelihood for $(\phi, b_\perp, h)$ is given by

$$\ln(\mathcal{L}_1) = -\frac{1}{2} \sum_i \left[\frac{\Delta_{\perp,i}^2}{\left(\Sigma_{\perp,i}^2 + h^2\right)} + \ln\left(\Sigma_{\perp,i}^2 + h^2\right) \right]. \tag{4.10}$$

Here, $\Delta_{\perp,i}$ is the perpendicular displacement of a maser spot with position (x_i, y_i) from the line,

$$\Delta_{\perp,i} = y_i \cos(\phi) - x_i \sin(\phi) - b_\perp, \tag{4.11}$$

and $\Sigma_{\perp,i}^2$ is the projection of $\mathbf{S}_i$ onto the space perpendicular to the line,

$$\Sigma_{\perp,i}^2 = \gamma_i^2 \left[\sigma_x^2 \sin^2(\phi) - 2\sigma_{xy} \sin(\phi)\cos(\phi) + \sigma_y^2 \cos^2(\phi)\right]. \tag{4.12}$$

Similarly, we can write the projection of $\mathbf{S}_i$ onto the line of the disk as

$$\Sigma_{\parallel,i}^2 = \gamma_i^2 \left[\sigma_x^2 \cos^2(\phi) + 2\sigma_{xy} \sin(\phi)\cos(\phi) + \sigma_y^2 \sin^2(\phi)\right]. \tag{4.13}$$

Equation 4.13 effectively gives the uncertainty in the radial coordinate for a maser spot (i.e., it is the projection of $\mathbf{S}$ onto the plane of the disk). The Keplerian disk model predicts that a maser with observed velocity v_i should lie at an orbital radius of

$$r_{\mathrm{orb},i} = \frac{k}{\left(v_i - v_0\right)^2}. \tag{4.14}$$

This is to be compared with the measured orbital radius, which is given by

$$\Delta_{\parallel,i} = \sqrt{(x - x_0)^2 + (y - y_0)^2}, \tag{4.15}$$

where x and y are the projected coordinates of a maser spot observed at (x_i, y_i) onto the disk, and are themselves given by

$$x = x_i \cos^2(\phi) + y_i \sin(\phi)\cos(\phi) - b_\perp \sin(\phi), \tag{4.16a}$$

$$y = x_i \sin(\phi)\cos(\phi) + y_i \sin^2(\phi) + b_\perp \cos(\phi). \tag{4.16b}$$

The likelihood for this parallel component of the model is then obtained by assuming that the observed orbital radii differ from the model orbital radii only by a Gaussian uncertainty with variance $\Sigma^2_{\parallel,i}$ in the radial direction (i.e., they deviate only by an uncertainty associated with the beam size). Doing so yields

$$\ln(\mathcal{L}_2) = -\frac{1}{2}\sum_i \left[\frac{\left(\Delta_{\parallel,i} - r_{\mathrm{orb},i}\right)^2}{\Sigma^2_{\parallel,i}} + \ln\left(\Sigma^2_{\parallel,i}\right) \right]. \tag{4.17}$$

We can combine Equation 4.17 with Equation 4.10 to yield an overall likelihood of the model,

$$\ln(\mathcal{L}) = \ln(\mathcal{L}_1) + \ln(\mathcal{L}_2). \tag{4.18}$$

Our final maser disk model has six free parameters: V_0, x_0, ϕ, $b_\perp$, h, and k. We fit for these using the same MCMC procedure described in § 4.3.2 for the HI model fitting, and we use flat priors for all parameters.

4.5 Results

We have summarized the velocity measurements from this work, along with others from the literature, in Table 4.4. The final measured differences between the galaxy and SMBH velocities are plotted in Figure 4.7. In this section we discuss details regarding the recession velocity and SMBH velocity measurements for each individual galaxy.

Table 4.3. Fitting results for tilted-ring and maser rotation curve models

Parameter	NGC 2273	NGC 4258	NGC 1194
V_0 (km s^{-1})	$1840.0^{+2.4}_{-2.1}$	$454.1^{+5.6}_{-5.5}$	$4088.6^{+5.8}_{-5.6}$
x_0 (arcsec)	$0.0^{+5.1}_{-5.0}$	-4.4 ± 15.6	-2.2 ± 5.9
y_0 (arcsec)	$-1.2^{+6.9}_{-6.5}$	$-47.8^{+21.7}_{-21.4}$	$-2.1^{+7.7}_{-7.6}$
V_0 (km s^{-1})	$1850.8^{+13.5}_{-13.9}$	...	4088.8 ± 5.3
x_0 (mas)	$0.0553^{+0.0086}_{-0.0087}$	...	$0.306^{+0.056}_{-0.055}$
ϕ (degrees)	332.97 ± 0.42	...	$336.67^{+0.95}_{-0.93}$
$b_\perp$ (mas)	-0.0490 ± 0.0032	...	-0.237 ± 0.053
h (mas)	$0.0220^{+0.0031}_{-0.0029}$	...	$0.167^{+0.049}_{-0.033}$
k (mas km^2 s^{-2})	$2.680^{+0.027}_{-0.029} \times 10^5$	...	$1.157^{+0.017}_{-0.018} \times 10^6$

Note. — *Top*: Results from fitting the HI tilted-ring model described in § 4.3.1 to NGC 2273, NGC 4258, and NGC 1194. V_0 is the recession velocity of the galaxy, x_0 is the offset of the fitted center in right ascension from the phase center of the observations, and y_0 is the offset of the fitted center in declination from the phase center of the observations. *Bottom*: Results from fitting the maser disk model described in § 4.4.1 to NGC 2273 and NGC 1194. V_0 is the velocity of the SMBH, x_0 is its offset in RA from the phase center of the observations, ϕ is the position angle (measured east of north) of the edge-on accretion disk, $b_\perp$ is the perpendicular distance of the disk from the origin (i.e., from the phase center), h is the Gaussian thickness of the disk, and k is the Keplerian constant. For all parameters in this table, the listed "best fit" quantities are the 50th percentile values of the posterior distributions, with 1σ uncertainties given as the 16th and 84th percentiles.

Table 4.4. Galaxy and SMBH recession velocities

Galaxy	$v_{\rm galaxy}$ (km s^{-1})	Method; citation	$v_{\rm SMBH}$ (km s^{-1})	Method; citation	Difference (km s^{-1})
NGC 1194	$\left\{4088.6^{+5.8}_{-5.6}\right\}$ 4098 ± 30 4082.8 ± 7.3 4076 ± 5	HI tilted-ring fitting; this work HI integrated intensity profile; this work Optical spectra; this work HI single-dish profile; Theureau et al. (2005)	4088.8 ± 5.3	Maser rotation curve; this work	-0.2 ± 7.9
J0437+2456	$\left\{4887.6 \pm 7.1\right\}$ 4835 ± 23	Optical spectra; this work Optical spectra; Huchra et al. (1992)	4818.0 ± 10.5	Maser rotation curve; Gao et al. (2017)	69.6 ± 12.7
NGC 2273	$\left\{1840.0^{+2.4}_{-2.1}\right\}$ 1850 ± 4 1839 ± 4 1893 ± 6	HI tilted-ring fitting; this work HI integrated intensity profile; this work HI single-dish profile; Bottinelli et al. (1990) Optical spectra; Nelson & Whittle (1995)	$1850.8^{+13.5}_{-13.9}$	Maser rotation curve; this work	-10.8 ± 14.1
ESO 558-G009	7606 ± 86 $\left\{7674 \pm 27\right\}$	HI integrated intensity profile; this work Optical spectra; Huchra et al. (2012)	7618.2 ± 14.0	Maser rotation curve; Gao et al. (2017)	55.8 ± 30.4
UGC 3789	3214 ± 66 $\left\{3257 \pm 16\right\}$ 3325 ± 24	HI integrated intensity profile; this work Optical spectra; Huchra et al. (2012) HI single-dish profile; Theureau et al. (1998)	3259.75 ± 1.00	Maser disk modeling; Reid et al. (2013)	-2.8 ± 16.0
Mrk 1419	5041 ± 118 $\left\{4947 \pm 8\right\}$	HI integrated intensity profile; this work HI single-dish profile; Springob et al. (2005)	4954.5 ± 15	Maser rotation curve; Kuo et al. (2011)	-7.5 ± 17.0
NGC 4258	$\left\{454.1^{+5.6}_{-5.5}\right\}$ 461 ± 0.3 449 ± 7 443 ± 3	HI tilted-ring fitting; this work HI integrated intensity profile; this work HI single-dish profile; Fisher & Tully (1981) HI single-dish profile; Staveley-Smith & Davies (1987)	466.87 ± 0.49	Maser disk modeling; Humphreys et al. (2013)	-15.8 ± 5.6
NGC 5765b	8418 ± 95 $\left\{8299.2 \pm 18.7\right\}$ 8329 ± 30	HI integrated intensity profile; this work Optical spectra; this work HI single-dish profile; Haynes et al. (2011)	8322.22 ± 1.13	Maser disk modeling; Gao et al. (2016)	-23.0 ± 18.7
NGC 6264	$\left\{10151.4 \pm 7.6\right\}$ 10177 ± 28 10161 ± 76	Optical spectra; this work Optical spectra; Huchra et al. (1992) Optical spectra; Koranyi & Geller (2002)	10189.26 ± 1.20	Maser disk modeling; Kuo et al. (2013)	-37.9 ± 7.7
NGC 6323	7835 ± 117 $\left\{7772 \pm 35\right\}$	HI integrated intensity profile; this work Optical spectra; Marzke et al. (1996)	$7834.28^{+2.1}_{-2.2}$	Maser disk modeling; Kuo et al. (2015)	-62.3 ± 35.1

Note. — Comparison of galaxy recession velocities ($v_{\rm galaxy}$) and SMBH systemic velocities ($v_{\rm SMBH}$) from the literature, along with the methods used to measure them; details for individual galaxies are given in § 4.5. The listed galaxy recession velocities have been measured in this work using either HI tilted-ring fitting (§ 4.3.2) or HI integrated intensity profile centroiding (§ 4.3.3), and in other works using HI single-dish profile centroiding or optical spectral line fitting. Velocities enclosed in curly brackets $\{\}$ are those that we have used to compare with the SMBH velocities. The listed SMBH velocities have been measured in this work using maser rotation curve modeling (§ 4.4.1), and in other works using either maser rotation curve modeling or full maser disk modeling. The final velocity differences are given as $v_{\rm galaxy} - v_{\rm SMBH}$; only two galaxies, J0437+2456 and NGC 6264, show statistically significant differences between the galaxy and SMBH velocities. All velocities are quoted in the barycentric reference frame and using the optical convention.

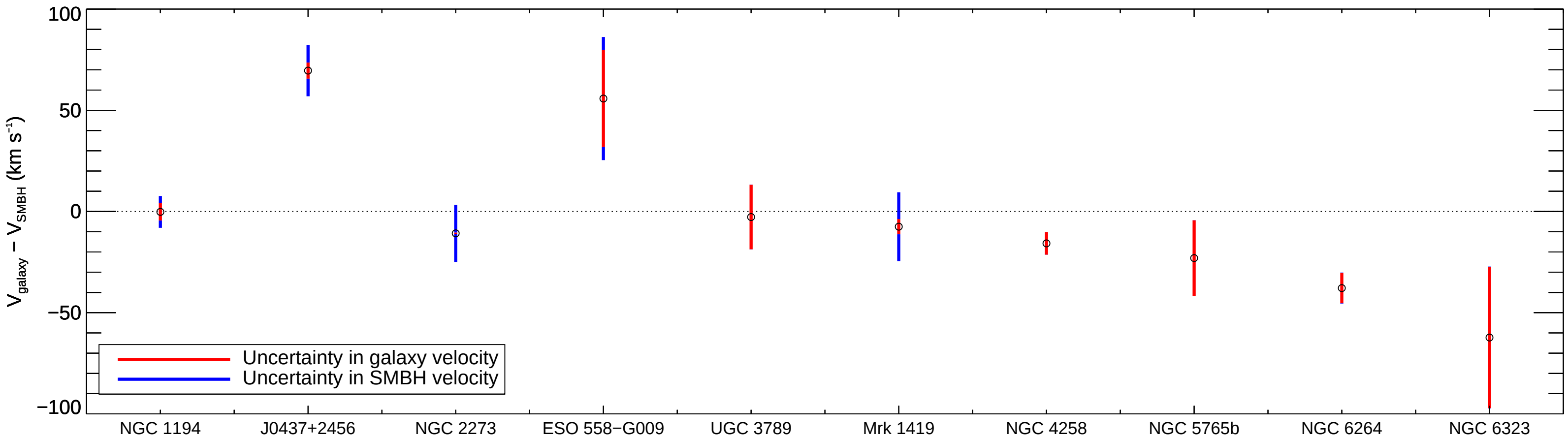

Fig. 4.7.— Differences between galaxy and SMBH systemic velocities. The colors in the error bars show the quadrature contribution to the overall uncertainty from both measurements; red corresponds to the uncertainty contribution from the galaxy recession velocity measurement, and blue corresponds to that from the SMBH velocity measurement. Two galaxies, J0437+2456 and NGC 6264, show statistically significant differences between the SMBH and host galaxy velocities.

Table 4.5. Velocity measurements from SDSS spectra

		Measured recession velocity (km s^{-1})			
Species	Rest wavelength (Å)	NGC 1194	J0437+2456	NGC 5765b	NGC 6264
[O II]	3727.092	...	4814.3 ± 77.3	8307.5 ± 20.6	10070.3 ± 28.2
[O II]	3729.875	...	4814.3 ± 77.3	8307.5 ± 20.6	10070.3 ± 28.2
[Ne III]	3869.860	4011.8 ± 18.3	4836.1 ± 14.5	8278.5 ± 4.3	10122.4 ± 4.2
Hζ	3890.166	...	...	8251.6 ± 0.9	10140.6 ± 1.8
[Ne III]	3968.590	...	...	8278.5 ± 4.3	10122.4 ± 4.2
Hε	3971.198	...	...	8251.6 ± 0.9	10140.6 ± 1.8
Hδ	4102.892	...	...	8251.6 ± 0.9	10140.6 ± 1.8
Hγ	4341.692	4073.6 ± 2.5	...	8251.6 ± 0.9	10140.6 ± 1.8
[O III]	4364.435	...	...	8295.7 ± 0.8	10146.5 ± 1.1
He II	4687.068	4100.0 ± 32.2	...	8268.7 ± 5.2	10143.8 ± 6.9
[Ar IV]	4712.670	...	...	8318.1 ± 20.9	10158.6 ± 17.3
[Ar IV]	4741.530	...	...	8318.1 ± 20.9	10158.6 ± 17.3
Hβ	4862.691	4073.6 ± 2.5	4881.1 ± 2.7	8251.6 ± 0.9	10140.6 ± 1.8
[O III]	4960.295	4069.9 ± 1.3	4887.1 ± 1.5	8295.7 ± 0.8	10146.5 ± 1.1
[O III]	5008.240	4069.9 ± 1.3	4887.1 ± 1.5	8295.7 ± 0.8	10146.5 ± 1.1
[N I]	5199.349	...	...	8270.9 ± 57.5	10152.6 ± 43.9
[N I]	5201.705	...	...	8270.9 ± 57.5	10152.6 ± 43.9
[Fe VII]	5722.300	...	...	8311.1 ± 11.4	10189.4 ± 16.9
He I	5877.249	...	...	8282.6 ± 8.0	10144.6 ± 14.6
[Fe VII]	6088.700	...	...	8311.1 ± 11.4	10189.4 ± 16.9
[O I]	6302.046	4067.5 ± 16.9	4871.4 ± 9.3	8264.7 ± 5.2	10116.8 ± 11.8
[S III]	6313.810	...	...	...	10127.6 ± 28.7
[O I]	6365.535	...	...	8264.7 ± 5.2	10116.8 ± 11.8
[Fe X]	6376.270	...	...	8252.1 ± 27.0	...
[N II]	6549.860	4081.2 ± 4.2	4879.7 ± 1.7	8259.2 ± 1.0	10144.6 ± 2.6
Hα	6564.632	4073.6 ± 2.5	4881.1 ± 2.7	8251.6 ± 0.9	10140.6 ± 1.8
[N II]	6585.270	4081.2 ± 4.2	4879.7 ± 1.7	8259.2 ± 1.0	10144.6 ± 2.6
He I	6679.995	...	...	8282.6 ± 8.0	10144.6 ± 14.6
[S II]	6718.294	4083.8 ± 5.5	4869.0 ± 4.0	8258.1 ± 1.9	10146.1 ± 2.9
[S II]	6732.674	4083.8 ± 5.5	4869.0 ± 4.0	8258.1 ± 1.9	10146.1 ± 2.9
[Ar III]	7137.770	...	...	8285.4 ± 7.6	10145.3 ± 7.7
Average (lines):		4071.7 ± 8.1	4882.2 ± 7.7	8271.1 ± 23.2	10144.0 ± 7.9
Continuum:		4133.9 ± 17.3	4921.4 ± 19.1	8352.3 ± 31.9	10234.8 ± 26.5
Final:		4082.8 ± 7.3	4887.6 ± 7.1	8299.2 ± 18.7	10151.4 ± 7.6

Note. — A list of the optical emission lines used to measure redshifts from SDSS spectra. We list the recession velocities as measured from each line species individually, along with the associated statistical uncertainty in the fit. We also list the final velocity, which is a weighted average of the individual line velocities. The uncertainty in the final velocity is a quadrature sum of the statistical uncertainty in the mean, the absolute calibration uncertainty of 2 km s^{-1} for SDSS spectra, and the magnitude of the scatter in velocities as measured using the different lines. Rest wavelengths for each transition have been taken from the Atomic Spectra Database (ASD) provided by the National Institute of Standards and Technology (NIST). In the second row from the bottom we list the velocities derived from the pPXF continuum fitting procedure, and the bottom row contains the final combined recession velocity measurements.

4.5.1 NGC 1194

We fit a tilted-ring model to the HI disk in NGC 1194, using VLA data originally presented in Sun et al. (2013); the results of the tilted-ring fitting are listed in the top portion of Table 4.3, and the resulting velocity map is shown in Figure 4.8. The velocity we derive from the spatially integrated HI profile matches that obtained from the tilted-ring model, though the uncertainty is considerably larger in the former. Theureau et al. (2005) measured a single-dish HI velocity of 4076$\pm$5 km s^{-1}, consistent with our tilted-ring model fit of $4088.6^{+5.8}_{-5.6}$ km s^{-1}.

We have also used an optical spectrum (wavelength coverage ~4000-9000 Å) from the Sloan Digital Sky Survey (SDSS; Eisenstein et al. 2011) to measure the recession velocity. The spectral fitting was performed in two steps. First, we fit the stellar continuum using the penalized pixel-fitting (pPXF) code developed by Cappellari (2017), which fits for both the recession velocity and velocity dispersion using stellar population templates. The stellar templates come from Tremonti et al. (2004), who generated the templates using the simple stellar population models of Bruzual & Charlot (2003). All emission lines were masked out during continuum fitting. We then subtracted this best-fit continuum model and fit Gaussians to all identified emission lines (listed in Table 4.5). Each emitting species was constrained to have the same redshift (e.g., all [O III] lines have the same redshift, which may be different from that of the [O I] or [N II] lines), but otherwise all three Gaussian parameters (i.e., center, amplitude, and standard deviation) were independently initialized for each line within a wide, flat prior range. Because several of the emission lines overlap – most notably the [NII] and Hα lines – we performed simultaneous Gaussian fits to all of them. Our resulting best-fit values for the recession velocity are listed in Table 4.5.

For the emission line velocity measurement, we consider three primary contributions to the uncertainty: a statistical uncertainty associated with the line-fitting, a systematic uncertainty associated with the absolute wavelength calibration of the spectrum (which is 2 km s^{-1} for SDSS spectra; Abazajian et al. 2009), and a systematic uncertainty arising from the choice of lines to fit. The first two of these uncertainties are readily quantified, but the third is less clear. In principle it is possible that some of the line emission (from, e.g., [OIII]) arises from gas with a systematically different dynamical behavior than that of the galactic barycenter. To mitigate this source of uncertainty, we have incorporated the scatter (quantified as the standard deviation) between velocity measurements for the individual line species into the final uncertainty. All sources of uncertainty were added in quadrature to arrive at the final value, which is listed in Table 4.5.

We estimate the systematic uncertainty in the continuum velocity measurement by making a series of separate pPXF fits to a sliding 500 Å segment of the spectrum, and then calculating the χ^2-weighted variance of all such fits. This systematic uncertainty is then added in quadrature with the statistical uncertainty from the fit to the entire spectrum to arrive at the total uncertainty for the continuum-derived velocity measurement. The final optical value for NGC 1194 (4082.8 ± 7.3 km s^{-1}) is taken to be the weighted mean of the fits from the continuum and from the emission lines. This velocity measurement matches well with our HI tilted-ring model results.

The bottom section of Table 4.3 contains the results from our maser disk model fit to NGC 1194, plotted in Figure 4.9. Our measured SMBH velocity is 4088.8 ± 5.3 km s^{-1}, achieving an uncertainty smaller than the conservative 15 km s^{-1} value reported in Kuo et al. (2011). We find no significant difference between the galaxy and SMBH velocities in NGC 1194.

4.5.2 J0437+2456

No HI was detected in our VLA observations of J0437+2456, and the only literature velocity we found was 4835 ± 23 km s^{-1} from the CfA Redshift Survey catalog (ZCAT; Huchra et al. 1992)[2]. In an effort to improve the uncertainties, we used an optical spectrum (wavelength coverage ∼4000-10000 Å) from the Baryon Oscillation Spectroscopic Survey (BOSS; Dawson et al. 2013) to measure the recession velocity

[2]There are actually three additional velocity measurements listed in the NASA/IPAC Extragalactic Database (NED), all obtained from SDSS. However, for two of these velocity measurements the SDSS pipeline misclassified J0437+2456. Because the templates used by the SDSS pipeline to determine the recession velocity depend on the classification of the object (see Bolton et al. 2012), we have elected to make our own measurement of the recession velocity for J0437+2456 using the highest sensitivity SDSS spectrum available.

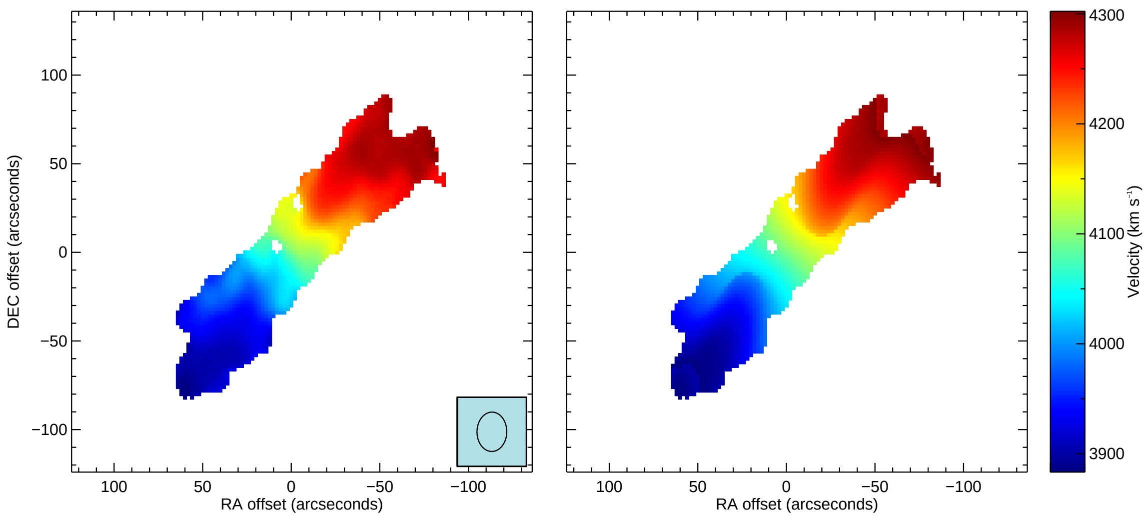

Fig. 4.8.— Observed (left) and modeled (right) velocity maps of the HI in NGC 1194, masked as described in § 4.2.1. The coordinate axes mark the offset in right ascension and declination from the phase center of the observations (see Table 4.1), and the half-power beam shape is shown in the bottom right-hand corner of the left plot. The model velocity map has been constructed from the model cube and masked in the same manner as the data.

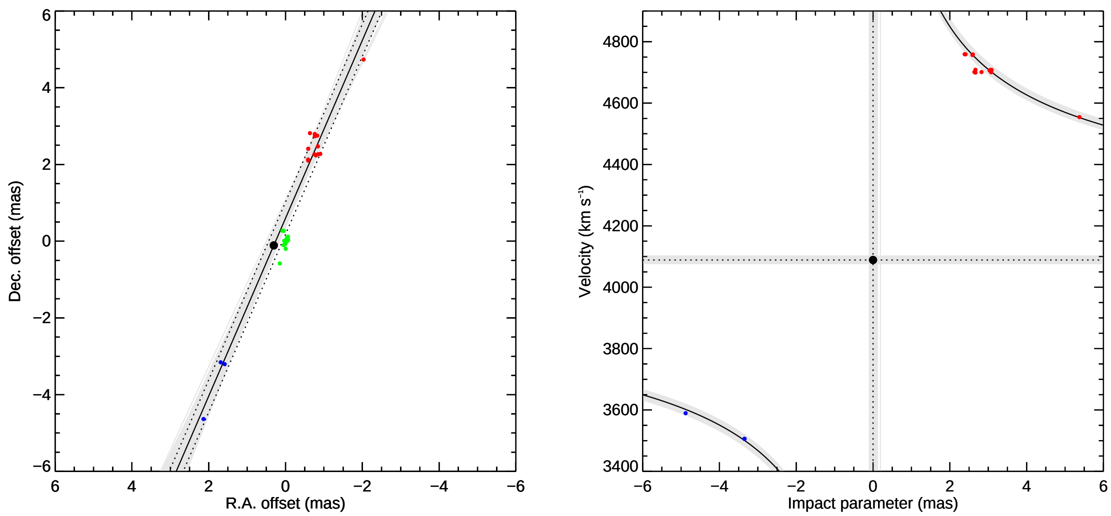

Fig. 4.9.— *Left*: Map of the maser system in NGC 1194, with redshifted, systemic, and blueshifted maser spots plotted as red, green, and blue points, respectively. The best-fit plane of the disk is plotted as a solid black line, and the dotted lines are offset by a perpendicular distance h above and below the disk. *Right*: The best-fit rotation curve for NGC 1194 is plotted as a solid black line, and the best-fit velocity and dynamic center position are marked with horizontal and vertical dotted lines, respectively. In both panels, the location of the dynamic center is plotted as a black point and the light grey lines show the fits from 100 different samplings of the posterior distribution.

of J0437+2456 to be 4887.6 ± 7.1 km s^{-1}. We have used the same fitting procedure and uncertainty calculations as for NGC 1194 (see § 4.5.1), and the results are listed in Table 4.5.

The SMBH velocity for J0437+2456 was measured by Gao et al. (2017), who modeled the maser rotation curve using a method similar to that described in § 4.4.1. The authors used a two-step method to model the rotation curve, first measuring the disk's orientation on the sky and then rotating their coordinate system accordingly before performing the fit. This approach avoids the need to include a position angle parameter in the fit, and though the authors assumed a thin disk (i.e., no parameter was included to account for potential disk thickness), they also included inclination angle as a fitted parameter. Otherwise their method matches well with ours, and it yields a SMBH velocity of 4818.0 ± 10.5 km s^{-1}.

We find a significant (5.5σ) difference between the galaxy and SMBH velocities for J0437+2456: the SMBH is blueshifted with respect to its host galaxy by 69.6 ± 12.7 km s^{-1}. If we consider the velocities derived from the stellar continuum and optical emission lines separately, we see a 4.7σ and 4.9σ difference, respectively, between the SMBH and galaxy velocities. We can further subdivide the emission line measurements and consider only those expected to be the most reliable tracers of the galaxy systemic velocity. Boroson 2005 claims that the low-ionization [O II], [N II], and [S II] lines provide the most reliable measurements, while the high-ionization [O III] lines are systematically blueshifted in a large fraction of galaxies. Our velocity measurement of 4814.3 ± 77.3 km s^{-1} from the [O II] $\lambda3727$ doublet is consistent with no SMBH peculiar motion, but the uncertainty is large because the lines are so weak. We measure more precise velocities of 4879.7 ± 1.7 km s^{-1}, 4869.0 ± 4.0 km s^{-1}, and 4887.1 ± 1.5 km s^{-1} for the [N II], [S II], and [O III] lines, respectively, all of which individually show significant deviations from the SMBH velocity (and we note that the [O III] lines do not display any systematic blueshift in J0437+2456). A weighted average of the velocity measurements from only the low-ionization lines (including [O II]) returns 4878 ± 1.6 km s^{-1} (a 5.6σ deviation from the SMBH velocity), and adding in the [O III] lines modifies the result to 4882.8 ± 1.1 km s^{-1} (a 6.1σ deviation from the SMBH velocity). The consistency between the stellar and gas velocities, and their common offset from the SMBH velocity, supports the interpretation of this system as a SMBH displaying peculiar motion.

It is possible that a misplacement of the SDSS fiber used to observe J0437+2456, or tracking drift in the center of that fiber during the course of the observation, could give rise to a systematic velocity offset that would mimic the signature of SMBH peculiar motion. The listed central position of the fiber coincides with the PanSTARRS position to within several mas, and the worst-case image smearing induced by tracking errors in SDSS observations isn't expected to exceed $\sim$0.06 arcseconds (Gunn et al. 2006). We thus take 0.1 arcseconds to be a conservative upper limit to the magnitude of fiber displacement. For a simulated rotating disk of material, a fiber with an aperture of 3 arcseonds that is misplaced from the galactic center by 0.1 arcseconds can pick up velocity offsets of up to $\sim$20 km s^{-1}. The exact value of the systematic velocity offset depends on a number of factors, including the direction of the fiber misplacement with respect to the symmetry axis of the rotating disk and the form of the rotation curve for the observed material. Additional observations, ideally of spatially resolved gas and stellar kinematics (using, e.g., an integral field unit), will be necessary to provide a check against such systematics that can arise from fiber-fed spectroscopic measurements.

Assuming the measured velocity offset is real, it is natural to ask what the expected spatial separation of the SMBH from the galactic center might be. Adopting a constant Milky Way-like central bulge mass density of $\rho \approx 190$ M$_\odot$ pc^{-3} (see, e.g., Sofue 2013), we can estimate the maximum separation using

$$r_{\text{sep}} = \sqrt{\frac{3(\Delta v)^2}{4\pi G\rho}}, \tag{4.19}$$

where Δv is the observed velocity difference between the SMBH and galaxy recession velocities. For J0437+2456, we estimate a value of $r_{\text{sep}} \approx 37$ pc, which corresponds to approximately 0.1 arcseconds on the sky.

The VLBI location of the maser system from Gao et al. (2017) is 04:37:03.6840 +24:56:06.837, with an uncertainty of 1.3 mas in right ascension and 2 mas in declination. In Table 4.6 we compare this SMBH position to the position of the galaxy as measured in three different astrometrically calibrated sky surveys: PanSTARRS, 2MASS, and AllWISE. The galaxy positions from all three catalogs have a right ascension that is consistent with that of the SMBH, but both PanSTARRS and AllWISE show a statistically significant declination offset between the galaxy and SMBH. The magnitude of this positional offset is $\sim$0.05 arcseconds in the optical (from PanSTARRS, detected at 3.3σ) and $\sim$0.25 arcseconds in the IR (from AllWISE, detected at 7.0σ), both of which match well with our rough prediction from the peculiar velocity. In both cases, the SMBH appears to be offset to the south of the host galactic center. We note that the PanSTARRS and AllWISE measurements are actually themselves statistically different from one another, perhaps indicating that the PanSTARRS position is being affected by extinction from dust within J0437+2456.

4.5.3 NGC 2273

We used the VLA to observe HI in NGC 2273, and as with NGC 1194 (§ 4.5.1) the HI disk is well-fit by a tilted-ring model. The results of the tilted-ring fitting are listed in the top portion of Table 4.3, and the resulting velocity map is shown in in Figure 4.10. The data are well-fit by the model, and our final velocity measurement of $1840.0^{+2.4}_{-2.1}$ km s^{-1} has uncertainties consistent with the observed signal-to-noise ratio. Though we also calculate the recession velocity from the spatially integrated HI profile, the uncertainty in that result is larger than what we obtain from the tilted-ring model.

Previous measurements of the recession velocity of NGC 2273 include both single-dish HI profile fitting and optical spectral line measurements. Bottinelli et al. (1990) record the recession velocity as the midpoint of the HI line profile between the two points at 20% of the peak value. The quoted uncertainty depends on an empirically derived function of both the profile width and the spectral resolution (see the original paper for details), but their velocity of 1839 ± 4 km s^{-1} matches well with our result from the tilted-ring model. Nelson & Whittle (1995) took an optical spectrum of NGC 2273 and cross-correlated it with templates of stellar spectra – a method developed by Tonry & Davis (1979) – to derive a recession velocity and associated uncertainty.

Table 4.6. Positional offsets for J0437+2456 and NGC 6264

Galaxy	Catalog	R.A. (J2000)	Decl. (J2000)	Δ_α (mas)	Δ_δ (mas)
J0437+2456	PanSTARRS	04:37:03.6830	+24:56:06.890	-15 ± 13	$+53 \pm 16$
	2MASS	04:37:03.6852	+24:56:06.918	$+18 \pm 70$	$+81 \pm 60$
	AllWISE	04:37:03.6870	+24:56:07.090	$+45 \pm 39$	$+253 \pm 36$
	Average	04:37:03.6835	+24:56:06.923	-8 ± 12	$+86 \pm 14$
NGC 6264	PanSTARRS	16:57:16.1280	+27:50:58.560	$+3 \pm 15$	-17 ± 9
	2MASS	16:57:16.1244	+27:50:58.657	-51 ± 90	$+80 \pm 80$
	AllWISE	16:57:16.1318	+27:50:58.539	$+60 \pm 36$	-38 ± 35
	Average	16:57:16.1285	+27:50:58.560	$+10 \pm 14$	-17 ± 9

Note. — Positions for J0437+2456 and NGC 6264 taken from the PanSTARRS, 2MASS, and AllWISE catalogs. The positional offsets in both right ascension (Δ_α) and declination (Δ_δ) are defined such that $\Delta \equiv P_{\rm galaxy} - P_{\rm SMBH}$, and the quoted 1σ errors represent the uncertainty in the galaxy position, which dominates over the uncertainty in the SMBH position in all cases.

The authors recognized that their measured value of 1893 ± 6 km s^{-1} is considerably larger than the HI results, and they posit that this discrepancy might be caused by dust in the nuclear region of the galaxy. We note that Nelson & Whittle (1995) separately measured [O III] velocities and "stellar velocities" (from the Ca II triplet and Mg b); we only quote the stellar velocity in Table 4.4, but their measurement for [O III] alone is 1939 ± 10 km s^{-1} and thus even more discrepant from the HI values. For our purposes, we retain the tilted-ring model result as the final recession velocity for NGC 2273.

We measured the SMBH velocity in NGC 2273 by modeling the rotation curve of the maser disk, and the results are listed in the bottom section of Table 4.3 and plotted in Figure 4.11. Our best-fit velocity is $1850.8^{+13.5}_{-13.9}$ km s^{-1}. As with NGC 1194, we determine a tighter constraint on the recession velocity than Kuo et al. (2011). We find that there is no significant difference between the galaxy and SMBH velocities in NGC 2273.

4.5.4 ESO 558-G009

Though we detected HI in our VLA observations of ESO 558-G009 (see Figure 4.2), the signal-to-noise ratio was insufficient to fit a tilted-ring model. We did measure a recession velocity of 7606 ± 86 km s^{-1} using the spatially integrated HI profile, but the uncertainty in this measurement is large. Huchra et al. (2012) measured a recession velocity of 7674 ± 27 km s^{-1} using optical spectra, and we adopt their measurement.

As with J0437+2456 (§ 4.5.2), the SMBH velocity for ESO 558-G009 was measured by Gao et al. (2017) via maser rotation curve modeling. We do not find a significant difference between the galaxy and SMBH velocities.

4.5.5 UGC 3789

We used the VLA observations of UGC 3789 from Sun et al. (2013) to measure a recession velocity from the spatially integrated HI profile, though as with ESO 558-G009 the resulting value of 3214 ± 66 km s^{-1} comes with a large uncertainty. Single-dish HI measurements made by Theureau et al. (1998) using the NRT suffer from

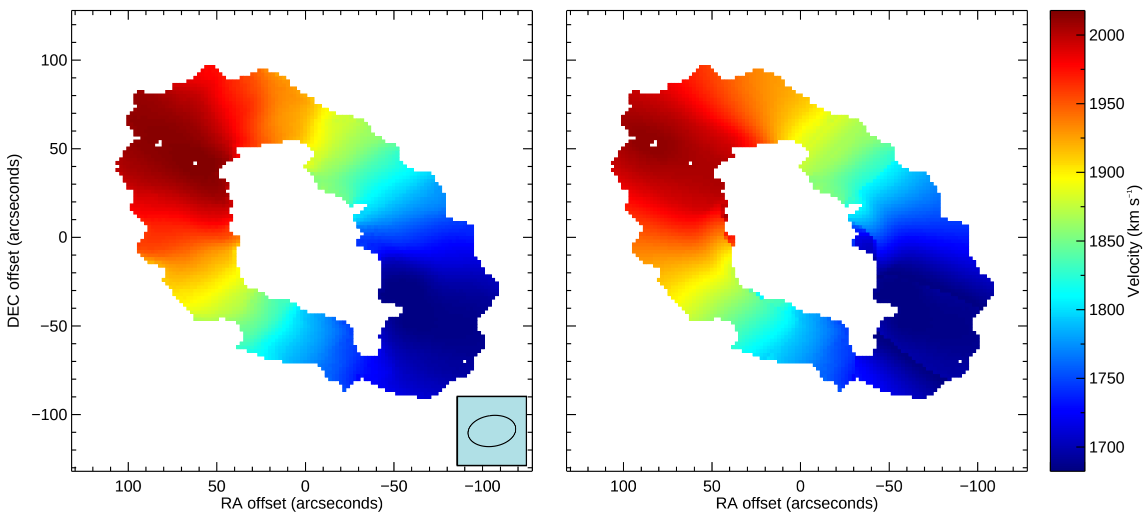

Fig. 4.10.— Same as Figure 4.8, but for NGC 2273

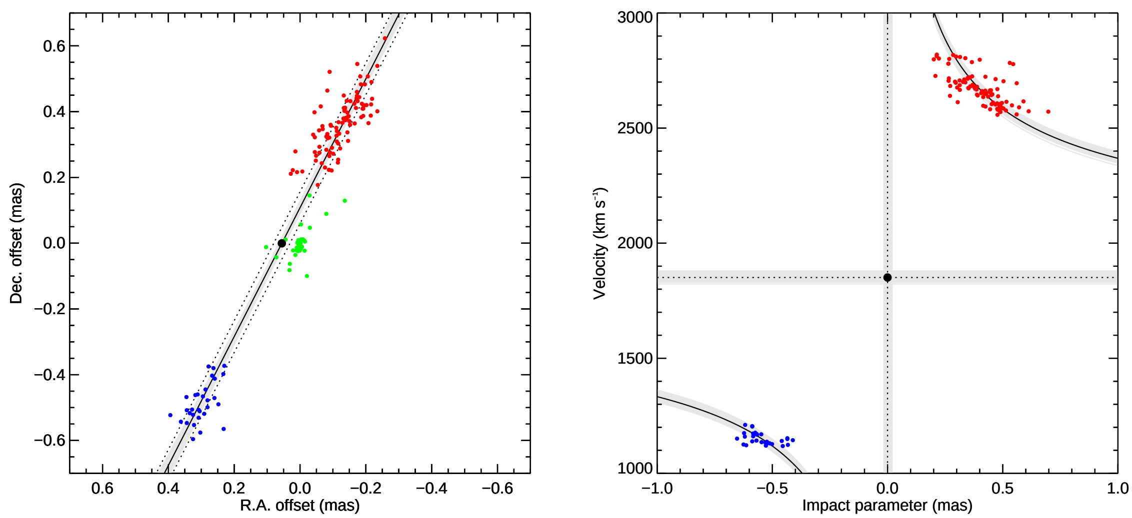

Fig. 4.11.— Same as Figure 4.9, but for NGC 2273.

contamination by UGC 3797, located $\sim$4.3 arcminutes away. Huchra et al. (2012) have an optical measurement of 3325 ± 24 km s^{-1} for the recession velocity, which we adopt for this work.

The SMBH velocity for UGC 3789 has been precisely measured by Reid et al. (2013) as part of the MCP. The authors used multiple epochs of high-sensitivity VLBI and spectral monitoring to construct a geometric and kinematic model of the maser disk, constraining the SMBH velocity to a precision of $\sim$1 km s^{-1} in a manner that is fully independent of any galaxy-scale recession velocity measurements. We find no significant difference between the galaxy and SMBH velocities in UGC 3789.

4.5.6 Mrk 1419

As with UGC 3789, we measure a recession velocity (5041 ± 118 km s^{-1}) from the spatially integrated HI profile of Mrk 1419 (using data taken by Sun et al. 2013), but the large uncertainty is insufficiently discriminating for our purposes. Springob et al. (2005) measured a single-dish HI recession velocity of 4947 ± 8 km s^{-1} by fitting a first-order polynomial to the wings of the HI profile and using it to identify the 50% flux level points on either side of the profile (i.e., the velocity at which the flux density reaches 50% of the peak for the spectral horn on that side of the profile). The recession velocity was then taken to be the average of these two velocities, and the authors determined the uncertainty in the velocity by simulating the observations using realistic noise and instrumental effects. We adopt their measurement.

The SMBH velocity for Mrk 1419 was measured to be 4954.5 ± 15 by Kuo et al. (2011) using maser rotation curve modeling. There is no significant difference between the galaxy and SMBH velocities in Mrk 1419.

4.5.7 NGC 4258

We used archival VLA data to fit a tilted-ring model to the HI disk in NGC 4258; the results are listed in the top portion of Table 4.3, and the resulting velocity map is shown in Figure 4.12. Our best-fit recession velocity is $454.1^{+5.6}_{-5.5}$ km s^{-1}. The data have very high signal-to-noise, and there is evidence from the velocity map that the tilted-ring model fails to reproduce various dynamical structures in the disk; the uncertainty in the recession velocity for this galaxy is thus larger than what one might expect from consideration of signal-to-noise alone. The velocity we derive from the spatially integrated HI profile matches that obtained from the tilted-ring model. We consider the quoted uncertainty in the profile-derived recession velocity (obtained using Equation 4.5) to be an underestimate, because although it is driven down to small values by the extremely high signal-to-noise, it does not account for systematic deviations from an idealized HI profile.

NGC 4258 is a well-studied galaxy, and there are many examples of recession velocity measurements in the literature. Staveley-Smith & Davies (1987) used the 76-m telescope at Jodrell Bank to measure a HI recession velocity of 443 ± 3 km s^{-1} as the mean of the profile between the two points at 50% of the peak flux value. Though the uncertainty quoted in this measurement is small, it may be an underestimate for the same reasons we've described above regarding our spatially integrated HI velocity measurements. An independent measurement by Fisher & Tully (1981), using the 43-m radio telescope at Green Bank, obtained 449 ± 7 km s^{-1}. Both of these measurements are consistent with our result from the tilted-ring model fitting, which we retain as the recession velocity measurement for NGC 4258.

Humphreys et al. (2013) measured the velocity of the SMBH in NGC 4258 to be 466.87 ± 0.49 km s^{-1} via full-disk modeling of the maser system. We have converted their value to the optical convention in the barycentric frame using

$$v_{\text{opt,bary}} = \left(\frac{v_{\text{rad,LSR}}}{1 - \frac{v_{\text{rad,LSR}}}{c}} \right) - 8.13 \text{ km s}^{-1}. \tag{4.20}$$

Here, $v_{\text{rad,LSR}}$ is the velocity measured using the radio convention in the LSR frame, and $v_{\text{opt,bary}}$ is the velocity measured using the optical convention in the barycentric frame. Similar conversions have been made for other velocity measurements throughout this chapter, when necessary.

We do not find a significant difference between the galaxy and SMBH velocities in NGC 4258.

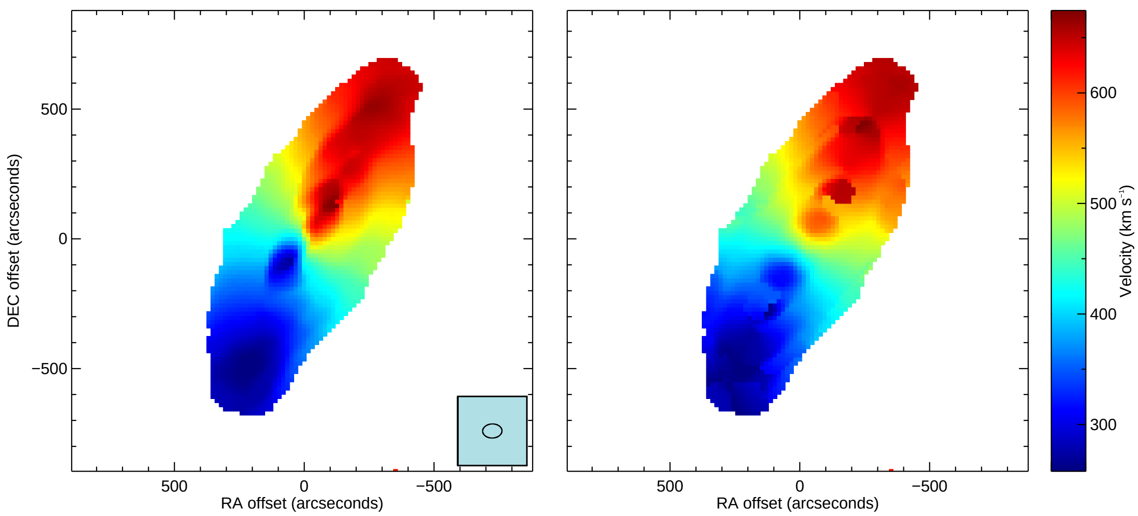

Fig. 4.12.— Same as Figure 4.8, but for NGC 4258.

4.5.8 NGC 5765b

We detected HI in our VLA observations of NGC 5765b, but the gas shows strong signs of kinematic disturbance (see Figure 4.4) from an interaction with the nearby (separation of ∼22 arcseconds) companion galaxy NGC 5765a. The gas from both galaxies is spatially blended even in the VLA observations (Figure 4.4), which also show a large HI tail offset by ∼2 arcminutes from the optical center of either galaxy. The integrated HI profile (Figure 4.6) for NGC 5765b is thus contaminated by emission from NGC 5765a, and so our velocity measurement derived from this profile is an unreliable tracer of the galaxy's motion. This same issue holds true for the Arecibo HI spectrum of NGC 5765b measured by Haynes et al. (2011).

We have thus used an optical spectrum from SDSS (Eisenstein et al. 2011) to measure the recession velocity of 8299.2 ± 18.7 km s^{-1}, using the same fitting procedure and uncertainty calculation as for NGC 1194 (§ 4.5.1). The results from individual emission line and continuum fits are listed in Table 4.5.

The SMBH velocity for NGC 5765b is 8322.22 ± 1.13 km s^{-1}, from Gao et al. (2016), who performed a full disk model of the maser system in this galaxy as part of the MCP. We find no significant difference between the galaxy and SMBH velocities in NGC 5765b.

4.5.9 NGC 6264

We did not detect HI emission in our VLA observations of NGC 6264. Beers et al. (1995) report a recession velocity of 10177 ± 28 km s^{-1}, citing a private communication with Huchra, J. An independent measurement is presented by Koranyi & Geller (2002), who measured a recession velocity of 10161 ± 76 km s^{-1} for NGC 6264 using the same cross-correlation method as Huchra et al. (2012). The authors added an uncertainty of 65 km s^{-1} in quadrature to that produced by the algorithm to account for possible systematic velocity offsets of the line-emitting region from the galaxy, increasing the uncertainty substantially over the pre-corrected value of 39 km s^{-1}.

We have used an optical spectrum from SDSS (Eisenstein et al. 2011) to measure the redshift of NGC 6264 via the same fitting procedure and uncertainty calculation employed for NGC 1194 (§ 4.5.1). The results from individual emission line and continuum fits are listed in Table 4.5, and our final recession velocity measurement is 10151.4 ± 7.6 km s^{-1}.

The SMBH velocity for NGC 6264 (10189.26 ± 1.20 km s^{-1}) was determined by Kuo et al. (2013), who performed a full disk model of the maser system in this galaxy as part of the MCP. The SMBH is redshifted with respect to its host galaxy by 37.9 ± 7.7 km s^{-1} (see Table 4.4). However, this apparent offset is driven almost entirely by the optical emission line velocity measurement, which deviates from the SMBH velocity by 5.7σ. The stellar continuum, by contrast, shows only a minor discrepancy with the SMBH velocity (they differ by 1.7σ), and in the opposite direction from that derived using the emission lines. That is, the emission line velocity is blueshifted by 5.7σ with respect to the SMBH velocity, while the continuum-derived velocity is redshifted by 1.7σ with respect to the SMBH velocity. It is thus plausible that the SMBH and stellar system share a common velocity while the optical emission lines trace gas that is blueshifted with respect to its host galaxy, possibly because they are preferentially tracing shocked gas (see, e.g., Comerford et al. 2017).

Nevertheless, if we proceed with the interpretation that the velocity offset between the SMBH and its host galaxy is caused by SMBH peculiar motion, then we can use Equation 4.19 to estimate an expected spatial separation of $r_{\mathrm{sep}} \approx 20$ pc, corresponding to 0.03 arcseconds at the distance to NGC 6264. Kuo et al. (2011) measured the VLBI maser position to be 16:57:16.1278 +27:50:58.5774, with an uncertainty of 0.3 mas in right ascension and 0.5 mas in declination. We can see in Table 4.6 that the position of NGC 6264 as measured by PanSTARRS, 2MASS, and AllWISE is consistent with both our estimate and with no separation.

4.5.10 NGC 6323

We detected weak HI emission in our VLA observations of NGC 6323 (see Figure 4.5), but it wasn't strong enough to fit a tilted-ring model. The recession velocity of 7835 ± 117 km s^{-1} that we measured from the spatially integrated HI profile has a large uncertainty, also caused by the low signal-to-noise of the data.

An optical recession velocity measurement of 7772 ± 35 km s^{-1} was made by Marzke et al. (1996), who used the same template-matching methods as Huchra et al. (2012). We adopt their value as the recession velocity for NGC 6323.

The SMBH velocity for NGC 6323 has been measured by Kuo et al. (2015), who performed a full disk model of the maser system in this galaxy as part of the MCP. We do not find a significant difference between the galaxy and SMBH velocities in NGC 6323.

4.6 Discussion

The ideal recession velocity measurement would perfectly reflect the motion of the galactic barycenter. For galaxies with an undisturbed HI disk, we have shown that spatially resolved disk modeling is a viable method for obtaining a precise measurement of the galaxy's recession velocity. Optical spectra can be used to complement the HI measurements, and we have done so here where such spectra exist.

If the spatial and kinematic offsets we see in J0437+2456 are genuinely tracing the SMBH motion, then the matching magnitude of the positional offset with the prediction from Equation 4.19 is most easily explained by a solitary SMBH undergoing small-amplitude oscillations about the galactic center. Such a scenario is expected in the aftermath of a binary SMBH merger, whereby the resulting post-merger SMBH experiences a kick that ejects it from the core of the galaxy. Dynamical friction will quickly decay the SMBH orbit down to roughly the core radius, but beyond this point it ceases to operate as efficiently and the oscillations that occur on the core scale itself can last more than an order of magnitude longer than the initial decay timescale (see Gualandris & Merritt 2008). J0437+2456 resides in a small group of galaxies (Crook et al. 2007), so it could plausibly have experienced the relatively recent galaxy merger (leading to a binary SMBH merger event) necessary for this interpretation to hold.

The observed velocity and positional offsets in J0437+2456 could also be explained if the SMBH is still in the process of inspiraling (i.e., post-galaxy merger but pre-SMBH merger; see, e.g., Comerford et al. 2009). The stellar mass interior to a $\sim$0.1 arcsecond orbital radius is expected to be roughly an order of magnitude larger than the mass of the SMBH itself, so the SMBH binary will not have hardened yet and the motion of the SMBHs will still be strongly influenced by the stellar potential. Future observations should be able to place constraints on the presence of a possible companion SMBH.

We caution that both J0437+2456 and NGC 6264 have recession velocities measured only from optical emission lines and stellar continua in SDSS spectra, and that neither has corroborating HI measurements. Of particular concern is the possibility that the SDSS fiber during the J0437+2456 observations was spatially offset from the galactic center; an offset of $\gtrsim$0.1 arcseconds in the fiber placement could plausibly account for a large fraction of the observed velocity signal. Future observations – deeper HI spectra, spatially resolved optical spectroscopy, or both – will be necessary to confirm whether these velocity offsets are real or whether the optically derived velocities are systematically shifted with respect to the galaxy's recession velocity.

For the remaining eight galaxies in our sample, five have SMBH peculiar velocity measurements that are currently limited by the precision in the host galaxy recession velocity, two are limited by the precision in the SMBH velocity, and one (NGC 1194) has comparable uncertainties in both measurements. In cases where the SMBH velocity is the limiting factor, a complete maser disk model (as opposed to simply measuring the rotation curve) would substantially decrease the uncertainties. For galaxies where the galactic recession velocity is the limiting factor, spatially resolved optical spectroscopy (such as provided by integral field units) will likely be a promising method to explore.

Peculiar velocity measurements for any single source are not by themselves enough to unambiguously identify the mechanism driving the motion. However, making measurements of both positional and velocity offsets between a SMBH and its host galaxy, and/or making statistical measurements of velocity offsets for several sources, will allow us to narrow the range of possibilities. Having a representative statistical sample of SMBH peculiar velocity measurements will help to constrain the efficiency of SMBH binary coalescence, a question that is becoming increasingly relevant as pulsar timing arrays push down the upper limit on a stochastic gravitational wave background.

Chapter 5

A geometric distance to CGCG 074-064

Note: the material presented in this chapter has been undertaken as part of the Megamaser Cosmology Project and in collaboration with Jim Braatz, Mark Reid, Jim Condon, Feng Gao, Christian Henkel, Cheng-Yu Kuo, Fred Lo, and Wei Zhao.

5.1 Introduction

Almost ninety years after Hubble's seminal work (Hubble 1929), observational cosmology remains as focused as ever on measuring a precise and accurate value of the Hubble constant, H_0. Today, measurements of the cosmic microwave background (CMB) at high redshift ($z \approx 1100$) determine the angular-size distance to the surface of last scattering and set a basic framework for cosmology (Bennett et al. 2013; Planck Collaboration et al. 2016a). These observations, in the context of the ΛCDM cosmological model, predict a very precise value for H_0, (66.93 ± 0.62 km s^{-1} Mpc^{-1}; Planck Collaboration et al. 2016b). Astrophysically measured values, however, are in tension with this prediction. For example, Freedman et al. (2012) measure $H_0 = 74.3 \pm 2.6$ km s^{-1} Mpc^{-1} and Riess et al. (2018) measure $H_0 = 73.48 \pm 1.66$ km s^{-1} Mpc^{-1} from standard candles and distance ladders connecting to type Ia supernovae (SNe Ia). Despite numerous attempts to reconcile these results (e.g., Efstathiou 2014, Spergel et al. 2015), it is still unclear whether this discrepancy arises from unaccounted systematic uncertainties in the measurements or if it is a sign that the ΛCDM cosmological model is in need of revision.

Water megamasers residing in the accretion disks around supermassive black holes (SMBHs) provide a unique way to bypass the distance ladder and make one-step, geometric distance measurements to their host galaxies. The archetypal megamaser disk system is the nearby (7.6 Mpc) Seyfert 2 galaxy NGC 4258 (Claussen et al. 1984; Nakai et al. 1993). The masers in this system reside in a thin, edge-on annulus at distances $r \approx 0.14$-0.28 pc from the central SMBH. Emission near the recession velocity ("systemic lines") comes from the near side of the disk, and "high-velocity lines" with $V \approx \pm 1100$ km s^{-1} come from the two tangent points. The Keplerian rotation curve of the high-velocity lines imply a central mass of 3.9×10^7 M$_\odot$. The velocities of individual systemic features are increasing by $\sim$9 km s^{-1} yr^{-1}, caused by the centripetal acceleration of clouds moving across our line of sight. The distance D to NGC 4258 has been measured in two independent ways: (1) from proper motions $\dot{\theta}$ via the relation $V = D\dot{\theta}$, and (2) from accelerations via the relation $a = V_r^2/r = V_r^2/D\theta$, where V_r, a, θ, and $\dot{\theta}$ are measured from spectral monitoring observations

(Herrnstein et al. 1999). The current precision on the distance to NGC 4258 stands at $\lesssim$3%, including systematic uncertainties (Humphreys et al. 2013, Riess et al. 2016). NGC 4258 thus serves as an "anchor" in the aforementioned distance ladder, where it is used as a one-step calibrator of the Leavitt law for Cepheid variable stars (thereby providing a two-step calibration of SNe Ia). Unfortunately, the proximity of NGC 4258 precludes its use for a direct measurement of H_0.

However, this "megamaser technique" can be applied to galaxies at distances much greater than 7 Mpc. The primary goal of the Megamaser Cosmology Project (MCP) is to constrain H_0 to a precision of several percent by making one-step, geometric distance measurements to megamaser galaxies in the Hubble flow (Reid et al. 2013; Kuo et al. 2013; Kuo et al. 2015; Gao et al. 2016). H_0 measurements made using the megamaser technique are independent of standard candles and the CMB, and thus provide a key piece of evidence for interpreting the current tension between distance ladder and CMB-derived H_0 values.

In this work we present a megamaser distance measurement to the galaxy CGCG 074-064, whose maser system was discovered in 2015 as part of the survey component of the MCP. This chapter is organized as follows. In § 5.2 we describe the monitoring and mapping observations and data reduction procedures. § 5.3 goes over our measurement techniques for determining maser positions and accelerations, and in § 5.4 we detail the H_0 measurement. § 5.5 discusses the observed VLBI continuum emission and spectral variability of the maser features. Unless otherwise specified, all velocities referenced in this work use the optical definition in the barycentric reference frame. The conversion from barycentric to CMB frame velocities is $v_{\mathrm{CMB}} = v_{\mathrm{bary}} + 263.3$ km s^{-1} for CGCG 074-064 (Hinshaw et al. 2009).

5.2 Observations and data reduction

There are two classes of observations necessary for making a Hubble constant measurement using a disk maser system: (1) high-sensitivity very long baseline interferometric (VLBI) observations to map the spatial distribution of the masers, and (2) short-cadence ($\sim$monthly) spectral monitoring observations spanning a sufficiently long time baseline to measure the accelerations of the systemic maser features. We used the Very Long Baseline Array (VLBA), augmented with the addition of the Robert C. Byrd Green Bank Telescope (GBT) and the phased Karl G. Jansky Very Large Array (VLA), to map the maser system in CGCG 074-064. The bulk of the monitoring spectra were taken with the GBT, though we used the VLA to observe during the summer months when the weather in Green Bank makes K-band observations inefficient.

5.2.1 GBT monitoring observations

We performed ∼monthly spectral monitoring observations of CGCG 074-064 from 2015 October through 2017 May, for a total of 20 epochs (see Table 5.1). A total of 16 monitoring spectra were taken with the GBT. Our general observing strategy and data reduction process follow similar procedures to those detailed in previous MCP papers (Braatz et al. 2010, Pesce et al. 2015), so in this section we give only a brief overview. All GBT data were reduced using GBTIDL[1].

For each 3-hour GBT monitoring epoch we performed nodding observations with two of the seven beams of the K-band Focal Plane Array (KFPA), using the Versatile GBT Astronomical Spectrometer (VEGAS) as the backend. The spectrometer was configured with four overlapping 187.5 MHz spectral windows, covering recession velocities from 3500–12500 km s^{-1} contiguously with 5.722 kHz (∼0.08 km s^{-1}) spectral channels. Both left circular polarization (LCP) and right circular polarization (RCP) were observed simultaneously in each of the two beams, and we performed hourly observations of a nearby bright (>1 Jy) continuum source to derive pointing and focus corrections.

During data reduction we smoothed the reference beam spectrum with a 64-channel boxcar function prior to differencing. For every monitoring run, all integrations in both polarizations were averaged using a $\tau/T_{\rm sys}^2$ weighting scheme (τ is the integration exposure time and $T_{\rm sys}$ is the system temperature) chosen to minimize the final noise level. A (typically third-order) polynomial was fit to line-free spec-

[1] http://gbtidl.nrao.edu/

tral channels and subtracted to remove any residual baseline structure from the final spectrum. Table 5.1 lists the system temperatures and sensitivities achieved for all monitoring observations.

Figure 5.1 shows the CGCG 074-064 maser spectrum averaged over all GBT epochs. This spectrum represents the product of some $\sim$40 hours of integration, and it achieves an RMS noise level of 0.33 mJy per 0.32 km s^{-1} spectral channel. Maser emission is detected all the way down to the sensitivity limit, and individual maser features are seen out to velocity extremes of 7892 km s^{-1} on the redshifted side and 5846 km s^{-1} on the blueshifted side (corresponding to an orbital velocity of $\sim$1066 km s^{-1}).

5.2.2 VLA monitoring observations

We used the VLA to observe during the 2016 summer months, when the level of atmospheric water vapor at the Green Bank site would have made K-band observations inefficient. In total, four 3-hour tracks were covered by the VLA (see Table 5.1). All VLA data were reduced and imaged using standard procedures within CASA[2].

The first three tracks were observed with the VLA in B configuration, and the September track was observed while the VLA was transitioning between B and A configurations[3]. We configured the correlator to place three overlapping 64 MHz windows covering the three sets of maser features, with 4096 15.625 kHz ($\sim$0.21 km s^{-1}) channels in each spectral window. An additional 8 128 MHz spectral windows with coarser (2 MHz; $\sim$26.5 km s^{-1}) channel spacing were placed on each side of the maser profile, resulting in a net $\sim$2 GHz increase in bandwidth for a significant improvement in continuum sensitivity.

During reduction, we first corrected for antenna positions and atmospheric opacity before solving for delay and phase solutions on the flux calibrator (3C 286, which also doubled as our bandpass calibrator). These solutions were applied to the flux

[2] `https://casa.nrao.edu/`

[3] We note that the August and September VLA tracks were observed during the period of time in semester 16B when the online tropospheric delay model was misapplied. Though our observations are negligibly affected by this issue, we nevertheless applied a tropospheric delay error correction during the data reduction procedure for these tracks.

Table 5.1. CGCG 074-064 monitoring observation details

Epoch	Date	Telescope	T_{sys} (K)	Sensitivity (mJy)	Synthesized beam ($'' \times ''$, $^\circ$)	Continuum flux density (μJy)
1	2015 Oct 15	GBT	42.1	3.8	...	...
2	2015 Nov 13	GBT	44.4	2.9	...	...
3	2015 Dec 18	GBT	41.3	2.7	...	...
4	2016 Jan 12	GBT	45.9	2.9	...	...
5	2016 Feb 26	GBT	43.7	3.2	...	...
6	2016 Mar 22	GBT	47.8	2.7	...	...
7	2016 Apr 10	GBT	43.7	2.7	...	...
8	2016 Jun 08	VLA	...	1.3	0.38×0.31, -2.79	62.1 ± 6.0
9	2016 Jun 13	GBT	49.5	3.2	...	...
10	2016 Jul 10	VLA	...	2.8	0.38×0.34, 17.12	83.3 ± 12.8
11	2016 Aug 15	VLA	...	3.0	0.36×0.33, 45.05	90.7 ± 11.7
12	2016 Sep 10	VLA	...	2.1	0.25×0.15, 80.69	58.9 ± 8.7
13	2016 Oct 09	GBT	47.6	3.0	...	...
14	2016 Nov 18	GBT	50.4	3.1	...	...
15	2016 Dec 14	GBT	35.2	2.2	...	...
16	2017 Jan 25	GBT	50.3	3.2	...	...
17	2017 Feb 16	GBT	37.7	2.5	...	...
18	2017 Mar 15	GBT	40.0	2.7	...	...
19	2017 Apr 11	GBT	64.7	4.3	...	...
20	2017 May 09	GBT	42.3	2.8	...	...

Note. — Monitoring observation details. The sensitivity is listed per 5.722 kHz (0.08 km s^{-1}) channel for all GBT observations and per 15.625 kHz (0.21 km s^{-1}) channel for all VLA observations. The RMS sensitivity for each epoch was determined using the line-free velocity range spanning from 7100 km s^{-1} to 7300 km s^{-1}. The synthesized beam sizes are quoted as the FWHM of the major $\times$ minor axes of the restoring elliptical Gaussian, with position angles measured east of north. The continuum flux densities measured for the VLA tracks are quoted as the peak value of the unresolved point source measured in a $\sim$2 GHz bandwidth centered at a rest-frame frequency of 22.2 GHz.

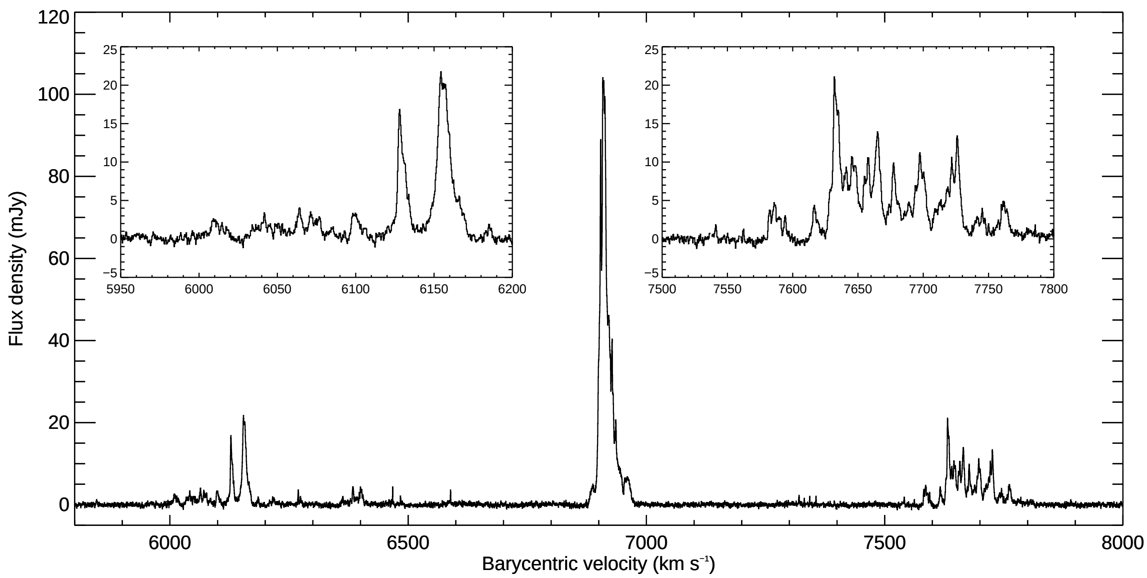

Fig. 5.1.— 22 GHz GBT spectrum of CGCG 074-064, plotted as a weighted average over all epochs. The two inset plots show zoomed-in spectra of the strongest high-velocity maser features. The RMS noise level in this spectrum is 0.33 mJy per 0.32 km s^{-1} spectral channel.

calibrator, which we then used to obtain the bandpass solutions. The brightest systemic maser features exceeded ∼150 mJy for all VLA tracks, and by averaging over a 10 km s^{-1} window in both polarizations we were able to track the phase solutions on individual baselines with a two-minute cadence. After applying the bandpass, flux, and phase calibrations we performed a round of (typically minor) data flagging and repeated the calibration procedure once more before splitting out the calibrated science target. We then performed a series of phase and amplitude self-calibration steps, once again using the brightest systemic maser features. We stopped iterating self-calibration once there was no noticeable increase in the signal-to-noise ratio (S/N), which typically occurred after 2-3 rounds.

Prior to imaging, we performed continuum subtraction on the uv data. We imaged the continuum and spectral line cubes separately, using the `CLEAN` algorithm with natural uv weighting for both. The continuum is unresolved in our VLA observations, and it is spatially coincident with the maser emission. Combining all VLA tracks, we measure an average continuum level of 72.3 ± 4.8 μJy at a representative rest-frame frequency of 22.2 GHz. The continuum level shows strong (greater than ∼50%) variability from one epoch to another, with a similar magnitude and timescale to that seen in the nuclear continuum emission from the megamaser galaxy NGC 4258 (Herrnstein et al. 1997). Unlike in NGC 4258, we do not find evidence for a correlation between the continuum level and the average flux density of any group of maser features.

5.2.3 VLBI mapping observations

In total, we observed 10 6-hour VLBI tracks (see Table 5.2). The first track was phase-referenced to measure the absolute position of CGCG 074-064, while the subsequent 9 tracks were self-calibrated on the strongest systemic maser features (see Table 5.3). As with the single-dish monitoring observations we have generally followed the same observing and data reduction procedures used for previous MCP targets (Reid et al. 2009, Kuo et al. 2011, Gao et al. 2016), so this section focuses primarily on differences from previous MCP papers. All VLBI data were calibrated in AIPS[4] and imaged with CASA.

For the phase-referenced track, we observed using only the VLBA antennas. The correlator was configured with two overlapping 128 MHz spectral windows placed to either side of the systemic features. Both windows contained the systemic complex of maser features, with one window shifted blueward and the other shifted redward to cover the high-velocity maser features. Each spectral window was spanned by 256 channels spaced contiguously every 0.5 MHz ($\sim$6.7 km s^{-1}), and we observed in dual circular polarization. We used J1410+0731 as our phase-reference calibrator (separated from CGCG 074-064 by 2.3 degrees), switching between target and calibration observations on a 3-minute duty cycle. We observed J1415+1320 hourly as a delay calibrator, and the entire track was bracketed by "geodetic" observations (see Reid et al. 2009). We measure the absolute position of the maser system (defined as the intensity-weighted mean position of all systemic maser features) to be:

$$
\begin{aligned}
\alpha_{\mathrm{J2000}} &= 14:03:04.457746 \\
\delta_{\mathrm{J2000}} &= +08:56:51.03483
\end{aligned}
$$

The resulting statistical and relative calibration uncertainties are much smaller than the absolute astrometric uncertainties for the phase-reference source, so we take the absolute positional uncertainties for CGCG 074-064 to be 0.78 mas in right ascension and and 1.15 mas in declination (Table 5.3).

The self-calibrated tracks were observed using the High Sensitivity Array (HSA), composed of the VLBA plus the GBT and phased-VLA. We used the same correlator configuration as for the phase-referenced track, but in addition we obtained a second "zoom" correlator pass with a higher-resolution channel spacing of 25 kHz ($\sim$0.34 km s^{-1}) across three 64 MHz spectral windows contiguously covering the three sets of maser features. As with the phase-referenced track, we performed hourly delay calibration observations of J1415+1320. The VLA was "phased-up" every 10 minutes

[4] `http://www.aips.nrao.edu/`

by observing J1351+0830, located 2.9 degrees away from CGCG 074-064. Each track was bracketed by observations of either 4C39.25 or 3C286, which served as both fringe finders and bandpass calibrators. During data processing the strongest systemic features, located between 6900 km s^{-1} and 6920 km s^{-1}, were used to self-calibrate the phases.

After calibration we concatenated all of the phase-referenced tracks, weighting each track by its RMS (i.e., using $1/\sigma^2$ weighting). We then imaged the dataset in CASA, using the `CLEAN` algorithm with natural uv weighting. The RMS of the final data cube is 0.49 mJy beam^{-1} in a single $\sim$0.34 km s^{-1} channel. Prior to mapping the maser system, we averaged to $\sim$2 km s^{-1} channels, corresponding to a typical maser feature linewidth. The locations of the maser spots in the cube were then measured using the technique described in § 5.3.1, and the maser map is shown in Figure 5.2.

We imaged the line-free channels in our combined VLBI data and detected a marginally-resolved continuum source with a peak flux density of 31.2$\pm$6.0 μJy beam^{-1}; the continuum contours are shown in Figure 5.2. The peak of the continuum emission is located 0.35 mas above (i.e., north of) the disk plane, and it is aligned in right ascension with the systemic features. The VLBI continuum is roughly a factor of 2 weaker than what was observed with the VLA, which could be explained by (1) the presence of an intermediate-scale component that is resolved out on very long baselines, or (2) source variability, which we know from the VLA observations is large enough to potentially account for the entirety of the flux difference.

5.3 Measurements

The input data for our disk modeling consists of an on-sky position (x, y), a line-of-sight velocity v, and a line-of-sight acceleration a for each maser "spot" (i.e., for each velocity channel in the VLBI map). In this section we detail how the maser positions and accelerations are measured. Table 5.4 lists all measured (and some modeled) quantities for each maser spot.

Table 5.2. CGCG 074-064 VLBI observation details

Project code	Date	Antennas	Synthesized beam (mas × mas, °)	Sensitivity (mJy)	Observing mode
BB370Z	2016 Jan 19	VLBA	2.33×0.36, -18.18	1.30[a]	Phase-ref.
BB370D	2016 Feb 11	VLBA+GBT+VLA	1.29×0.47, 176.5	1.44[b]	Self-cal.
BB370E	2016 Feb 21	VLBA+GBT+VLA	1.05×0.36, -6.88	1.26	Self-cal.
BB370G	2016 Feb 28	VLBA+GBT+VLA	1.48×0.34, 165.7	1.01	Self-cal.
BB370H	2016 Mar 10	VLBA+VLA[c]	1.40×0.35, -17.24	2.09	Self-cal.
BB370J	2016 Mar 21	VLBA+GBT+VLA	1.28×0.36, -9.63	0.95	Self-cal.
BB370L	2016 Mar 24	VLBA+GBT+VLA	1.29×0.36, -14.26	1.07	Self-cal.
BB370U	2016 May 16	VLBA+GBT+VLA	1.13×0.36, 172.6	1.01	Self-cal.
BB370Y	2016 Jun 17/18	VLBA+GBT+VLA	1.02×0.36, -6.30	1.29[d]	Self-cal.
BB370AB	2016 Jun 19/20	VLBA+GBT+VLA	1.31×0.34, 168.2	1.76	Self-cal.
...	...	...	1.12×0.40, -6.91	0.49	...

Note. — VLBI observation details. All tracks were 6 hours in length. The RMS sensitivity for each track was determined using the line-free velocity range spanning from 7100 km s^{-1} to 7300 km s^{-1}. All tracks prior to BB370U were taken with the VLA in C-configuration, while all subsequent tracks had the VLA in B-configuration. The synthesized beam sizes are quoted as the FWHM of the major × minor axes of the restoring elliptical Gaussian, with position angles measured east of north.

[a] The sensitivity in the phase-referenced track is calculated per 0.5 MHz ($\sim$6.7 km s^{-1}) channel from the default "continuum-like" correlator pass (i.e., without re-correlating at finer spectral resolution).

[b] The sensitivity in the self-calibrated tracks is calculated per 25 kHz ($\sim$0.34 km s^{-1}) channel from a second "zoom" correlator pass.

[c] No fringes were found at the GBT for this track, so all baselines containing the GBT were flagged.

[d] The GBT had poor pointing corrections for the first $\sim$2 hours of this track, so all GBT baselines were flagged during this time period.

Table 5.3. VLBI positions for CGCG 074-064 and calibrators

Name	R.A. (J2000)	decl. (J2000)	Uncertainty in R.A. (mas)	Uncertainty in decl. (mas)	Purpose
4C39.25	09:27:03.013938	+39:02:20.85177	0.13	0.10	fringe finder/bandpass calibrator
3C286	13:31:08.288051	+30:30:32.95925	0.17	0.17	fringe finder/bandpass calibrator
J1351+0830	13:51:16.919081	+08:30:39.90354	0.09	0.19	VLA “phase-up” calibrator
J1410+0731	14:10:35.075347	+07:31:21.48972	0.78	1.15	phase reference calibrator
J1415+1320	14:15:58.817511	+13:20:23.71291	0.02	0.04	delay calibrator
CGCG 074-064	14:03:04.457746	+08:56:51.03483	0.78	1.15	science target

Note. — VLBI positions for CGCG 074-064 and calibrators. The positions for the calibrators are from the VLBA Calibrator Survey, and the position for CGCG 074-064 is measured in reference to J1410+0731. The astrometric uncertainty in the phase reference calibrator J1410+0731 dominates the absolute position uncertainty for CGCG 074-064.

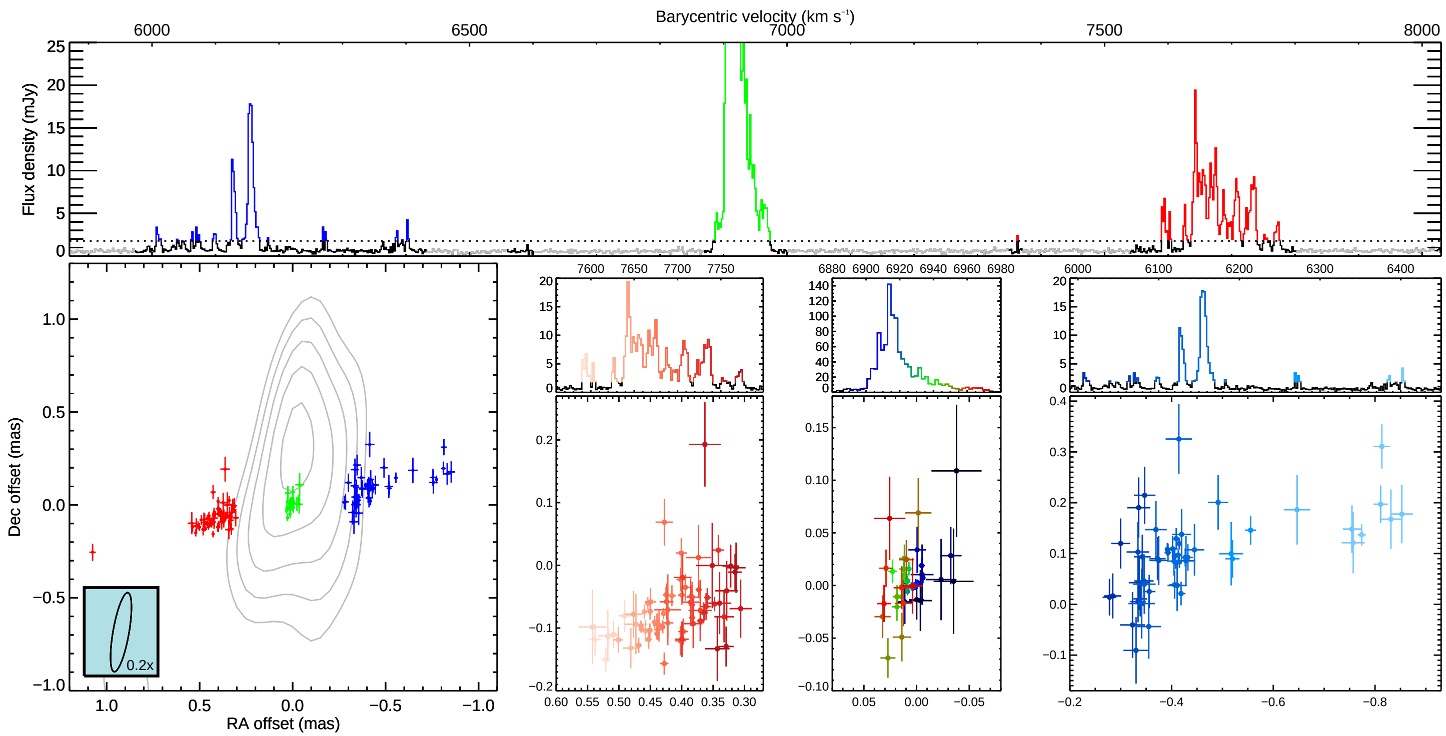

Fig. 5.2.— Results from our VLBI observations of CGCG 074-064, obtained by combining all self-calibrated tracks as described in § 5.2.3. *Top*: Spectrum (in black) extracted from the best-fit maser spot in each channel of the data cube, with the horizontal dotted line marking the 8σ threshold we used as our cutoff for mapping (see § 5.3.1); 1σ in this spectrum is 0.22 mJy for a single $\sim$2 km s^{-1} channel. Segments of the spectrum colored in blue, green, and red correspond to those channels meeting our S/N threshold from the blueshifted, systemic, and redshifted maser complexes, respectively. Segments of the spectrum shaded in gray correspond to those line-free channels that were used to measure the continuum level. *Bottom left*: Map of the maser system in CGCG 074-064, with maser spot positions extracted from the data cube as described in § 5.3.1. Only maser spots with S/N exceeding our 8σ threshold are shown, with 1σ uncertainties in right ascension and declination plotted as horizontal and vertical lines, respectively. Blue, green, and red points mark blueshifted, systemic, and redshifted masers, respectively. The gray contours show the 22 GHz continuum level, which peaks at a value of 31 μJy beam^{-1}; the contours start at 3σ and are spaced every 0.5σ (the 1σ continuum level is 6 μJy beam^{-1}). The half-power restoring beam shape, scaled down by a linear factor of 5, is shown at the bottom left-hand corner. *Bottom right*: From left to right, zoomed-in maps (lower panels) and spectra (upper panels) of the redshifted, systemic, and blueshifted maser complexes. The maser spots in every map-spectrum pair are colored by velocity.

Table 5.4. Measurements for individual maser spots in CGCG 074-064

Spot type	Velocity (km s^{-1})	S_ν (mJy)	σ_S (mJy)	x (mas)	σ_x (mas)	y (mas)	σ_y (mas)	a (km s^{-1} yr^{-1})	σ_a (km s^{-1} yr^{-1})	Accel. meas.
b	6007.40	3.376	0.219	−0.277944	0.012987	0.014065	0.036364	0.00	2.00	0
b	6009.41	2.524	0.202	−0.284287	0.015984	0.016585	0.044755	0.00	2.00	0
b	6011.43	1.915	0.206	−0.335289	0.021484	0.190261	0.060154	0.00	2.00	0
b	6013.45	1.987	0.176	−0.299844	0.017765	0.119853	0.049743	0.00	2.00	0
b	6039.63	1.958	0.190	−0.336206	0.019375	0.042687	0.054250	0.00	2.00	0
b	6047.69	1.763	0.179	−0.347021	0.020260	0.214663	0.056729	0.00	2.00	0
b	6049.69	1.659	0.194	−0.323243	0.023369	−0.040505	0.065432	0.00	2.00	0
b	6061.79	1.901	0.139	−0.334031	0.014673	0.005382	0.041085	0.00	2.00	0
b	6063.79	2.839	0.256	−0.345758	0.018015	0.046097	0.050441	0.00	2.00	0
b	6069.85	3.379	0.211	−0.338244	0.012509	0.010836	0.035024	0.00	2.00	0
b	6071.85	1.634	0.173	−0.333876	0.021175	0.103042	0.059291	0.00	2.00	0
b	6073.87	2.491	0.196	−0.342440	0.015711	0.093658	0.043992	0.00	2.00	0
b	6075.89	1.648	0.194	−0.330131	0.023582	−0.090599	0.066029	0.00	2.00	0
b	6096.03	2.009	0.175	−0.374747	0.017438	0.086320	0.048827	0.00	2.00	0
b	6098.03	2.633	0.155	−0.356053	0.011809	0.025191	0.033064	0.00	2.00	0
b	6100.05	2.551	0.195	−0.372329	0.015299	0.089837	0.042836	0.00	2.00	0
b	6118.17	1.244	0.154	−0.341211	0.024818	0.001524	0.069489	0.00	2.00	0
b	6120.19	1.597	0.162	−0.369258	0.020344	0.147119	0.056963	0.00	2.00	0
b	6124.23	1.894	0.216	−0.355075	0.022808	−0.043718	0.063862	0.75	0.86	1
b	6126.23	11.314	0.253	−0.391736	0.004473	0.108043	0.012524	2.19	1.00	1
b	6128.25	9.903	0.289	−0.406277	0.005832	0.095345	0.016330	0.16	0.42	1
b	6130.27	7.530	0.243	−0.392998	0.006443	0.101862	0.018040	−0.12	1.12	1
b	6132.27	5.083	0.237	−0.402082	0.009313	0.109155	0.026076	−0.30	0.95	1
b	6134.29	2.060	0.218	−0.346388	0.021137	0.039726	0.059182	−0.05	1.40	1
b	6138.31	1.272	0.158	−0.414300	0.024836	0.325445	0.069540	0.64	1.51	1
b	6142.35	1.948	0.171	−0.428298	0.017569	0.085690	0.049193	0.93	1.11	1
b	6144.37	1.990	0.179	−0.410938	0.018036	0.037089	0.050500	1.43	1.14	1
b	6146.37	2.128	0.191	−0.419762	0.017958	0.137704	0.050281	0.20	0.86	1
b	6148.39	3.724	0.183	−0.406011	0.009830	0.038509	0.027523	−0.21	1.15	1
b	6150.41	6.095	0.228	−0.409150	0.007492	0.129366	0.020976	−1.26	1.88	1
b	6152.41	16.674	0.389	−0.407896	0.004664	0.083119	0.013059	−1.14	0.91	1
b	6154.43	17.811	0.379	−0.414906	0.004254	0.119691	0.011912	−1.00	0.63	1
b	6156.45	17.611	0.386	−0.415397	0.004388	0.083462	0.012286	−1.00	0.67	1
b	6158.47	13.316	0.246	−0.413215	0.003694	0.097113	0.010343	−0.63	0.55	1
b	6160.47	8.019	0.258	−0.426922	0.006447	0.092346	0.018052	−1.34	0.66	1
b	6162.49	5.188	0.218	−0.418659	0.008391	0.021247	0.023494	−1.22	0.94	1
b	6164.51	3.374	0.173	−0.404812	0.010265	0.084971	0.028742	0.40	1.31	1
b	6168.53	2.154	0.197	−0.444982	0.018324	0.107379	0.051307	0.52	1.39	1
b	6182.63	2.156	0.208	−0.491537	0.019296	0.200689	0.054030	0.00	2.00	0
b	6269.24	3.389	0.174	−0.555363	0.010290	0.145977	0.028813	0.77	0.85	1
b	6273.27	2.874	0.192	−0.519689	0.013329	0.089751	0.037320	−0.85	7.82	1
b	6275.28	1.833	0.206	−0.517265	0.022471	0.099622	0.062920	−0.17	5.00	1
b	6363.90	1.678	0.207	−0.646719	0.024705	0.186230	0.069173	1.11	2.21	1
b	6384.04	2.158	0.182	−0.754662	0.016825	0.148142	0.047111	2.08	2.68	1
b	6386.06	2.953	0.196	−0.811090	0.013273	0.197093	0.037164	−0.21	1.44	1
b	6394.12	1.892	0.149	−0.813485	0.015704	0.310792	0.043971	0.26	1.61	1
b	6400.16	1.687	0.178	−0.831268	0.021109	0.167669	0.059104	0.20	0.67	1
b	6402.18	4.224	0.163	−0.773766	0.007703	0.136922	0.021568	−1.69	1.13	1
b	6404.18	2.012	0.218	−0.757077	0.021672	0.121209	0.060681	0.64	0.47	1
s	6883.56	1.846	0.167	−0.035132	0.018090	0.003964	0.050653	3.79	0.99	1
s	6885.58	1.605	0.182	−0.037922	0.022666	0.108927	0.063466	5.29	0.34	1
s	6887.60	3.966	0.207	−0.003615	0.010446	−0.014367	0.029248	7.48	1.14	1
s	6889.60	5.088	0.172	−0.000118	0.006777	−0.013557	0.018976	4.07	0.65	1
s	6891.62	3.157	0.220	−0.023267	0.013921	0.005585	0.038978	3.03	0.69	1
s	6893.64	3.860	0.199	−0.005208	0.010320	0.010339	0.028896	3.32	0.47	1
s	6895.64	3.330	0.163	−0.032478	0.009801	0.028351	0.027443	3.90	0.51	1
s	6897.66	4.354	0.166	0.011185	0.007604	−0.015560	0.021290	4.58	0.51	1
s	6899.68	5.186	0.205	−0.000542	0.007909	0.033921	0.022144	4.14	0.70	1
s	6901.70	17.878	0.252	−0.004818	0.002819	0.018911	0.007892	2.88	0.34	1
s	6903.70	31.308	0.290	−0.006048	0.001852	0.007253	0.005185	3.74	0.35	1
s	6905.72	30.949	0.298	0.000727	0.001925	0.001076	0.005389	3.70	0.51	1
s	6907.74	78.324	0.430	−0.001684	0.001098	0.001946	0.003076	4.29	0.34	1
s	6909.74	55.770	0.446	−0.000841	0.001598	0.001317	0.004475	5.09	0.49	1
s	6911.76	62.678	0.433	0.000075	0.001382	0.001069	0.003870	4.80	0.32	1
s	6913.78	141.932	0.761	−0.000235	0.001073	0.000422	0.003004	4.52	0.18	1
s	6915.78	101.527	0.581	0.003071	0.001144	−0.002041	0.003204	5.00	0.33	1
s	6917.80	97.521	0.517	0.001595	0.001061	−0.000490	0.002971	3.97	0.38	1
s	6919.82	52.796	0.367	0.004136	0.001389	−0.001493	0.003888	5.41	0.32	1
s	6921.84	44.124	0.296	0.003561	0.001343	0.000006	0.003761	5.03	0.25	1
s	6923.84	36.993	0.243	0.004897	0.001315	−0.000504	0.003683	4.23	0.23	1
s	6925.86	33.717	0.237	0.008619	0.001404	−0.005553	0.003930	4.27	0.39	1
s	6927.88	20.570	0.257	0.010160	0.002495	0.006029	0.006986	4.80	0.28	1

Table 5.4—Continued

Spot type	Velocity (km s^{-1})	S_ν (mJy)	σ_S (mJy)	x (mas)	σ_x (mas)	y (mas)	σ_y (mas)	a (km s^{-1} yr^{-1})	σ_a (km s^{-1} yr^{-1})	Accel. meas.
s	6929.88	21.657	0.235	0.009010	0.002174	−0.001465	0.006086	3.67	0.11	1
s	6931.90	32.331	0.287	0.008474	0.001772	0.004227	0.004963	3.35	0.30	1
s	6933.92	17.911	0.204	0.007263	0.002281	0.015850	0.006387	2.85	0.28	1
s	6935.94	20.715	0.232	0.014173	0.002241	−0.010805	0.006275	3.51	0.15	1
s	6937.94	11.335	0.206	0.013116	0.003629	−0.000257	0.010161	3.01	0.29	1
s	6939.96	10.184	0.208	0.022818	0.004083	0.013412	0.011433	3.93	0.36	1
s	6941.98	16.558	0.237	0.011322	0.002859	0.010201	0.008006	5.16	0.25	1
s	6943.98	10.711	0.210	0.012328	0.003915	0.015598	0.010963	5.32	0.37	1
s	6946.00	9.138	0.219	0.018609	0.004790	−0.020259	0.013413	4.91	0.18	1
s	6948.02	10.677	0.208	0.018585	0.003888	−0.010616	0.010885	4.10	0.21	1
s	6950.03	7.925	0.187	0.011536	0.004718	0.025865	0.013211	4.32	0.48	1
s	6952.04	5.273	0.179	0.027189	0.006795	−0.068867	0.019025	3.33	0.52	1
s	6954.06	4.762	0.198	0.013983	0.008315	−0.049035	0.023283	4.10	0.78	1
s	6956.08	3.013	0.180	−0.001626	0.011923	0.068991	0.033385	4.37	0.38	1
s	6958.08	5.348	0.196	0.032240	0.007326	−0.029615	0.020513	4.25	0.26	1
s	6960.10	6.582	0.221	0.009676	0.006719	0.024511	0.018813	4.53	0.32	1
s	6962.12	4.382	0.173	0.012500	0.007883	−0.016891	0.022071	4.71	0.22	1
s	6964.13	6.037	0.194	0.028999	0.006418	0.016363	0.017969	4.75	0.26	1
s	6966.14	5.599	0.206	0.014081	0.007344	−0.002140	0.020564	4.29	0.57	1
s	6968.16	5.615	0.178	0.030896	0.006327	−0.017234	0.017715	3.98	0.42	1
s	6970.18	3.333	0.158	0.003880	0.009484	−0.000390	0.026555	3.86	0.70	1
s	6972.18	2.892	0.207	0.025563	0.014298	0.063771	0.040035	5.70	0.87	1
r	7362.94	2.405	0.201	1.075722	0.016677	−0.254655	0.046694	0.00	2.00	0
r	7590.54	5.745	0.198	0.520871	0.006895	−0.150159	0.019307	1.73	1.72	1
r	7592.55	4.032	0.183	0.538103	0.009059	−0.118222	0.025366	−0.33	1.03	1
r	7594.57	6.752	0.173	0.517295	0.005116	−0.113936	0.014324	1.25	1.13	1
r	7596.59	2.817	0.209	0.517788	0.014819	−0.112587	0.041494	0.17	0.87	1
r	7598.59	2.969	0.137	0.491063	0.009216	−0.080545	0.025805	−0.35	1.68	1
r	7602.63	5.187	0.206	0.508567	0.007934	−0.110228	0.022217	−0.70	1.65	1
r	7624.79	3.507	0.205	0.481158	0.011673	−0.131880	0.032685	2.65	1.12	1
r	7626.79	6.045	0.224	0.500969	0.007417	−0.118882	0.020768	−0.22	0.68	1
r	7628.81	2.395	0.207	0.472951	0.017265	−0.093891	0.048342	−0.05	1.03	1
r	7636.87	2.525	0.169	0.476766	0.013365	−0.077961	0.037422	2.56	0.83	1
r	7638.87	6.306	0.198	0.457630	0.006286	−0.104438	0.017601	−0.16	0.84	1
r	7640.89	9.846	0.198	0.459508	0.004032	−0.074159	0.011289	0.73	0.70	1
r	7642.91	19.419	0.209	0.464452	0.002149	−0.101649	0.006016	−0.55	0.51	1
r	7644.93	13.219	0.206	0.464897	0.003109	−0.096724	0.008706	0.19	0.51	1
r	7646.93	6.979	0.155	0.468485	0.004433	−0.127446	0.012413	−0.01	0.71	1
r	7648.95	9.721	0.171	0.454110	0.003509	−0.060436	0.009826	0.09	0.60	1
r	7650.97	8.671	0.235	0.452579	0.005421	−0.118197	0.015180	−0.11	0.73	1
r	7652.97	7.221	0.175	0.450337	0.004854	−0.073305	0.013590	0.29	0.63	1
r	7654.99	10.119	0.204	0.450651	0.004029	−0.103736	0.011280	0.23	0.68	1
r	7657.01	9.427	0.167	0.443158	0.003543	−0.090596	0.009921	0.15	0.70	1
r	7659.03	8.284	0.235	0.439732	0.005669	−0.092666	0.015873	−0.28	0.96	1
r	7661.03	4.388	0.201	0.436020	0.009158	−0.096148	0.025642	−0.60	1.05	1
r	7663.05	4.409	0.179	0.449712	0.008101	−0.058255	0.022684	0.52	1.23	1
r	7665.07	6.831	0.218	0.438191	0.006371	−0.093915	0.017839	0.01	0.59	1
r	7667.07	10.870	0.171	0.428966	0.003141	−0.076839	0.008796	−0.04	0.61	1
r	7669.09	8.080	0.241	0.437657	0.005957	−0.102372	0.016681	−1.49	1.04	1
r	7671.11	6.581	0.197	0.415597	0.005990	−0.048441	0.016773	0.28	0.72	1
r	7673.11	9.502	0.163	0.439379	0.003424	−0.108919	0.009587	0.70	0.53	1
r	7675.13	12.663	0.237	0.430218	0.003749	−0.098045	0.010498	0.73	0.45	1
r	7677.15	8.122	0.185	0.424934	0.004566	−0.046912	0.012786	−0.28	0.74	1
r	7679.17	3.581	0.155	0.422214	0.008675	−0.091851	0.024290	−0.75	1.16	1
r	7681.17	2.539	0.171	0.427576	0.013448	0.068849	0.037653	−0.27	1.51	1
r	7683.19	3.697	0.119	0.427772	0.006413	−0.156690	0.017956	−0.11	1.32	1
r	7685.21	4.054	0.172	0.400575	0.008486	0.019645	0.023761	−0.14	1.72	1
r	7687.21	7.765	0.218	0.399758	0.005606	−0.047359	0.015697	0.12	0.73	1
r	7689.23	4.817	0.163	0.401288	0.006782	−0.022707	0.018990	0.38	1.17	1
r	7691.25	4.358	0.168	0.394125	0.007724	−0.035156	0.021628	−0.37	1.09	1
r	7693.25	2.096	0.214	0.422163	0.020384	−0.070841	0.057075	−0.23	1.72	1
r	7695.27	3.862	0.171	0.383193	0.008876	−0.050899	0.024854	0.07	0.89	1
r	7697.29	3.488	0.184	0.424187	0.010553	−0.058105	0.029548	−0.30	1.32	1
r	7699.31	3.991	0.169	0.402095	0.008448	−0.120179	0.023655	0.53	0.76	1
r	7701.31	1.973	0.184	0.373291	0.018698	0.012332	0.052355	−1.18	0.82	1
r	7703.33	4.709	0.176	0.397584	0.007492	−0.105620	0.020977	−1.45	1.86	1
r	7705.35	6.535	0.207	0.384838	0.006334	−0.049391	0.017736	−0.80	1.29	1
r	7707.35	9.090	0.212	0.383340	0.004660	−0.063113	0.013049	−0.72	0.85	1
r	7709.37	7.529	0.188	0.383429	0.004993	−0.083395	0.013981	−0.13	1.32	1
r	7711.39	6.907	0.170	0.372725	0.004911	−0.038938	0.013752	−0.32	0.93	1
r	7713.41	2.894	0.197	0.385841	0.013588	−0.058749	0.038047	2.32	5.36	1
r	7715.41	1.755	0.155	0.370448	0.017716	−0.071974	0.049604	0.29	2.05	1

Table 5.4—Continued

Spot type	Velocity (km s^{-1})	S_ν (mJy)	σ_S (mJy)	x (mas)	σ_x (mas)	y (mas)	σ_y (mas)	a (km s^{-1} yr^{-1})	σ_a (km s^{-1} yr^{-1})	Accel. meas.
r	7719.45	2.597	0.183	0.381596	0.014109	−0.093085	0.039506	0.01	1.52	1
r	7721.45	3.254	0.222	0.398543	0.013637	−0.019367	0.038182	−1.60	1.61	1
r	7723.47	5.666	0.173	0.365010	0.006091	−0.075791	0.017054	0.56	1.37	1
r	7725.49	3.092	0.157	0.399598	0.010187	−0.117785	0.028524	−0.21	2.05	1
r	7727.50	5.086	0.222	0.341512	0.008733	0.024298	0.024452	−0.72	1.80	1
r	7729.51	5.312	0.205	0.361076	0.007708	−0.065725	0.021582	0.79	1.44	1
r	7731.53	8.311	0.227	0.359201	0.005453	−0.051405	0.015267	0.07	1.31	1
r	7733.55	7.784	0.189	0.370060	0.004860	−0.088595	0.013607	−0.29	1.54	1
r	7735.55	9.273	0.194	0.347674	0.004179	−0.061689	0.011700	0.56	1.15	1
r	7737.57	7.964	0.193	0.363805	0.004842	−0.074981	0.013559	−0.25	3.99	1
r	7739.59	3.004	0.221	0.332475	0.014687	−0.082128	0.041124	0.16	1.40	1
r	7751.67	2.534	0.212	0.306113	0.016766	−0.069067	0.046946	3.49	2.34	1
r	7753.69	1.995	0.178	0.339655	0.017813	−0.060381	0.049878	2.02	3.17	1
r	7755.70	2.085	0.180	0.328370	0.017232	−0.040601	0.048248	3.13	4.07	1
r	7757.71	1.608	0.197	0.351276	0.024550	−0.000312	0.068740	0.57	1.67	1
r	7759.73	1.749	0.212	0.363014	0.024225	0.192861	0.067830	−0.30	2.62	1
r	7767.79	2.729	0.198	0.313366	0.014487	−0.003837	0.040564	1.89	1.34	1
r	7769.80	2.826	0.175	0.321913	0.012354	−0.001195	0.034591	1.06	1.36	1
r	7771.81	3.564	0.205	0.329258	0.011507	−0.129414	0.032220	0.50	1.24	1
r	7773.83	3.968	0.208	0.314932	0.010507	−0.010824	0.029421	1.49	0.87	1
r	7775.84	1.844	0.171	0.343236	0.018591	−0.133009	0.052055	0.23	2.22	1

Note. — Measurements for individual maser spots. The “spot type” column 1 indicates which velocity group the maser spot belongs to (“b” for blueshifted, “s” for systemic, “r” for redshifted). The velocities in column 2 are quoted using the optical convention in the barycentric reference frame. Columns 3 and 4 list the maser flux density and RMS from the VLBI channel maps. Columns 5 through 8 list the position measurements and associated uncertainties. Column 9 lists either the measured or modeled acceleration for each maser spot, and column 10 lists the associated uncertainties obtained from the disk modeling. Column 11 indicates whether the acceleration for the maser spot was measured (“1”) or modeled (“0”).

5.3.1 Position fitting for the maser spots

Even at the superb angular resolution afforded by VLBI, individual masers are unresolved point sources. In any single velocity channel of a `CLEAN`ed image, a maser "spot" thus takes on the appearance of the restoring beam. This beam is a two-dimensional (2D) elliptical Gaussian of known dimensions and position angle determined from the *uv* coverage of the observation and the weighting scheme used during the `CLEAN`ing process (see Table 5.2), so every maser spot in the data cube will necessarily share these characteristics. The only unknown parameters for any given maser spot are then the centroid (i.e., the coordinate location in right ascension and declination of the Gaussian) and the amplitude.

We used a least-squares fitting routine (Markwardt 2009) to determine the amplitude and centroid of any maser spot within each velocity channel. The fitted model was a 2D elliptical Gaussian with major axis, minor axis, and position angle fixed to match the restoring beam parameters. Initial guesses for the centroid and amplitude were obtained using the location and value of the brightest pixel in each channel, and converged fits had typical reduced-χ^2 values of $\sim$1.

For an image containing only a 2D elliptical Gaussian and some normally-distributed noise, we define the measured S/N to be the amplitude of the best-fit Gaussian divided by the RMS of the signal-free regions of the image (i.e., the standard deviation of the pixel values far from the peak of the Gaussian). If we fit such an image using the model described above, the uncertainty in a measurement of one of the centroid coordinates (σ_x) will be related to the full width at half maximum (FWHM, Δ_x) of the restoring beam along that direction by (see, e.g., Condon 1997)

$$\sigma_x = \frac{1}{2}\frac{\Delta_x}{(S/N)}. \tag{5.1}$$

Though Equation 5.1 only strictly holds for an image with uncorrelated noise from pixel to pixel, we expect an analogous expression to hold in the case of oversampled data (for which noise will be correlated for pixels within a resolution element of one another). To test this, we fit a suite of 10^5 mock images containing point sources with known positions and S/N. We found that for measured S/N values greater than $\sim$8, the uncertainty in the centroid coordinates are well-described by Equation 5.1 (see Figure 5.3). For our final VLBI map (see Figure 5.2) we thus retain only those maser spots with measured $S/N \geq 8$, to which we assign positional uncertainties using Equation 5.1.

5.3.2 Measuring accelerations from monitoring spectra

We measured accelerations using a time-dependent Gaussian decomposition of the maser spectrum. For each of N Gaussians, the free parameters are the amplitude A, the linewidth σ, the initial central velocity v_0 (referenced to a particular observing epoch), and its linear drift in time a (i.e., the measured acceleration). The model spectrum at each epoch t (where $t = 0$ corresponds to the reference epoch) is then obtained by summing each of the individual Gaussians,

$$S(v,t) = \sum_{n=1}^{N} A_n \exp\left(-\frac{\left(v - (v_{0,n} + a_n t)\right)^2}{2\sigma_n^2}\right). \tag{5.2}$$

Here, the index n indicates the values for the nth Gaussian. The individual amplitudes are allowed to vary from one epoch to the next, while the line widths are held fixed. The fitting was performed using a least-squares routine, choosing random initial guesses for each of the parameters. Nine consecutive monitoring epochs were fit simultaneously, and the fitting procedure was repeated 100 times for each set of nine consecutive spectra, with typical reduced-χ^2 values between 1.2 and 1.7. See "Method 2" from Reid et al. (2013) for further details regarding the fitting process.

We applied this fitting technique separately to each group of maser features. The systemic features were fit within the velocity range 6880–6975 km s^{-1}, the blueshifted features within the range 6120–6405 km s^{-1}, and the redshifted features within the range 7580–7780 km s^{-1}. The best-fit accelerations were binned as a function of v_0 to match the VLBI spectral binning, and an acceleration measurement was assigned to each channel as the χ^2-weighted mean of all fitted accelerations within that channel. The uncertainty in the measurement is similarly assigned to be the weighted standard deviation of the individual fitted accelerations within that channel.

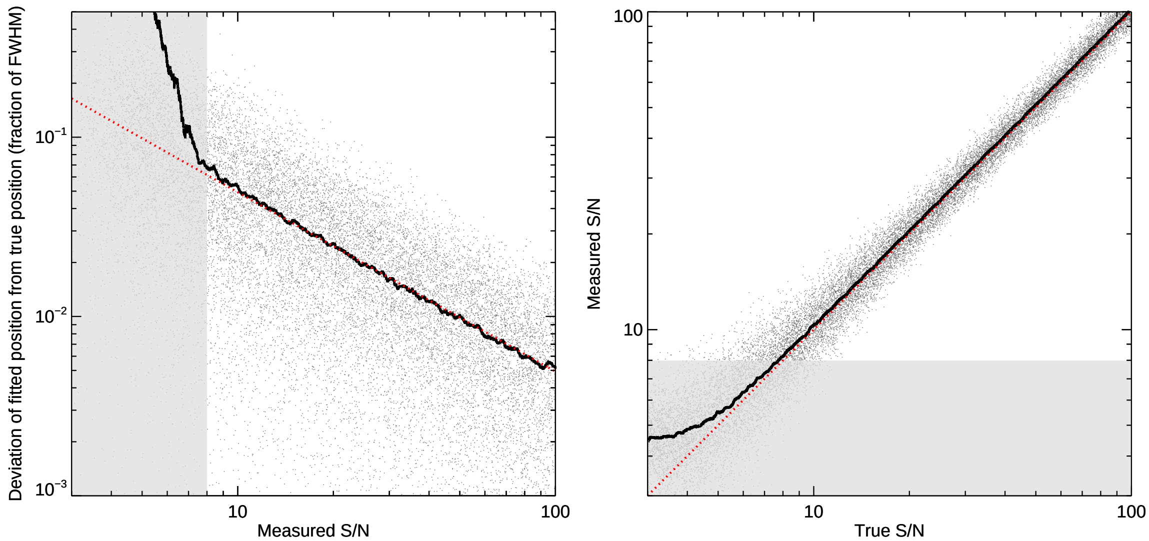

Fig. 5.3.— *Left*: Centroid position measurement offsets versus S/N for a set of 10^5 simulated point-source images. The offsets are plotted as the absolute deviation between the measured position and the true position along a single axis (arbitrarily chosen to be the beam major axis), expressed as a fraction of the beam FWHM along that axis. A running average every 10^3 points is plotted as a solid black curve, and the theoretical noise limit given by Equation 5.1 is plotted as a dotted red curve. We can see that the measurements adhere to the theoretical limit only for measured S/N values that are $\gtrsim$8. *Right*: Measured S/N versus input (i.e., modeled) S/N for the same set of 10^5 simulated images. For a real image we do not have access to the "true" S/N, so we would like to use only those for which the measured S/N matches it well. We can see that our adopted $S/N \geq 8$ threshold, chosen so that the positional uncertainties match those given by Equation 5.1, also allows us to exclude points for which our estimate of the S/N is unreliable. As in the left panel, the solid black curve is a running average (every 10^3 points), and the red dotted curve is the theoretical curve (in this case it is simply the $y = x$ line). The gray shaded region in each plot indicates measurements that we would not have included in our final VLBI map (i.e., they fall below our measured S/N threshold).

Several of the high-velocity maser features detected in the VLBI map, particularly in the blueshifted complex, are too weak in individual monitoring spectra to obtain an acceleration measurement. We would like to include these data points in the disk modeling, as they are still capable of constraining the properties (i.e., location, velocity) of the dynamic center. In past MCP works, we have assigned a nominal acceleration measurement (e.g., 0 ± 2 km s^{-1} yr^{-1}) to such weak maser features; here, we opt for an alternative treatment that incorporates the accelerations into the disk model. See Appendix D.1 for details.

The accelerations and uncertainties are shown in Figure 5.4. We can see that the systemic features share a roughly constant acceleration with a mean of 4.38 km s^{-1} yr^{-1} and an RMS of 0.66 km s^{-1} yr^{-1}, suggesting that they mostly reside in a thin annulus with little spread in orbital radius. The redshifted features show a mean acceleration of 0.06 km s^{-1} yr^{-1} (RMS of 0.65 km s^{-1} yr^{-1}), and the blueshifted features have a mean of -0.35 km s^{-1} yr^{-1} (RMS of 1.11 km s^{-1} yr^{-1}). Both sets of high-velocity features have accelerations that are consistent with zero, as expected for masers located near the midline of the disk.

5.4 Determining the Hubble constant

To measure H_0, we fit a three-dimensional warped disk model to the (x, y, v, a) measurements obtained for each velocity channel of the VLBI map. Appendix D describes this model in detail. Our fitting procedure requires that we explore a moderately high-dimensional ($d = 368$, primarily nuisance parameters) parameter space subject to several strong correlations between model parameters (e.g., between D and $M_{\rm BH}$). Past MCP papers have used a modified Metropolis-Hastings (MH) Markov Chain Monte Carlo (MCMC) algorithm to sample the posterior (see Reid et al. 2013 for a detailed description), but in this work we have instead opted to use a Hamiltonian Monte Carlo (HMC) sampler implemented in the PyMC3[5] code (Salvatier et al. 2016). HMC methods take advantage of the posterior geometry to efficiently explore the "typical set" (i.e., the region containing the bulk of the probability mass) even

[5] `https://github.com/pymc-devs/pymc3`

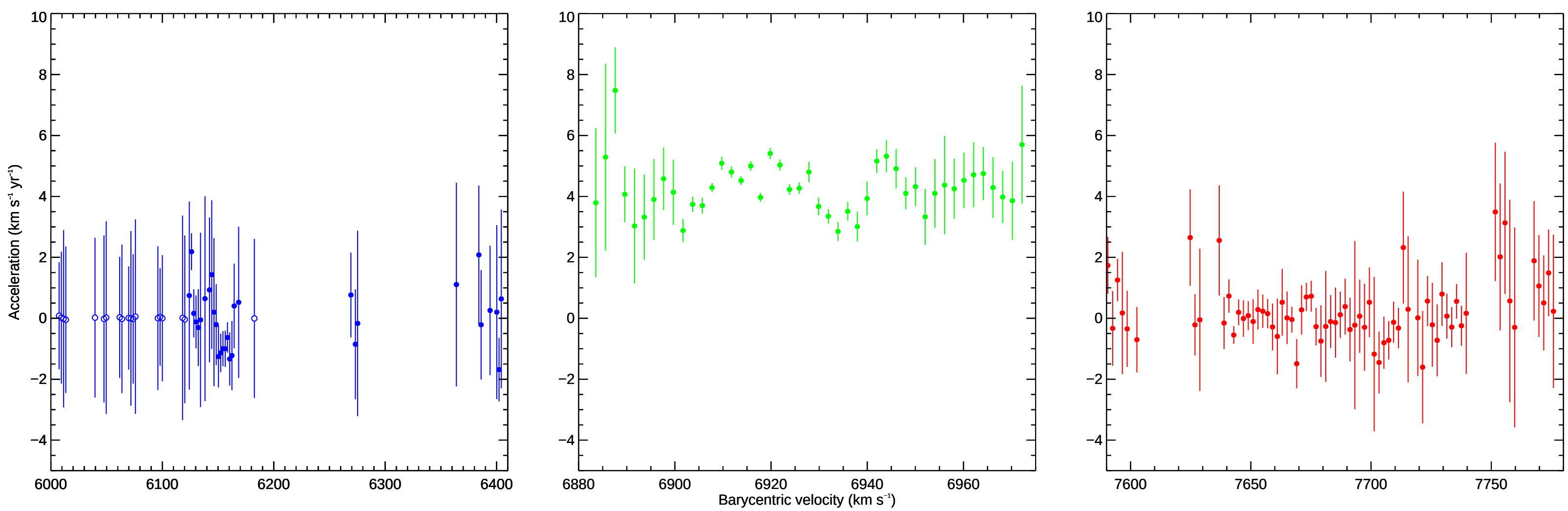

Fig. 5.4.— Acceleration measurements for the three sets of maser features, with data points colored by velocity complex (blue for blueshifted features, green for systemic features, and red for redshifted features). The accelerations have been measured as described in § 5.3.2, with uncertainties assigned according to the model described in Appendix D.1. Unmeasured accelerations (i.e., those that were fit by the model) are plotted using open circles.

in complex and high-dimensional spaces; see Betancourt (2017) for an overview of HMC. Appendix D.1 details our likelihood function and the priors assigned to all parameters.

5.4.1 Results from disk fitting

Table 5.5 lists the best-fit values and associated uncertainties for all modeled disk parameters, and Figure 5.5 shows the full posterior distributions and all two-parameter correlation diagrams for the same set of parameters. Figure 5.6 shows a map of the maser system as seen in the sky plane (left panel) and in the plane of the disk (cenral panel), overplotted on the best-fit disk model. We can see from the map that the maser disk shows only a modest warp in position angle, and from the parameters listed in Table 5.5 we find that the disk is consistent with having zero warping in the inclination direction.

The right panel of Figure 5.6 shows the rotation curve traced out by the masers, which is consistent with the Keplerian behavior expected for gas orbiting in a point-source potential. We constrain the mass of the SMBH in CGCG 074-064 to be $2.36^{+0.20}_{-0.18} \times 10^7$ $M_\odot$, comparable to other megamaser systems which typically have a SMBH mass of $\sim 10^7$ $M_\odot$ (see, e.g., Kuo et al. 2011). The innermost masers reside at orbital radii of $\sim$0.3 mas, corresponding to $\sim$0.12 pc at a distance of 85 Mpc. From the right panel of Figure 5.6 we can see that the maser velocities are well fit by a Keplerian rotation curve even at these inner radii, implying a lower limit to the enclosed mass density of $\sim 3.3 \times 10^9$ $M_\odot$ pc^{-3}.

Our disk modeling does not directly return a posterior distribution for H_0, but instead constrains both the angular diameter distance to the maser disk (D) and the central SMBH redshift (z_0) separately. To determine H_0 from these values, we use an expression adapted from Hogg (1999),

$$H_0 = \frac{c}{D\left(1+z_0\right)} \int_0^{z_0} \frac{dz}{\sqrt{\Omega_m \left(1+z\right)^3 + \left(1-\Omega_m\right)}}, \tag{5.3}$$

which assumes a flat ΛCDM cosmology. We use the cosmological parameter values from Planck Collaboration et al. (2016b), namely $\Omega_m = 0.308 \pm 0.012$. For CGCG 074-064, applying Equation 5.3 results in a $\sim$2.7% reduction in the value of H_0 compared to simply using

$$H_0 = \frac{cz_0}{D}. \tag{5.4}$$

The posterior distribution for H_0 is shown in Figure 5.7. We have assumed a peculiar velocity for CGCG 074-064 of 0 ± 273.2 km s^{-1} (normally distributed in the CMB frame; obtained from a private communication with Michael Hudson, based on the peculiar velocity model from Carrick et al. 2015), which has been incorporated into the quoted uncertainty on H_0. Our best-fit distance of $D = 82.98^{+7.33}_{-6.48}$ Mpc and CMB-frame velocity of $cz_0 = 7174.21^{+1.64}_{-1.82}$ km s^{-1} correspond to a Hubble constant measurement of $H_0 = 83.91^{+7.83}_{-7.45}$ km s^{-1} Mpc^{-1}.

5.4.2 MCMC quality assurance

A useful quantity for assessing MCMC performance, and one that is unique to HMC samplers, is the "energy." In the HMC approach, the model parameters (denoted q) are joined by a set of dual "momentum" parameters (denoted p) that together define a phase space having twice the dimensionality of the model. By choosing these momenta in such a way that phase space volume is conserved under transformations (i.e., p transforms opposite to q under any choice of parameterization), one can construct a Hamiltonian function $\mathcal{H}(q, p)$ that also remains invariant under transformations. By analogy with physical systems the value of the Hamiltonian at any point in phase space is called the "energy" at that point, and the structure of the phase space is such that it can be decomposed into concentric surfaces of constant energy. The HMC strategy then consists of repeating a two-step procedure: (1) selecting parameters (q, p) that define a constant-energy "level set" on which (2) Hamilton's equations are then used to determine the trajectory from which a sample is drawn. In other words, the algorithm first transitions across energy level sets in a probabilistic manner, and it then moves within the chosen level set in a deterministic manner.

By comparing the distribution of energies (the "marginal energy distribution") to

Table 5.5. Disk fitting results for CGCG 074-064

Parameter	Units	Prior	Posterior
D	Mpc	$\mathcal{U}(10, 200)$	$82.98^{+7.33}_{-6.48}$
$M_{\rm BH}$	10^7 M$_\odot$	$\mathcal{U}(0.1, 10.0)$	$2.28^{+0.20}_{-0.18}$
${v_0}^a$	km s^{-1}	$\mathcal{U}(6500, 7500)$	$6910.91^{+1.64}_{-1.82}$
x_0	mas	$\mathcal{U}(-1.0, 1.0)$	0.0013 ± 0.0010
y_0	mas	$\mathcal{U}(-1.0, 1.0)$	0.0056 ± 0.0030
i_0	degree	$\mathcal{U}(70.0, 110.0)$	$82.6^{+3.0}_{-2.4}$
$\frac{di}{dr}$	degree mas^{-1}	$\mathcal{U}(-100.0, 100.0)$	$19.8^{+5.1}_{-7.2}$
Ω_0	degree	$\mathcal{U}(50.0, 150.0)$	97.9 ± 1.3
$\frac{d\Omega}{dr}$	degree mas^{-1}	$\mathcal{U}(-100.0, 100.0)$	$8.2^{+2.5}_{-2.6}$
H_0	km s^{-1} Mpc^{-1}	...	$83.91^{+7.83}_{-7.45}$

Note. — Fitting results for the global parameters describing the maser disk, marginalized over all other parameters. For the posteriors, we quote the 50th percentile value as the "best-fit" and we use the 16th and 84th percentile values to quantify the uncertainty. The function $\mathcal{U}(a, b)$ denotes a flat ("uniform") distribution with a value $1/(b - a)$ within the range $[a, b]$ and zero everywhere else.

[a]We directly model z_0 in the CMB frame (see Appendix D), which we have converted in this table to v_0 (optical convention) in the barycentric frame. The conversion is $v_0 = cz_0 - 263.3$ km s^{-1}.

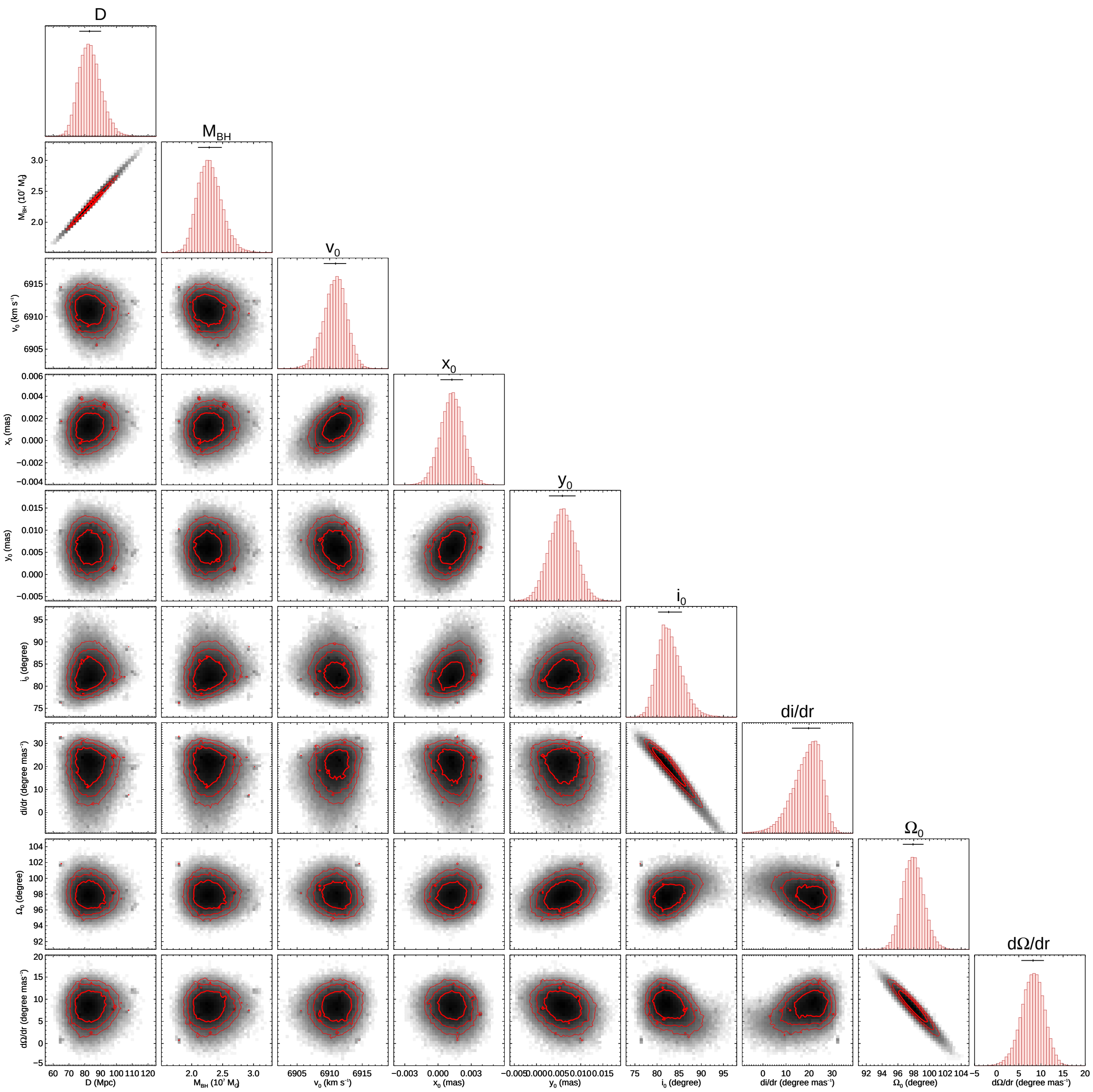

Fig. 5.5.— Posterior probability distributions (diagonal) and pairwise parameter correlations (lower triangle) for the warped disk model fit to the maser system in CGCG 074-064. The greyscale in the correlation plots indicates the 2D histogram intensity, with 1σ, 2σ, and 3σ contours overplotted in red. The 1D histograms along the diagonal show the fully-marginalized posterior distributions for each parameter; the black horizontal bars above each histogram show the range from 16th to 84th percentile for each posterior distribution, with the 50th percentile point marked.

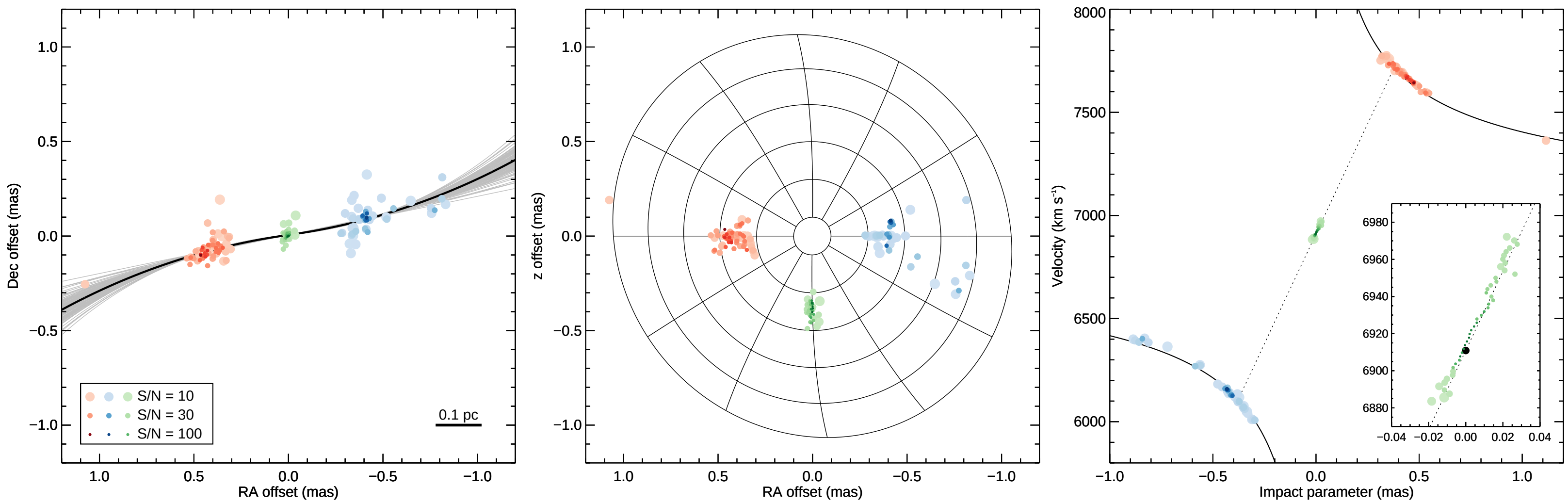

Fig. 5.6.— Map of the maser distribution in CGCG 074-064 atop our best-fit warped disk model as seen in the sky plane (left) and face-on (center), and the corresponding rotation curve (right). The data points are colored by velocity group, with the red points corresponding to redshifted features, the blue points to blueshifted features, and the green points to systemic features. The colors are darker for higher S/N, and the symbol sizes are proportional to $(S/N)^{-1/2}$ (so that data points with larger uncertainties appear larger; see the legend in the left panel). In all panels, the solid black lines trace the best-fit disk model, while in the left panel the light gray lines show the fits from 100 different samplings of the posterior distribution. In the right panel the dashed black line shows the average annulus for the systemic features (i.e., if the systemic features all originate from a thin ring at a single orbital radius, we would expect them to fall on or near this line), and the inset plot shows a zoom-in on the systemic features with the position of the SMBH marked as a black point. The "impact parameter" is defined to be $r\sin(\phi)$ for every maser spot.

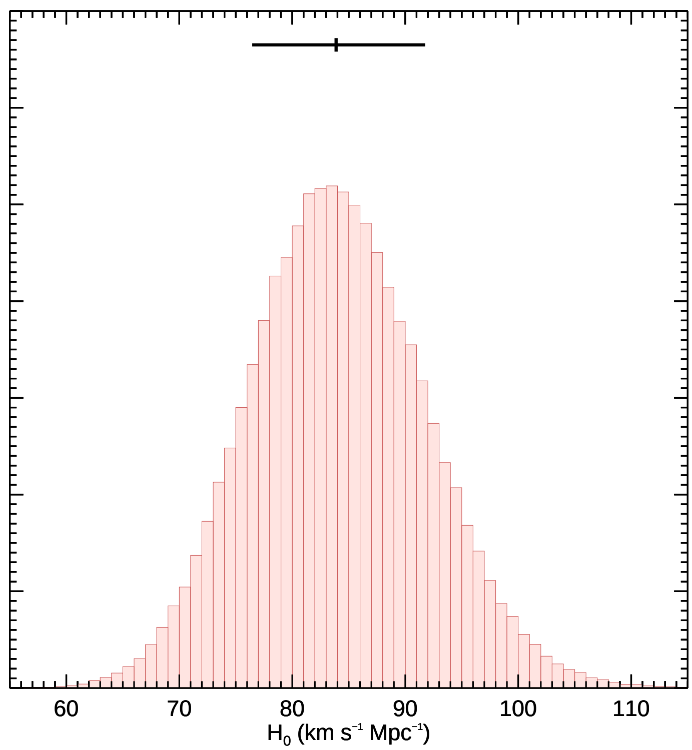

Fig. 5.7.— Marginalized posterior distribution for H_0, derived from the modeled parameters D and z_0 using Equation 5.3. The black horizontal bar marks the range from 16th to 84th percentile, with the 50th percentile point indicated. We find a value of $H_0 = 83.91^{+7.83}_{-7.45}$ km s^{-1} Mpc^{-1}.

the distribution of energy transitions (the "energy transition distribution"), we can assess how efficiently the sampler is exploring the parameter space. Ideally, these two distributions will have comparable widths. If the marginal energy distribution is much broader than the energy transition distribution then the sampler must take many steps to walk across the relevant range of level sets, and the parameter space exploration will proceed inefficiently. The energy transition distribution is determined by the momentum sampling distribution at a given q, which we can optimize using an initial set of "tuning" trials (see Betancourt 2017 and references therein for a description of the optimization procedure). For our model, we found that a set of $\sim 10^4$ tuning trials was sufficient to yield a marginal energy distribution that is well-matched to the energy transition distribution (see right panel of Figure 5.8).

With some confidence that the parameter space is being explored efficiently, our primary convergence metric is the autocorrelation function (ACF), ρ. For an MCMC chain of length N, ρ is given by

$$\rho(\ell) = \frac{\sum_{i}^{N-\ell} (x_i - \bar{x})(x_{i+\ell} - \bar{x})}{\sqrt{\sum_{i}^{N-\ell} (x_i - \bar{x})^2 (x_{i+\ell} - \bar{x})^2}}. \tag{5.5}$$

Here, ℓ is the lag, x_i is the i^{th} sample of parameter x, and $\bar{x}$ is the mean value of x over the chain. The "autocorrelation time" τ is the lag value at which the ACF first drops below zero, which gives an indication of how far apart two samples in the chain must be such that they are no longer correlated with one another. Qualitatively, we would like $N \gg \tau$ for all parameters to ensure robust convergence.

Evaluating τ as simply the first zero-crossing of the ACF is likely to underestimate the true correlation length of the chain, because the finite variance of the ACF can cause one lag value to dip below zero long before the running mean would do so (see, e.g., bottom left panel of Figure 5.8). We thus smooth the ACF using a boxcar width of 5×10^3 trials prior to evaluating τ, though we find that the precise value of τ is not very sensitive to the choice of smoothing function (τ changes by $\sim 10\%$ when the boxcar width is varied by a factor of 2). More quantitatively precise methods are possible, such as locating the "knee" of the MCMC chain's power spectrum (e.g., Dunkley et al. 2005), but we only require an order of magnitude estimate. We find autocorrelation times of $\tau < 5 \times 10^4$ for all parameters, and we thus truncate the MCMC sampling at $N = 5 \times 10^5$. The posterior distributions (see Figures 5.5 and 5.7) are then generated using the final 2.5×10^5 samples.

While the behaviors of the ACF and energy distributions are promising, we note that the results of our HMC disk fitting have yet to be corroborated by the original MH code used by the MCP for all previous measurements. Efforts to fit the CGCG 074-064 data with the MH code have so far resulted in similar parameter estimates to those produced by the HMC code, but the MH code produces substantially ($\gtrsim$50%) wider posterior distributions. These differences may be caused by a lack of convergence in one or both codes, or by some undiagnosed issues with one or both of the models underpinning the codes. The results presented here should thus be taken as preliminary.

5.5 Discussion

5.5.1 VLBI continuum emission

The continuum source detected in our VLBI data (see Figure 5.2) shows a perpendicular offset from the maser disk, reminiscent of the continuum structure seen towards the disk in NGC 4258 (Herrnstein et al. 1997) and suggesting a jet origin. The measured disk inclination angle (see Table 5.5) indicates that it is tilted by $\sim$7° from being perfectly edge-on, such that we are "looking up" onto the disk. With a peak surface brightness of 31.2 μJy beam^{-1}, the brightness temperature of the continuum source is at least 6.5×10^4 K.

This measured disk orientation suggests that relativistic beaming cannot be the source of the apparent one-sidedness of the (presumably intrinsically symmetric) jet, because the observed northern component of the jet is tilted away from us. An alternative explanation for the lack of an observed southern jet component could be that our line of sight to that component passes through the maser disk, while emission

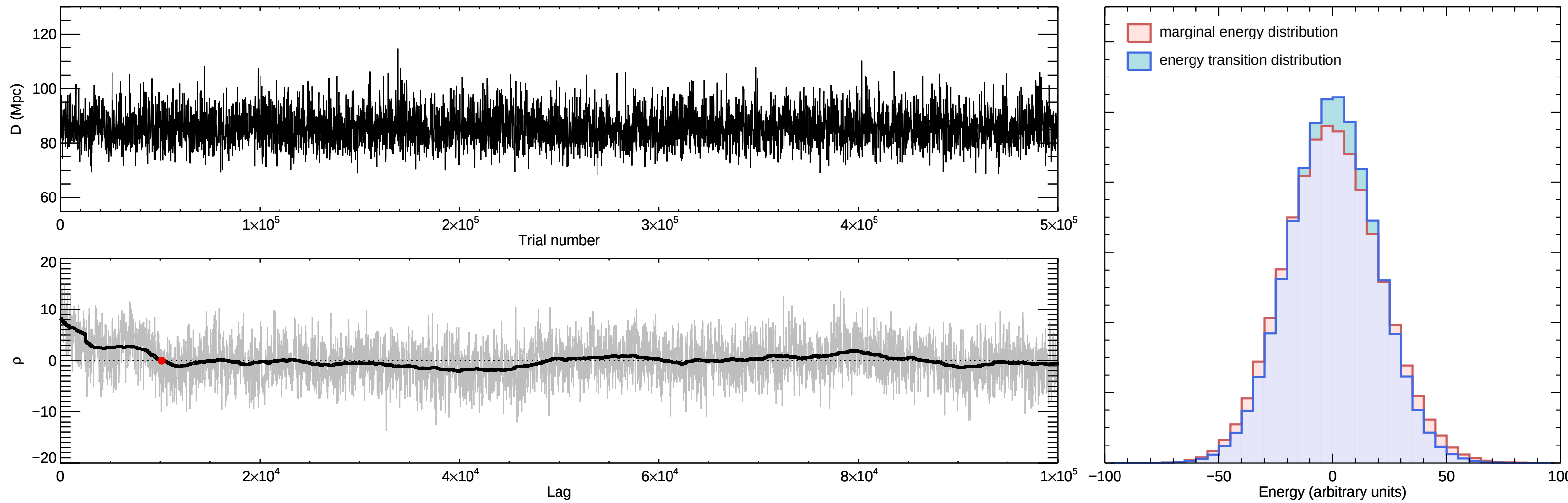

Fig. 5.8.— Example quality checks for the MCMC chain. *Top left*: Trace plot for the model parameter D, thinned by a factor of 100 for visualization. *Bottom left*: Autocorrelation function (ρ) for the model parameter D is plotted in gray, and a running average for every 5×10^3 points is overplotted in black. The first zero crossing of the smoothed ACF is marked with a red point, and occurs at a lag of 10150 for this parameter. *Right*: Comparison of the marginal energy distribution (red) and the energy transition distribution (blue) for all MCMC samples, where the marginal energy distribution has had the mean subtracted out so that it is centered on zero. We can see that the widths of these two distributions are very well-matched, indicating that the sampler is efficiently exploring parameter space.

from the northern jet component reaches us unimpeded. X-ray irradiation from the central AGN may produce layers of hot ($\sim 10^4$ K) ionized material above and below the molecular disk, providing an absorption opportunity for emission that must pass through the disk along the line of sight (Neufeld & Maloney 1995). Herrnstein et al. (1996a) estimate the free-free optical depth in this layer to be ∼2–3 at a frequency of 22 GHz for the disk in NGC 4258; a similar level of absorption would be sufficient to explain the asymmetric flux densities of the two jet components in CGCG 074-064.

If the nuclear continuum provides the seed photons for the systemic maser complex, as suggested by Miyoshi et al. (1995) for NGC 4258, then we can estimate the maser gain from the observed strength of the systemic features. In the absence of free-free attenuation, a ~ 30 μJy continuum would require an amplification of 5×10^3 to power the ∼150 mJy systemic masers (corresponding to an optical depth of $\tau \approx -8.5$).

5.5.2 Variability of the maser features

In both our GBT and VLA monitoring observations of CGCG 074-064, we found that the strongest systemic features (i.e., those that could be identified in individual scans) often show substantial (∼50%) variability on timescales of ∼tens of minutes. In one case – that of the 6915 km s^{-1} line during the 2016 October GBT observation – the flux density increased by a factor of ∼3 over the course of half an hour from 100 mJy to 300 mJy; if intrinsic to the maser system, this behavior would correspond to an increase of ~ 60 $L_{\odot}$ in isotropic luminosity across a region no larger than ∼3 AU in size (as determined by light-travel time). The magnitude of this variability, and the fact that it is uncorrelated between different maser features, indicates that observational effects (e.g., fluctuations in antenna gain or atmospheric opacity) are unlikely to be the cause.

Such rapid variability has been seen before in at least three other H_2O megamaser systems – Circinus (Greenhill et al. 1997a), NGC 3079 (Vlemmings et al. 2007), and ESO 558-G009 (Pesce et al. 2015) – and in the IC 10 kilomaser system (Argon et al. 1994). There are several possible explanations for this variability, and they all fall into three general categories:

1. Variability in a background source that gets amplified by the maser. The strongest such variability occurs when the maser is unsaturated, and the background source could be either the compact radio continuum from the nucleus (e.g., Haschick et al. 1990) or another maser cloud having nearly the same line-of-sight velocity (e.g., Deguchi & Watson 1989). In the former case the observed maser variability is inherited from the properties of the nuclear source, and we would expect different systemic features to show correlated fluctuations. In the case of two aligned maser clouds, the variability timescale is determined by their mutual transverse velocity and physical sizes. For the $\sim$hundreds of km s^{-1} velocities typical of gas orbiting at tenths of a parsec from a $\sim 10^7$ M$_\odot$ SMBH, an implausibly small $\sim$100 R$_\oplus$ masing region would be required to explain variability on hourly timescales.

2. Variability that is intrinsic to the maser. Strong variability implies changes in the maser opacity that are $\gtrsim$1, which corresponds to changes in the masing gas that cover a size scale comparable to the maser gain length, ℓ. Over the range of expected physical conditions in these systems, $\ell \gg 1$ AU (Greenhill et al. 1997a). Conservative estimates of the gain length just barely allow for some change propagating at c to traverse ℓ within the variability timescale. Shock-pumped masers (e.g., Elitzur et al. 1989) cannot meet this requirement, and radiatively-pumped masers would require the pumping source to be both compact (i.e., with size $\lesssim \ell$) and located effectively within the masing region itself. While the 22 GHz maser transition in AGN accretion disks is primarily thought to be pumped by collisional processes (see, e.g., Lo 2005), it is also known to have a radiative pumping branch (Gray et al. 2016). We thus cannot easily rule out radiative pumping by, e.g., a local variable source as a potential driver of the observed rapid variability.

3. Variability caused by foreground effects modulating an otherwise roughly constant maser flux. The two most well-studied such effects are gravitational lensing-induced diffraction (GLID; see Deguchi & Watson 1986) by an intervening foreground lens and interstellar scintillation (ISS; see Narayan 1992)

caused by a foreground Galactic scattering screen. GLID can produce the observed variability timescales and amplitudes, but it places severe constraints on the size of the masing region. For an extremely conservative lower limit on the maser size of 1 AU (corresponding to the typical size of Galactic masers), the lens must have a mass smaller than 10^{-2} $M_\odot$ and be located at a distance of several Mpc. We know from microlensing experiments (e.g., Tisserand et al. 2007) that the density of such objects is much less than the matter density in the Universe, meaning that for $M_{\rm lens} < 10^{-2}$ $M_\odot$ the alignment probability for the Earth-lens-source system (see Eq. 57 of Deguchi & Watson 1986) should be small. ISS has thus been the preferred explanation for the rapid variability seen in other megamaser sources.

Though it seems that ISS provides the most plausible explanation for the strong variability seen in CGCG 074-064, the number of megamaser systems that are now known to display apparently ISS-induced variability, and the strength of the variability in these systems ($\sim$tens of percent or greater), is surprising. Furthermore, it is not clear that ISS can satisfactorily account for the observed properties of this variability across all of these systems.

The MASIV VLA survey (Lovell et al. 2003) found that only a tiny fraction ($\lesssim$1%) of compact extragalactic radio continuum sources show strong ($\gtrsim$10%) and rapid (timescales of $\sim$several hours) ISS-induced variability at an observing frequency of 5 GHz. They also found the expected correlation between variability amplitude and line-of-sight emission measure from the Galactic ionized medium, which essentially amounts to greater variability being seen at lower absolute Galactic latitudes (Lovell et al. 2008). The presence of such variability in $\gtrsim$10% of all disk megamaser systems, and the lack of an obvious correlation with Galactic latitude[6], is then surprising. The substantially higher observing frequency of $\sim$22 GHz for the maser systems compared to the targets of the MASIV survey only compounds the problem.

For ISS, the characteristic variability timescale is set by the transverse velocity of

[6] Though the Circinus galaxy and ESO 558-G009 both lie within 10° of the Galactic plane (Circinus has a Galactic latitude of $b \approx -4°$ and ESO 558-G009 has $b \approx -7°$), neither NGC 3079 (with $b \approx 48°$) nor CGCG 074-064 (with $b \approx 65°$) follow this trend.

the scattering screen and the size of either the "scintle" (if the phase-coherent region of the scattering medium has a larger angular size than the source) or the source (if the source is larger in angular size than the scintle). In the weak scattering limit, the scintle size goes as $\nu^{-1/2}$, so all else being equal we would in general expect only a factor of $\sim$2 shorter variability timescales at 22 GHz than what is seen at 5 GHz if the scintle sets the relevant size scale. If instead the angular size of the source sets the relevant timescale then the magnitude of the variability would be decreased by a dilution factor roughly equal to the ratio of the source size to the scintle size, an expectation that is inconsistent with the observed (strong) variability. Furthermore, the timescales for all scintillating maser galaxies are of the same order of magnitude while their distances differ by more a factor of $\sim$20; if the maser spot size were setting the variability timescale, then we would expect the timescale to decrease inversely with the distance to the maser galaxy.

We have highlighted a couple of the outstanding issues with ISS as an explanation for the strong and rapid variability observed in a number of megamaser systems, but a more thorough investigation is warranted and will be left for future work.

Chapter 6

Summary

In this thesis I have synthesized a number of projects related to H_2O megamasers in AGN accretion disks. My research on this front has leveraged the unique geometry and simple dynamics of these disk megamaser systems to provide powerful astrophysical tools for studying AGN, SMBHs, and cosmology.

Chapter 2 addresses several new scientific questions that can be explored using the MCP's extensive monitoring campaign of 22 GHz disk megamaser spectra with the GBT. The spectra in this dataset are unique in their ability to probe the accretion disks of nearby AGN at sub-parsec scales, and the dataset itself is unmatched in the sensitivity and time coverage for each target. In brief:

1. We present a comprehensive collection of Keplerian disk megamaser spectra. We also present dynamic spectra for the most heavily monitored of these sources.

2. We find that the redshifted high-velocity maser features are brighter, on average, than the blueshifted features for our sample of 32 megamaser disks. This asymmetry is predicted by the spiral shock model of MM98. The parent population, however, is statistically consistent with having no asymmetry.

3. We also test the MM98 prediction that the high-velocity features should exhibit nonzero line-of-sight velocity drifts. We find no systematic drifts. Furthermore, the statistically significant detection of both positive and negative velocity drifts within the same set of features (as we have for several sources) is inconsistent with the MM98 model's predictions.

4. We argue that the intra-day variability observed in ESO 558-G009 is most likely caused by ISS, and we derive parameters of the scattering screen under different assumptions about the scattering regime. Though the measurements are currently sparse, we find that they are most consistent with a relatively nearby ($\sim$70 pc) scattering screen.

5. We test six maser systems for a radially-propagating change in maser activity, which could be the result of variable output from the central engine. No such signal is detected in any of the galaxies.

6. We measure upper limits on the toroidal and radial magnetic field strengths in the accretion disks of 7 galaxies using the Zeeman effect, and we find that the magnetic fields must be less than several hundred mG in each case. This is beginning to probe the regime where the magnetic pressure becomes comparable to the gas pressure in the disk.

Chapter 3 presents 321 GHz ALMA observations of NGC 5793, NGC 1068, NGC 1386, NGC 4945, and the Circinus galaxy. All galaxies are detected in continuum emission, and Circinus and NGC 4945 also display H_2O megamaser emission. For NGC 4945 these data represent the first detection of submillimeter megamaser activity, while for Circinus we confirm the results of Hagiwara et al. (2013), with an updated calibration. In both cases the 321 GHz spectra appear structurally comparable to those of the 22 GHz masers.

The continuum emission in NGC 5793 and NGC 4945 is well-resolved and spatially extended along the optical major axes of these galaxies, which are both edge-on spirals. This continuum is likely dominated by thermal emission from dust grains in the disk, and we use the observed fluxes to derive approximate ISM masses. For the other three galaxies, the continuum emission is centrally-concentrated and thus likely contains a substantial non-thermal component from the AGN.

Though the 22 GHz maser emission in Circinus is associated with both the accretion disk and a molecular outflow, it is unclear whether the 321 GHz emission traces both environments or just the disk. A comparison of the spectral structure between the two transitions implies that the 321 GHz masers likely trace the accretion disk, in which case their increased velocity span would indicate that they probe smaller radial separations from the central SMBH than the mapped 22 GHz masers do. This prediction can be confirmed by future ALMA observations of Circinus, which should seek to obtain a map of the maser features at the highest possible angular resolution.

Chapter 4 introduces the idea of using H_2O megamasers in AGN accretion disks as dynamical tracers to measure SMBH peculiar motion, and we have applied this approach to a sample of galaxies for which VLBI data and maser rotation curves exist in the literature. The galaxy recession velocities are measured using a combination of spatially resolved HI disk modeling, HI integrated intensity profile fitting, and optical spectral line and continuum fitting.

For two out of ten galaxies in our sample – J0437+2456 and NGC 6264 – we find a statistically significant (>3σ) difference between the SMBH velocity and its host galaxy's recession velocity. In NGC 6264 the velocity of the stellar system matches that of the SMBH, and it seems likely that the apparent velocity offset between the optical emission lines and the SMBH arises from blueshifted ionized gas in the host galaxy, perhaps caused by AGN-driven shocks. For J0437+2456, the velocity of the stellar system matches that of the optical emission lines, and both show a systematic redshift with respect to the SMBH velocity. Furthermore, measurements of the galactic position from both PanSTARRS and AllWISE show statistically significant offsets (by roughly ∼0.1 arcseconds in declination) from the SMBH position, which match what we would expect given the magnitude of the measured velocity offset. J0437+2456 is thus our most promising candidate for a true SMBH peculiar motion system. We stress, however, that systematic effects arising from SDSS fiber misplacement can plausibly account for a large fraction of the observed velocity signal, and that additional observations will be necessary to corroborate the reality of the detected velocity offset.

In Chapter 5, we have presented a geometric distance measurement to the galaxy CGCG 074-064 of $82.98^{+7.33}_{-6.48}$ Mpc, made using the megamaser technique as part of the MCP. The strength (typical flux density >200 mJy) and orderly accelerations (nearly constant at 4.4 km s^{-1} yr^{-1} across the entire systemic velocity complex) of the systemic features in this system have enabled a high-precision distance measurement with uncertainties of only ∼9%. Our 3D warped disk modeling constrains both the distance and recession velocity for CGCG 074-064, which we combine to determine a value for the Hubble constant of $H_0 = 83.91^{+7.83}_{-7.45}$ km s^{-1} Mpc^{-1}. These values are preliminary, and we are in the process of validating them using an independent disk-fitting code.

Our VLBI observations of the maser system in CGCG 074-064 have also revealed a weak (∼30 μJy beam^{-1}), marginally-resolved continuum source that appears to originate from a nuclear jet. The one-sided nature of this jet emission and its strength relative to the maser emission are both reminiscent of what has been previously seen in NGC 4258. In addition, our spectral monitoring observations have revealed that the systemic maser features in CGCG 074-064 are highly variable, with flux densities changing by as much as a factor of 3 on timescales of tens of minutes. Interstellar scintillation appears to be the most plausible explanation for this variability, though we note several unresolved issues with this explanation that will need to be addressed in future work.

6.1 Open questions

Below I have listed (in no particular order) a few of the questions that I still have about disk megamaser systems, along with a brief synopsis of my current thoughts about each of them. To the best of my knowledge, these questions are all currently unresolved.

1. Why do the systemic features in many disk maser systems (e.g., NGC 4258, NGC 5765b, CGCG 074-064) seem to be so radially concentrated while the high-velocity features are spread out in radius? There is strong evidence that the systemic features in these systems reside within a single thin annulus (i.e., they are strongly concentrated around one orbital radius). Evidence for systemic features residing near a single radius include the linear gradient in position-velocity diagrams[1] and roughly constant line-of-sight accelerations. For NGC 4258 and CGCG 074-064 the systemic features have a radial concentration of $\Delta R/R \lesssim 0.1$, while for NGC 5765b they have $\Delta R/R \approx 0.17$; in all three cases the high-velocity features show $\Delta R/R \approx 1$. This arrangement is doubly surprising when considering that dynamical constraints alone should provide velocity coherence along a longer path for the systemic features than for the high-velocity features (see § 1.3.2 and Figure 1.4). Herrnstein et al. (2005) invoke a quirk of geometry to explain the situation seen in NGC 4258, whereby

[1] In principle, a linear gradient in position-velocity space could also be caused by solid body rotation, but that would imply a large disk mass inconsistent with the rotation curve traced by the high-velocity features.

the systemic features lie on the bottom of a "bowl" where the line of sight is tangent to the near side of the warped disk (see Fig. 11 in their paper). While this model does a good job of explaining the observed behavior of the systemic positions and velocities (and even seems to explain the location of a flaring feature), it's unclear whether it can generalize to other maser disks with substantially less pronounced warping. An alternative explanation might be the presence of radial structure in the disks (e.g., the spiral shocks from the Maoz & McKee 1998 model), which could naturally confine the systemic features by limiting the radial range of the inverted water population. Such a spiral structure model could also naturally account for the observed gradient in line-of-sight accelerations with velocity seen in the systemic masers in the NGC 4258 system (Humphreys et al. 2008), which cannot be explained by the bowl model alone.

2. Relatedly, how important is spiral structure (or radial substructure in general) in disk maser systems? Humphreys et al. (2008) measure an acceleration gradient of $\sim$0.01 yr^{-1} across the systemic feature complex in NGC 4258. The authors show that this magnitude of acceleration can be explained if the masers are passing through a spiral arm containing $\sim$15% of the total available disk mass. Alternatively, if the spiral structure is itself hosting the masing gas, then the acceleration gradient could correspond to the pitch angle of the spiral. The sense of the acceleration gradient is consistent with a trailing spiral arm; i.e., more redshifted systemic features show larger accelerations (and thus should reside at smaller orbital radii), which matches the expected behavior if the masers reside within a trailing spiral structure. As I previously mentioned, something like spiral structure would also naturally explain the radial confinement of systemic features in a number of disk systems. Furthermore, the quasi-periodic spacing of high-velocity maser features seen in NGC 4258 (Argon et al. 2007), and in general the apparent clumping of high-velocity features in a number of other disk systems (see, e.g., Reid et al. 2013, Gao et al. 2016), are also suggestive of there being some sort of radial structure in these disks. A quantitative assessment of

just how periodic and/or clumped the high-velocity features are in all mapped disk systems is certainly warranted.

3. Are the systemic features amplifying a background continuum source (e.g., from the AGN), and/or is such a source required for us to observe systemic maser emission? If so, why don't the high-velocity features seem to share this need? Claims that the systemic features in NGC 4258 are amplifying the nuclear continuum emission date at least as far back as Watson & Wallin (1994), and this idea has persisted in the literature (see, e.g., Miyoshi et al. 1995, Herrnstein et al. 1997, Maoz & McKee 1998). In NGC 4258 the systemic features are an order of magnitude stronger than the strongest high-velocity features, so the notion that they might be amplifying background continuum is at least initially plausible. Further scrutiny raises the potentially troubling question of why the systemic features – which have access to longer dynamics-limited gain paths (see § 1.3.2) and background continuum to amplify – are *only* an order of magnitude stronger than the disadvantaged high-velocity features, though perhaps this could be chalked up to coincidence. Yet we now know of a large number of maser disk systems for which the high-velocity emission is comparable to or stronger than the systemic emission (see Figure 2.1), and a quick tally from Table 2.1 indicates that only ∼one-third of the known disk masers have stronger systemic flux than either redshifted or blueshifted flux (i.e., consistent with a random group being the strongest). Furthermore, several of the mapped disk systems show no compact 22 GHz continuum emission even with deep VLBI integrations (e.g., Reid et al. 2009, Gao et al. 2016).

4. Why don't we see any backside masers? To date, there have been no detections in any system of systemic maser features with the negative line-of-sight accelerations that would indicate that they reside on the far side ("backside") of the maser disk. The standard explanation for this (lack of) observation seems to be that the systemic features are amplifying continuum emission, and thus that any backside systemic masers would be far too weak to detect compared to the frontside systemic masers. The lack of backside masers can thus be considered

a point in favor of the notion that systemic features do require background continuum emission to amplify, because dynamical considerations alone would permit them. Another potential reason why we don't see back-side masers is because there is a region (at smaller orbital radii than the masing gas) where the water population is not inverted, or where the material is otherwise opaque, and which can thus absorb any incoming maser emission (see, e.g., Fig. 1 of Watson & Wallin 1994).

5. How thick is the maser disk? And do the masers reside in the disk midplane? Argon et al. (2007) isoolated the strongest systemic features within a portion of the NGC 4258 disk that is viewed edge-on, and they observed that the vertical displacements (i.e. perpendicular to the disk) of these features displayed an approximately Gaussian distribution with σ of $\sim$5 μas (corresponding to $\sim$40 AU at the 7.6 Mpc distance to NGC 4258). The authors interpreted this spread to be the scale height of the disk, which would imply an aspect ratio of $\sim 10^{-3}$; for a disk in hydrostatic equilibrium, this aspect ratio corresponds to the ratio of the sound speed to the orbital velocity at that radius (Pringle 1981). The derived sound speed of $\sim$1.5 km s^{-1} matches well with the observed maser linewidths, and the corresponding gas temperature of $\sim$600 K is within the range known to be conducive to maser activity at 22 GHz (see, e.g., Gray et al. 2016). Yet measuring such tiny positional offsets necessarily required centroiding at a level roughly 10^3 times smaller than the VLBI beam, and the typical assumptions for how centroiding precision scales with signal-to-noise may no longer hold true at that point[2]. Even if calibration effects remain negligible, and even if the intrinsic sizes of the maser clouds are small enough to avoid violating the point-source assumption, some of the observed scatter may still be caused by unmodeled curvature in the maser disk rather than corresponding to a true

[2]During a conversation with Jim Moran, I was informed that plans are in place to observe NGC 4258 using the RadioAstron satellite in conjunction with ground-based antennas. The anticipated angular resolution is $\sim$10 μas, and the baseline will be oriented perpendicular to the maser disk in an effort to measure its thickness. These observations will hopefully place comparable (or better) limits on the scale height than the extant VLBI measurements, and they will avoid much of the ambiguity currently associated with the centroiding procedure.

scale height. The measured "scale height" value should thus be taken as an upper limit on the true scale height, which then begins to appear problematically small if the masers are in fact tracing the midplane disk material (as predicted by, e.g., Neufeld & Maloney 1995). A possible workaround is that the masers don't actually reside in the disk midplane, but rather occupy a very thin layer (perhaps near the disk surface) whose vertical structure is not indicative of the underlying disk scale height.

6. Which of the hyperfine transitions are contributing to the masing at 22 GHz? We know that the 22 GHz transition actually consists of six hyperfine components (often referred to as "magnetic substates" and corresponding to total angular momentum quantum number changes of $F = 7 - 6$, $6 - 5$, $5 - 4$, $6 - 6$, $5 - 5$, and $5 - 6$) spread across a frequency range corresponding to $\sim$6 km s^{-1} in equivalent velocity (see, e.g., Kukolich 1969). In thermal equilibrium, the $F = 7 - 6$ transition is the strongest and the weakest (by a factor of $\sim 10^3$) is the $F = 5 - 6$ transition. We thus expect that an unsaturated maser should have an intensity dominated by the $F = 7 - 6$ transition, and that as saturation increases the intensities of all six hyperfine transitions should approach equality (Goldreich et al. 1973). However, the narrow frequency separation of the hyperfine transitions (i.e., comparable to or smaller than typical maser linewidths) and the small intrinsic sizes of masing gas clouds (i.e., typically much smaller than a VLBI beam) has made it difficult to test these predictions, and observational efforts to do so have had mixed results. By fitting multiple Gaussian components to seemingly isolated maser lines in single-dish spectra, Turner et al. (1970) found that the $F = 6 - 5$ transition seemed to be the strongest in the Galactic water masers from W3(OH), W3, and VY CMa. Moran et al. (1973) found that the $F = 7 - 6$ and $F = 6 - 5$ transitions were strongest in VLBI observations of spatially coincident masers in W49 and Orion A, respectively. Walker (1984) performed a statistical test on the water masers in W49, and found that the velocity spacings between spatially coincident (at VLBI resolution) maser spots were consistent with all six hyperfine transitions

being equally likely. Attempts to assess different hyperfine contributions using line profile analysis alone are even more fraught (e.g., Nedoluha & Watson 1991), as line-of-sight velocity gradients in the masing medium can mimic the presence of multiple components (Vlemmings & van Langevelde 2005). I find the current ignorance to be rather concerning, as at best we seem to have a roughly ± 3 km s^{-1} uncertainty in the absolute velocity of any observed maser line. At worst, we have a ± 6 km s^{-1} uncertainty in the *relative* velocities between any two maser lines in a single spectrum; to my knowledge, this source of uncertainty is not adequately being accounted for in any current dynamical models of H_2O maser systems.

7. Is the masing medium a clumpy one? Neufeld et al. (1994) recognized fairly early on that accretion disk material being irradiated by X-rays could develop a two-phase structure, with a hot ($T \approx 5000$–8000 K) atomic component comprising the bulk of the volume coexisting with cooler ($T \approx 600$–2500 K) molecular zones. For these two phases to be in pressure equilibrium, the molecular regions must be much denser than the atomic regions, which implies a clumpy medium[3]. If the sizes of these masing clumps are small compared to the dynamics-limited gain paths (see § 1.3.2), then the maser gain within a particular clump will be material-limited instead. In this case the observed maser emission likely arises where two or more velocity-coherent clumps align along the line of sight (see, e.g., Kartje et al. 1999), and the general triple-peaked spectral structure then manifests because it represents where such alignments are most likely to occur. Transverse motions of these clumps could provide a natural explanation for the rapid variability seen in many disk maser systems (see § 2.5), as the act of moving into and out of alignment will result in large gain changes on timescales determined by the cloud sizes and relative transverse velocities. For a cloud size of $\sim$10 AU and a transverse velocity of $\sim$100 km s^{-1}, the expected variability timescale of $\sim$6 months is of the right order to match the observations.

[3]Though Collison & Watson (1995) presented the important addition of cool dust to the Neufeld et al. (1994) model of the masing medium, this dust is incapable of providing pressure support and thus does not change the prediction that the medium should be clumpy.

8. What is the saturation level and beaming angle of the masers? We expect these two quantities to be related in general (see, e.g., Equation 1.11), with the beam size decreasing as the saturation level increases. Direct observational access to the beaming angle is not possible for any single maser spot, but we can estimate it statistically using the observed angular spread of the systemic maser features in disk systems. For a perfectly edge-on disk systemic maser emission should be beamed primarily in the radial direction, and thus the azimuthal extent of the observed systemic maser spots provides an estimate for roughly how off-center we can be viewing the maser from and still receive appreciable flux. Each of the disk maser systems with a VLBI map and disk model thus provides an estimate of the beaming angle θ, at least for the systemic masers, and we consistently find that $\theta \lesssim 10^\circ$.[4] The degree of saturation is in principle more observationally accessible for individual maser spots, because it affects the relationship between maser linewidth and intensity (Goldreich & Kwan 1974) and because it determines the variability in intensity per unit change in maser gain. However, the intensity-linewidth relationship is complicated by the unknown contributions from hyperfine structure, line-of-sight velocity gradients, and (if the rate at which the population relaxes to a Maxwellian distribution exceeds the decay rate of the maser states) infrared line trapping (Anderson & Watson 1993). Variability measurements also provide very little in the way of quantitative assessments of the saturation level. Qualitatively, with all else being equal the same maser will exhibit more pronounced variability (upon some change in gain) if it is unsaturated than if it is saturated; translating from an observed degree of variability to a saturation level, however, requires detailed knowledge of the maser geometry and pump rate.

9. Why are H_2O megamasers almost exclusively observed in Seyfert 2 galaxies?[5]

[4]Specifically, for NGC 4258 and CGCG 074-064 we find $\theta \approx 8^\circ$ (Humphreys et al. 2013, § 5.4.1), while in UGC 3789 and NGC 5765b we see $\theta \approx 10^\circ$ (Reid et al. 2013, Gao et al. 2016), in NGC 6264 we see $\theta \approx 6^\circ$ (Kuo et al. 2013), and in NGC 6323 we see $\theta \approx 4.5^\circ$ (Kuo et al. 2015).

[5]Note that megamaser emission has been seen towards so-called narrow-line Seyfert 1 galaxies (e.g., NGC 4051; Hagiwara et al. 2003, Tarchi et al. 2011), LINER galaxies (e.g., NGC 2639; Braatz et al. 1996), and Seyfert galaxies of intermediate (Sy 1.5, Sy 1.9, etc.) type (e.g., NGC 4151; Braatz

This question is perhaps the most puzzling of the bunch because, while all of the previous questions remain unanswered (or incompletely answered) largely because of the difficulty of observationally accessing the requisite information, we should be perfectly capable of simply detecting maser emission from a non-Seyfert 2 galaxy (if it's there to be detected). The standard explanation for why H_2O megamasers are at least preferentially seen towards Seyfert 2 galaxies is based on orientation effects, because Seyfert 2 systems are expected to present a nearly edge-on view of the accretion disk. However, we already know of a number of megamaser systems that clearly trace non-disk material (e.g., Circinus [Greenhill et al. 2003b], NGC 1068 [Greenhill et al. 1996], NGC 1052 [Claussen et al. 1998]), and there's no obvious reason why material that is physically distinct from the disk should nevertheless care about the disk's orientation. Yet for some reason, each of these maser systems resides in a Seyfert 2 galaxy. Furthermore, large and sensitive surveys of Seyfert 1 galaxies[6] have performed dismally, even though the standard AGN unification picture has these galaxies being more or less identical to Seyfert 2 galaxies except for their orientation.

6.2 Looking ahead

As the MCP nears completion, the focus of megamaser science is shifting in new directions. A number of current and planned facilities will be critical for pushing the field forward, and in this section I briefly outline some of the most important among these.

The VLBA, with sensitivity augmented by the GBT and phased-VLA, remains a primary workhorse for 22 GHz maser science. Many of the maser systems discovered by the MCP survey show spectral structure indicative of dynamics more complicated than that of a simple disk. High-sensitivity VLBI observations of these systems are

et al. 2004). However, there remains a notable dearth of observed megamaser emission from "pure" Seyfert 1 galaxies (i.e., those with no indications of some sort of hybrid activity), and the vast majority of all known megamasers reside in relatively unambiguous Seyfert 2 systems. The converse question – do all Seyfert 2 galaxies harbor a H_2O megamaser? – is similarly interesting.

[6] Jim Braatz has informed me of a recent GBT survey of $\sim$400 Seyfert 1 galaxies to look for H_2O megamaser emission. None were found.

necessary to reveal the spatial structure of the maser emission and to shed light on its origin. The nature of non-disk megamaser emission is currently poorly understood, and the potential for these non-disk masers to probe nuclear jet or outflow activity (or as-yet-unidentified dynamics) remains to be explored.

ALMA has already shown promise for pushing megamaser science beyond the 22 GHz transition, opening up observational access to a large number of additional maser transitions in the millimeter and submillimeter wavelength regime. A better understanding of submillimeter megamasers will expand the pool of galaxies on which we can apply the maser-specific techniques that have been so fruitful at 22 GHz, and studies that incorporate multiple transitions in the same source will yield tight constraints on the physical conditions of the gas and dust in AGN accretion disks. Though submillimeter megamaser science is currently limited by the small number of galaxies known to host submillimeter megamasers, the field is still in its infancy and new observations are being proposed every cycle. ALMA will soon be joined by NOEMA in the northern hemisphere, providing access to the entire sky, and the near future will undoubtedly see surveys of megamaser systems in many of these submillimeter transitions. VLBI mapping at these frequencies is already being pioneered by the Event Horizon Telescope project, and the use of these facilities for megamaser science will be a natural next step.

As of the writing of this thesis, the design specifications for the ngVLA[7] call for a collecting area $\sim 7\times$ that of the VLA. With such a boost in sensitivity we will be able to study megamaser systems within a volume that is $\sim 20\times$ larger than what we can currently access, enabling detections of hundreds more systems that will provide a statistically robust sample. Population-level studies will aid in addressing the questions outlined in § 6.1 (and many others), and the deluge of precisely measured SMBH masses will extend the science to include studies of galaxy-SMBH coevolution. The ngVLA will also see deeper into the closest megamaser systems, detecting masers down to $7\times$ fainter flux densities and well into the wings of the spectral profiles. This increased velocity coverage will substantially improve our models for all currently known disk megamaser systems. If the ngVLA provides long-baseline (>1000 km)

[7] `http://ngvla.nrao.edu/page/refdesign`

capabilities, efficiency will be improved still further by enabling us to simultaneously carry out mapping and monitoring observations.

Space-based VLBI of NGC 4258 is already underway using the 10-meter RadioAstron satellite, which observes in conjunction with ground-based antennas on baselines as long as $\sim$27 Earth diameters (corresponding to an angular resolution of $\sim$8 μas at the observing frequency of 22 GHz; Baan et al. 2018). A concept for a 25-meter space VLBI station – called ARISE (Advanced Radio Interferometry between Space and Earth) – has been proposed but so far lacks funding (Ulvestad 2000). But whatever the current status of space-VLBI may be, the ever-decreasing cost of spaceflight and the ever-increasing demand for better angular resolution seem destined to ultimately drive an industry of spaceborne radio antennas. A phased-ngVLA joining forces with future space-based VLBI stations will give us access to an unprecedented combination of sensitivity and angular resolution, yielding the prospect of precision improvements (for nearly all classes of megamaser-specific measurements) exceeding two orders of magnitude.

Appendices

Appendix A

Kernel density estimation

In essence, the kernel density estimation (KDE) technique as used in Chapter 2 is simply an alternative to a traditional histogram (though in each case we have shown it alongside such a histogram). In a standard histogram, a single data point falls into a "bin" of width h, unit height, and fixed edgepoints. The bin width is usually determined by the sample size and spread, with the optimal result being a compromise between data resolution and population per bin. The bin edgepoints, however, are often more arbitrarily defined. The KDE approach solves this issue by eliminating the use of bins; instead, each data point is represented by a "kernel" of some predefined functional form. In Figures 2.2 and 2.3 we used a Gaussian kernel of the form

$$K(u) = \frac{1}{\sqrt{2\pi}} e^{-u^2/2}. \tag{A.1}$$

This kernel has been scaled by h relative to a normal (i.e., unit area) Gaussian kernel, such that the area under the curve for a given data point matches what would be found in a typical histogram of bin width h. The final kernel density estimator is then just a sum of the kernels for all data points, which can be written as

$$f(x) = \sum_{i=1}^{N} K\left(\frac{x - X_i}{h}\right). \tag{A.2}$$

Here, N is the number of data points, X_i is the center of the kernel for data point i (i.e., the value of that data point), and h is the kernel width. In our case, X_i is the isotropic luminosity (for Figure 2.2) or the logarithm of the flux ratio (for Figure 2.3) for a single source. Under the assumption that our underlying distribution is at least approximately Gaussian, we have used the bin width derived by Silverman (page 45, equation 3.28):

$$h = \left(\frac{4\sigma^5}{3N}\right)^{1/5}. \tag{A.3}$$

Here, σ is the standard deviation of the sample.

Appendix B

Transverse motion along the line of sight to ESO 558-G009

This appendix describes the model used to fit for the distance to the scattering screen causing the scintillation seen towards ESO 558-G009 (§ 2.5.2). Our goal is to transform from the Galactic Cartesian coordinate system (X, Y, Z) to a coordinate system (x, y, z) where the line of sight to ESO 558-G009 is aligned with the z-axis. We define $\hat{\boldsymbol{z}}$ to be pointing away from ESO 558-G009 and $\hat{\boldsymbol{y}}$ to be the projection of the North Ecliptic Pole onto the plane perpendicular to $\hat{\boldsymbol{z}}$. The unit vector $\hat{\boldsymbol{x}}$ is then defined to be $\hat{\boldsymbol{x}} \equiv \hat{\boldsymbol{z}} \times \hat{\boldsymbol{y}}$.

The standard spherical Galactic coordinates (ℓ, b) can be converted to Galactic Cartesian unit vectors using the transformation:

$$\begin{aligned} X &= \cos(\ell)\cos(b) \\ Y &= \sin(\ell)\cos(b) \\ Z &= \sin(b) \end{aligned} \tag{B.1}$$

We can thus define a unit vector $\hat{\boldsymbol{r}} = (X, Y, Z)$ that points in the direction of any Galactic coordinate location (ℓ, b).

The North Ecliptic Pole has Galactic coordinates $(\ell, b) = (96.3840, 29.8117)$, with corresponding unit vector $\hat{\boldsymbol{r}}_{\mathrm{NEP}} = (-0.0965, 0.8623, 0.4972)$. The coordinates for ESO 558-G009 are $(\ell, b) = (233.6609, -6.9598)$, with unit vector $\hat{\boldsymbol{r}}_{\mathrm{ESO}} = (-0.5882, -0.7996, -0.1212)$. From our description above of the desired coordinate system, we have the following expressions for the coordinate unit vectors:

$$\begin{aligned} \hat{\boldsymbol{x}} &= \frac{\hat{\boldsymbol{r}}_{\mathrm{NEP}} \times \hat{\boldsymbol{r}}_{\mathrm{ESO}}}{|\hat{\boldsymbol{r}}_{\mathrm{NEP}} \times \hat{\boldsymbol{r}}_{\mathrm{ESO}}|} \\ \hat{\boldsymbol{y}} &= \hat{\boldsymbol{r}}_{\mathrm{ESO}} \times \hat{\boldsymbol{x}} \\ \hat{\boldsymbol{z}} &= -\hat{\boldsymbol{r}}_{\mathrm{ESO}} \end{aligned} \tag{B.2}$$

These evaluate to $\hat{\boldsymbol{x}} = (0.4064, -0.4218, 0.8105)$, $\hat{\boldsymbol{y}} = (-0.6992, 0.4275, 0.5731)$, and $\hat{\boldsymbol{z}} = (0.5882, 0.7996, 0.1212)$. We'll henceforth refer to this new coordinate system as the "source" coordinate system.

B.1 Solar motion with respect to the LSR

The first component of the transverse motion comes from the Sun's deviation from its orbital motion. From Coşkunoğlu et al. (2011), the Sun's peculiar motion relative to the LSR has components $\boldsymbol{v}_{\odot} = (8.50, 13.38, 6.49)$ km s^{-1}, with magnitude $v_{\odot} = 17.13$ km s^{-1} and corresponding unit vector $\hat{\boldsymbol{r}}_{\odot} = (0.4962, 0.7811, 0.3789)$. The parallel and perpendicular components of this velocity are then simply its projections onto the coordinate axes:

$$\begin{aligned} v_{\odot,\parallel} &= \boldsymbol{v}_{\odot} \cdot \hat{\boldsymbol{z}} \\ v_{\odot,\perp} &= \sqrt{(\boldsymbol{v}_{\odot} \cdot \hat{\boldsymbol{x}})^2 + (\boldsymbol{v}_{\odot} \cdot \hat{\boldsymbol{y}})^2} \end{aligned} \tag{B.3}$$

These evaluate to $v_{\odot,\parallel} = 16.48$ km s^{-1} and $v_{\odot,\perp} = 4.66$ km s^{-1}, with source components $(v_x, v_y, v_z)_{\odot} = (3.07, 3.50, 16.48)$ km s^{-1}.

B.2 Earth's orbital motion

The second component of the transverse motion comes from the Earth's orbit around the Sun. For simplicity, we'll model this orbit as circular about the North Ecliptic Pole, with orbital velocity $v_\oplus = 30$ km s^{-1}. If we define a position angle $\phi = \omega t$ measured clockwise from the negative x-axis, then we can decompose the Earth's orbital motion into the source components:

$$\begin{aligned} v_{x,\oplus}(t) &= v_\oplus \sin(\phi_0 + \omega t) \\ v_{y,\oplus}(t) &= v_\oplus \cos(\phi_0 + \omega t) \cos(i) \\ v_{z,\oplus}(t) &= -v_\oplus \cos(\phi_0 + \omega t) \sin(i) \end{aligned} \tag{B.4}$$

Here, ω is the orbital angular frequency of the Earth, $i = \pi/2 - \cos^{-1}(\hat{\boldsymbol{y}} \cdot \hat{\boldsymbol{r}}_{\rm NEP})$ is the inclination of the orbit relative to the line of sight to ESO 558-G009 (in our case, $i = 46.1°$), and ϕ_0 is an initial position angle that must be calibrated based on the known motion of the Earth.

On the vernal equinox (the origin of the ecliptic longitude), the Earth is moving towards ecliptic coordinates $(\lambda, \beta) = (90, 0)$. The equivalent Galactic coordinates are $(\ell, b) = (186.3725, -0.0200)$, so the corresponding velocity vector is $\boldsymbol{v}_{\oplus,\rm eq} = (-29.814, -3.33, 0.009)$ km s^{-1}. Decomposing this into source coordinates yields $(v_x, v_y, v_z)_{\oplus,\rm eq} = (-10.704, 19.428, -20.199)$ km s^{-1}.

Since our model uses only a crude approximation for what in reality is a moderately noncircular orbit, small deviations from the model will grow with time. We'd thus need to calibrate it using the vernal equinox closest in time to the observations. This occurred on 2012 May 20, which corresponds to a Modified Julian Date of MJD = 56006. We obtain a value of $\phi_0 = 6.096$.

B.3 Solar orbital motion

The third component of the transverse motion comes from the Sun's orbit about the Galactic center, relative to that of the scattering screen. From Reid et al. (2014), the distance from the Galactic center to the Sun is $R_0 = 8.34$ kpc. If we denote the distance from the Sun to the scattering screen as D and the distance from the scattering screen to the Galactic center as R, then the law of cosines gives us an expression:

$$R = \sqrt{D^2 + R_0^2 + 2DR_0\cos(\theta)} \tag{B.5}$$

Here, θ is the angle between $\ell = 180^\circ$ and the direction to ESO 558-G009 (i.e., $\theta = \ell - 180^\circ$).

If we define α to be the angle between the Sun and the scattering screen, as seen from the Galactic center, then we have a second expression for R:

$$R = D\cos(\theta - \alpha) + R_0\cos(\alpha) \tag{B.6}$$

Combining Equations B.5 and B.6 yields a numerically invertible expression for α in terms of D. Once we know α, we can use it to determine the component of the scattering screen's orbital motion that lies along the same direction as the Sun's orbital motion. If the orbital velocity of the scattering screen is V_s, then the parallel component is just $V_s\cos(\alpha)$.

The line of sight towards ESO 558-G009 is such that the scattering screen lies outside of the solar orbit. The rotation curve of the Milky Way is known to be very nearly flat at these outer radii (see Reid et al. 2014), with an orbital velocity of 240 km s^{-1}. We can thus set $V_s = V_\odot = 240$ km s^{-1}, and we obtain a net apparent motion of the scattering screen (directed along the Sun's orbital velocity vector) of:

$$V_\parallel = V_\odot\big(1 - \cos(\alpha)\big) \tag{B.7}$$

The Sun's orbital motion is directed towards the Galactic coordinates $(\ell, b) = (90, 0)$, which is directed along the Y-axis. The perpendicular component of the scattering screen's orbital velocity (i.e., the component directed along the X-axis) will then just be $V_\perp = -V_\odot \sin(\alpha)$. We can now use our previously-derived unit vectors to transform this into the source frame. Doing so yields:

$$
\begin{aligned}
V_x &= V_\odot\Big[-0.4064\sin(\alpha) - 0.4218\big(1-\cos(\alpha)\big)\Big] \\
V_y &= V_\odot\Big[0.6992\sin(\alpha) + 0.4275\big(1-\cos(\alpha)\big)\Big] \\
V_z &= V_\odot\Big[-0.5882\sin(\alpha) + 0.7996\big(1-\cos(\alpha)\big)\Big]
\end{aligned}
\tag{B.8}
$$

Combining this with Equations B.3 and B.4 allows us to fully characterize the transverse motion of the scattering screen, as seen from Earth, in terms of t (which is known for every observation) and D (which we would like to know). For a nearby screen, $D \ll R_0$, and the transverse motion becomes a function of t only.

Appendix C

Constructing the covariance matrix for a Gaussian beam

When determining the position of a point source as seen with an interferometer, the (relative) positional uncertainty along any direction is proportional to the beam size in that direction. For a Gaussian synthesized beam, this uncertainty is fully characterized by a symmetric two-dimensional covariance matrix, $\mathbf{S}$. The diagonal elements of the covariance matrix correspond to the variances in the x and y directions (typically taken to be right ascension and declination), and the off-diagonal elements contain the covariance between x and y (i.e., information about the orientation of the Gaussian). Writing $\mathbf{S}$ out in matrix form, we have

$$\mathbf{S} = \begin{pmatrix} \sigma_x^2 & \sigma_{xy} \\ \sigma_{xy} & \sigma_y^2 \end{pmatrix}. \tag{C.1}$$

If σ_{xy} is zero then the beam is aligned with the coordinate axes, but in general the beam will have some dimensions $b \times a$ and a position angle θ that is misaligned in our coordinate system. In this case, the beam can be described as a Gaussian with variances a^2 and b^2 that has been rotated by θ with respect to our coordinate system. If we were to operate with $\mathbf{S}$ on a unit vector $\hat{\boldsymbol{v}}$ that points along one of the principle axes of the beam (let's say the a-axis), the only effect would be to scale the length of $\hat{\boldsymbol{v}}$ by the variance along that axis (i.e., a^2). That is, $\hat{\boldsymbol{v}}$ is an eigenvector of $\mathbf{S}$ with eigenvalue a^2:

$$\mathbf{S}\hat{\boldsymbol{v}} = a^2\hat{\boldsymbol{v}}. \tag{C.2}$$

An analogous expression holds for the vector pointed along the b-direction, and we can combine these two equations using the matrix expression

$$\mathbf{SV} = \mathbf{VD}. \tag{C.3}$$

Here, $\mathbf{V}$ is the matrix whose columns are the eigenvectors of $\mathbf{S}$, and $\mathbf{D}$ is the diagonal matrix whose elements are the corresponding eigenvalues of $\mathbf{S}$. $\mathbf{D}$ is thus the covariance matrix as viewed from a coordinate system that aligns with the principle axes of the beam, which we know is related to our coordinate system by nothing more than a rotation. We can see that $\mathbf{V}$ must then be the rotation matrix that transforms from our coordinate system to the beam-aligned coordinate system, which we can re-denote as $\mathbf{R}$. Writing these two matrices out explicitly yields:

$$\mathbf{D} = \begin{pmatrix} a^2 & 0 \\ 0 & b^2 \end{pmatrix}, \tag{C.4}$$

$$\mathbf{R} = \begin{pmatrix} \cos(\theta) & -\sin(\theta) \\ \sin(\theta) & \cos(\theta) \end{pmatrix}. \tag{C.5}$$

Rearranging the terms in Equation C.3 and substituting in $\mathbf{R}$ for $\mathbf{V}$ thus yields an expression for the covariance matrix in terms of the beam parameters:

$$\mathbf{S} = \mathbf{RDR}^{-1}. \tag{C.6}$$

Appendix D

Disk model

Our disk model (§ 5.4) is very similar to that used by Reid et al. (2013) and Humphreys et al. (2013). We include global parameters describing the angular size distance D to the SMBH, the SMBH mass M_{BH}, the SMBH redshift z_0, and the on-sky coordinates of the SMBH (x_0, y_0). We also include several global parameters describing the warped geometry of the disk, which is parameterized by an inclination angle $i(r)$ and position angle $\Omega(r)$ that vary as a function of orbital radius as

$$i(r) = i_0 + \frac{di}{dr} r, \tag{D.1}$$

$$\Omega(r) = \Omega_0 + \frac{d\Omega}{dr} r. \tag{D.2}$$

The modeled geometric parameters are then i_0, $\frac{di}{dr}$, Ω_0, and $\frac{d\Omega}{dr}$.

Each maser spot is assigned a location (r, ϕ) within the disk, where r is the spherical radius measured from the BH and ϕ is the azimuthal angle measured from the line of sight (oriented such that the systemic features are located at $\phi \approx 0°$ and the redshifted features are located at $\phi \approx 90°$). The sky-plane position of the maser spot is denoted (x, y), with the x-axis aligned with right ascension (so that positive points to the east) and the y-axis aligned with declination (so that positive points to the north). The z-axis is then directed along the line of sight, so that positive z points away from us. The inclination angle i is defined to be the angle that the disk normal makes with respect to the line of sight, such that $i = 90°$ corresponds to a perfectly edge-on disk and $i = 0°$ corresponds to a disk whose angular momentum vector is aligned with the $+z$-axis. The position angle Ω is then defined to be the angle that the receding portion of the disk midplane makes east of north (i.e., clockwise down from the y-axis). Note that both i and Ω are functions of r.

We can transform from the disk frame to the sky frame by rotating first by i about the x-axis, then by Ω about the z-axis. This transformation can be expressed as a product of two rotation matrices,

$$\begin{pmatrix} x \\ y \\ z \end{pmatrix} = \begin{pmatrix} \sin(\Omega) & -\cos(\Omega) & 0 \\ \cos(\Omega) & \sin(\Omega) & 0 \\ 0 & 0 & 1 \end{pmatrix} \begin{pmatrix} 1 & 0 & 0 \\ 0 & \sin(i) & -\cos(i) \\ 0 & \cos(i) & \sin(i) \end{pmatrix} \begin{pmatrix} r\sin(\phi) \\ 0 \\ -r\cos(\phi) \end{pmatrix}, \tag{D.3}$$

where we have for simplicity used a pre-rotation disk orientation of $i = \Omega = 90°$. After accounting for the location of the BH itself, we obtain the sky frame coordinates of the maser spot to be

$$x = x_0 + r\big[\sin(\phi)\sin(\Omega) - \cos(\phi)\cos(\Omega)\cos(i)\big], \tag{D.4a}$$

$$y = y_0 + r\big[\sin(\phi)\cos(\Omega) + \cos(\phi)\sin(\Omega)\cos(i)\big], \tag{D.4b}$$

$$z = -r\cos(\phi)\sin(i). \tag{D.4c}$$

(Note that the z coordinate of the BH is fixed at $z = 0$ by our choice of coordinate system.) We can similarly express the sky frame components of the maser spot's velocity and acceleration as

$$v_x = v\big[\cos(\phi)\sin(\Omega) + \sin(\phi)\cos(\Omega)\cos(i)\big], \tag{D.5a}$$

$$v_y = v\big[\cos(\phi)\cos(\Omega) - \sin(\phi)\sin(\Omega)\cos(i)\big], \tag{D.5b}$$

$$v_z = v\sin(\phi)\sin(i), \tag{D.5c}$$

and

$$a_x = a\big[-\sin(\phi)\sin(\Omega) + \cos(\phi)\cos(\Omega)\cos(i)\big], \tag{D.6a}$$

$$a_y = a\big[-\sin(\phi)\cos(\Omega) - \cos(\phi)\sin(\Omega)\cos(i)\big], \tag{D.6b}$$

$$a_z = a\cos(\phi)\sin(i), \tag{D.6c}$$

respectively.

The orbital velocity v and acceleration a are determined assuming circular orbits about a point mass,

$$v(r) = \sqrt{\frac{GM_{\mathrm{BH}}}{rD}}, \tag{D.7}$$

$$a(r) = \frac{GM_{\mathrm{BH}}}{r^2 D^2}, \tag{D.8}$$

where we've converted r from angular units to physical ones using the angular size distance to the SMBH, D.

The redshift imparted by the relativistic Doppler effect is given by (Rybicki & Lightman 1986)

$$1 + z_D = \gamma\left(1 - \frac{v}{c}\cos(\theta)\right), \tag{D.9}$$

where $\gamma = \left(1 - \frac{v^2}{c^2}\right)^{-1/2}$ is the Lorentz factor and θ is the angle between the velocity vector and the line of sight. We can obtain $\cos(\theta)$ by taking the dot product between $\vec{v}/v$ and $-\hat{z}$, which results in

$$1 + z_D = \gamma\left(1 + \frac{v}{c}\sin(\phi)\sin(i)\right). \tag{D.10}$$

In a Schwarzschild spacetime, the gravitational redshift z_g of a photon emitted at radius r and received at infinity is given by (Schutz 2009)

$$1 + z_g = \left(1 - \frac{R_s}{rD}\right)^{-1/2}, \tag{D.11}$$

where $R_s = 2GM_{\mathrm{BH}}/c^2$ is the Schwarzschild radius for the SMBH.

The observed redshift of the maser spot, z, will then be given by the product of both the Doppler and gravitational effects with the SMBH redshift, z_0:

$$1 + z = (1 + z_D)(1 + z_g)(1 + z_0). \tag{D.12}$$

Here, z_0 is the redshift measured in the CMB frame. In this work we use the optical convention for all velocities, so the observed velocities are related to the redshift by simply

$$v_{\mathrm{obs}} = cz. \tag{D.13}$$

D.1 Constructing the likelihood function

For each data point i, we have a measurement of its on-sky position (x_i, y_i), line-of-sight velocity v_i, and line-of-sight acceleration a_i. Each of these measurements is independent of the others, and each must be treated differently in the likelihood function.

The uncertainties in our position measurements come in the form of a covariance matrix $\mathbf{S}_i$, given by

$$\mathbf{S}_i = \frac{k}{4R_i^2}\begin{pmatrix} \sigma_x^2 & \sigma_{xy} \\ \sigma_{xy} & \sigma_y^2 \end{pmatrix}, \tag{D.14}$$

where R_i is the signal-to-noise ratio of data point i, the matrix entries are the (co)variances caused by the synthesized beam shape (see Appendix C), and k is a scaling factor that accounts for additional sources of uncertainty beyond the statistical fitting error from the maser spot fitting procedure outlined in § 5.3.1 (i.e., it is the equivalent of the "error floors" used in previous MCP papers). For a beam with dimensions $\beta \times \alpha$ oriented at a position angle θ (measured east of north), we can express the (co)variances as

$$\sigma_x^2 = \alpha^2 \cos^2(\theta) + \beta^2 \sin^2(\theta), \tag{D.15a}$$

$$\sigma_{xy} = \left(\beta^2 - \alpha^2\right) \sin(\theta) \cos(\theta), \tag{D.15b}$$

$$\sigma_y^2 = \alpha^2 \sin^2(\theta) + \beta^2 \cos^2(\theta). \tag{D.15c}$$

For a Gaussian beam, the conditional probability to measure a maser spot to be at $\mathbf{z}_i \equiv \binom{x_i}{y_i}$ when its "true" location is $\mathbf{Z}_i \equiv \binom{X_i}{Y_i}$ is then given by (e.g., Hogg et al. 2010, Eq. 27)

$$\begin{aligned} p\left(x_i, y_i | \mathbf{S}_i, X_i, Y_i\right) &= \frac{1}{2\pi\sqrt{\det\left(\mathbf{S}_i\right)}} \exp\left(-\frac{1}{2}\left[\mathbf{z}_i - \mathbf{Z}_i\right]^{\mathrm{T}} \mathbf{S}_i^{-1}\left[\mathbf{z}_i - \mathbf{Z}_i\right]\right) \\ &= \frac{2R_i^2}{\pi k \alpha \beta} \exp\left(-\frac{2R_i^2}{k\alpha^2\beta^2}\left[\sigma_y^2\left(x_i - X_i\right)^2 - 2\sigma_{xy}\left(x_i - X_i\right)\left(y_i - Y_i\right) + \sigma_x^2\left(y_i - Y_i\right)^2\right]\right) \end{aligned} \tag{D.16}$$

The likelihood to find all maser spots at their observed positions (given the model-predicted "true" positions) is then the product of these conditional probabilities,

$$\mathcal{L}_1 = \prod_i p\left(x_i, y_i | \mathbf{S}_i, X_i, Y_i\right), \tag{D.17}$$

which is equivalent to a log-likelihood of

$$\ln\left(\mathcal{L}_1\right) = \sum_i \left[\ln\left(\frac{2R_i^2}{\pi k \alpha \beta}\right) - \frac{2R_i^2}{k\alpha^2\beta^2}\left(\sigma_y^2\left(x_i - X_i\right)^2 - 2\sigma_{xy}\left(x_i - X_i\right)\left(y_i - Y_i\right) + \sigma_x^2\left(y_i - Y_i\right)^2\right)\right]. \tag{D.18}$$

The uncertainties associated with our velocity and acceleration measurements are both one-dimensional, and they therefore result in simpler functional forms for the likelihood expressions than the positional uncertainties do. However, the exact values for our velocity and acceleration uncertainties are not as rigorously defined as those for the position measurements. As with the k parameter in the position likelihood function, we have chosen to incorporate these uncertainties into the model itself, an approach that is similar to the "error floor" treatments used in previous MCP papers.

For the acceleration measurements, we construct a parameter μ_a to be an error floor that gets added in quadrature with the measurement uncertainties. The conditional probability to measure a maser spot to have acceleration a_i when its "true" acceleration is A_i and its measurement uncertainty is $\sigma_{a,i}$ is then given by

$$p\left(a_i|\sigma_{a,i}, A_i\right) = \frac{1}{\sqrt{2\pi\left(\sigma_{a,i}^2 + \mu_a^2\right)}} \exp\left(-\frac{\left(a_i - A_i\right)^2}{2\left(\sigma_{a,i}^2 + \mu_a^2\right)}\right). \tag{D.19}$$

We can then multiply the conditional probabilities for all maser spots to construct the likelihood,

$$\ln\left(\mathcal{L}_2\right) = -\frac{1}{2}\sum_i \left[\frac{\left(a_i - A_i\right)^2}{\sigma_{a,i}^2 + \mu_a^2} + \ln\left[2\pi\left(\sigma_{a,i}^2 + \mu_a^2\right)\right]\right], \tag{D.20}$$

which is effectively a χ^2 function plus a regularization term to constrain the error floor parameter μ_a. For those features that were too weak to measure accelerations directly (see § 5.3.2), we have set $\sigma_{a,i}$ to be 2 km s^{-1} yr^{-1} and we have allowed a_i to be a free parameter in the model.

Our velocity "measurements" are obtained in a qualitatively different manner than either the position or acceleration measurements, and should thus be thought about somewhat differently. The velocity v_i we associate with any particular maser spot simply corresponds to the central velocity of a spectral channel in a VLBI map. The calibration uncertainties in these velocities are negligible, so the effective uncertainty arises instead because (1) the spectral channels are discretized and finitely wide, and (2) a maser line may span more than one channel. While our position and acceleration measurements are made using centroiding techniques and thus are continuous across their measurement domains, our velocity measurements take on discretized values in integer multiples of the channel width, with offsets determined by the specific spectral gridding scheme. This discretization will necessarily introduce some uncertainty into our velocity measurements, though the exact value that this uncertainty should take is not obvious. An additional source of uncertainty arises for maser lines that span multiple spectral channels, in which case the velocity of any one channel is not necessarily reflective of the true maser velocity. We have averaged the VLBI data to channels that are roughly the width of a typical maser feature ($\sim$2 km s^{-1}) in an effort to minimize this problem, but we cannot eliminate it; at best, such averaging simply ensures that all measured velocities are "close" to their true values.

Though it seems plausible that the magnitude of the velocity uncertainty should be comparable to the channel spacing, it remains unclear what precise value the uncertainty should take. We thus opt to determine the uncertainties empirically. We introduce two new global parameters, $\sigma_{v,\mathrm{sys}}$ and $\sigma_{v,\mathrm{hv}}$, that describe the velocity uncertainties for the systemic and high-velocity features, respectively. From here, we proceed as before by first constructing the conditional probability,

$$p\left(v_i|\sigma_{v,\mathrm{sys}}, \sigma_{v,\mathrm{hv}}, V_i\right) = \begin{cases} \dfrac{1}{\sqrt{2\pi\sigma_{v,\mathrm{sys}}^2}} \exp\left(-\dfrac{\left(v_i - V_i\right)^2}{2\sigma_{v,\mathrm{sys}}^2}\right) & \text{for systemic features} \\ \dfrac{1}{\sqrt{2\pi\sigma_{v,\mathrm{hv}}^2}} \exp\left(-\dfrac{\left(v_i - V_i\right)^2}{2\sigma_{v,\mathrm{hv}}^2}\right) & \text{for high-velocity features} \end{cases}, \tag{D.21}$$

and then multiplying the conditional probabilities for all maser spots to obtain the likelihood,

$$\ln\left(\mathcal{L}_3\right) = \begin{cases} -\dfrac{1}{2}\displaystyle\sum_i \left[\dfrac{\left(v_i - V_i\right)^2}{\sigma_{v,\mathrm{sys}}^2} + \ln\left(2\pi\sigma_{v,\mathrm{sys}}^2\right)\right] & \text{for systemic features} \\ -\dfrac{1}{2}\displaystyle\sum_i \left[\dfrac{\left(v_i - V_i\right)^2}{\sigma_{v,\mathrm{hv}}^2} + \ln\left(2\pi\sigma_{v,\mathrm{hv}}^2\right)\right] & \text{for high-velocity features} \end{cases}. \tag{D.22}$$

Having constructed the likelihood functions for all three measurement classes we can now combine them to obtain the overall likelihood function, given some choice of model parameters:

$$\ln\left(\mathcal{L}\right) = \ln\left(\mathcal{L}_1\right) + \ln\left(\mathcal{L}_2\right) + \ln\left(\mathcal{L}_3\right). \tag{D.23}$$

The final model contains 13 global parameters: D, M_{BH}, z_0, x_0, y_0, i_0, $\frac{di}{dr}$, Ω_0, $\frac{d\Omega}{dr}$, and the nuisance parameters k, μ_a, $\sigma_{v,\mathrm{sys}}$, and $\sigma_{v,\mathrm{hv}}$. It also contains many other nuisance parameters associated with the positions of individual maser spots and the accelerations of the weakest spots (see § 5.3.2). For a fit to N_r, N_b, and N_s redshifted, blueshifted, and systemic maser spots, respectively, the model will have $2\,(N_r + N_b + N_s)$ additional free parameters corresponding to a (r, ϕ) pair for every maser feature. Similarly, for N_a maser features with fitted (rather than measured) accelerations, the model gains an additional N_a free parameters. For this work, $N_r = 71$, $N_b = 49$, $N_s = 45$, and $N_a = 20$, bringing the total number of parameters to 363. There are four independent measurements for every data point except for those with fitted accelerations, for a total of $4(N_r + N_s + N_b) - N_a = 640$ model constraints.

We assigned uniform priors to all parameters. Table 5.5 lists the priors for all non-nuisance parameters. Both $\sigma_{v,\mathrm{sys}}$ and $\sigma_{v,\mathrm{hv}}$ were assigned uniform priors in the range $[0.1, 20]$ km s^{-1}, μ_a was assigned a uniform prior on $[0.01, 10]$ km s^{-1} yr^{-1}, and k was assigned a uniform prior on $[0, 100]$. All r parameters for the maser spots were assigned uniform priors within the range $[0.01, 2.0]$ mas. The ϕ parameters were assigned uniform priors in the range $[0, \pi]$ for the redshifted features, $[\pi, 2\pi]$ for the blueshifted features, and $[-\frac{\pi}{2}, \frac{\pi}{2}]$ for the systemic features. The priors on unmeasured acceleration values for weak maser spots were uniform in the range $[-20.0, 20.0]$ km s^{-1} yr^{-1}.

References

Abazajian, K. N., Adelman-McCarthy, J. K., Agüeros, M. A., et al. 2009, ApJS, 182, 543

Anderson, N., & Watson, W. D. 1993, ApJ, 407, 620

Antonucci, R. 1993, ARA&A, 31, 473

Antonucci, R. R. J., & Miller, J. S. 1985, ApJ, 297, 621

Argon, A. L., Greenhill, L. J., Moran, J. M., et al. 1994, ApJ, 422, 586

Argon, A. L., Greenhill, L. J., Reid, M. J., Moran, J. M., & Humphreys, E. M. L. 2007, ApJ, 659, 1040

Arzoumanian, Z., Brazier, A., Burke-Spolaor, S., et al. 2014, ApJ, 794, 141

Baan, W., Alakoz, A., An, T., et al. 2018, ArXiv e-prints, arXiv:1801.08796

Baan, W. A., & Haschick, A. D. 1984, ApJ, 279, 541

Babak, S., Petiteau, A., Sesana, A., et al. 2016, MNRAS, 455, 1665

Balbus, S. A., & Hawley, J. F. 1991, ApJ, 376, 214

Barrows, R. S., Comerford, J. M., Greene, J. E., & Pooley, D. 2016, ApJ, 829, 37

Barth, A. J., Boizelle, B. D., Darling, J., et al. 2016, ApJ, 822, L28

Beers, T. C., Kriessler, J. R., Bird, C. M., & Huchra, J. P. 1995, AJ, 109, 874

Begelman, M. C., Blandford, R. D., & Rees, M. J. 1980, Nature, 287, 307

Begeman, K. G. 1989, A&A, 223, 47

Bekenstein, J. D. 1973, ApJ, 183, 657

Bennett, C. L., Larson, D., Weiland, J. L., et al. 2013, ApJS, 208, 20

Bernath, P. 2005, Spectra of Atoms and Molecules (Oxford University Press)

Betancourt, M. 2017, ArXiv e-prints, arXiv:1701.02434

Bignall, H. E., Jauncey, D. L., Lovell, J. E. J., et al. 2004, in European VLBI Network on New Developments in VLBI Science and Technology, ed. R. Bachiller, F. Colomer, J.-F. Desmurs, & P. de Vicente, 19–22

Blandford, R. D., & Payne, D. G. 1982, MNRAS, 199, 883

Bolton, A. S., Schlegel, D. J., Aubourg, É., et al. 2012, AJ, 144, 144

Bonning, E. W., Shields, G. A., & Salviander, S. 2007, ApJ, 666, L13

Boroson, T. 2005, AJ, 130, 381

Boroson, T. A., & Lauer, T. R. 2009, Nature, 458, 53

Bottinelli, L., Gouguenheim, L., Fouque, P., & Paturel, G. 1990, A&AS, 82, 391

Braatz, J. 2002, in IAU Symposium, Vol. 206, Cosmic Masers: From Proto-Stars to Black Holes, ed. V. Migenes & M. J. Reid, 396

Braatz, J., Greenhill, L., Reid, M., et al. 2007, in IAU Symposium, Vol. 242, Astrophysical Masers and their Environments, ed. J. M. Chapman & W. A. Baan, 399–401

Braatz, J., Condon, J., Constantin, A., et al. 2015, IAU General Assembly, 22, #2255730

Braatz, J. A. 1996, PhD thesis, , Univ. Maryland, (1996) Braatz, J. A., & Gugliucci, N. E. 2008, ApJ, 678, 96

Braatz, J. A., Henkel, C., Greenhill, L. J., Moran, J. M., & Wilson, A. S. 2004, ApJ, 617, L29

Braatz, J. A., Reid, M. J., Humphreys, E. M. L., et al. 2010, ApJ, 718, 657

Braatz, J. A., Wilson, A. S., & Henkel, C. 1994, ApJ, 437, L99

—. 1996, ApJS, 106, 51

—. 1997, ApJS, 110, 321

Braatz, J. A., Wilson, A. S., Henkel, C., Gough, R., & Sinclair, M. 2003, ApJS, 146, 249

Bragg, A. E., Greenhill, L. J., Moran, J. M., & Henkel, C. 2000, ApJ, 535, 73

Bruzual, G., & Charlot, S. 2003, MNRAS, 344, 1000

Campanelli, M., Lousto, C. O., Zlochower, Y., & Merritt, D. 2007, Physical Review Letters, 98, 231102

Cappellari, M. 2017, MNRAS, 466, 798

Carrick, J., Turnbull, S. J., Lavaux, G., & Hudson, M. J. 2015, MNRAS, 450, 317

Cernicharo, J., Pardo, J. R., & Weiss, A. 2006, ApJ, 646, L49

Churchwell, E., Witzel, A., Huchtmeier, W., et al. 1977, A&A, 54, 969

Claussen, M. J., Diamond, P. J., Braatz, J. A., Wilson, A. S., & Henkel, C. 1998, ApJ, 500, L129

Claussen, M. J., Heiligman, G. M., & Lo, K. Y. 1984, Nature, 310, 298

Claussen, M. J., & Lo, K.-Y. 1986, ApJ, 308, 592

Claussen, M. J., Reid, M. J., Schneps, M. H., et al. 1988, in IAU Symposium, Vol. 129, The Impact of VLBI on Astrophysics and Geophysics, ed. M. J. Reid & J. M. Moran, 231

Coşkunoğlu, B., Ak, S., Bilir, S., et al. 2011, MNRAS, 412, 1237

Collison, A. J., & Watson, W. D. 1995, ApJ, 452, L103

Comerford, J. M., Barrows, R. S., Greene, J. E., & Pooley, D. 2017, ApJ, 847, 41

Comerford, J. M., & Greene, J. E. 2014, ApJ, 789, 112

Comerford, J. M., Schluns, K., Greene, J. E., & Cool, R. J. 2013, ApJ, 777, 64

Comerford, J. M., Gerke, B. F., Newman, J. A., et al. 2009, ApJ, 698, 956

Compiègne, M., Verstraete, L., Jones, A., et al. 2011, A&A, 525, A103

Condon, J. J. 1997, PASP, 109, 166

Cordes, J. M., & Lazio, T. J. W. 2002, ArXiv Astrophysics e-prints, astro-ph/0207156

Courtes, G., & Cruvellier, P. 1961, Publications of the Observatoire Haute-Provence, 5

Cresci, G., Hicks, E. K. S., Genzel, R., et al. 2009, ApJ, 697, 115

Crook, A. C., Huchra, J. P., Martimbeau, N., et al. 2007, ApJ, 655, 790

Crusius, A., & Schlickeiser, R. 1988a, A&A, 196, 327

—. 1988b, A&A, 195, L9

Dawson, K. S., Schlegel, D. J., Ahn, C. P., et al. 2013, AJ, 145, 10

de Vaucouleurs, G., & Bollinger, G. 1979, ApJ, 233, 433

Deguchi, S. 1994, ApJ, 420, 551

Deguchi, S., & Watson, W. D. 1986, ApJ, 307, 30

—. 1989, ApJ, 340, L17

Dennett-Thorpe, J., & de Bruyn, A. G. 2002, Nature, 415, 57

Dos Santos, P. M., & Lepine, J. R. D. 1979, Nature, 278, 34

Draine, B. T. 2003, ARA&A, 41, 241

Dunkley, J., Bucher, M., Ferreira, P. G., Moodley, K., & Skordis, C. 2005, MNRAS, 356, 925

Edelson, R. A., & Krolik, J. H. 1988, ApJ, 333, 646

Efstathiou, G. 2014, MNRAS, 440, 1138

Eichler, D., & Smith, M. 1983, Nature, 303, 779

Einstein, A. 1916, Deutsche Physikalische Gesellschaft, 18, 318

—. 1917, Physikalische Zeitschrift, 18, 121

Eisenstein, D. J., Weinberg, D. H., Agol, E., et al. 2011, AJ, 142, 72

Elitzur, M. 1990, ApJ, 363, 638

—. 1992, ARA&A, 30, 75

Elitzur, M., Hollenbach, D. J., & McKee, C. F. 1989, ApJ, 346, 983

Elitzur, M., McKee, C. F., & Hollenbach, D. J. 1991, ApJ, 367, 333

Elmegreen, B. G., & Morris, M. 1979, ApJ, 229, 593

Elmouttie, M., Haynes, R. F., Jones, K. L., et al. 1997, MNRAS, 284, 830

Eracleous, M., Boroson, T. A., Halpern, J. P., & Liu, J. 2012, ApJS, 201, 23

Favata, M., Hughes, S. A., & Holz, D. E. 2004, ApJ, 607, L5

Fiebig, D., & Güsten, R. 1989, A&A, 214, 333

Fisher, J. R., & Tully, R. B. 1981, ApJS, 47, 139

Foreman-Mackey, D., Hogg, D. W., Lang, D., & Goodman, J. 2013, PASP, 125, 306

Fouque, P., Durand, N., Bottinelli, L., Gouguenheim, L., & Paturel, G. 1990, A&AS, 86, 473

Freedman, W. L., Madore, B. F., Scowcroft, V., et al. 2012, ApJ, 758, 24

Freedman, W. L., Madore, B. F., Gibson, B. K., et al. 2001, ApJ, 553, 47

Gabor, J. M., & Bournaud, F. 2013, MNRAS, 434, 606

Gallimore, J. F., Baum, S. A., O'Dea, C. P., Brinks, E., & Pedlar, A. 1996, ApJ, 462, 740

Gallimore, J. F., Henkel, C., Baum, S. A., et al. 2001, ApJ, 556, 694

Gao, F., Braatz, J. A., Reid, M. J., et al. 2016, ApJ, 817, 128

—. 2017, ApJ, 834, 52

García-Burillo, S., Combes, F., Usero, A., et al. 2014, A&A, 567, A125

Gardner, F. F., & Whiteoak, J. B. 1982, MNRAS, 201, 13P

Gardner, F. F., Whiteoak, J. B., Norris, R. P., & Diamond, P. J. 1992, MNRAS, 258, 296

Goldreich, P., & Keeley, D. A. 1972, ApJ, 174, 517

Goldreich, P., Keeley, D. A., & Kwan, J. Y. 1973, ApJ, 182, 55

Goldreich, P., & Kwan, J. 1974, ApJ, 190, 27

Goodman, J., & Weare, J. 2010, Communications in applied mathematics and computational science, 5, 65

Gray, M. D., Baudry, A., Richards, A. M. S., et al. 2016, MNRAS, 456, 374

Greenhill, L. J., Ellingsen, S. P., Norris, R. P., et al. 1997a, ApJ, 474, L103

Greenhill, L. J., & Gwinn, C. R. 1997, Ap&SS, 248, 261

Greenhill, L. J., Gwinn, C. R., Antonucci, R., & Barvainis, R. 1996, ApJ, 472, L21

Greenhill, L. J., Henkel, C., Becker, R., Wilson, T. L., & Wouterloot, J. G. A. 1995a, A&A, 304, 21

Greenhill, L. J., Jiang, D. R., Moran, J. M., et al. 1995b, ApJ, 440, 619

Greenhill, L. J., Kondratko, P. T., Lovell, J. E. J., et al. 2003a, ApJ, 582, L11

Greenhill, L. J., Kondratko, P. T., Moran, J. M., & Tilak, A. 2009, ApJ, 707, 787

Greenhill, L. J., Moran, J. M., & Herrnstein, J. R. 1997b, ApJ, 481, L23

Greenhill, L. J., Moran, J. M., Reid, M. J., et al. 1994, in Bulletin of the American Astronomical Society, Vol. 26, American Astronomical Society Meeting Abstracts #184, 966

Greenhill, L. J., Booth, R. S., Ellingsen, S. P., et al. 2003b, ApJ, 590, 162

Gualandris, A., & Merritt, D. 2008, ApJ, 678, 780

Gundermann, E. J. 1965, PhD thesis, HARVARD UNIVERSITY.

Gunn, J. E., Siegmund, W. A., Mannery, E. J., et al. 2006, AJ, 131, 2332

Hagiwara, Y., Diamond, P. J., & Miyoshi, M. 2002, A&A, 383, 65

Hagiwara, Y., Diamond, P. J., Miyoshi, M., Rovilos, E., & Baan, W. 2003, MNRAS, 344, L53

Hagiwara, Y., Diamond, P. J., Nakai, N., & Kawabe, R. 2001, ApJ, 560, 119

Hagiwara, Y., Horiuchi, S., Doi, A., Miyoshi, M., & Edwards, P. G. 2016, ApJ, 827, 69

Hagiwara, Y., Kohno, K., Kawabe, R., & Nakai, N. 1997, PASJ, 49, 171

Hagiwara, Y., Miyoshi, M., Doi, A., & Horiuchi, S. 2013, ApJ, 768, L38

Haschick, A. D., & Baan, W. A. 1985, Nature, 314, 144

Haschick, A. D., & Baan, W. A. 1991, in Astronomical Society of the Pacific Conference Series, Vol. 16, Atoms, Ions and Molecules: New Results in Spectral Line Astrophysics, ed. A. D. Haschick & P. T. P. Ho, 67

Haschick, A. D., Baan, W. A., & Peng, E. W. 1994, ApJ, 437, L35

Haschick, A. D., Baan, W. A., Schneps, M. H., et al. 1990, ApJ, 356, 149

Hawley, J. F., Gammie, C. F., & Balbus, S. A. 1996, ApJ, 464, 690

Haynes, M. P., Giovanelli, R., Martin, A. M., et al. 2011, AJ, 142, 170

Heckman, T. M. 1980, A&A, 87, 152

Henkel, C., Braatz, J. A., Greenhill, L. J., & Wilson, A. S. 2002, A&A, 394, L23

Henkel, C., Guesten, R., Downes, D., et al. 1984, A&A, 141, L1

Henkel, C., Peck, A. B., Tarchi, A., et al. 2005, A&A, 436, 75

Henkel, C., Wouterloot, J. G. A., & Bally, J. 1986, A&A, 155, 193

Herrnstein, J. R. 1997, PhD thesis, HARVARD UNIVERSITY

Herrnstein, J. R., Greenhill, L. J., & Moran, J. M. 1996a, ApJ, 468, L17

Herrnstein, J. R., Moran, J. M., Greenhill, L. J., et al. 1996b, in Astronomical Society of the Pacific Conference Series, Vol. 103, The Physics of Liners in View of Recent Observations, ed. M. Eracleous, A. Koratkar, C. Leitherer, & L. Ho, 193

Herrnstein, J. R., Moran, J. M., Greenhill, L. J., et al. 1997, ApJ, 475, L17

Herrnstein, J. R., Moran, J. M., Greenhill, L. J., & Trotter, A. S. 2005, ApJ, 629, 719

Herrnstein, J. R., Moran, J. M., Greenhill, L. J., et al. 1999, Nature, 400, 539

Hinshaw, G., Weiland, J. L., Hill, R. S., et al. 2009, ApJS, 180, 225

Hinshaw, G., Larson, D., Komatsu, E., et al. 2013, ApJS, 208, 19

Ho, P. T. P., Martin, R. N., Henkel, C., & Turner, J. L. 1987, ApJ, 320, 663

Hoffman, L., & Loeb, A. 2006, ApJ, 638, L75

Hogg, D. W. 1999, ArXiv Astrophysics e-prints, astro-ph/9905116

Hogg, D. W., Bovy, J., & Lang, D. 2010, ArXiv e-prints, arXiv:1008.4686

Hubble, E. 1929, Proceedings of the National Academy of Science, 15, 168

Huchra, J. P., Geller, M. J., Clemens, C. M., Tokarz, S. P., & Michel, A. 1992, Bulletin d'Information du Centre de Donnees Stellaires, 41, 31

Huchra, J. P., Macri, L. M., Masters, K. L., et al. 2012, ApJS, 199, 26

Huchtmeier, W. K., Witzel, A., Kuehr, H., Pauliny-Toth, I. I., & Roland, J. 1978, A&A, 64, L21

Humphreys, E. M. L., Argon, A. L., Greenhill, L. J., Moran, J. M., & Reid, M. J. 2005a, in Astronomical Society of the Pacific Conference Series, Vol. 340, Future Directions in High Resolution Astronomy, ed. J. Romney & M. Reid, 466

Humphreys, E. M. L., Greenhill, L. J., Reid, M. J., et al. 2005b, ApJ, 634, L133

Humphreys, E. M. L., Reid, M. J., Greenhill, L. J., Moran, J. M., & Argon, A. L. 2008, ApJ, 672, 800

Humphreys, E. M. L., Reid, M. J., Moran, J. M., Greenhill, L. J., & Argon, A. L. 2013, ApJ, 775, 13

Ishihara, Y., Nakai, N., Iyomoto, N., et al. 2001, PASJ, 53, 215

Jaffe, W., Meisenheimer, K., Röttgering, H. J. A., et al. 2004, Nature, 429, 47

Józsa, G. I. G., Kenn, F., Klein, U., & Oosterloo, T. A. 2007, A&A, 468, 731

Ju, W., Greene, J. E., Rafikov, R. R., Bickerton, S. J., & Badenes, C. 2013, ApJ, 777, 44

Karachentsev, I. D., Makarov, D. I., & Kaisina, E. I. 2013, AJ, 145, 101

Kardashev, N. S. 1986, AZh, 63, 845

Kartje, J. F., Königl, A., & Elitzur, M. 1999, ApJ, 513, 180

Keating, S. K., Everett, J. E., Gallagher, S. C., & Deo, R. P. 2012, ApJ, 749, 32

Kennicutt, Jr., R. C., Freedman, W. L., & Mould, J. R. 1995, AJ, 110, 1476

Kim, D.-C., Evans, A. S., Stierwalt, S., & Privon, G. C. 2016, ApJ, 824, 122

Kim, M., Ho, L. C., Peng, C. Y., & Im, M. 2007, ApJ, 658, 107

Komossa, S., Burwitz, V., Hasinger, G., et al. 2003, ApJ, 582, L15

Kondratko, P. T., Greenhill, L. J., & Moran, J. M. 2005, ApJ, 618, 618

—. 2008, ApJ, 678, 87

Kondratko, P. T., Greenhill, L. J., Moran, J. M., et al. 2003, in Bulletin of the American Astronomical Society, Vol. 35, American Astronomical Society Meeting Abstracts, 1311

Koranyi, D. M., & Geller, M. J. 2002, AJ, 123, 100

Kormendy, J., & Richstone, D. 1995, ARA&A, 33, 581

Krips, M., Martín, S., Eckart, A., et al. 2011, ApJ, 736, 37

Kukolich, S. G. 1969, The Journal of Chemical Physics, 50, 3751

Kuo, C.-Y. 2011, PhD thesis, University of Virginia

Kuo, C. Y., Braatz, J. A., Reid, M. J., et al. 2013, ApJ, 767, 155

Kuo, C.-Y., Reid, M. J., Braatz, J. A., et al. 2017a, ArXiv e-prints, arXiv:1712.09170

Kuo, C. Y., Braatz, J. A., Condon, J. J., et al. 2011, ApJ, 727, 20

Kuo, C. Y., Braatz, J. A., Lo, K. Y., et al. 2015, ApJ, 800, 26

Kuo, C. Y., Constantin, A., Braatz, J. A., et al. 2017b, ArXiv e-prints, arXiv:1712.04204

Lang, R., & Bender, P. L. 1973, ApJ, 180, 647

Lenz, D. D., & Ayres, T. R. 1992, PASP, 104, 1104

Lepine, J. R. D., & Marques Dos Santos, P. 1977, Nature, 270, 501

Litvak, M. M. 1973, ApJ, 182, 711

—. 1974, ARA&A, 12, 97

Liu, X., Civano, F., Shen, Y., et al. 2013, ApJ, 762, 110

Lo, K. Y. 2005, ARA&A, 43, 625

Lovell, J. E. J., Jauncey, D. L., Bignall, H. E., et al. 2003, AJ, 126, 1699

Lovell, J. E. J., Rickett, B. J., Macquart, J.-P., et al. 2008, ApJ, 689, 108

Ludwig, R. R., Greene, J. E., Barth, A. J., & Ho, L. C. 2012, ApJ, 756, 51

Magain, P., Letawe, G., Courbin, F., et al. 2005, Nature, 437, 381

Makishima, K., Fujimoto, R., Ishisaki, Y., et al. 1994, PASJ, 46, L77

Mamyoda, K., Nakai, N., Yamauchi, A., Diamond, P., & Huré, J.-M. 2009, PASJ, 61, 1143

Maoz, E. 1995, ApJ, 447, L91

Maoz, E., & McKee, C. F. 1998, ApJ, 494, 218

Markwardt, C. B. 2009, in Astronomical Society of the Pacific Conference Series, Vol. 411, Astronomical Data Analysis Software and Systems XVIII, ed. D. A. Bohlender, D. Durand, & P. Dowler, 251

Marzke, R. O., Huchra, J. P., & Geller, M. J. 1996, AJ, 112, 1803

McCallum, J. N., Ellingsen, S. P., Jauncey, D. L., Lovell, J. E. J., & Greenhill, L. J. 2005, AJ, 129, 1231

McCallum, J. N., Ellingsen, S. P., & Lovell, J. E. J. 2007, MNRAS, 376, 549

McCallum, J. N., Ellingsen, S. P., Lovell, J. E. J., Phillips, C. J., & Reynolds, J. E. 2009, MNRAS, 392, 1339

Merritt, D., Berczik, P., & Laun, F. 2007, AJ, 133, 553

Merritt, D., Milosavljević, M., Favata, M., Hughes, S. A., & Holz, D. E. 2004, ApJ, 607, L9

Milosavljević, M., & Merritt, D. 2003, ApJ, 596, 860

Miyoshi, M., Moran, J., Herrnstein, J., et al. 1995, Nature, 373, 127

Modjaz, M., Moran, J. M., Kondratko, P. T., & Greenhill, L. J. 2005, ApJ, 626, 104

Moran, J., Greenhill, L., Herrnstein, J., et al. 1995, Proceedings of the National Academy of Science, 92, 11427

Moran, J. M. 1997, in Astronomical Society of the Pacific Conference Series, Vol. 113, IAU Colloq. 159: Emission Lines in Active Galaxies: New Methods and Techniques, ed. B. M. Peterson, F.-Z. Cheng, & A. S. Wilson, 402

Moran, J. M., Papadopoulos, G. D., Burke, B. F., et al. 1973, ApJ, 185, 535

Mullaney, J. R., Ward, M. J., Done, C., Ferland, G. J., & Schurch, N. 2009, MNRAS, 394, L16

Nakai, N., Inoue, M., & Miyoshi, M. 1993, Nature, 361, 45

Narayan, R. 1992, Philosophical Transactions of the Royal Society of London Series A, 341, 151

Nasonova, O. G., de Freitas Pacheco, J. A., & Karachentsev, I. D. 2011, A&A, 532, A104

Nedoluha, G. E., & Watson, W. D. 1991, ApJ, 367, L63

—. 1992, ApJ, 384, 185

Nelson, C. H., & Whittle, M. 1995, ApJS, 99, 67

Neufeld, D. A., & Maloney, P. R. 1995, ApJ, 447, L17

Neufeld, D. A., Maloney, P. R., & Conger, S. 1994, ApJ, 436, L.127

Neufeld, D. A., & Melnick, G. J. 1991, ApJ, 368, 215

Norris, R. P. 1984, Proceedings of the Astronomical Society of Australia, 5, 514

Peiris, H. V., Komatsu, E., Verde, L., et al. 2003, ApJS, 148, 213

Pesce, D. W., Braatz, J. A., Condon, J. J., et al. 2015, ApJ, 810, 65

Pesce, D. W., Braatz, J. A., & Impellizzeri, C. M. V. 2016, ApJ, 827, 68

Planck Collaboration, Abergel, A., Ade, P. A. R., et al. 2011, A&A, 536, A21

—. 2014a, A&A, 571, A11

Planck Collaboration, Ade, P. A. R., Aghanim, N., et al. 2014b, A&A, 571, A16

Planck Collaboration, Adam, R., Ade, P. A. R., et al. 2016a, A&A, 594, A1

Planck Collaboration, Ade, P. A. R., Aghanim, N., et al. 2016b, A&A, 594, A13

Planck Collaboration, Aghanim, N., Ashdown, M., et al. 2016c, A&A, 596, A107

Ponomarev, V. O., Smith, H. A., & Strelnitski, V. S. 1994, ApJ, 424, 976

Pringle, J. E. 1981, ARA&A, 19, 137

Reid, M. J., Braatz, J. A., Condon, J. J., et al. 2009, ApJ, 695, 287

—. 2013, ApJ, 767, 154

Reid, M. J., & Honma, M. 2014, ARA&A, 52, 339

Reid, M. J., & Moran, J. M. 1981, ARA&A, 19, 231

Reid, M. J., Moran, J. M., & Gwinn, C. R. 1988, in IAU Symposium, Vol. 129, The Impact of VLBI on Astrophysics and Geophysics, ed. M. J. Reid & J. M. Moran, 169–174

Reid, M. J., Menten, K. M., Brunthaler, A., et al. 2014, ApJ, 783, 130

Remijan, A., Adams, M., Akiyama, E., et al. 2015, ALMA Cycle 3 Technical Handbook Version 1.0

Rice, M. S., Martini, P., Greene, J. E., et al. 2006, ApJ, 636, 654

Richards, G. T., Vanden Berk, D. E., Reichard, T. A., et al. 2002, AJ, 124, 1

Richards, J. L., Max-Moerbeck, W., Pavlidou, V., et al. 2011, ApJS, 194, 29

Rickett, B. J., Kedziora-Chudczer, L., & Jauncey, D. L. 2002, ApJ, 581, 103

Riess, A. G., Filippenko, A. V., Challis, P., et al. 1998, AJ, 116, 1009

Riess, A. G., Macri, L. M., Hoffmann, S. L., et al. 2016, ApJ, 826, 56

Riess, A. G., Casertano, S., Yuan, W., et al. 2018, ApJ, 855, 136

Rothman, L. S., Gordon, I. E., Babikov, Y., et al. 2013, J. Quant. Spec. Radiat. Transf., 130, 4

Rudnick, L., & Edgar, B. K. 1984, ApJ, 279, 74

Runnoe, J. C., Eracleous, M., Pennell, A., et al. 2017, MNRAS, 468, 1683

Rybicki, G. B., & Lightman, A. P. 1986, Radiative Processes in Astrophysics, 400

Salvatier, J., Wiecki, T. V., & Fonnesbeck, C. 2016, PeerJ Computer Science, 2, e55

Sandage, A., & Tammann, G. A. 1976, ApJ, 210, 7

Sandage, A. R. 1970, Physics Today, 23, 34

Sawada-Satoh, S., Inoue, M., Shibata, K. M., et al. 2000, PASJ, 52, 421

Schlickeiser, R. 1984, A&A, 136, 227

Schutz, B. 2009, A First Course in General Relativity

Scoville, N., Aussel, H., Sheth, K., et al. 2014, ApJ, 783, 84

Shklovsky, I. S. 1982, in IAU Symposium, Vol. 97, Extragalactic Radio Sources, ed. D. S. Heeschen & C. M. Wade, 475–481

Silverman, B. 1986, Density Estimation for Statistics and Data Analysis, Chapman & Hall/CRC Monographs on Statistics & Applied Probability (Taylor & Francis)

Sofue, Y. 2013, PASJ, 65, 118

Sorce, J. G., Tully, R. B., & Courtois, H. M. 2012, ApJ, 758, L12

Spaans, M. 2005, ArXiv Astrophysics e-prints, astro-ph/0501069

Spergel, D. N., Flauger, R., & Hložek, R. 2015, Phys. Rev. D, 91, 023518

Springob, C. M., Haynes, M. P., Giovanelli, R., & Kent, B. R. 2005, ApJS, 160, 149

Staveley-Smith, L., & Davies, R. D. 1987, MNRAS, 224, 953

Sullivan, III, W. T. 1973, ApJS, 25, 393

Sun, A.-L., Greene, J. E., Impellizzeri, C. M. V., et al. 2013, ApJ, 778, 47

Suyu, S. H., Auger, M. W., Hilbert, S., et al. 2013, ApJ, 766, 70

Suyu, S. H., Bonvin, V., Courbin, F., et al. 2017, MNRAS, 468, 2590

Tarchi, A., Castangia, P., Columbano, A., Panessa, F., & Braatz, J. A. 2011, A&A, 532, A125

Theureau, G., Bottinelli, L., Coudreau-Durand, N., et al. 1998, A&AS, 130, 333

Theureau, G., Coudreau, N., Hallet, N., et al. 2005, A&A, 430, 373

Tisserand, P., Le Guillou, L., Afonso, C., et al. 2007, A&A, 469, 387

Tonry, J., & Davis, M. 1979, AJ, 84, 1511

Tremonti, C. A., Heckman, T. M., Kauffmann, G., et al. 2004, ApJ, 613, 898

Trimble, V. 1996, PASP, 108, 1073

Trotter, A. S., Greenhill, L. J., Moran, J. M., et al. 1998, ApJ, 495, 740

Tully, R. B., Courtois, H. M., & Sorce, J. G. 2016, AJ, 152, 50

Tully, R. B., Courtois, H. M., Dolphin, A. E., et al. 2013, AJ, 146, 86

Turner, B. E., Buhl, D., Churchwell, E. B., Mezger, P. G., & Snyder, L. E. 1970, A&A, 4, 165

Ulvestad, J. S. 2000, Advances in Space Research, 26, 735

van der Kruit, P. C., Oort, J. H., & Mathewson, D. S. 1972, A&A, 21, 169

Vila Vilaro, B., Leon, S., Dent, W., et al. 2011, ALMA Cycle 0 Technical Handbook Version 1.0

Vlemmings, W., Diamond, P. J., & van Langevelde, H. J. 2001, A&A, 375, L1

Vlemmings, W. H. T., Bignall, H. E., & Diamond, P. J. 2007, ApJ, 656, 198

Vlemmings, W. H. T., & van Langevelde, H. J. 2005, A&A, 434, 1021

Walker, M. A. 1998, MNRAS, 294, 307

Walker, R. C. 1984, ApJ, 280, 618

Wang, J.-M., Chen, Y.-M., Hu, C., et al. 2009, ApJ, 705, L76

Wang, L., Greene, J. E., Ju, W., et al. 2017, ApJ, 834, 129

Watson, W. D., & Wallin, B. K. 1994, ApJ, 432, L35

Weaver, H., Williams, D. R. W., Dieter, N. H., & Lum, W. T. 1965, Nature, 208, 29

Wilson, A. S., Braatz, J. A., & Henkel, C. 1995, ApJ, 455, L127

Yamauchi, A., Nakai, N., Sato, N., & Diamond, P. 2005, in Astronomical Society of the Pacific Conference Series, Vol. 340, Future Directions in High Resolution Astronomy, ed. J. Romney & M. Reid, 241

Zhang, J. S., Henkel, C., Kadler, M., et al. 2006, A&A, 450, 933

Zhu, X.-J., Hobbs, G., Wen, L., et al. 2014, MNRAS, 444, 3709